JAERI-Review
99-003

PROGRESS REPORT ON NEUTRON SCATTERING RESEARCH (APRIL 1, 1997 - MARCH 31, 1998)

February 1999

(Eds.) Jun-ichi SUZUKI, Satoru FUJIWARA and Kazuya AIZAWA

日本原子力研究所
Japan Atomic Energy Research Institute

本レポートは，日本原子力研究所が不定期に公刊している研究報告書です。
入手の問合わせは，日本原子力研究所研究情報部研究情報課（〒319-1195　茨城県那珂郡東海村）あて，お申し越しください。なお，このほかに財団法人原子力弘済会資料センター（〒319-1195　茨城県那珂郡東海村日本原子力研究所内）で複写による実費頒布をおこなっております。

This report is issued irregularly.
Inquiries about availability of the reports should be addressed to Research Information Division, Department of Intellectual Resources, Japan Atomic Energy Research Institute, Tokai-mura, Naka-gun, Ibaraki-ken, 319-1195, Japan.

編集兼発行　　日本原子力研究所

JAERI-Review 99-003

Progress Report on Neutron Scattering Research
(April 1, 1997 - March 31, 1998)

(Eds.) Jun-ichi SUZUKI, Satoru FUJIWARA and Kazuya AIZAWA

Advanced Science Research Center
(Tokai Site)
Japan Atomic Energy Research Institute
Tokai-mura, Naka-gun, Ibaraki-ken

(Received January 14, 1999)

The present issue summarizes research progress in neutron scattering at Japan Atomic Energy Research Institute (JAERI) by utilizing the research reactor (JRR-3M) during the period between April 1, 1997 and March 31, 1998.

Keywords: Neutron Scattering and JRR-3M

中性子散乱成果報告集
(1997年度次報告)

日本原子力研究所先端基礎研究センター
(編)　鈴木　淳市・藤原　悟・相澤　一也

(1999年1月14日受理)

この小冊子は、日本原子力研究所の先端基礎研究センターに所属する中性子散乱グループの研究を中心に、改3号炉(JRR-3M)を利用した所内の中性子散乱研究、所外との協力研究および共同研究の1997年4月～1998年3月の期間における成果をまとめたものである。

日本原子力研究所(東海駐在)：〒319-1195　茨城県那珂郡東海村白方白根2-4

Contents

List of JAERI Instruments

A. Neutron Scattering Instruments

Beam Port	Instrument	Moderator	Instrument Staff
1G	High Resolution Powder Diffractometer (HRPD)	Thermal (H_2O)	Yukio Morii, Yutaka Shimojo
1G-A	Diffractometer for Biological Crystallography-I (BIX-I)	Thermal (H_2O)	Nobuo Niimura
2G	Triple-Axis Spectrometer (TAS-1)	Thermal (H_2O)	Toyotaka Osakabe, Susumu Katano
3G	Apparatus for Precise Neutron Optics and Neutron Diffraction Topography (PNO)	Thermal (H_2O)	Hiroshi Tomimitsu, Kazuya Aizawa
T2-1	Residual Stress Analysis Equipment (RESA)	Thermal (H_2O)	Nobuaki Minakawa
T2-3	Diffractometer for Biological Crystallography-II (BIX-II)	Thermal (H_2O)	Satoru Fujiwara, Nobuo Niimura
T2-4	Triple-Axis Spectrometer (TAS-2)	Thermal (H_2O)	Yoshinobu Ishii, Nobuaki Minakawa
C2-1	Low Energy Triple-Axis Spectrometer (LTAS)	Cold (Liquid H_2)	Naoto Metoki, Nobuaki Minakawa
C3-2	Small-Angle Neutron Scattering Instrument (SANS-J)	Cold (Liquid H_2)	Jun-ichi Suzuki, Satoshi Koizumi

B. Special Accessories

B-1. Cryostats, Magnets, and Furnaces

Accessory	Number	Performance	Instrument Staff
Dilution Refrigerator	1	T_{min}=10mK, H_{max}=5T (Vertical)	Naoto Metoki, Yoshihiro Koike
Dilution Refrigerator (Liquid-^{4}He-Free)	2	T_{min}=50mK	Yoshihiro Koike, Yukio Morii
10T Magnet (Liquid-^{4}He-Free)	1	T_{min}=100mK, H_{max}=10T (Vertical)	Yuki Matsuoka, Ken-ichi Oikawa, Susumu Katano
^{3}He Cryostat	1	T_{min}=0.3K, H_{max}=6T (Vertical)	Naoto Metoki
Orange Cryostat	1	T_{min}=1.5K	Toyotaka Osakabe
Horizontal Magnet	1	T_{min}=1.5K, H_{max}=5T (Horizontal)	Jun-ichi Suzuki, Masaya Watahiki
4K Cryostat	2	T_{min}=4K	Yutaka Shimojo
10K Cryostat	6	T_{min}=10K	Yutaka Shimojo
Frunace for Soft Matter	1	T=0～300°C	Satoshi Koizumi
Furnace	1	T_{max}=1,100K	Yoshinobu Ishii

B-2. Pressure Devices

McWhan Cell	3	P_{max}=2.5GPa	Toyotaka Osakabe
Sapphire Anvil Cell (under development)	several	P_{max}=5GPa	Toyotaka Osakabe
Oscillatory Shear Machine	1	T=RT～200°C, Amplitude=0.01～2mm, Frequency=0.1～100Hz	SatoshiKoizumi
Tension Testing Machine	1	Tensil Speed=0～0.01mm/sec, Range of Load=50～1,000kgf±1%	Nobuaki Minakawa

B-3. Detectors

Neutron Imaging Plate	several	Resolution=100μm	Yuko Haga, Nobuaki Minakawa

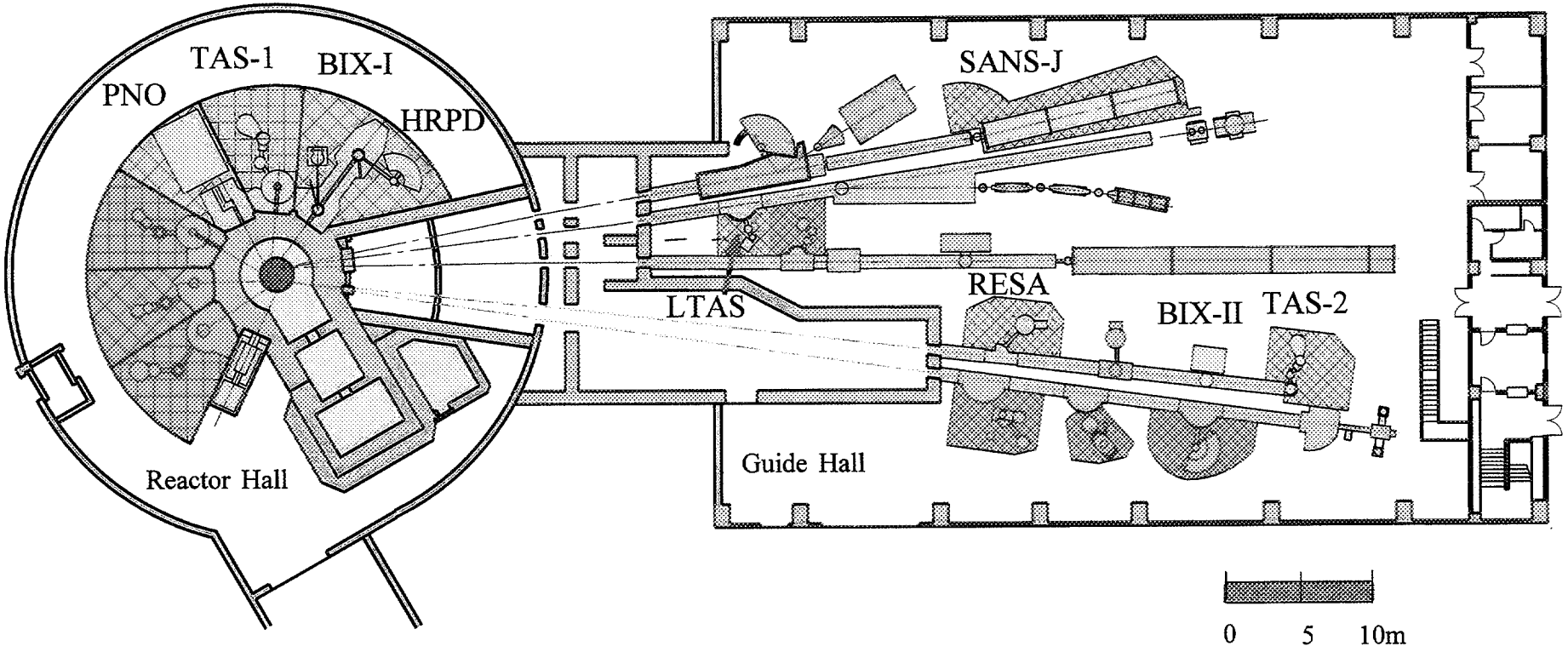

Neutron Scattering Instruments of JAERI Groups

Members of Neutron Scattering Groups in JAERI

1. Topics at JAERI

More than 80 experiments in covering the wide scientific field that includes soft matter, strongly correlated electron systems, materials science, etc. were carried out on the 9 neutron scattering instruments in Japanese Fiscal Year (JFY) 1997. Some topics obtained for each scientific field are reported in this chapter. Understanding the nature of the matter under extreme conditions (low temperature, high magnetic field, and high pressure) is one of the main subjects at JAERI. The development of a liquid-^{4}He-free 10 Tesla magnet and dilution refrigerator is also summarized in this chapter. This concept makes it possible to get the extreme condition easily with low operating cost. New scientific fields will be opened using these accessories at JAERI. All the research reports appear in the next chapter.

Biology

Hydrogen atoms in a protein play an essential role in performing specific functions of the protein, as well as contribute through hydrogen-bond network to the stability of the protein. Neutron diffraction, from which positions of the hydrogen atoms can be determined, is important in studying the structure-function relationship and stability of proteins. We constructed a diffratometer with a neutron imaging plate, BIX-II, and started a new project to explore the protonation of amino acid residues in the protein at various pH (**Fujiwara, 2.1.1**). Using hen egg-white Lysozyme as a model protein, neutron diffraction of single crystals of this protein at various pH has been measured.

Small-angle neutron scattering is also important to get in situ structural information. Crystallization of thermolysin (**Ooshima, 2.1.3**) and hydrocarbon uptakes by insect lipophorin (**Katagiri, 2.1.4**) were measured with SANS-J. Although these are preliminary experiments, more studies will start in the near future.

Soft Matter

For a glass-forming copolyester polymer, a neutron polarization analysis was performed to separate the elastic spin-incoherent (ESINC) scattering from the elastic coherent scattering. By the elastic coherent scattering, a pico-second motion of this glass-forming material was investigated. The elastic incoherent structure factor (EISF), on the other hand, gave a long time-averaged self-correlation for local motions of segmental units trapped in "structural cage" of the glassy state. The ESINC scattering obtained at far above the glass transition temperature T_g visualized the appearance of EISF for rotational relaxation of segmental units in a loose cage, which strongly contributes on the anharmonic increase of mean square displacements. At around or below T_g, the ESINC scattering was well described by the Debye-Waller factor, originating from the harmonic vibrational motions in a tight cage (**Koizumi, 2.2.1-2**).

A share flow, imposed on a semidilute polymer solution in a single phase, enhances concentration fluctuations toward phase separation. In order to study such share-induced phase separation, SANS measurements on a semidilute solution of high molecular weight deuterated polystyrene and dictyl phthalate were carried using a newly developed dynamic data acquisition system. It became clear that the structures induced by oscillatory share flow are the distinctive phase-separated structures rather than the concentration fluctuation in a single phase (**Saito, 2.2.3**).

Strongly Correlated Electron Systems and Superconductivity

The superconducting gap observed in the spin excitation spectra of a heavy fermion superconductor UPd_2Al_3 is one of the most exciting results in 1997. The fact that the superconducting gap which is a charge gap, appearing in the spin excitation gap, is a direct evidence that the origin of the superconductivity in this compound is magnetic (**Fig. 1**). The coupling of the magnetic and superconducting order-parameters was also found in UNi_2Al_3, UPt_3, and URu_2Si_2. Therefore, it is concluded that the coupling of the order-parameters would be a characteristic property in heavy fermion superconductors (**Metoki, 2.3.1; Honma, 2.3.2**).

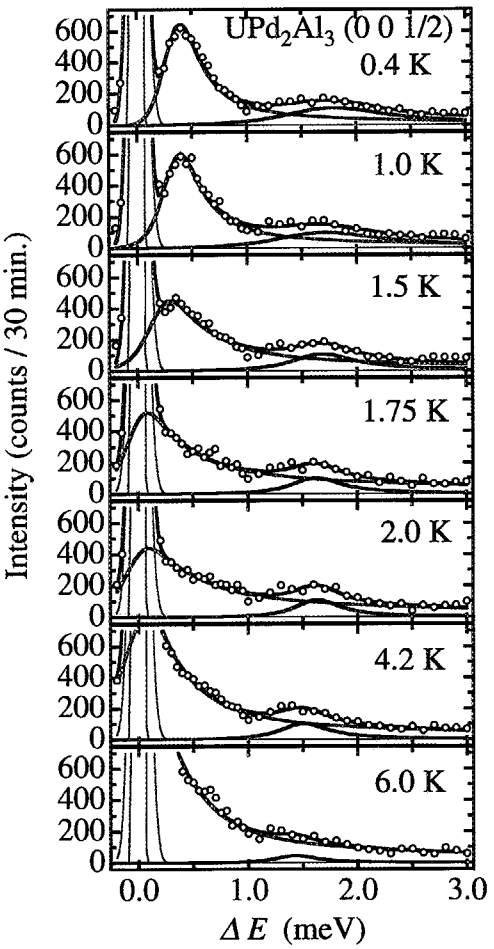

Fig.1 Neutron inelastic scattering profiles of UPd_2Al_3 at (0 0 1/2).

The antiferromagnetic correlation in UPt_3 has been studied at ultra-low temperatures. The (1/2 0 1) antiferromagnetic peak exhibits remarkable narrowing in the linewidth below 50 mK (**Fig. 2**), which would be a precursive phenomenon of the static and long range magnetic ordering (**Koike, 2.3.3**).

Experiments on CeP under magnetic field or under high pressure clarified that unusual magnetic properties of this compound originate from an appearance of 2 μ_B Ce ions with the Γ_7 crystal field ground state. Along the [001] direction these ions couple ferromagnetically over the double layers. Between these pairs, antiferromagnetic ordering of Ce ions of about 0.7 μ_B is formed with different periodicity. The appearance of these 2 μ_B Ce ions can be explained by the formation of the magnetic polaron state, which is stabilized more easily under high pressure than under magnetic field. Such magnetic polaron states are common phenomena in the semi-metallic Ce monopnictides (**Osakabe, 2.3.5**).

In the two-leg ladder material $Sr_{14}Cu_{24}O_{41}$, spin correlations are short-ranged, and a spin liquid ground state with a spin gap is formed. With hole doping, this system is expected to show a transition to the superconducting state. Recently such superconductivity has been observed in heavily Ca doped compound $Sr_{14-x}Ca_xCu_{24}O_{41}$ with x over 11.5 and under high pressures above about 3 GPa. In the neutron scattering experiments, the Ca concentration dependence of the spin gap energy and the spin excitations has been investigated. The result showed that the spin gap energy does not change from that of the pure system of about 32 meV. The dispersion relation of the spin excitations indicates that the exchange energy of this doped compound is still high ($\sim$ 100 meV). This Ca doped compound, moreover, forms an antiferromagnetic ordering below 2 K in the original spin singlet state. The magnetism found here should be considered in relation with its unique superconductivity (**Akimitsu, 2.3.10-11**).

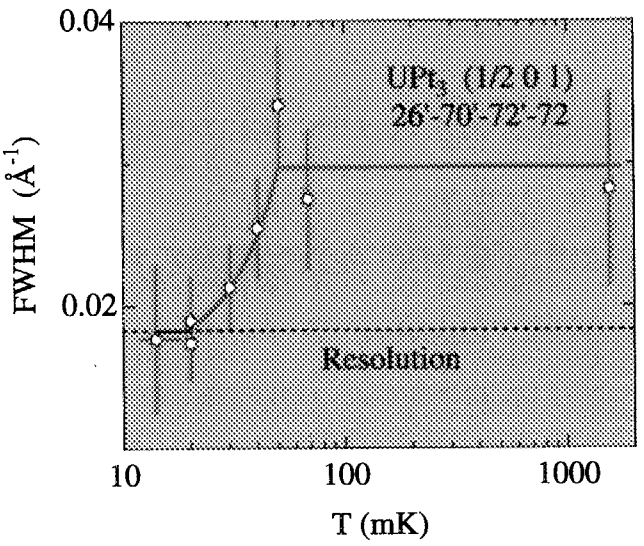

Fig.2 Temperature dependence of the linewidth of the (1/2 0 1) peak profile in UPt_3.

Vortex structures have been studied on several superconducting materials ($CeRu_2$, UPd_2Al_3, $Bi_2Sr_2CaCu_2O_{8+\delta}$, etc.) to investigate the exotic superconducting mixed state. For highly anisotropic layered superconductors like $Bi_2Sr_2CaCu_2O_{8+\delta}$, Josephson vortices were theoretically expected when the magnetic field is parallel to the CuO_2 layers. SANS experiments were intensively performed to observe the new-type vortex structure. However, it happens to be clear that a normal triangular vortex lattice becomes unstable and disappears even in the magnetic field slightly tilted ($\sim$15°) from the crystalline c axis. The angular dependence of the scattering profile shows the decrease of the correlation of the vortex line along the field. This disappearance of the vortex lattice would be understood from the line decomposition due to the weak coupling of the superconducting layers (**Suzuki, 2.3.14**).

Magnetism and Low Temperature Physics

It is theoretically predicted that Heisenberg spins on the kagomé lattice with an antiferromagnetic coupling show large fluctuation at finite temperatures. Therefore, the ground state of the kagomé lattice antiferromagnet is a main subject of low-dimensional magnets. Neutron diffraction measurements on $KCr_3(OD)_6(SO_4)_2$ and $KFe_3(OH)_6(SO_4)_2$ with kagomé lattices were carried out. For both compounds, so-called 120° structures were observed at low temperatures (**Inami, 2.4.3-4**).

The ternary system $R_3Pd_{20}X_6$ (R: rare earth, X: Si, Ge) attracts much attention because of the variety of the magnetic properties depending on the rare earth material. The characteristic feature of this system is the successive magnetic phase transition. Neutron diffraction measurements on $Nd_3Pd_{20}Ge_6$ revealed that the Nd atoms on simple cubic 8*c* site show type-II antiferromagnetic order below 1.75 K, whereas Nd atoms on fcc 4*a* site exhibit type-I antiferromagnetic order below the lower transition temperature of 0.54 K. In $U_3Pd_{20}Si_6$, surprisingly however, we found an antiferromagnetic structure of an 8*c* site coexists with a ferromagnetic structure of a 4*a* site (**Tateiwa, 2.4.7-8**).

Structural Physics

A focusing monochromator which consists of eleven slabs of bent Si(533) crystal has been installed at the high resolution powder diffractometer (HRPD). The monochromator provides neutron wavelength of 0.116 nm which is used for the structural analysis in a wide Q range of various materials such as KH_2PO_4 (**Yamamura, 2.5.4**) and hexagonal $BaTiO_3$ (**Noda, 2.5.5**) using the Rietveld fitting and the maximum entropy method.

The mechanism of 3-1 photoisomerization of the 3-cyanoethyl group in a cobaloxim complex has been studied by determining the molecular structure of (3-cyanopropyl-d^{α},d^{α})[(R)-1-1-phenylethylamine] cobaloxime before and after light irradiation (**Fig. 3**) (**Ohhara, 2.5.7-8**).

The compound $\{Fe(\eta^3\text{-}C_8H_{13})[P(OMe)_3]_3\}^+$ is interesting because of their suspected role in hydrosilations and other catalytic reactions involving metallo-silicon compounds. The molecular structure of $TaCp_2(H)(SiMe_2H)_2$ was determined (**Bau, 2.5.9**).

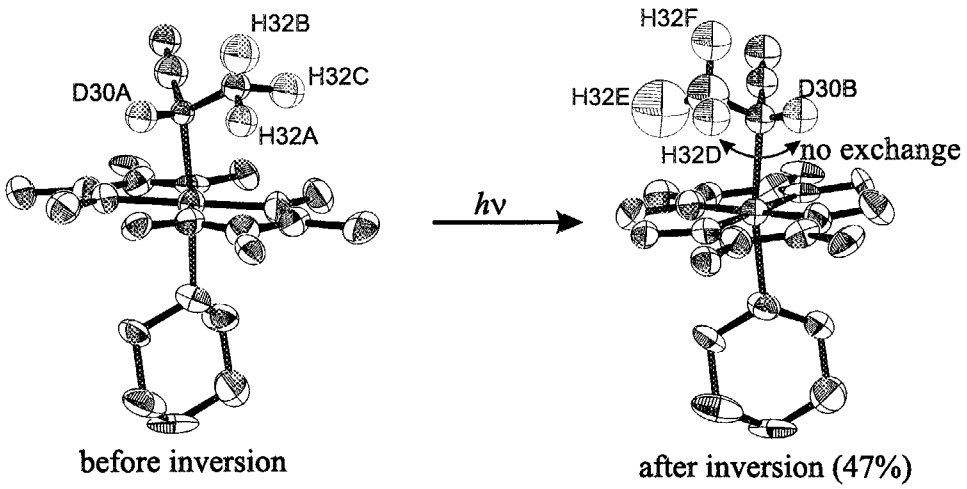

Fig.3 Molecular structure of (3-cyanopropyl-d^{α},d^{α})[(R)-1-1-phenylethylamine] cobaloxime before and after light irradiation.

Materials Science and Industrial Applications

Residual stress analyses have been carried out with the diffractometer, RESA. The investigation was performed on the round robin sample of the Technical Working Area 20 (TWA20) of the Versailles Project on Advanced Materials and Standards (VAMAS). It proved that the data quality is comparable to those of LANL, ORNL and NIST (**Minakawa, 2.6.4**). A welded stainless steel pipe (**Okido, 2.6.5**), a round steel bar (**Inoue, 2.6.6**), a heat treated steel pipe (**Inoue, 2.6.7**), and a SiC particulate reinforced aluminum alloy (**Akiniwa, 2.6.8**) are also investigated.

Fundamental Physics

The apparatus for precise neutron optics, PNO, has been used for interferometry experiments to evaluate neutron scattering length of some isotopes. The coherent scattering length of the ^{69}Ga and ^{71}Ga was evaluated to be 8.063±0.016 and 6.169 ± 0.015 fm, respectively. This method can provide the more accurate value of the neutron scattering length than the other method (**Fig. 4**) (**Tomimitsu, 2.7.1**).

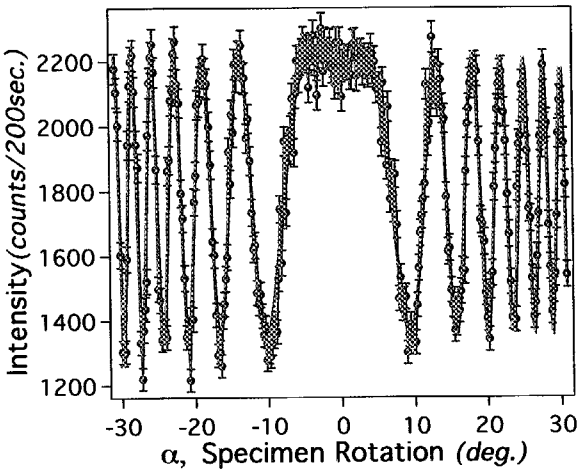

Fig.4 Intensity oscillation curve of ^{69}Ga.

Instrumentation and Methods

A new type of 10 Tesla vertical magnet was developed. The split pair magnet is cooled by two cryocoolers without liquid-^{4}He. The size of the room temperature bore diameter is 50 mm, and the gap is 20 mm. The magnet consists of an inner Nb-Sn coil and an outer Nb-Ti coil. Bi based superconducting current lead was used to reduce a heat load through the wire. The outer diameter, height, and weight of this magnet are 600 mm, 760 mm and 280 kg, respectively. The magnet is cooled down to 3 K in 52 hours, and excited up to 10 Tesla within about 15 minuets. A stable continuous operation at 10 Tesla has been obtained.

A new liquid-^{4}He-free dilution refrigerator (DR) named "mK cryocooler" was developed. The mK cryocooler has no 1 K pot. The ^{3}He-^{4}He mixture is cooled by a pulse-tube/GM hybrid refrigerator and liquefied by a Joule-Thomson (JT) valves. A prototype of the mK cryocooler was made and tested to get mK temperatures (**Fig. 5**). After adjusting JT impedance and improving thermal contact and isolation of the DR elements, the lowest temperature of 77 mK was obtained. It took about 1 day to cool to 4 K and additional about 8 hours to the lowest temperature. Further cryogenic improvement enabled to cool rare-earth compounds to 41 mK in the preliminary neutron beam experiments. The compact mK cryocooler is very suitable for an easy, stable, and low-cost operation. It is convenient for not only neutron scattering experiments but also other sciences. It also can eliminate the loss of neutron beam due

to the transfer of liquid-^{4}He to a conventional DR (**Koike, 2.8.1**).

The neutron imaging plate (NIP) is a powerful detector. However, the disadvantage of the NIP is a point of γ-ray sensitivity. In order to build a new diffractometer for biology at a high γ-ray area of JRR-3M to use an intense beam, it was required to study how to reduce the γ-ray background. The energy dependence of γ-ray sensitivity of the neutron imaging plate (NIP) has been measured. The γ-ray sensitivity is equivalent to one half of that of a neutron at a γ-ray energy less than 300 keV, and 1/40 at greater than 300 keV. The shielding effect of lead for γ-rays in the reactor hall of JRR-3M was also measured for the NIP. It was found that 40 mm thick lead is sufficient to reduce γ-ray background to 1/10. Covering the NIP with an 1 mm thick lead foil provides a decrease of the γ-ray background without reduction of the neutron signal (**Kurihara, 2.8.7; Kumazawa, 2.8.8**).

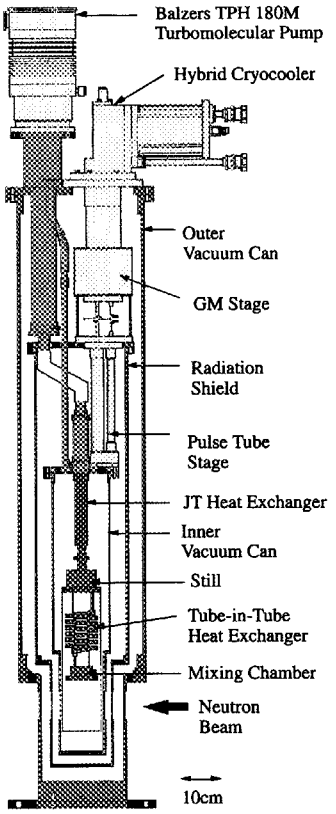

Fig.5 Schematic drawing of the mK cooler.

International Collaborations

Under the US-Japan collaboration, the upgrade of the WAND (Wide-Angle Neutron Diffractometer) has been done. Due to the age of more than 10 years, the old detector got worse in the sensitivity and uniformity. The total counting rate of the detector was also limited to about 10^4 cps due to the usage of a single position sensitive wire. A new ^{3}He detector was developed in order to improve such performance of the WAND and begin studies on the strongly correlated electron systems giving weak signals. The new detector has 624 anodes with 0.2° in pitch and covers a wide scattering range of 125°. The multi-anode system gives a possibility to detect the signal accumulated with high rate (10^5 cps/pixel and 10^7 cps in overall). This produces the capability also for fast time-resolved measurements.

The cooperative research program with BATAN, National Atomic Energy Agency of Indonesia, was carried out. Mr. Sudaryanto stayed at JAERI for four months to study polymer structure by small-angle neutron scattering (**Sudaryanto, 2.2.9**). Five researchers made short visits to BATAN.

2. Research Reports

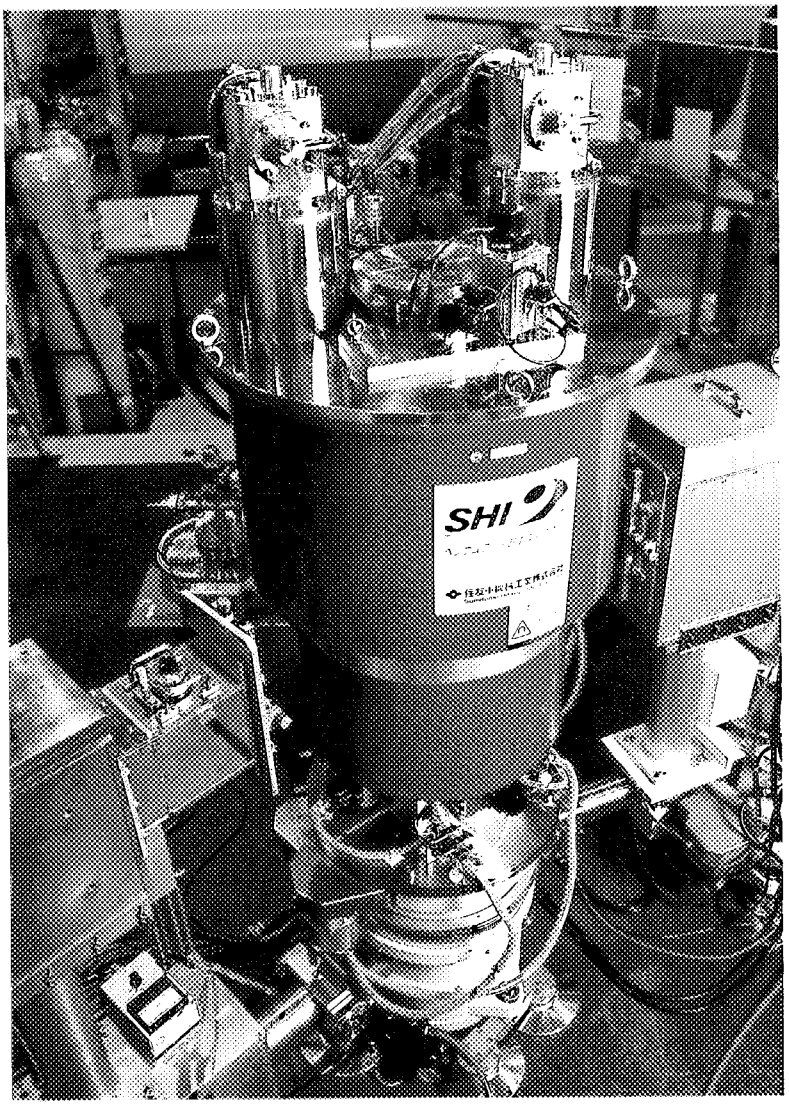

New Liquid-^{4}He-Free 10 Tesla Magnet on a Triple-Axis Spectrometer

This is a blank page.

2.1 Biology

2.1.1

Neutron Diffraction Measurements of Single Crystrals of Hen Egg-White Lysozyme grown at pH 4.9

S. Fujiwara, Y. Yonezawa[1], Y. Karasawa, Y. Minezaki, I. Tanaka, and N. Niimura

Japan Atomic Energy Research Institute, Tokai, Ibaraki 319-1195
[1]Tsukuba College of Technology, Tsukuba, Ibaraki 305-0821

Hydrogen atoms in a protein play an essential role in performing specific functions of the protein, as well as contribute through hydrogen-bond network to the stability of the protein. Particularly, it was suggested from calorimetry measurements that pH dependence of charge distribution of the protein may have important effects on thermodynamic characterization of the proteins[1]. It is thus important to study the pH dependence of protonation of amino acid residues in the protein, in order to elucidate the relationship between structural data and thermodynamic data. Neutron diffraction is unique and powerful in locating the positions of the hydrogen atoms in the protein. We have started a project which explore the protonation of amino acid residues in the protein at various pH.

We chose hen egg-white (HEW) lysozyme as a model protein. Crystals of HEW lysozyme were grown in D_2O at various pH with a concentration gradient method[2]. It was found that the crystals can be grown at pH between 3 and 7. The space group of the crystals was $P4_32_12$, and the cell parameters were a=b=7.91nm and c=3.66nm. Quality of the crystals was checked extensively by measuring the neutron diffraction patterns with BIX-2[3]. The best crystal of HEW lysozyme grown at pH 4.9 was selected as a starter, since the optimum pH of lysozyme activity is 5.0. (The structure of the protein at pH 7 was solved with Laue method[4].) The size of the crystal was about 2 mm×1mm×1 mm.

Data collection of neutron diffraction is the most time-consuming step, so an efficient data-collection strategy should be considered. The strategy could be different in different samples. We measured the neutron diffraction patterns of the lysozyme crystal using the oscillation method with the oscillation range of 0.2, 0.4, and 0.6 degrees. The data that covered the range of 2.4 degrees were collected. We analyzed these data with DENZO and SCALEPACK[5]. It was found that the number of independent reflections was the largest in the data obtained by 0.4 degrees' oscillation. We thus employed the oscillation method of 0.4 degrees to collect the data from the HEW lysozyme crystal. We have started the data collection, and the measurement is now under progress. So far, about 1500 independent reflections were collected.

References

1) S. Kidokoro: Personal communication.
2) M. Ataka and T. Katsura: JAERI Memo 61 (1992) 92-213.
3) S. Fujiwara et al.: Physica B (in press)
2) N. Niimura et al.: Nature Struc. Biol. 4 (1997) 909-914.
5) Z. Otwinowski and W. Minor: Methods

2.1.2 Data collection of triclinic hen egg-white lysozyme by BIX-II

Y.Minezaki, S.Fujiwara, N.Niimura

Advanced Science Research Center, Japan Atomic Energy Research Institute, Tokai, Ibaraki, 319-11

We have already reported the neutron crystal structure analysis of tetragonal hen egg-white (HEW) lysozyme, and the positions of 960 hydrogen atoms in the protein and 157 bound water molecules were determined[1]. The discussion of the nature of the bound water molecules of HEW lysozyme is now under way. It is very interesting to know how many bound water molecules among 157 determined are inherent in HEW lysozyme. The neutron crystal structure analysis of triclinic HEW lysozyme (P1, a=27.2A, b=31.9A, c=34.2A, alpha=88.4, beta=108, gamma=111.7) might provide the answer. We have planned the neutron crystal structure analysis of triclinic HEW lysozyme for that purpose and tried the data collection by using BIX-I and BIX-II. In this report, we will show the preliminary results of data collection method of triclinic HEW lysozyme by using BIX-II.

We have used a single crystal, the size of which was 1.5*1.5*1.5 mm3. The crystal was kindly provided by Harata Group of NIBHT. The very high resolution X-ray structure analysis of triclinic HEW-lysozyme has been already reported by his group[2].

One example of the diffraction pattern obtained by BIX-II for 16 hours exposure time is shown in Fig.1. The minimum d-spacing among the observed diffraction spots is 1.8 A. In order to estimate the proper exposure time for the measurement, we collected images of one hour exposure time 20 times separately. We added two images, three images, and so on till 20 images in the computer. Each resultant corresponds to the image of two hours exposure data, three hours and so on to 20 hours, respectively. From these resultants images we concluded that the minimum exposure time to obtain the maximum number of Bragg reflections is 4 hours.

We have examined the scan condition for the data collection. Four kinds of method, A) 0.2 degree step scan method (where the sample is still during the measurement and after the measurement the sample is rotated by 0.2 degree), B) 0.2 degree sample oscillation during the measurement, C,D)1.0 degree oscillation and E) 1.6 degree oscillation, have been tried. In each measurement, the total sample crystal rotation angle was 2.0 degree and total measurement time of 2.0 degree was kept constant. All the data reduction processes were carried out by using Mac-Denzo. The parameter 'mosaicity' was chosen as 2.0 degree or 1.3 degree. Total number of the collected Bragg reflections and I/s were summarized in Table 1.

It is concluded from the Table that for the triclinic HEW lysozyme; 1) the smaller the sample oscillation is, the higher I/s is and the more the obtaied number of Bragg reflections is., and 2)there is not so much difference between 0.2 degree step scan method and 0.2 degree sample oscillation method.

Table 1

set name	scan method	mos.	total	mean-I	mean-s	mean-I/s
A-set	0.2 step		763	15989	1436.7	10.8
B-set	0.2 osc.	2.0	712	16204	1436.7	10.6
C-set	1.0 osc.	2.0	675	11325	1553.6	7.34
D-set	1.0 osc.	1.3	605	11186	1403.8	7.61
E-set	1.6 osc.	1.3	579	10640	1527.2	6.94

References

[1] N.Niimura, Y.Minezaki, et al., NATURE structural biology 4 11 (1997) 909-912.

[2] K. Harata, et al., PROTEINS:Structure, Function, and Genetics 30 (1998) 232-243.

Fig.1

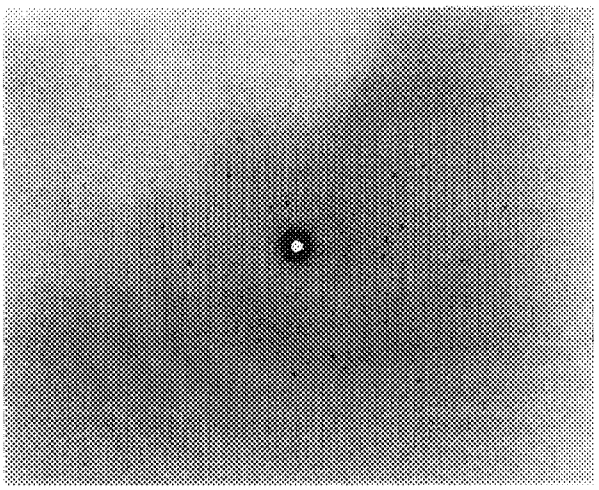

2.1.3 Mechanism of Crystallization of Thermolysin: A Small Angle Neutron Scattering Study

H. Ooshima, K. Igarashi, J. Kato, S. Fujiwara[1], I. Tanaka[1] and N. Niimura[1]

Department of Bioapplied Chemistry, Osaka City University, Osaka 558-8585, Japan

[1]Japan Atomic Energy Research Institute, Tokai, Ibaraki 319-1195, Japan

The crystallization of protease thermolysin proceeds through two step; formation of primary particles (oligomers) and crystal growth by highly ordered aggregation of the primary particles [1]. In the present work, size of the primary particles and its distribution were investigated by small angle neutron scattering (SANS).

SANS experiments were performed at 5 °C for supersaturated and undersaturated thermolysin - D_2O solution. Supersaturation was varied with pH. Wavelength of neutron was 7 Å.

Figure 1 presents a Guinier-plot obtained for the undersaturated solution (3 mg/mL, pH 12.5). Rg was estimated as 16.8 Å, which corresponds to the size of monomeric molecule. This means that thermolysin was dissolved completely in the undersaturation condition. For the super-saturated solution (3 mg/mL, pH 7.5), a different scattering pattern was obtained as shown in Figure 2, indicating the presence of oligomers with uniform size. The estimated Rg was 75.5 Å. The size corresponds to the size of three unit cells (36 thermolysin molecules). This result suggests that growth unit in the crystallization of thermolysin is the oligomers with 75.5 Å of Rg.

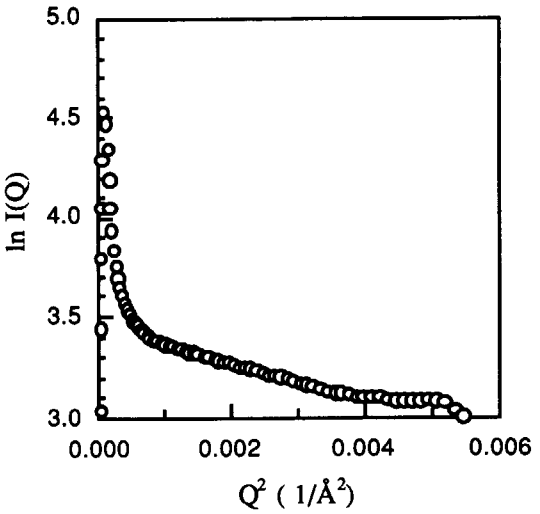

Fig. 1 a Guinier plot of scattering data (thermolysin: 3 mg/mL, pH 12.5)

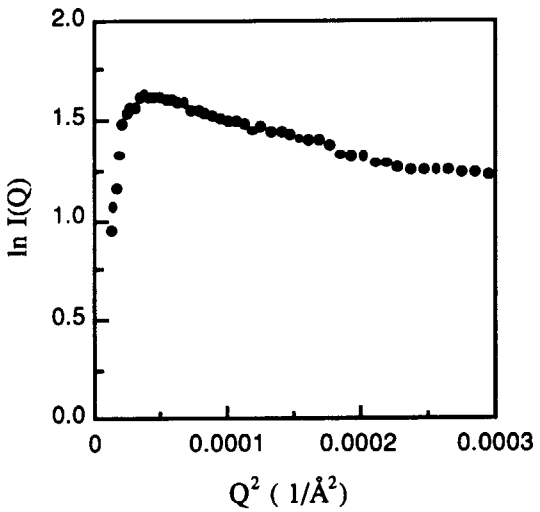

Fig. 2 a Guinier plot of scattering data (thermolysin: 3 mg/mL, pH 7.3)

References

[1] G. Sazaki et al., Journal of Crystal Growth, 130, 357-367 (1993).

2.1.4 Uptake of Hydrocarbons by Insect Lipophorin

C. Katagiri, S. Fujiwara[1], I. Tanaka[1], N. Niimura[1], S. Koizumi[1], M. Sato[2] and Y. Ito[3]

Institute of Low Temperature Science, Hokkaido University, Sapporo 060-0842
[1]Advanced Science Research Center, JAERI, Tokai, Ibaraki 319-1195
[2]Graduate School of Yokohama City University, Yokohama, Kanagawa 236-0027
[3]Faculty of Liberal Arts and Education, Yamanashi University, Koufu 400-0016

Since lipids are not water soluble, they are carried in blood as lipoproteins, macromolecular particles in which the lipids are complexed with a variety of apoproteins. Lipoproteins from different animals have basically a common molecular architecture. The surface is covered with hydrophilic groups of phospholipids and apoproteins, whereas the core contains apolar lipids. Despite the common structural organisation, lipoproteins vary in physiological function, chemical composition, and metabolism. Mammalian lipoproteins transport mainly triacylglycerol and cholesterol esters and are metabolised in peripheral cell and liver. An insect lipoprotein, lipophorin, works as a reusable shuttle to transport diacylglycerol and hydrocarbons from the sites of synthesis, absorption, and storage to sites of utilisation. Diacylglycerol is utilised as a fuel for flight. Hydrocarbons protect insects from desiccation at the cuticular surface.

Lipophorin forms a sphere-like particle of about 170-Å diameter with a particle weight of about 6.0×10^5. All phospholipid constituents of the lipophorin are located in the outer surface with apoprotein. The hydrocarbon component is located in the core of the particle. In the present study, we aimed to observe the process of the transportation of hydrocarbons by the lipophorin. For this purpose, we purified the silkworm pupal lipophorin which does not contain hydrocarbons, and incubated it with the cockroach integument, the site of hydrocarbon synthesis. The structural changes from the hydrocarbon-free to hydrocarbon-containing lipophorin were detected by time-resolved small-angle neutron scattering apparatus (SANS-J). Although the hydrocarbon-free lipophorin is known to take hydrocarbons up *in vitro* from cockroach integument, appreciable changes including profiles (Fig. 1) and Rg (data not shown) were not found during incubation. To overcome this problem, we are currently attempting to modify the incubation procedures.

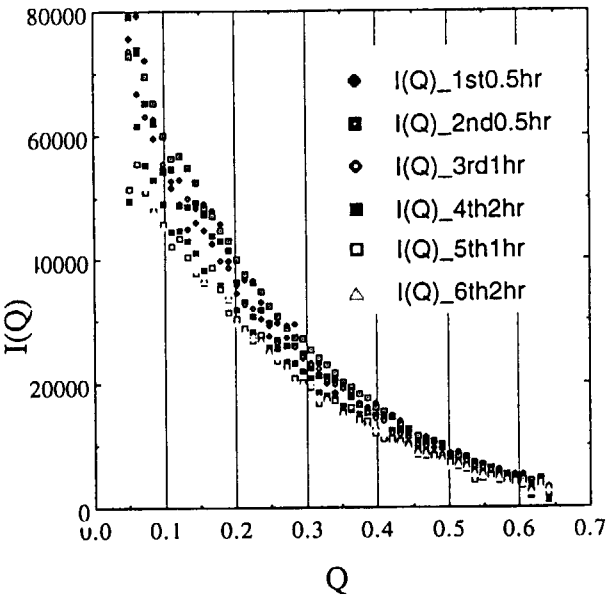

Fig. 1 Time-reolved small-angle neutron scattering profiles of hydrocarbon-free lipophorin which was incubated with cockroach integument.

2.2 Soft Matter

2.2.1 Direct Observation on Elastic Incoherent Structure Factor of Glass-forming Material by Neutron Polarization Analysis I.

Satoshi Koizumi and Toshiya Inami

Advanced Science Research Center, Japan Atomic Energy Research Institute,
Tokai-mura, Ibaraki-ken 319-1195, Japan.

Although the glassy materials have been studied extensively from normal liquids to biopolymers, there still remain several unsettled and attractive topics [1]. In this report, we intend to elucidate an origin of the anharmonic vibrational behavior of glassy materials, employing a unique combination of anisotropic glass-forming copolyester and the neutron polarization analysis [2,3] which allows us to observe the elastic spin incoherent (INC) neutron scattering originating from hydrogen. The elastic incoherent structure factor (EISF), in other words, a long time-averaged self-correlation of local motions, provides information of "*structural cage*" trapping segmental units in a glassy state.

The studied material; thermotropic random copolyester of p-hydroxybenzoic acid (HBA) and 2-hydroxy-6-naphthoic acid (HNA) of 73/27 (mol/mol) having number-average molecular weight of 2.0×10^4, is unique to form an anisotropic glass (or pseudo-hexagonal phase) below T_g (=393K) without perfect crystallization [4,5]. Because of the rigid backbone composed of rigid phenylene and naphtalene groups, which have all hydrogen in a specimen, this material preserves a preferential orientation of rigid chains during a solidification below melting point T_m (=558K). The anisotropic orientation of molecular axis (MA) is greatly advantageous to discuss a relaxational motion in a glassy state.

The neutron polarization analyses have been performed with the polarization triple axis spectrometer TAS-1 at JRR3M at Japan Atomic Energy Research Institute (JAERI) [6]. We employed the Heusler alloys (Cu_2MnAl) as a polarizing monochromator and an analyzer. The spin-flipper was located between the polarizer and the sample position. By using the polarized incident neutron of λ=2.42 A, the polarization of our setup has been determined as 90%$\pm$1 as a whole instrument. We fixed the Heusler analyzer at the angle to obtain the elastic scattering (an energy resolution of ca. 0.6mev) and measured the scattered neutron intensity over a wide scattering angle 2θ from 10° to 90°. The scattering q-vector ($q=4\pi/\lambda\sin(\theta)$) was set parallel ($\phi$=0°) or normal ($\phi$=90°) to a direction of the MA (see a inset of Fig. 1). The obtained spectra were corrected for the background scattering. The transmission of the sample specimens was more than 90% so that the effect of multiple scattering was neglected in our data analyses.

Figure 1 shows the elastic scattering profiles of ϕ=90° obtained at 300K for both conditions of the spin-flipper *on* and *off*. In the case of spin-flipper *off*, corresponding to spin non-flip process, the intense equatorial reflection (110) of the pseudo-hexagonal phase [5] can be observed at around 2θ=30°, while in the case of the spin-flipper *on*, corresponding to spin flip process, the INC scattering can be observed without any reflection.

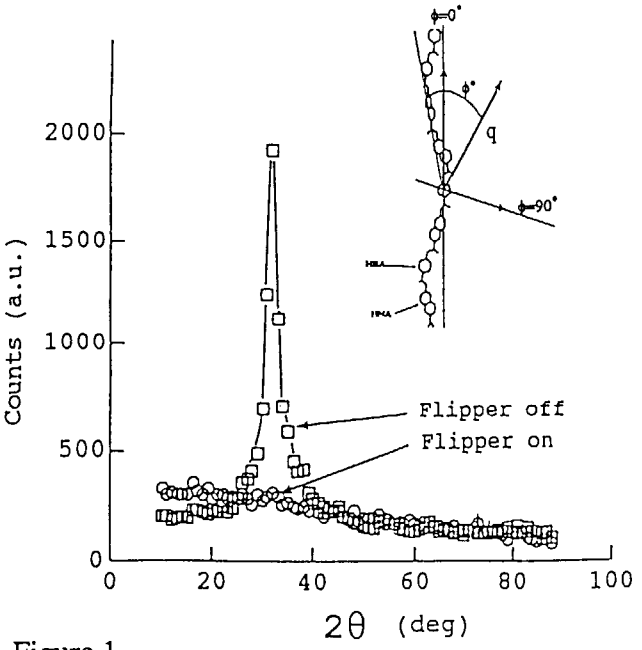

Figure 1

The differential scattering cross sections, for conditions of spin *flip* and *non-flip*, can be given as follows [2,3],

$$\left(\frac{d\sigma}{d\Omega}\right)_{sf} \sim \frac{2}{3}\left(\frac{d\sigma}{d\Omega}\right)_{INC}$$

$$\left(\frac{d\sigma}{d\Omega}\right)_{nsf} \sim \frac{1}{3}\left(\frac{d\sigma}{d\Omega}\right)_{INC} + \left(\frac{d\sigma}{d\Omega}\right)_{COH} \qquad (1)$$

where the subscripts refer to spin-flip (sf), non-spin-flip (nsf), coherent (COH) and spin incoherent (INC) scattering. Thus the spin-flop process is composed of the INC scattering, while the non-spin-flop process is composed of both coherent and INC scattering. Taking account into the instrumental inefficiency of polarization, the elastic coherent and elastic incoherent scattering cross sections have been successfully decomposed (see Figure 2). The details of data treatments should be referred in ref.[7]. It should be stressed that the elastic INC scattering cross section provides a long time-averaged self-correlation of local (hydrogen) motions trapped in a structural cage in a glassy or liquid state. We will discuss the details of physical pictures for this study in the following report of part II.

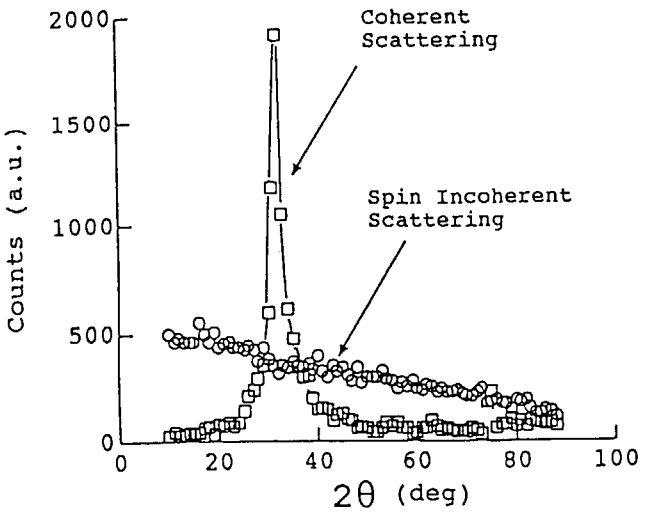

Figure 2

Reference:

[1] C. A. Angell *Science* **267**, 1924 (1995).
[2] R. M. Moon, T. Riste and W. C. Koehler. *Phys. Rev.* **181**, 920 (1969).
[3] W. G. Williams *"Polarized Neutrons"* Oxford Series on Neutron Scattering in Condensed Matter No.1, by Oxford University Press, New York; G. L. Squires "Introduction to The Theory of Thermal Neutron Scattering" Dover Publications, New York.
[4] A. H. Windle, V. Christopher, G. Ruth, M. D. Athene and R. M. Geoffrey *Faraday Discuss. Chem. Soc.* **79**, 55 (1985); J. Blackwell, A. Biswas, A. G. Genaro and R. A. Chivers *Faraday Discuss. Chem. Soc.* **79**, 73 (1985).
[5] D. J. Wilson, C. G. Vonk and A. H. Windle *Polymer* **34**, 227 (1993).
[6] S. Katano et al. in preparation.
[7] J. C. Dore, J. H. Clarke and J. T. Wenzel. *Nucl. Instrum. Methods* **138**, 317 (1976).

2.2.2 Direct Observation on Elastic Incoherent Structure Factor of Glass-forming Material by Neutron Polarization Analysis II.

Satoshi Koizumi and Toshiya Inami

Advanced Science Research Center, Japan Atomic Energy Research Institute,
Tokai-mura, Ibaraki-ken 319-1195, Japan.

In the report of part I, we demonstrated the useful application of the neutron polarization analysis to observe selectively the elastic spin-incoherent (INC) scattering of a glass-forming copolyester polymer. For next steps, we observed the temperature dependence of the elastic INC scattering. The details of experiments and studied materials are reported in the part I. Figure 1 and 2 show the results obtained for the scattering geometry of ϕ=90° (see Fig. 1 of part I).

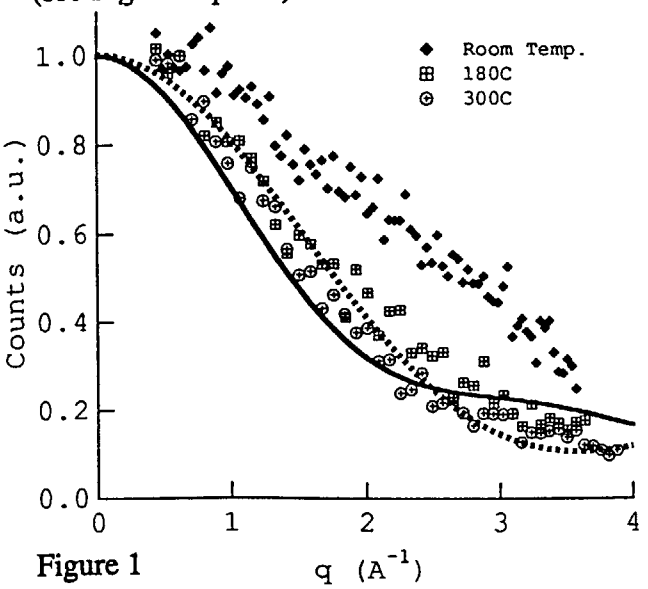

Figure 1

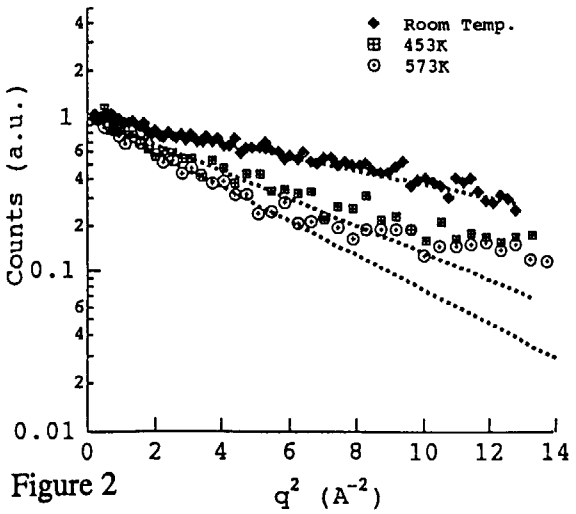

Figure 2

At 300K, the asymptotic q-behavior of INC scattering decrease monotonously as increasing q. On the other hand, at the temperature above Tg (453K and 573K), the asymptotic q-behavior becomes steeper as a function of q, having a minimum at around 2.5 A^{-1} . In Fig. 2 of a logarithmic plot as a function of q^2, we discuss the anharmonic behavior more quantitatively. At the temperature of 453 K and 573 K, the scattering profiles deviate from exponential decay in a q-region higher than 6 A^{-2}, while at 300K the scattering profile decreases exponentially in a whole q-region.

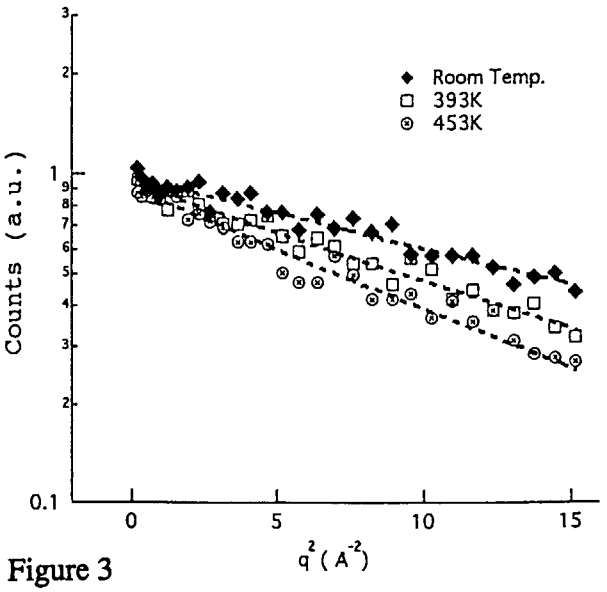

Figure 3

On the other hand, in Fig.3, which obtained for the scattering geometry of ϕ=0°, the scattering profile decreases exponentially in a whole q-region even for higher temperature above Tg.

From the exponential behavior observed in a low q-region of q^2<4 A^{-2}, we estimated an apparent mean square displacement $\langle u^2 \rangle_{app}$ through DWF (~ $\exp(-\langle u^2 \rangle_{app} q^2)$). In Fig.4, the filled circles or squares indicate the mean square displacements obtained by using polarized neutron analyses for the scattering

geometry of ϕ=0° or 90°, respectively. The open circles or squares indicate those estimated by non-polarized neutron, which have been reported in ref. [1]. Both results obtained by using polarized and non-polarized neutron agree well with each other. The increase of $\langle u^2\rangle_{app}$, obtained for ϕ=90°, is two-steps and linearly as a function of temperature T (K); from 8K to 300K, the harmonic increase of $\langle u^2\rangle_{app} \sim 1.7\times10^{-4}$ T and from 300K to 558K, the anharmonic increase of $\langle u^2\rangle_{app} \sim 7.0\times10^{-4}$ T. The anharmonic increase of $\langle u^2\rangle_{app}$ seems to result from the fast relaxation whose onset temperature is far below Tg. This observation is consistent with the recent studies [2,3]. On the other hand, that for ϕ=0° increases more gradually than that for ϕ=90° at around Tg. These observations of the anisotropic increase of $\langle u^2\rangle$ suggests that there exists an *anisotropic structural cage* at around Tg.

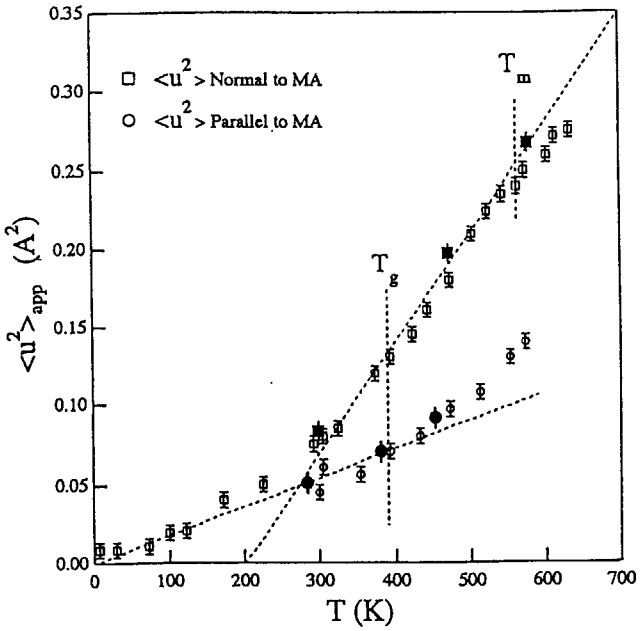

Figure 4

For the scattering geometry of ϕ=90°, we observed the anharmonic behaviors from two aspects of the increase of $\langle u^2\rangle$ and the q-behavior of INC scattering. We employ a following physical picture of a tight cage and a loose cage, characterizing the anharmonicity [4]. In a low temperature region, the segmental units should be trapped tightly in a glassy state (*tight cage*) where the local vibrational motion is crucial to determine the asymptotic q-behavior for elastic INC scattering through DWF including $\langle u^2\rangle$. As increasing temperature closer to Tg or above Tg, the tight cage might become a *loose cage* so that the additional relaxational process might appear in a loose cage. The segmental units of aromatic groups are covalently connected with each other along a direction of molecular axis (MA), while in a direction normal to MA, a non-covalent interaction is crucial. The cage formed around the segmental units should be *anisotropic*. Therefore, it might be possible for aromatic groups to have a rotational libration or relaxation in an *anisotropic cage*, especially in a direction normal to MA.

According to the proposed picture, the scattering law, for a direction normal to MA (ϕ=90°), should be given as follows [5],

$$S(q,\omega=0) \sim \exp(-\langle u^2\rangle q^2)[EISF(q,\omega)\delta(\omega)+QEL(q,\omega=0)] \quad (1)$$

which is composed of DWF of a first term and relaxational contributions (EISF and QEL) of a second term. When temperature is low enough, the relaxational contribution of a second term should disappear in a tight cage.

There is a report for isolated glassy polyester that one of the dihedral angle along MA is easy to rotate as a result of two competitive factors, i.e., steric repulsion and resonance stabilization [6]. Thus when temperature is high enough, the rotational motion of aromatic groups about MA must be crucial to describe the local relaxational motion. In a case of the free rotational motion, in which a particle (hydrogen) can move on a circle of a radius r obeying a Fickian diffusion equation, the elastic and quasielastic components in eq.(1) is composed of the Bessel function of the first kind $J_m(x)$ as follows [5],

$$EISF(q,\omega,\phi) \sim J_0^2(qr\sin\phi)$$

$$QEL(q,\omega,\phi) \sim \sum_{m=1}^{\infty} J_m^2(qr\sin\phi)\times\frac{1}{\pi}\frac{D_r m^2}{(D_r m^2)^2+\omega^2} \quad (2)$$

where D_r is a rotational diffusion coefficient and ϕ is an angle between MA and the scattering

vector q. In Fig. 1, we plotted the calculated scattering curve based upon the free rotational model of eq.(2), in which we employed $r\sin\phi=1.4$ and considered finite terms from m=1 to m=3 for calculating QEL contributions (see Fig.4). The calculated curve describes well the observed INC (or EISF). A more quantitative analysis of our future work requires to consider the long range [7] or short range [8,9] heterogeneity of a glass state, which results in the distribution of parameters such as rotational diffusion coefficient D_r, angle ϕ and radius r. Thus it is suggested that the appearance of EISF for a rotational relaxation in a loose cage is crucial to contribute on the anharmonic behaviors of increase of $\langle u^2 \rangle$ and the anharmonic q-behavior. In a crossover temperature from a tight cage to a loose cage, the structural cage becomes anisotropic so that the anisotropic motion of segmental units in a direction normal to a local molecular axis, provides the larger increase of $\langle u^2 \rangle$ than that parallel to MA.

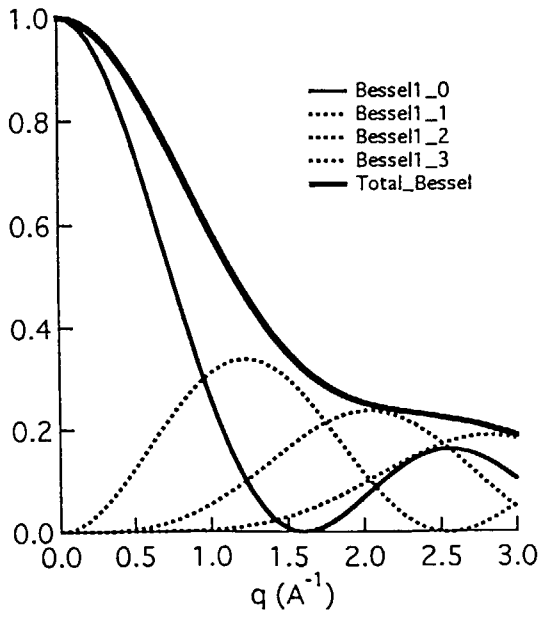

Figure 4 Free rotation model, composed of the Bessel function of the first kind $J_m(x)$. The thin solid line and broken lines indicate the elastic incoherent structure factor (EISF) amd the quasielatic components. The thick solid line shows the total contribution describing the elastic incoherent scattering.

We wish to Dr. T. Shiwaku of Polyplastic Co. Ltd. for supplying a sample specimen. We are also grateful to Professor T. Kanaya of Kyoto Univ. for helpful discussions.

References:

[1] S. Koizumi *J. Chem. Phys.* **107**, 603 (1997).

[2] T. Kanaya, T. Kawaguchi, and K. Kaji *J. Chem. Phys.* **104**, 3841 (1995).

[3] U. Buchenau, C. Schönfeld, D. Richter, T. Kanaya, K. Kaji, and R. Wehrmann, *Phys. Rev. Lett.* **73**, 2344 (1994).

[4] H. Tanaka *J. Chem. Phys.* **105**, 9375 (1996).

[5] M. Bee "*Quasielastic Neutron Scattering: Principles and Applications in Solid State Chemistry, Biology and Materials science*"; Adam Hilger: Bristol, U.K., 1988.; A. J. Dianoux, F. Volino and H. Hervet *Molecular Physics* **30**, 1181 (1975); Bee, M.; Dianoux, A. J.; Volino, F.; *Molecular Physics* **51**, 221 (1984).

[6] A. H. Windle et al. *Macromolecules* **22**, 1129 (1989).

[7] E. W. Fischer *Physica A* **201**, 183 (1993).

[8] R. Zorn *Phys. Rev. B* **55**, 6249 (1997); T. Kanaya, T. Tukushi. and K. Kaji *Prog. Theor. Phys.*, **126**, 133(1997).

[9] S. Koizumi *Physica B* in press.

2.2.3

Light Scattering and Small-Angle Neutron Scattering Studies of Shear-Induced Structures in Semidilute Polymer Solutions under Oscillatory Shear Flow

S. Saito, K. Matsuzaka, S. Koizumi[1)], S. Suehiro and T. Hashimoto

Department of Polymer Chemistry, Graduate School of Engineering, Kyoto University
Sakyo-ku, Kyoto 606-8501, Japan
1) Japan Atomic Energy Research Institute, Tokai 319-1106, Ibaraki, Japan

It has been reported that a shear flow, imposed on a semidilute polymer solution in a single phase, enhances concentration fluctuations toward phase separation. This phenomenon is so-called "shear-induced phase separation" and has been studied by light scattering, optical microscopy, and rheology measurement. Here, we report our investigation along this line for a semidilute polymer solution comprised of high molecular weight deuterated polystyrene (d-PS, M_w=3.15×10^6) and dioctyl phthalate (8.0 wt%) by combination of small angle light scattering (SALS) and small-angle neutron scattering (SANS).

On carrying out the SANS experiment, we performed the phase-resolved measurements by using the dynamic data acquisition system (DDAS), which was newly developed in JAERI. A sandwich type shear cell, drived by a servo-controlled hydraulic devise, imposes a oscillatory shear flow on the sample. The incident beam was irradiated along the velocity gradient direction.

Figure 1 shows the SALS and SANS profiles parallel and perpendicular to the flow direction at the representative strain phases ϕ=0° and 90° when an oscillatory shear flow of a strain amplitude γ_0=4.8 and a frequency ω=12.27 rad/s was imposed, where ϕ=0° means the phase at which the magnitude of strain is 0. The solid line indicates the scattering profile at quiescent state, and the dashed line indicates the Ornstein-Zernike function fitted to the experimental data. In higher q-region, the power low of $I(q)\sim q^{-2}$ can be observed, reflecting the form factor of polymer chain at Θ condition. The profiles indicated by symbols are those under shear flow. The open circles denote the scattering profiles parallel to the flow direction, and the closed squares denote those perpendicular to the flow direction. At ϕ=0°, in the lower q-region observed by SANS, the intensity level parallel to the flow is higher than that perpendicular to the flow. This means the existence of the anisotropic structures induced by the oscillatory shear flow. However, in the q-region of SALS, the intensity doesn't depend on the flow direction and the intensity level is higher than the OZ level which corresponds to the scattering from the concentration fluctuation in a single phase. This implies the existence of large scale isotropic inhomogeneity. At ϕ=90°, the SALS intensity parallel to the flow direction increases in the high-q region of SALS. This is caused by the development of the shear-induced structures through the process from ϕ=0° to 90°, which was reported previously.

In both SANS profiles at ϕ=0° and 90°, the power low of $I(q)\sim q^{-4}$ can be observed in the q-region lower than about 0.1 nm^{-1}. This has been known as Porod law, implying the existence of the distinct surface. From this result, we can conclude that the structures induced by oscillatory shear flow are the distinct phase-separated structures rather than the concentration fluctuation in a single phase.

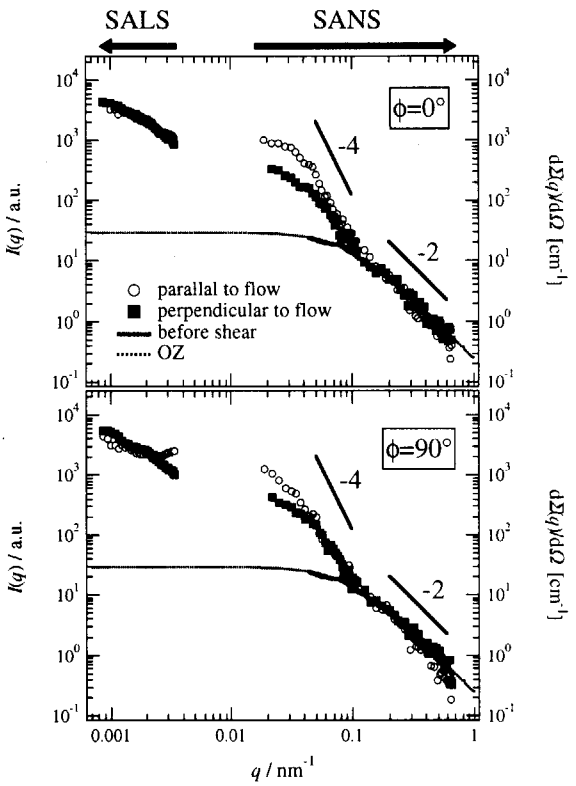

Fig.1 Scattering profiles parallel and perpendicular to the flow direction under oscilltory shear of γ_0=4.8 and ω=12.27 rad/s.

2.2.4

Morphological Characterisation of Bicontinuous Phase-separated Polymer Mixture and Microemulsions

Hiroshi Jinnai[1], Yukihiro Nishikawa[1], Kohtaro Kimishima[1], Takeji Hashimoto[1,2], Satoshi Koizumi[3]

[1]Hashimoto Polymer Phasing Project, ERATO, Japan Science and Technology Corporation, Keihanna Plaza, 1-7 Hikari-dai, Seika, Kyoto 619-0237, Japan
[2]Department of Polymer Chemistry, Kyoto University, 606-8501 Kyoto, Japan
[3]Japan Atomic Energy Research Institute, Tokai, 319-1195 Ibaraki, Japan

Recently, studies of bicontinuous and interpenetrating domain structures developed during phase separation processes, particularly via spinodal decomposition (SD), have been an attractive research theme among researchers dealing with binary mixtures of molecular fluids, binary alloys, and polymer blends over the past decades [1]. Similar kinds of bicontinuous structures have been observed in a water/oil/surfactant three-component microemulsion system in the one-phase region close to the three-phase boundary and in the vicinity of the hydrophile-lipophile balance temperature. It is interesting to examine the common and universal features, if they exist, of the bicontinuous structures observed in phase-separated polymer blends and in microemulsions [2].

In bicontinuous microemulsions, a theory developed by Berk [3] has been used to analyze scattering data and to generate the three dimensional (3d) morphology corresponding to the scattering data. A random Gaussian field that is generated by superposing many isotropically propagating sinusoidal waves with random phases is "clipped" to simulate the two-phase morphology whose essential features depend on the spectral function. Note that this idea was first developed by Cahn for generating the 3d morphology formed SD. Later, Chen et al. [4] proposed a peaked spectral function with a power law decay at large wave numbers which was able to reproduce their SANS intensity distributions from the microemulsions (called a modified Berk "M-B" theory).

We apply the theory to the scattering data from a polymer blend (which is in a non-equilibrium state) in order to see whether or not there are some common features shared by these two dynamically disparate systems. It is worth noting that the two systems have *very* different characteristic lengths: the characteristic length of the phase separated polymer blend used here is of the order of 10 μm, while that of the microemulsion is of the order of 100Å [5].

The polymer blend used in the present study was a near-critical mixture of perdeuterated polybutadiene (dPB) and polyisoprene (PI). Both polymers were synthesized by living anionic polymerization. The number-average molecular weight (Mn) of dPB and PI were, respectively, 61,000 and 141,000. For the microemulsion, ternary mixtures of heavy water (D_2O), n-octane, and tetraethylene glycol monodecyl ether (C4E10) were used. Volume fractions of the surfactant, water, and oil were, respectively, 0.132, 0.434, and 0.434. For the particular concentration of surfactant used here, the bicontinuous region spans the temperature range from about 17.75±0.25 to 22.0±0.5 ° C. The phase separation process of dPB/PI mixture was followed by a time-resolved light scattering (LS) experiment, while small-angle neutron scattering (SANS) measurements were made for the microemulsion using SANS-J instrument at JAERI.

Figure 1 shows the best fits of the M-B theory (solid line) for both the microemulsion at 20.3 ° C (part a) and for the dPB/PI mixture (part b) in log-log plots. An excellent agreement between the SANS profiles and the M-B theory was obtained. It is quite impressive that the M-B theory also reproduced the LS profile (part b) for the dPB/PI blend, especially in the high q-range including the shoulder. However, the fit was not as good in the low q range, i.e. $q < 0.1$ μm. The M-B theories showed shallower slope in this q-range than the experimental data. Furukawa [6] predicted $I(q) \sim q^2$ behavior in $q < q_m$ (q_m is the wavenumber at the maximum scattering intensity), if thermal fluctuations are significant. Hence the discrepancy of the slope in $q/q_m < 1$ between the theories and the LS data may be due to the small effect on the thermal fluctuations to the large scale morphology ($d \sim 7.1$ μm: d is the interdomain repeat distance). On the other hand, sizes of phase separated domains of the microemulsion are much smaller ($d \sim 303$ Å) and interfacial tension lower due to the existence of a surfactant film in the oil-water interface. In the latter case, the thermal noise is expected to have a larger effect on the microstructure, which leads to the weaker q dependence, i.e. $q \sim q^2$. In any event, the fact that the same theory (M-B theory) can reasonably describe scattering behavior of two systems having very different characteristic lengths is remarkable. We therefore conclude that the morphologies of the phase-separated polymer blend and the microemulsions are quite similar except for their length scales.

References

[1] J. D. Gunton, M. San Miguel, P. Sahni: in Phase Transitions and Critical Phenomena, C. Domb and J. L. Lebowitz Eds., Academic Press, New York, 1983, p. 269.
[2] W. Jahn, R. J. Strey: J. Phys. Chem., 92, (1988), 2294.
[3] N. F. Berk: Phys. Rev. Lett., 58 (1987) 93.
[4] S. H. Chen, D. D. Lee, S. L. Chang: J. Mol. Struct., 296 (1993), 259.
[5] H. Jinnai, T. Hashimoto, D. D. Lee, S. H. Chen: macromolecules, 30 (1997), 130.
[6] H. Furukawa, J. Phys. Soc. Jpn., 58 (1989), 216.

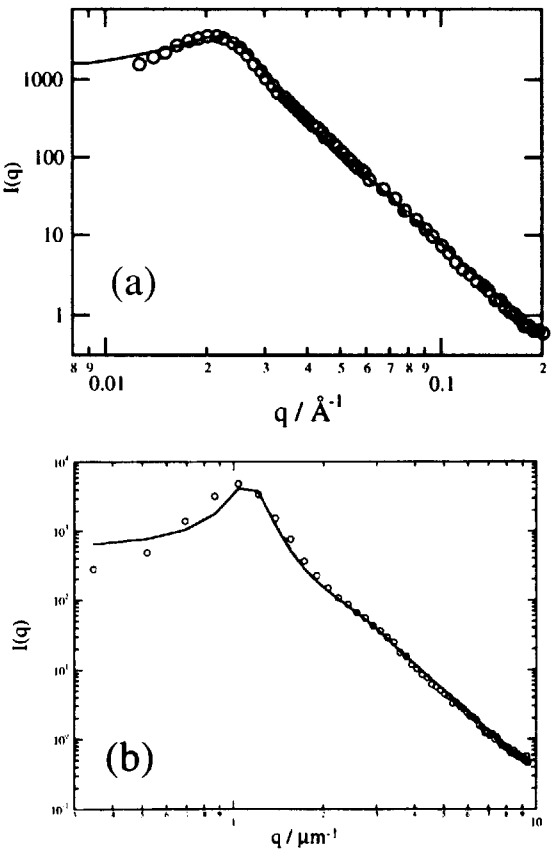

Figure 1. (a) Modified Berk model analysis of SANS profile of the one-phase microemulsion. (b) Modified Berk model analysis of scattering intensity of the dPB/PB blend. Solid lines show the best fit using the M-B therry.

2.2.5 Ultra Small Angle Neutron Scattering of N-isopropylacrylamide Gel

T.Okamoto[1], Y.Hirokawa[1], K.Aizawa[2], S.Koizumi[2], and T.Hashimoto[1,3]

[1]Hashimoto Polymer Phasing Project, ERATO, JST,
15 Morimoto-cho, Shimogamo Sakyo-ku, Kyoto 606-0805
[2]Japan Atomic Energy Reserch Institute, Tokai, Ibaraki 319-1195
[3]Graduate School of Engineering, Kyoto University, Kyoto 606-8501

Polymer gels are three-dimensionally cross-linked polymer network containing fluid. They are intriguing materials for polymer science and technologies. The characteristics of gels such as optical, mechanical, thermal properties, and so forth, are related to their inhomogeneities. The inhomogeneities of the gel are essential matters not only for the basic polymer science but also for the technologies. Many studies on the gel have been made so far, however, there are not so many reports relating to the internal structures and inhomogeneities of the gel. In order to understand the characteristics of the gel, it is important to study the internal structures.

The gel used in this work is N-isopropylacrylamide gel. The gel samples were prepared at 24.5°C. The observation of the internal structures of the samples was carried out by means of ultra small angle neutron scattering.

Figure 1 shows the double logarithmic plot of the scattering intensity as a function of the wave number q. The profile shows a maximum at a q value (ca. 0.0004nm^{-1}) corresponding to the spacing of 16μm. The spacing agrees well with that found by the confocal laser scanning microscopy[1]. It has a straight line with a slope of ca. 2.5 over the length scale of 6000 to 600nm, or 6 to 0.6μm, elucidating a fractal-like structure with mass fractal dimension of 2.5.

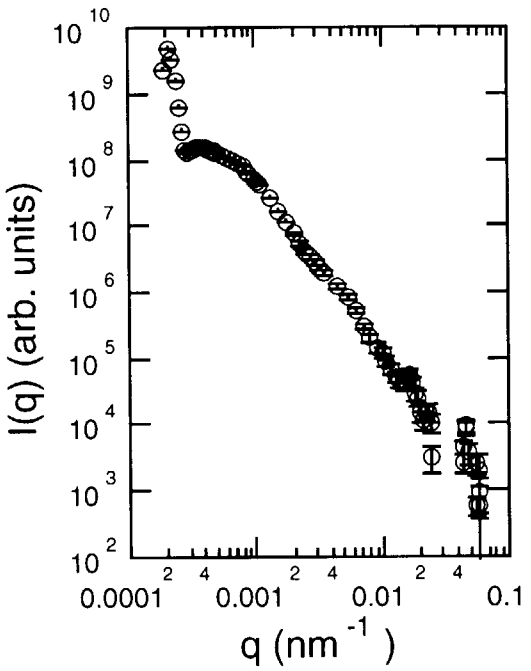

Fig.1 Double logarithmic plot of the scattering intensity as a function of the wave number q.

Reference

1) Hirokawa, Y., Jinnai, H., Okamoto, T., and Hashimoto, T., Polymer Preprints, Japan, **46** (1997) 1918-1919.

JP9950041

2.2.6 Observation of Internal Structure of Microcrystalline Cellulose

M. Sugiyama[a], K. Hara[b], N. Hiramatsu[c], and H. Iijima[d]

[a]*Department of Physics, Kyushu University, Fukuoka, 812-8581 Japan*
[b]*Institute of Environmental Systems, Kyushu University, Fukuoka, 812-8581 Japan*
[c]*Department of Applied Physics, Fukuoka University, Fukuoka, 814-0180, Japan*
[d]*Chemical Technology Department IV, Asahi Chemical Industry Co., Ltd., Nobeoka, Miyazaki 882-0847, Japan*

A microcrystalline cellulose, which has been recently developed by Asahi Chemical Industry Co., Ltd., is a fine particle with the average size of 3 μm. The unique property of this new material is that its aqueous suspension exhibits almost temperature-independent viscosity between 20 and 80°C. However, both the intra- and inter-particle structures are not yet understood; the perpose of our study is to descrive the structure of this thick aqueous suspension of microcrystalline cellulose with small-angle neutron scattering (SANS) technique.

An aqueous suspension of a specially prepared microcrystalline cellulose, which was viscous and opaque, was supplied by Asahi Chemical Industry Co., Ltd, Japan. Two samples were made for the SANS experiments: sample 1 and smaple 2 were aqueous suspensions with the concentration of a microcrystalline cellulose of 10 wt% and 1 wt%, respectively.

The SANS experiments were performed with a SANS-J spectrometer installed at JRR-3M in the Japan Atomic Energy Research Institute, Tokai, Japan. The profiles with a magnitude of the scattering vector (q) ranging from 5×10^{-3} to 5×10^{-2} Å^{-1} were measured with a 6-Å-wavelength neutron beam.

Figures 1 (a) and 1 (b) show double-logarithmic plots for the SANS profiles of samples 1 and 2, respectively. There was no difference in the profile shapes between samples 1 and 2. This result indicades that the observed profiles in the small q region are mainly due to the internal structure of the microcrystalline cellulose particle.

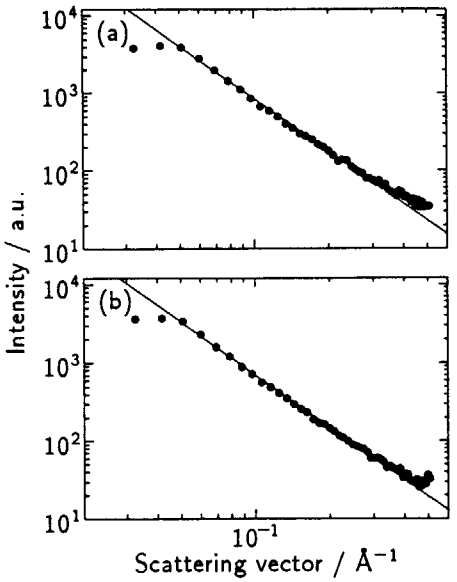

Fig. 1. Double-logarithmic plots of SANS profiles of sample 1 (10 wt%) (a) and sample 2 (1 wt%) (b). The slope of the straight lines in the figures is 2.2.

Moreover, in the q-range from 5×10^{-3} Å^{-1} to 3×10^{-2}, they could be well-fitted by power law curves: $I(q) = I_0 q^{-\alpha}$ with $\alpha = 2.2$. This behavior is characteristic of a fractal structure with a structure factor of $S(q) \propto q^{-D}$ (D is the fractal dimension).[1,2] Therefore, the internal structure of the microcrystalline cellulose particle has a fratcal structure with the dimension of 2.2.

References:

[1] D. W. Schaefer and K. D. Keefer: Phys. Rev. Lett. **56** (1986) 2199.
[2] J. Teixeira: J. Appl. Cryst. **21** (1988) 781.

2.2.7 PNO Study on Bovine Serum Albumin Gels

Y. IZUMI, K. SOMA, K.AIZAWA[1], S.KOIZUMI[1] AND H.TOMIMITSU[1]

Graduate School of Engineering, Yamagata University, Yonezawa, Yamagata 992-8510
[1]Advanced Science Research Center, JAERI, Tokai, Ibaraki 319-1195

Heat-induced gelation of proteins is very important for commercial production such as foods and pharmaceuticals. For example, some foods of milk and soy proteins have been traditionally manufactured by this principle. To control the process it is essential to understand the fundamental behavior of gelation. Heat-induced gelation is also important in manufacturing lines, because it can cause problems such as the fouling of pipes. Without sufficient imformation about the gelation mechanism, it is almost impossible to deal with such difficulties.

In present work, we intended to investigate the structure of a globular protein gel by PNO measurements. As the globular protein, we selected bovine serum albumin (BSA) by the following reasons. BSA is abundant in blood plasma and also the fifth component in whey protein. The chemical and biological properties have been reported in detail in previous reviews. BSA used was the pure commercial product from Sigma Chemical Co. The solvent used was the heavy water (>99.8%) purchased from CEA. By changing both the gelation temperature (T_{gel}) and the gelation time (G_{time}), three types of heat induced gels were prepared at 0.185M NaCl: gel A (T_{gel}=90°C, G_{tim}=5min), gel B(T_{gel}=80°C, G_{tim}=10min) and gel C (T_{gel}=70°C, G_{tim}=10min). The BSA concentration of the gels was constant (about 17.5wt%). The neutron scattering experiments were performed with the JAERI 3G PNO spectrometer installed at JRR-3M reactor of JAERI (Tokai). The PNO data were obtained at room temperature. The slit height correction has been performed to desmear the effect caused by the vertical divergence of the incident beam. The data is corrected for blank cell background. Data taken at λ=0.25nm cover the q-range 0.0002 nm^{-1} to 0.06nm^{-1}.

Fig. 1 shows the excess scattering curves I(q), radially averaged, in a double log presentation. The Porod behavior of $I(q) \propto q^{-4}$ is observed for each gel. By comparing the data with a monodispersed spheres scattering function, the diameters of junction zone of the present gels can be evaluated. Gel A, B and C correspond to junction zones with diameter of about 0.9, 26 and 32 μm, respectively.

These results indicate that the size of the junction zone decreases and the size distribution broadens as the gelation temperature elevates and that the PNO technique is useful to determine the size of the junction zone of micron order in gels.

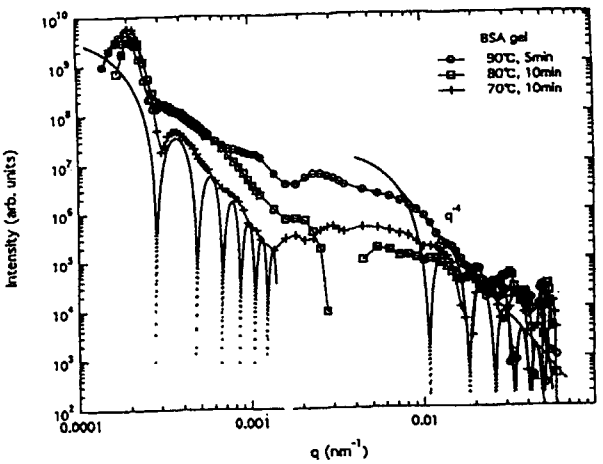

Fig. 1. Log-log plot of intensity vs. q for three gels. 90°C and 5min (gel A), 80°C and 10min (gel B), 70°C and 10min (gel C). The solid lines are guides to the eye. A monodisperse sphere scattering function is shown in gel A and gel C.

References

1) A.Tobitani, Ph. D. thesis, King's College London, University of London (1995).
2) K.Aizawa & H.Tomimitsu, Physica B 213&214(1995)884-886.

2.2.8 Interface scattering of strongly segregated polymer blend.

Hiroyuki Takeno, Takeji Hashimoto, Martin Weber[1]
and Satoshi Koizumi[2]
Kyoto University, Kyoto, 606-8501, Japan
[1]BASF, Germany
[2]Japan Atomic Energy Reserch Institute, Tokai, Ibaraki, 319-11, Japan

Recently numerous studies have been made on phase separation process of polymer blends. In the studies of phase separating structure, it is important to obtain information of the interfacial structure.

In this study, we have investigated the interface scattering for a strongly segregated polymer blend, deuterated polysulfone (dPSU) and polyamide, (PA) blend (dPSU/PA) by means of small-angle neutron scattering (SANS). dPSU/PA blend with a composition of 50/50 in weight percent was dissolved in o-chlorophenol at 50 °C and then prepared by precipitation into methanol. The precipitated sample was dried for 24 hours at 100 °C and pressed at 140 °C. The glass transition temperature of dPSU and PA are 180 °C and 110 °C, respectively. The obtained sample was annealed at 240 °C for a given time. SANS was measured as a function of annealing time t_{an}.

Figure 1 shows the scattering profiles of dPSU/PA at various annealing times. In the small-q region (e.g., for t_{an}=74 min. q<0.3 nm^{-1}) the scattering profiles obey Porod law which represents the scattering from sharp interface. {$I(q)=2\pi\Delta\rho^2 S_{sp}$, $\Delta\rho^2$: contrast factor, S_{sp}: interfacial area density} In the high-q(e.g., for t_{an}=74 min. q > 0.3 nm^{-1}), the scattering profiles have almost no q-dependence and the intensity is very weak. The result suggests that there are almost no thermal concentration fluctuations inside the domain because of strong segregation between dPSU and PA. Furthermore, we estimated S_{sp} from Porod law as a function of annealing time (Fig. 2). S_{sp} decreases with time with an exponent of -0.37 ($S_{sp}\sim t^{-0.37}$).

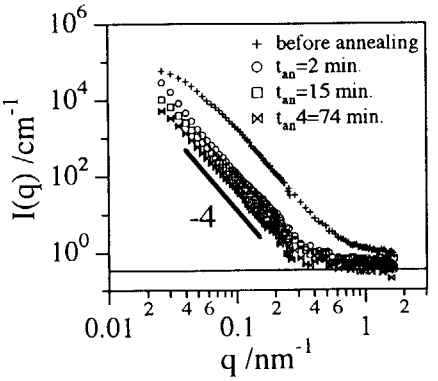

Fig. 1 SANS profile for dPSU/PA blend annealed at 240 °C.

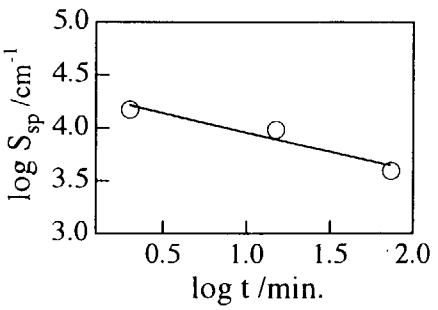

Fig. 2 log S_{sp} vs log t

JP9950044

2.2.9

Microphase Separated Structure of Segmented Polyurethane Studied by Using Small-Angle Neutron Scattering

Sudaryanto and Satoshi Koizumi[1]

National Atomic Energy Agency, Indonesia, Kawasan, PUSPIPTEK, Serpong, 15313, Indonesia.
[1]Japan Atomic Energy Research Institute, Tokai, Ibaraki, 319-1195, Japan

1. Introduction

Segmented polyurethanes (SPU), having hard segment (HS) and soft segment (SS), are known to form a microphase separated structure[1]. This peculiar structure brings SPU to be used in various ways such as biomedical materials, magnetic binders, elastomers, and adhesives.

Many studies have been performed to understand the microphase separated structure of SPU and its effect on various properties [2-6]. It is well known, therefore, that the formation of microphase separated structure highly affects the mechanical properties of SPU as well as their surface properties. Deeper understanding of SPU structure-properties correlation, however, is still needed, owing to their complexity of chemical and physical structures.

Previously, we have studied the relationship between microphase separation and surface properties of SPU[6]. The microphase separation structures were characterized by several methods such as differential scanning calorimetry (DSC), dynamic mechanical analysis, X-ray diffraction, and tensile test measurements. While, the surface properties were studied by X-ray photoelectron spectroscopy (XPS) and contact angle measurements. The results show that the existence of microphase separation results in increase of the surface free energy of SPU, with the soft segment being more predominant on the surface.

The aim of this study is, to investigate quantitatively the effect of the hard segment content and thermal treatment on the microdomain structure of SPU, by using small angle neutron scattering (SANS).

2. Experimental

The studied SPU is composed of 4,4'-diphenylmethane diisocyanate (MDI) and poly (propylene glycol) (PPG), chain extended with 1,4-butanediol (BD). Detailed explanations of samples preparation as well as their thermal, mechanical, and surface properties were reported elsewhere [6].

The SANS measurements were performed by SANS-J instrument (λ=0.6 nm). Samples used in this study were hydrogenated films of thickness of 1 mm and a larger area compared to the neutron beam size. Scattering data of each sample were collected for about 2.5 hours. Effects of thermal treatment were then investigated by placing the sample within a cell which allowed to perform *in situ* experiments at controlled temperature. Profiles of scattering intensity were collected at interest temperature around melting point for about 1 hour.

3. Result and Discussion

Figure 1 shows SANS profiles for three SPUs with various HS contents. q ($=4\pi\sin\theta/\lambda$) is the magnitute of the scattering vector with λ and 2θ being wavelength and scattering angle, respectively. SPU68 (SPU with HS content of 68 wt%) gives the highest intensity over a wide q range, with a sharp maximum at q = 0.33 nm^{-1}. On the other hand, other SPUs have no scattering maximum. SPU56, however, showed higher intensity than SPU32.

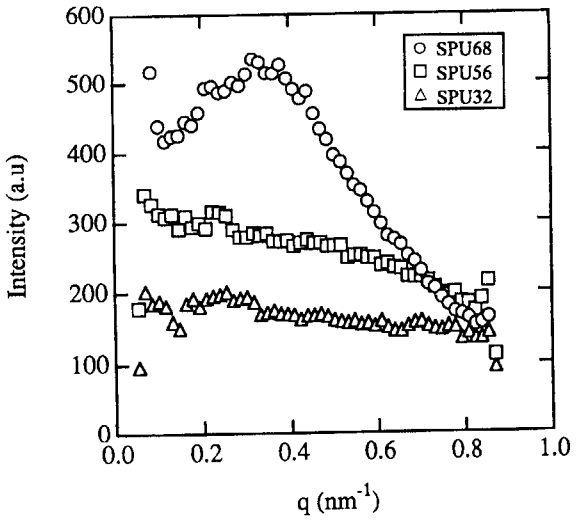

Fig. 1 SANS profiles obtained for SPU with various HS contents.

According to basic scattering laws, the scattering intensity (I(q)) depends on concentration fluctuation in the system, i.e., the contrast. For a two phase system the contrast value is represented by a mean-square fluctuation. Namely,

$$<\Delta\rho^2> = (\rho_1-\rho_2)^2\varphi_1\varphi_2$$

where ρ_i is the locally averaged scattering length for *i* th phase, and φ_i is the volume fractions for *i* th phase. Since $\varphi_1 + \varphi_2 = 1$, for a given value of $(\rho_1-\rho_2)^2$, the $<\Delta\rho^2>$ becomes maximum when $\varphi_1 = \varphi_2$. In other word, the largest product of $\varphi_1\varphi_2$, among three samples used in this study, must be obtained for SPU with HS content of 56 wt%. While, SPU with HS content of 68 wt% and 32 wt% must have similar values of $\varphi_1\varphi_2$ and $<\Delta\rho^2>$. But the experimental results show an opposite trend from the expected one over the whole q values. According to Chang and Wilkes, these results indicate that microphase separated structure consisting of hard and soft segment domains is formed with increasing HS content[3].

The interdomain distance ($d=2\pi/q_{max}$) formed in this SPU can be estimated to be 19 nm from the position of scattering maximum at q=0.3 nm^{-1}. This value is consistent with result obtained for several other SPU systems by using X-ray scattering, as reported previously[3,4].

These SANS results are well in agree with those obtained by DSC measurement, where the SPU68 has sharp melting peak at 180℃, SPU56 has broad one, and SPU32 had no endhotermic peak, which lead to conclusion that domain formation is clearly observed in the bulk of SPU with high HS content.

Figure 2 shows the SANS profiles of SPU68 with increasing temperature. It is clear that the scattering maximum increased with increasing temperature, which indicates microphase separation between hard and soft segment is developed. The peaks position was also shifted to lower q value with increasing temperature, which corresponds to the decrease in interdomain distance due to enlarging domain size. This result may also be due to the increased mobility of soft segment, which may lead the hard domains to move close each others. The vigorous movement of soft segment may also stimulate in the increase in phase separation.

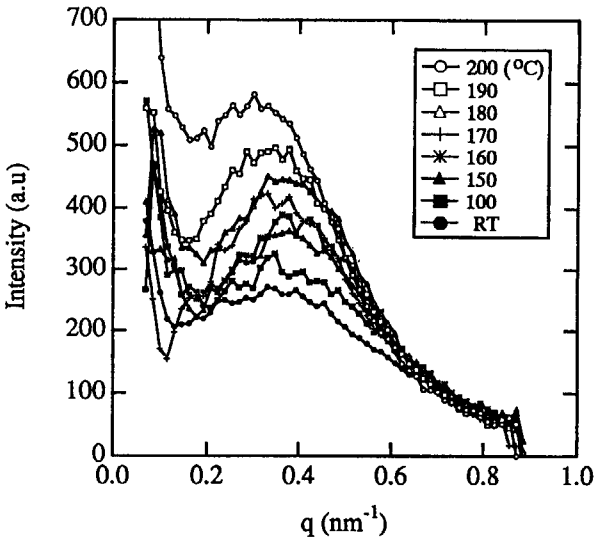

Fig. 2 SANS profiles of SPU68 at with increasing temperature. Each profile was collected at controlled temperature for 1 hour.

4. Conclusion

These SANS measurement support quantitatively the conclusion that microphase separated structure of SPU used in this study can be obviously observed at high HS content, i.e. more than 50 wt%, as determined previously by DSC and X-ray diffraction as well as tensile test measurement. The interdomain distance, was observed to be 19 nm for SPU with HS content 68wt%.

5. References

[1] J.Blackwell and C.D.Lee, in *Advances in Urethane Science and Technology*, K.C. Frisch and D.Klempner, Eds. Technomic, Lancer, PA, 1984, vol.9,pp.25-46.

[2] J.T.Koberstein and R.S.Stein, *J. Polym. Sci.Polym.Phys.Ed.*,21,1439 (1983).

[3] Y.P. Chang and G.L.Wilkes, *J.Polym.Sci. Polym.Phys.Ed.*,13,455(1975).

[4] G.L.Wilkes,S.Abouzahr, *Macromolecules*, 14,456(1984).

[5] J.T.Koberstein and L.M.Leung, *Macromolecules*, 25,6205(1992).

[6] K.Nakamae, T.Nishino, S.Asaoka, and Sudaryanto, *Int'l. J. Adhesion & Adhesive*, 16,233 (1996).

2.3 Strongly Correlated Electron Systems and Superconductivity

2.3.1 Anisotropic Superconducting Gap in a Heavy Fermion Superconductor UPd_2Al_3

N. Metoki[A], Y. Koike[A], Y. Haga[A], and Y. Ōnuki[A, B]

[A]*Advanced Science Research Center, JAERI, Tokai, Ibaraki 319-1195*
[B]*Graduate School of Science Department of Physics, Osaka University, Toyonaka, Osaka 560*

Anisotropic superconductivity in heavy fermion superconductor is one of the most exciting topics in the field of condensed matter physics. Recent intensive neutron scattering study on a heavy fermion superconductor UPd_2Al_3 revealed that the superconducting gap appears in the spin excitation spectra, indicating that the superconductivity is magnetic origin [1,2]. Since the *d*-wave pairing is reported by NMR studies [3,4], it is of particular interest to reveal the anisotropy of the superconducting gap. In this paper we report the result of the low energy spin excitation measured by neutron scattering.

Neutron scattering experiments were carried out using a cold neutron triple-axis spectrometer LTAS at the Japan Atomic Energy Research Institute (JAERI). The signal is integrated in a certain q-range using curved analyzer crystal. The single crystal sample, which is the same as measured before, is cooled in a liquid-helium-free ^{3}He-^{4}He dilution refrigerator down to 100 mK.

Figure 1 shows the result of the constant-E scan with the energy transfer ΔE = 0.6 meV at 0.1 K (a) and 2.1 K (b), below and above the superconducting transition temperature T_c = 1.9 K, respectively. Below T_c we found a clear peak around the (0.5 0 0.5) reciprocal lattice point. The intensity at low Q region is the background. The constant-Q profile with Q = (0.5 0 0.5) (Fig. 2) shows a weak but clear inelastic peak at ΔE = 0.7 meV. The spin excitation gap of about 0.7 meV $\approx$ 4 $k_B T_c$ is in the same order of the superconducting energy gap. This energy gap is a little larger than the one at (0 0 0.5), where we observed the gap of 0.36 meV $\approx$ 2.2 $k_B T_c$. This difference would be due to the anisotropy of the superconducting gap.

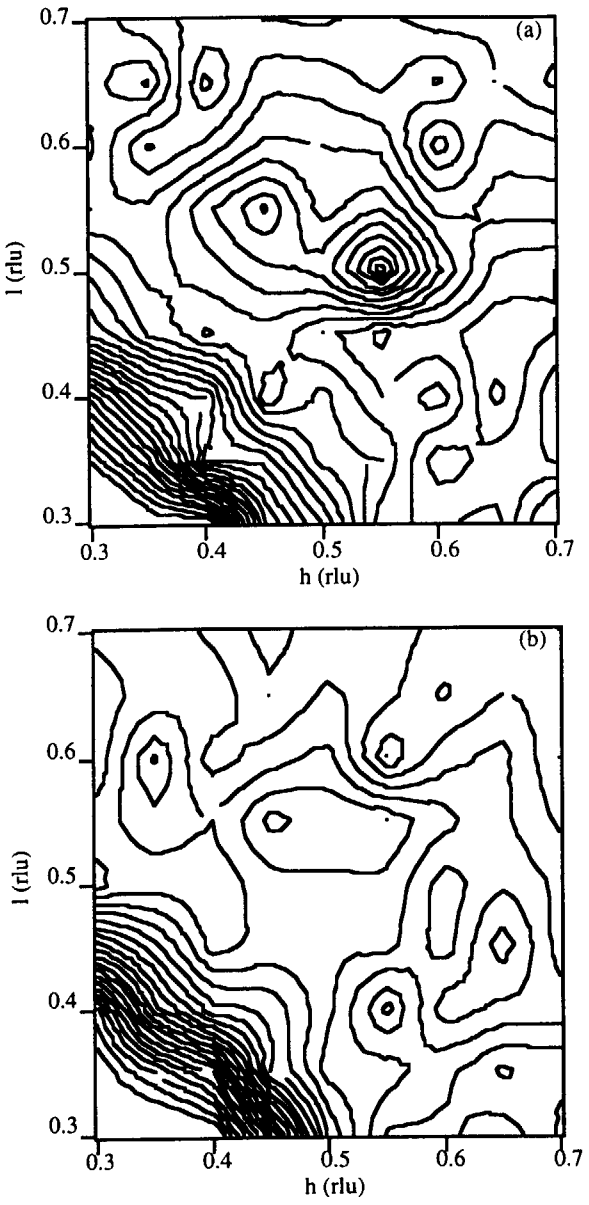

Fig. 1. The contour map of the constant-E profile of UPd_2Al_3 with ΔE = 0.6 meV at 0.1 K (a) and 2.1 K (b), respectively.

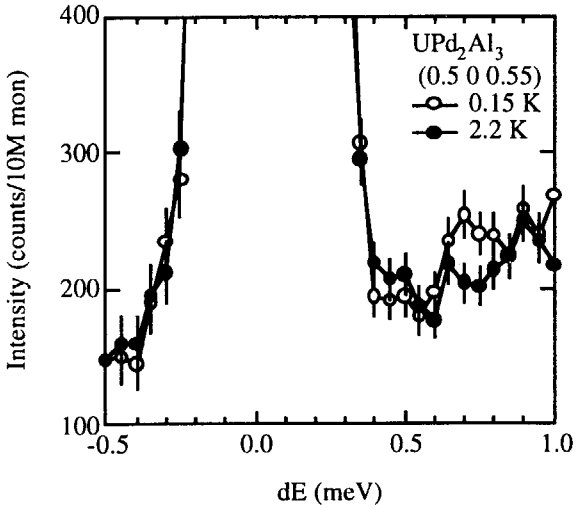

Fig. 2. The neutron inelastic scattering profile of UPd_2Al_3 at (0.5 0 0.5).

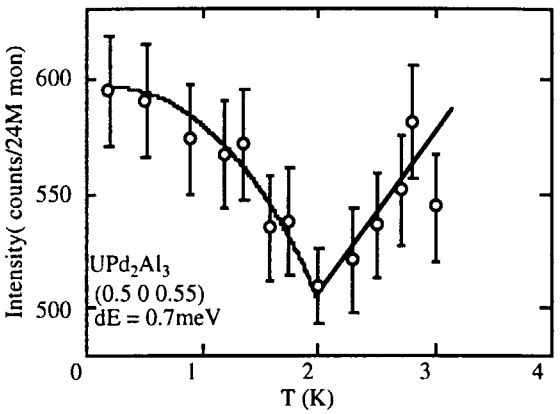

Fig. 3. The temperature dependence of the scattering intensity at (0.5 0 0.5) with ΔE = 0.7 meV. The solid line is guide for the eyes.

Figure 3 is the temperature dependence of the scattering intensity of this peak. Above T_c the intensity decreases with decreasing temperature. Below T_c, the intensity increases like superconducting order parameter. This temperature dependence is very similar to the one of the inelastic scattering peak observed at (0 0 0.5). See figure 3(b) in Ref. 1.

It is often observed that antiferromagnetic correlation with several independent modes coexists in heavy fermion systems like $CeRu_2Si_2$ [5]. Heavy fermion superconductor UPt_3 exhibits (1/2 0 1) antiferromagnetic peak below 5 K, while the (001) out-of-plane antiferromagnetic correlation coexists with a typical energy scale of 10 meV [6]. In addition to the antiferromagnetic ordering in URu_2Si_2, short range correlation around (1, 0.4 0) was reported [6]. It should be noted that in case of UPd_2Al_3 the (0 0 0.5) and (0.5 0 0.5) antiferromagnetic correlation strongly couple to the superconductivity, which makes this compound unique. The next step is to reveal the structure of the anisotropic superconducting gap.

We would like to thank M. Tachiki, M. Kohgi, and S. Koh for stimulating discussions.

References

[1] N. Metoki et al., J. Phys. Soc. Jpn. **66** (1997) 2560.
[2] N. Metoki et al., Phys. Rev. Lett. **80** (1998) 5417.
[3] M. Kyogaku et al., J. Phys. Soc. Jpn. **61** (1992) 2660.
[4] H. Tou et al., J. Phys. Soc. Jpn. **64** (1995) 725.
[5] L.P. Regnault et al., Phys. Rev. B**38** (1988) 4481.
[6] A.I. Goldman et al., Phys. Rev. B**36** (1987) 8523.
[7] G. Aeppli et al., Phys. Rev. Lett. **63** (1989) 676.
[8] W.J.L. Buyers et al., Physica **B199-200**, 95.

2.3.2 Unusual Temperature Dependence of the Tiny Moment in URu_2Si_2

T. Honma[1], Y. Haga[1], E. Yamamoto[1], N. Metoki[1], Y. Koike[1], H. Ohkuni[2] and Y. Ōnuki[1,2]

[1]Advanced Science Research Center, Japan Atomic Energy Research Institute, Tokai, Naka, Ibaraki 319-1195, Japan
[2]Graduate School of Science, Osaka University, Toyonaka 560-0043, Japan

URu_2Si_2 is a fascinating compound in which superconductivity coexists with antiferromagnetic ordering. Previous neutron scattering experiments revealed that a weak antiferromagnetic state with 0.02-0.04 μ_B/U develops below 17.5 K[1,2]. To shed more light on the interplay between magnetism and superconductivity, we have done neutron scattering experiments in the temperature range of 100 mK to 5 K. In this paper, we show an unusual temperature dependence of the antiferromagnetic Bragg peak intensity.

Single crystals were grown by the Czochralski pulling method in a tetra-arc furnace under the pure argon gas atmosphere. The typical size of the ingots was 3-4 mm in diameter and 40 mm in length. The samples were annealed at 1000°C for one week, which were wrapped in Ta and Zr foils and sealed in a quartz tube under vacuum of 1×10^{-7} torr.

The resistivities show a sharp peak at 17.5 K, which is reminiscent of a spin density wave antiferromagnet Cr. We observed an onset superconducting transition at 2.5 K and resistivity zero at 1.4 K. The residual resistivity ratio (RRR = ρ_{RT}/ρ_0) was 41.8.

Neutron scattering experiments were carried out by using a cold neutron triple-axis spectrometer LTAS installed in the research reactor JRR-3M at Japan Atomic Energy Research Institute. The neutron beam was monochromatized by a PG monochromator. The fixed incident neutron energy of 4.768 meV was used with a Be filter cooled down to 10 K.

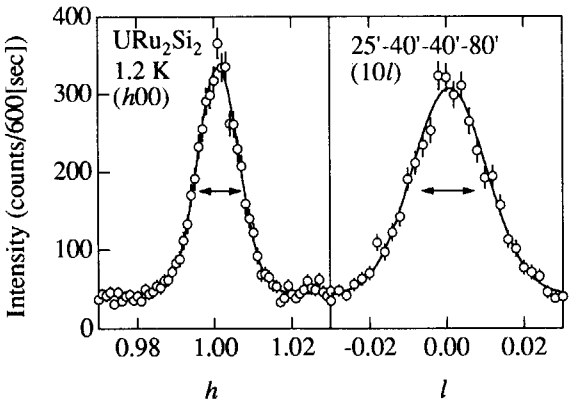

Fig.1 Profiles of the (1 0 0) magnetic Bragg peaks along the longitudinal and transverse directions at 1.2 K in URu_2Si_2. The solid lines are the results of least-square fit by the Gaussian function.

Figure 1 indicates the scattering profiles of the (1 0 0) magnetic Bragg peak along the longitudinal and transverse directions at 1.2 K. The profiles are described by a Gaussian line shape with a constant background. The linewidth is broader than the resolution in both directions indicated by arrows in Fig. 1. The spin correlation lengths are ξ_a=640±50Å and ξ_c=500±30Å, respectively, which are consistent

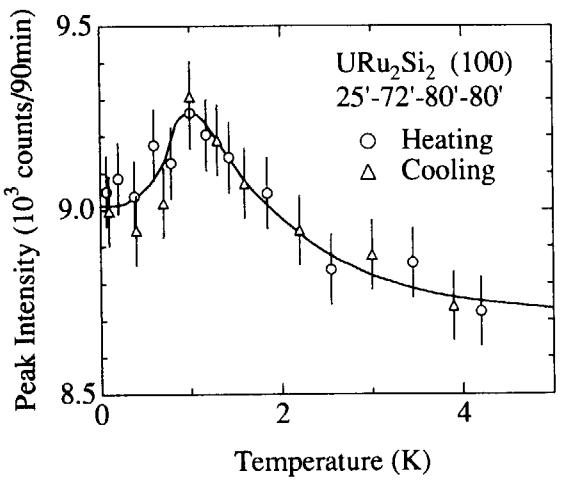

Fig. 2 Temperature dependence of the (1 0 0) magnetic Bragg peak intensity in URu_2Si_2. A solid line connecting the data is a guideline.

with previous studies within experimental errors[2,3]. We determined the magnitude of the ordered moment as $\mu_{ord} \sim 0.02\ \mu_B/U$ at 1.2 K, by comparing the integrated intensity with the one of the (1 0 1) nuclear Bragg peak. It is also in good agreement with previous results[2].

Figure 2 shows the temperature dependence of the peak intensity I(1 0 0). The intensity increases with decreasing the temperature. However, it shows a peak around 1 K which corresponds to the superconducting transition temperature T_c. Below 1 K, the intensity decreases rather steeply. The magnitude of the intensity reduction is about 2% of the maximum. From the magnetic structure of URu_2Si_2, it is clear that this anomaly cannot be explained by redistribution of the magnetic domains. It is thus concluded that the magnetic order parameter is coupled to the superconducting one. Similar results have been reported in other heavy fermion superconductors; UPt_3 (reduction rate of 5-10%, an ordered moment of 0.02 μ_B/U), UNi_2Al_3 (3%, 0.2 μ_B/U) and UPd_2Al_3 (1%, 0.85 μ_B/U)[4-6]. The coupling of the order parameters would be a characteristic feature in this system.

In conclution, we measured the temperature dependence of the (1 0 0) mangetic Bragg peak intensity in the temperature range of 100 mK to 5 K. We observed a steep decrease of the peak intensity below about T_c. This result indicates the interplay between magnetism and superconductivity in URu_2Si_2.

References

1) T. E. Mason et al., Phys. Rev. Lett. **65** (1990) 3189.

2) B. Fåk et al., J. Magn. Magn. Mater. **154** (1996) 339.

3) C. Broholm et al., Phys. Rev. B **43** (1991) 12809.

4) G. Aeppli et al., Phys. Rev. Lett. **63** (1989) 676.

5) N. Metoki et al., J. Phys. Soc. Jpn. **66** (1997) 2560.

6) N. Metoki et al., Phys. Rev. Lett. **80** (1998) 5417.

2.3.3

Neutron Scattering Study of the Antiferromagnetic Ordering in UPt_3 at Ultralow Temperatures

Y. Koike[a], N. Metoki[a], N. Kimura[b], E. Yamamoto[a], Y. Haga[a], Y. Ōnuki[a,c] and K. Maezawa[d]

[a] Advanced Science Research Center, Japan Atomic Energy Research Institute, Tokai, Naka, Ibaraki 319-1195, Japan

[b] Center for Low Temperature Science, Tohoku University, Sendai 980-0845, Japan

[c] Graduate School of Science, Osaka University, Toyonaka 560-0043, Japan

[d] Faculty of Engineering, Toyama Prefectural University, Toyama 939-0398, Japan

It is widely accepted that the magnetic ordering in UPt_3 plays an important role for the unconventional superconducting natures. However the origin of the magnetic correlation with a tiny magnetic moment ($0.02\mu_B$/U) is still an open question. The antiferromagnetic ordering was observed by muon spin resonance[1], neutron [2,3] and magnetic X-ray scattering measurements [4], while no trace of the magnetic transition was reported in specific heat[5], static susceptibility[6], and NMR[7] measurements. It is interpreted that the antiferromagnetic ordering is not true static and long range ordering but dynamical fluctuation. Meanwhile the anomaly observed in the specific heat[8,9] and thermal expansion measurements [10] at about 18 mK is suspected to be a signature of the long range ordering. To shed more light on this subject, the neutron scattering experiments have been carried out in order to study the antiferromagnetic correlation at ultralow temperatures.

Neutron scattering experiments were carried out using a cold neutron triple-axis spectrometer LTAS at the Japan Atomic Energy Research Institute (JAERI). The single crystal sample (3 x 3 x 30 mm^3) was cooled down in a ^{3}He-^{4}He dilution refrigerator below 20 mK. This ultralow temperature was obtained by a very good contact of the sample onto the OFC (oxygen free copper) sample holder attached on the mixing chamber. Details of the set up are described in ref. 11.

Figure 1 shows the temperature dependence of the scattering profile of a (0.5 0 1) antiferromagnetic peak. We observed the clear antiferromagnetic peak down to 20 mK. The peak intensity exhibits no significant change within an experimental accuracy (10%). However we found the remarkable temperature dependence of the linewidth. At 570 mK, for example, the linewidth of this peak 0.022 $Å^{-1}$ and 0.011 $Å^{-1}$ for the longitudinal and transverse directions, respectively, is broader than the resolutions (denoted by arrows in Fig. 1). The spin correlation length is estimated as 290 ± 50 Å and 550 ± 40 Å, respectively, which is in good agreement with the previous reports[2-4]. At 20 mK, however, almost a resolution limited peak was observed in both directions.

Figure 2(a) shows the temperature dependence of the longitudinal linewidth ($W_{//}$) of (0.5 0 1) peak profiles observed with the collimations of 26'-40'-20'-72'. The resolution of this condition is higher than the previous study[11]. The linewidth is steeply decrease below 50 mK and becomes a resolution limited below 20 mK. In Fig. 2(b), we show the temperature dependence of the spin correlation length ($\xi_{//}$). A finite spin correlation length is observed down to 20mK, but below 20 mK, the correlation length increases divergently.

The presence of the antiferromagnetic peak down to 20 mK is quite surprising. It means that the dynamical spin fluctuation exists at ultralow temperatures. The spin correlation length of about 400 Å, which is much longer than the one in the

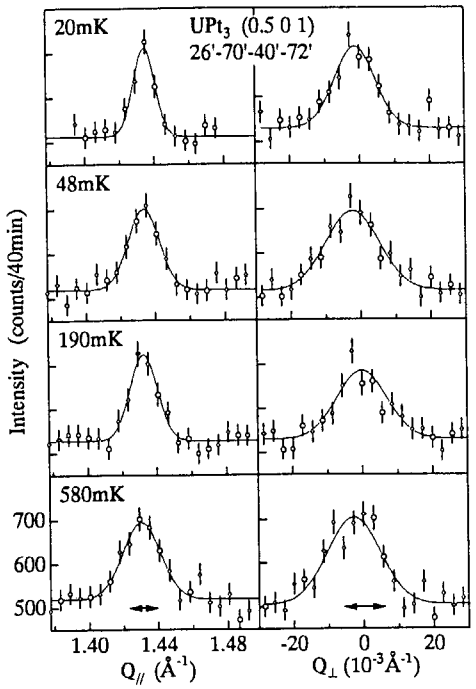

Fig. 1. Temperature dependence of the scattering profile of the (0.5 0 1) peak in the longitudinal ($Q_{//}$) and transverse ($Q_{\perp}$) directions for UPt_3. The arrows indicate the resolution.

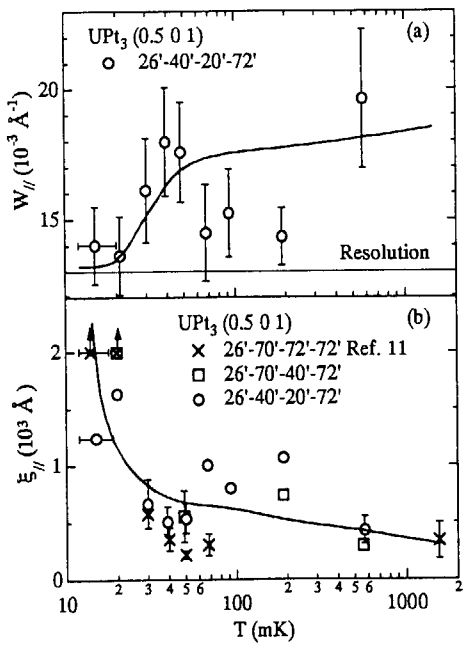

Fig. 2. (a) Temperature dependence of the linewidth ($W_{//}$) of (0.5 0 1) peak profile and (b) of the spin correlation length ($\xi_{//}$) in UPt_3. The crosses indicate the previous data shown in ref. 11. Solid lines are guide for the eyes.

short-range correlation system, is also very unusual. The steep increase of the correlation length below 20 mK suggests the static antiferomagnetic ordering at lower temperatures. It is quite interesting that this result corresponds to the anomalies in the specific heat[8,9] and thermal expansion [9]. The origin of this unusual magnetic fluctuation is unclear, and must be studied theoretically[13,14].

In conclusion, we found the long-range antiferromagnetic correlation in the heavy fermion superconductor UPt_3 below 20 mK in the neutron scattering experiments.

We would like to thank A. Sawada, T. C. Kobayashi, and K. Miyake for stimulating discussions.

References

[1] R. H. Heffner et al., Phys. Rew. B39 (1989)11345.
[2] G. Aeppli et al., Phys. Rev. Lett. 60 (1988) 615.
[3] G. Aeppli et al., Phys. Rev. Lett. 63 (1989) 676.
[4] E.D. Isaacs et al., Phys. Rev. Lett. 75 (1995) 1178.
[5] A. de Visser et al., Physica B147 (1987) 81.
[6] P.H. Frings et al., J. Magn. Magn. Mater. 31-34 (1983) 240.
[7] H. Tou et al., Phys. Rev. Lett. 77 (1996) 1374.
[8] E.A. Schuberth et al., Phys. Rev. Lett. 68 (1992) 117.
[9] E.A. Schuberth, Int. J. Mod. Phys. B10 (1996) 357.
[10] A. Sawada et al., Czech. J. Phys. 46 (1996) S2 803.
[11] Y. Koike et al., J. Phys. Soc. Jpn. 67 (1998) 1142.
[12] For example, I.A. Fomin and J. Flouquet, Solid State Commun. 98 (1996) 795.
[13] Y. Okuno et al., Meeting Abstracts of J. Phys. Soc. Jpn. Vol. 52 Issue 2, Part 3 (1997) p. 476.

2.3.4 Absence of magnetic ordering in a heavy fermion superconductor UBe_{13}

Y. Haga[1], Y. Koike[1], N. Metoki[1], E. Yamamoto[1], T. Honma[1] and Y. Ōnuki[1,2]

Japan Atomic Energy Research Institute, Tokai, Ibaraki 319-1195, Japan
Graduate School of Science, Osaka university, Toyonaka, Osaka 560-0043, Japan

In the heavy fermion superconductors such as UPt_3, URu_2Si_2 and UPd_2Al_3, antiferromagnetic (AF) ordering coexists with superconductivity. Magnetic interaction between 5*f* electrons plays a crucial role to form anisotropic superconducting state such as *d*- or *p*- wave pairing.

UBe_{13} with cubic structure is a candidate of a *p*-wave superconductor[1]. However, there is no evidence for magnetic ordering in UBe_{13} down to 25 mK in spite of a large paramagnetic Curie temperature θ_p of -100 K determined from magnetic susceptibility[2]. Specific heat is, however, reported to deviate from a power law behavior below 50 mK[2]. In order to clarify the origin of this anomaly, we performed a neutron scattering experiments on UBe_{13} in very low temperatures.

Polycrystalline sample of UBe_{13} was synthesized by arc-melting U and Be in an argon gas atmosphere. The sample were cooled by a ^{3}He-^{4}He dilution refrigerator down to 20 mK.

Neutron scattering experiments were performed using a cold neutron triple-axis spectrometer LTAS in JAERI with E_i = 4.674 meV.

Figure 1 shows elastic scattering profiles from UBe_{13} taken at 0.02 K and 0.77 K as well as the difference between them. Sharp nuclear Bragg peaks (200) and (222) are observed at both temperatures. Additional Bragg peaks such as (100), (110) or (111) indicated by arrows were not observed within an experimental error.

In order to examine a ferromagnetic ordering, we measured a temperature dependence of the (200) nuclear Bragg peak intensity, as shown in Fig. 2. The peak intensity increases gradually with decreasing temperature. However, there is no clear magnetic transition around 0.02 K. It is also noted that the intensity does not change upon superconducting transition at 0.8 K.

Lower limit of the detectable ordered moment size in the present experimental condition is estimated to be 0.3 μ_B/U for a simple anti-ferromagnetic ordering with $\boldsymbol{k}$ = (001). Since the experimental accuracy is not optimum, magnetic ordering with extremely small magnetic moment would not be detected. However, the anomaly in the specific heat below 50 mK is presumably attributed to nuclear quadrupole splitting of Be and additional magnetic contribution is extremely small[3]. Therefore, we conclude that magnetic ordering is absent in UBe_{13} down to 20 mK.

References

1) D.Einzel et al.: Phys. Rev. Lett. **56** (1986) 2513.
2) E.A. Schuberth: Int. J. Mod. Phys. B **10** (1996) 357.
3) W.G. Clark, et al.: J. Mag. Mag. Mat. **63-64** (1987) 396.

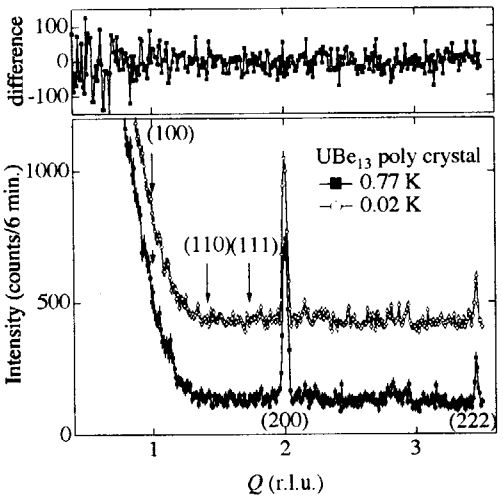

Fig. 1 Neutron diffraction profile for polycrystalline UBe_{13} taken at 0.77 K and 0.02 K (lower panel). Upper panel shows the difference between them.

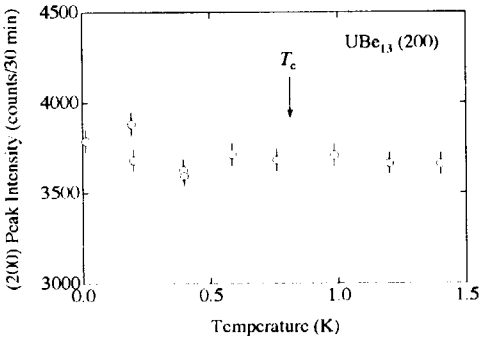

Fig. 2 Temperature dependence of (200) Bragg peak intensity for UBe_{13}.

JP9950049

2.3.5

Neutron Scattering Studies of the Low-Carrier System CeP under External Field

T. Osakabe, M. Kohgi[1], K. Iwasa[1], Y. Haga and T. Suzuki[2]

Advanced Science Research Center, Japan Atomic Energy Research Institute, Tokai, Ibaraki 319-11
[1]Department of Physics, Tokyo Metropolitan University, Hachioji, Tokyo 192-03
[2]Department of Physics, Tohoku University, Sendai 980-77

CeP is a low-carrier-density semi-metallic compound with NaCl-type crystal structure. Recently, Tohoku Univ. group have successfuly made high quallity single crystal samples of CeP. In paticular, the de Haas-van Alphen signal was detected on samples of batch no.2, 3 and 7 (we will abbreviate these to "CeP#2" etc.) It has been revealed by macroscopic measurements such as magnetization or specific heat measurements that CeP#2 and CeP#3 show unusual magnetic phase diagrams under magnetic field or under high pressure[1-3]. Although the static measurements gave no definite information about the datailes of the phass diagrams, our neutron scattering studies revealed that there are actually defferent phases in the diagrams. In this report, we briefly show the recent results of our neutron scattering experiments on CeP#3 and CeP#7 under external field.

Fig. 1 shows the phase diagrams determined by the neutron diffraction experiments on CeP#3 under magnetic field below 6T and under high pressure below 1.7 GPa. The magnetic structures in each phases are schematically shown at the bottom of the phase diagrams, where long and short arrows indicate the Ce ferromagnetic sheets with moment values for each Ce ion to be about 2 and 0.7 μ_B .

These two phase diagrams are quite similar. There is a scalling of 1GPa of pressure to 12T of magnetic field. At zero magnetic field with ambient pressure, CeP#3 show typical type-I antifferomagnetic ordering below the Neel temperature of T_N=10.5K, where each ferromagnetically orderd (001) plane stacks antifferomagnetically with the direction of the magnetic moment perpendicular to the plane. The magnetic moment per Ce atom is estimated to be $0.8\mu_B$+-0.1 μ_B, a value close to that of a Γ_7 crystal field state Ce^{3+} ion (0.7 μ_B).
The most prominat feature of the magnetic structures under magnetic field or under high pressure is that they are composed of two almost independent systems: one is the ferromagnetically coupled 2 μ_B Ce double-layer lattice and the other is the Γ_7 Ce lattice, which is in the crystal field ground state, sandwiched by the 2 μ_B Ce double-layers. The former appers with first order nature below T_{C2} and forms a kind of magnetic frame, while the latter undergoes an antifferomagnetic ordering below around T_{C1} almost independently within the 2 μ_B Ce frame. The interesting point is that many different magnetic phases appers in a quite systematic way under high pressure compared with under magnetic field. This means that the formation of the 2 μ_B Ce double-layer

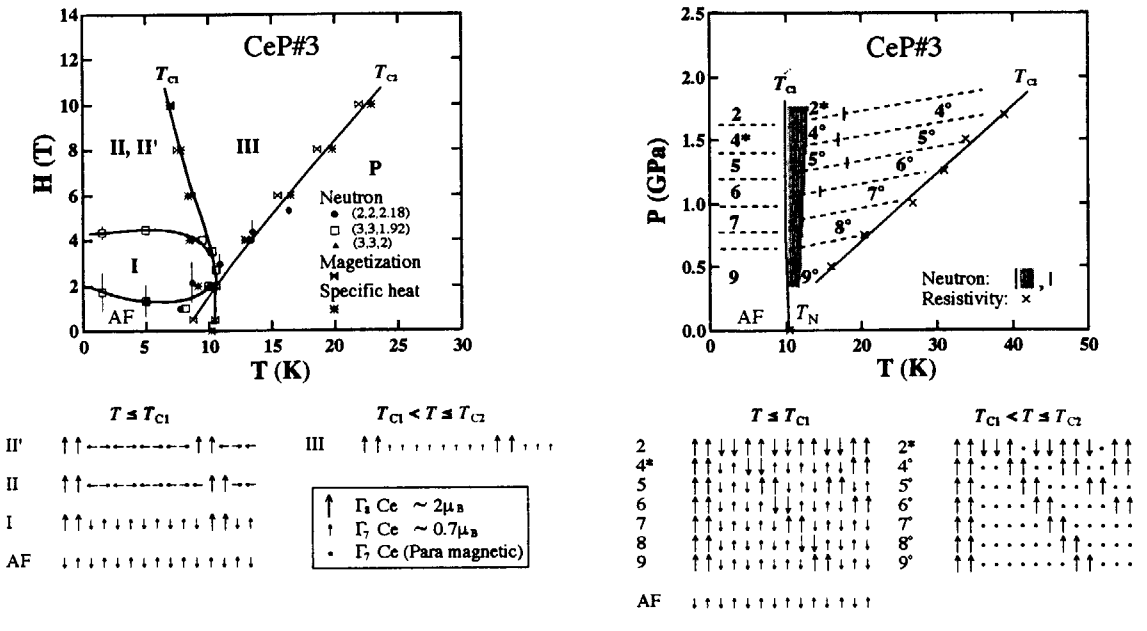

Fig.1 Phase diagrams of CeP#3 under magnetic field and under high pressure.

lattice is more sensitive to high pressure than magnetic field. This is also demonstrated by the fact that, in the magntic diffraction patterns, the widths of satellite peaks which originate from the 2 μ_B double-layer lattice are rather narrower under high pressure than under magnetic field. More detailed discussions concerning the experimental results have already given in separate papers[4-6].

The temperature dependence of the specific heat on CeP#7 was also measured so far. At zero magnetic field with ambient pressure, type-I antifferomagnetic ordering temperature of CeP#7 is identical with those of CeP#2 and CeP#3. Wnen the magnetic field applied, on the other hand, the transition temperature of T_{C2} slightly decreases compared to those of CeP#2 and CeP#3. In addition, the observed peak at T_{C2} is considerably broad, that is, the transition at T_{C2} is not clear in CeP#7. We also carried out the neutron diffraction experiments on CeP#7 under magnetic field below 6T. The results show that there is no such distinct satellite peak as observed in the diffraction patterns of CeP#3. These facts mean that, although the dHvA signal is detected on CeP#7, this sample has less quality for the formation of the 2 μ_B Ce double-layer lattice under magnetic field than CeP#2 and CeP#3. In the work of this year, we have carried out neutron diffraction experiments on CeP#7 under high pressure of 1.2 GPa to investigate the conditon of the formation of the 2 μ_B Ce double-layer lattice.

Fig.2 shows the diffraction pattern of CeP#7 at the pressure of 1.2 GPa. The magnetic structures derived from the diffraction patterns are schmatically shown at the bottom of the figures. It is quit intereiting that, different from the case under magnetic field, the magnetic structures of CeP#7 are identical with those of CeP#3 at the same pressure value of 1.2 GPa.

The above feature of CeP under magnetic field and high pressure can be explaned by the magnetic polaron model proposed by Kasuya et al., in which the combined effect of the Wigner crystallization due to the low carrier density and the Γ_8 p-f mixing stabilizes the magnetic polaron state[7]. The 2 μ_B Ce state observed below T_{C2} can be understood as the polarized 4f Γ_8 state caused by the strong magnetic polaron effect, in which the Γ_8 level is pulled down below the Γ_7 crystal field ground state.

In the framework of the magnetic polaron model, the increase of T_{C2} with increasing magnetic field is clearly due to the Zeeman energy gain of the Γ_8 Ce layers. On the other hand, the successive increase of the ratio of the Γ_8 Ce layers to all Ce layers under high pressure is due to the increase of the carrier (p-hole at Γ point) number as the result of the increase of the p-f mixing caused by applying pressure. Thus, the increas of T_{C2} is due to the p-f mixing energy gain. It is concluded that high pressure more stailizes the magnetic polaron lattice than magnetic field because high pressure is favorable for p-f mixing energy gain. This is also demonstrated by the experimental results on CeP#7.

1) T. Suzuki, JJAP Series 8(1993)267
2) N. Môri, Y. Okayama, H. Takahashi, Y. Haga and T. Suzuki, JJAP Series 8(1993) 183
3) Y. Haga, Thesis, Tohoku Univ.(1995)
4) M. Kohgi et al., Phys. Rev. B49 (1994) 7068
5) T. Osakabe et al., Physica B230-232 (1997) 645
6) M. Kohgi et al., J. Phys. Soc. Jpn.65 (1996) Suppl. B 99
7) T. Kasuya et al., J. Phys. Soc. Jpn.62 (1993)3376; T. Kasuya et al. , Solid State Commun. 93(1995)307

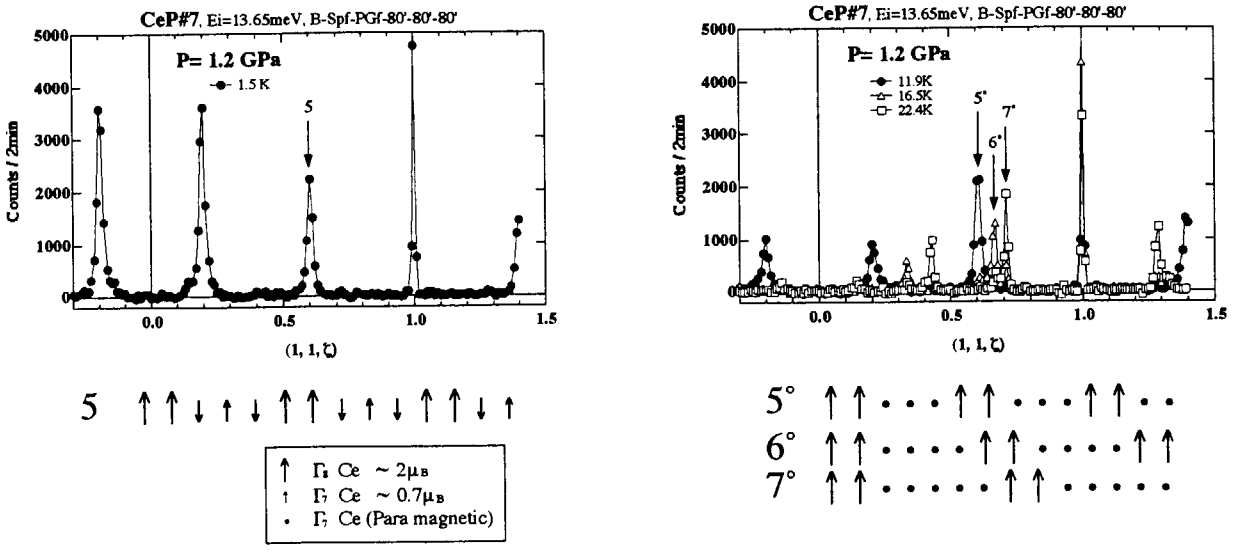

Fig.2 Magnetic diffraction patterns and magnetic structures of CeP#7 under the pressure of 1.2GPa.

2.3.6

Neutron Diffraction Study of the Kondo Antiferromagnet $CePt_2Sn_2$

H. Kadowaki, T. Sasaki, K. M. Kojima,[1] Y. J. Uemura,[1] G. M. Luke,[1] Y. Fudamoto,[1] T Osakabe,[2] Y Koike,[2] N. Metoki,[2] S. Katano,[2] K. Ohoyama,[3] M. Ohashi,[3] Y. Echizen,[4] T. Takabatake[4]

Department of Physics, Tokyo Metropolitan University, Hachioji-shi, Tokyo 192-0397
[1]Department of Physics, Columbia University, New York, NY 10027, U. S. A.
[2]Advanced Science Research Center, Japan Atomic Energy Research Institute, Tokai, Ibaraki 319-11
[3]Institute for Material Research, Tohoku University, Sendai 980
[4]Faculty of Science, Hiroshima University, Higashi-Hiroshima 739

The competition between Kondo spin fluctuation and exchange interactions produce a very heavy electron system of $CePt_2Sn_2$ which is characterized by a very large $\gamma > 3$ J/mole K^2 and a low Néel temperature $T_N = 0.9$ K.[1] Powder diffraction studies were performed to reveal the crystal structure and the magnetic structure using HERMES and TAS-2. The crystal structure is a $CaBe_2Ge_2$-type (P4/nmm) with a small monoclinic distortion. We performed the Rietveld analysis (RIETAN) assuming $P2_1/m$ and $P2_1$ space groups using diffraction data taken at $T=1.8$ K $> T_N$. A result for the $P2_1/m$ structure is shown in Fig. 1. One can see that there is certain discrepancy, though quality of fitting is not so bad. Below Néel temperature weak magnetic reflections were observed. Detail of the magnetic profile is being analyzed now. The magnetic structure is a single-k type with a modulation vector (1/3 0 1/2). In Fig. 2 an approximate magnetic structure, i.e., tentative result and to be revised, is illustrated.

Reference

1) W. P. Beyermann et al.: Phys. Rev Lett. **66** (1991) 3289

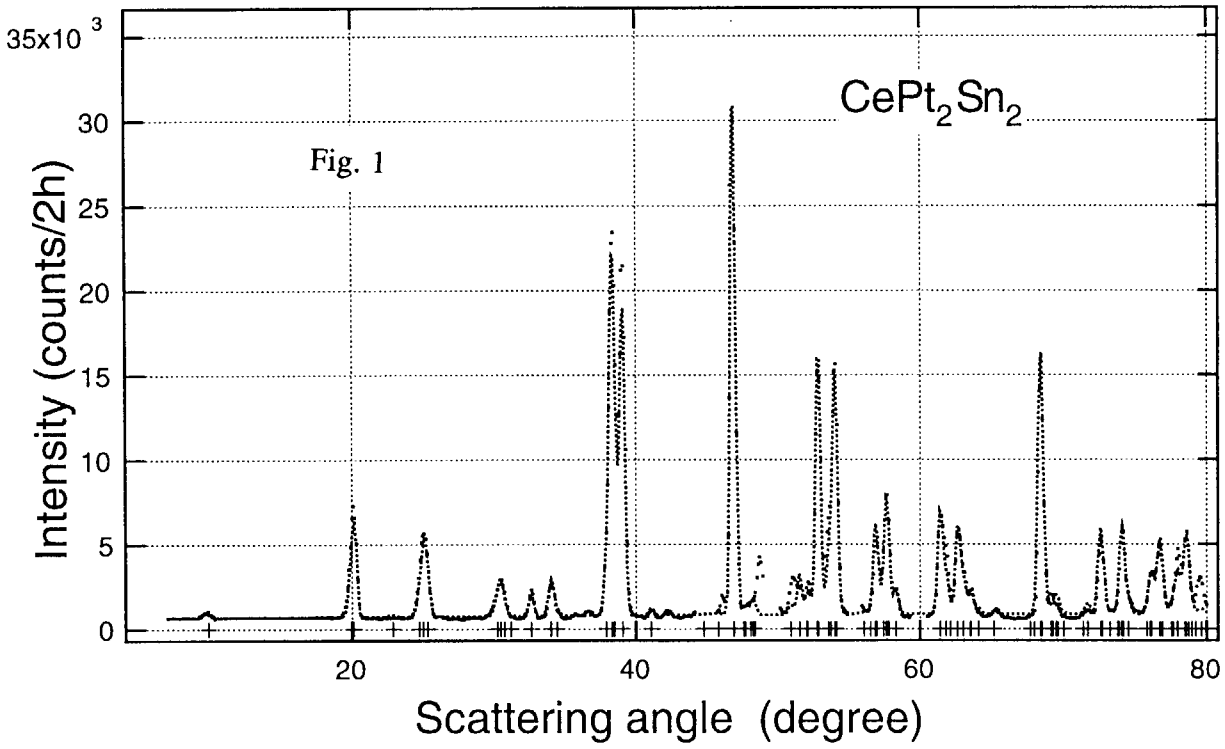

Fig. 2

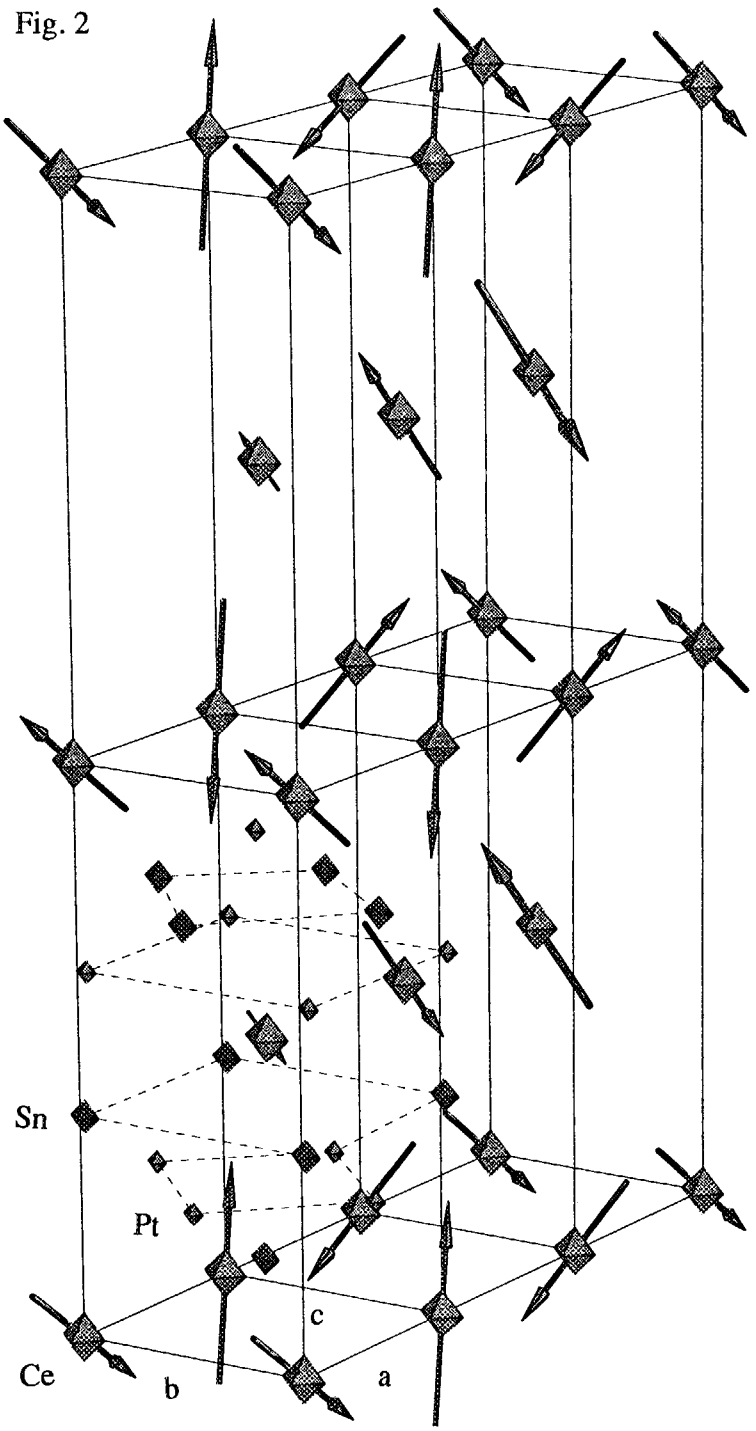

JP9950051

2.3.7 Crystal Electric Field of PrPtBi

T. Osakabe, M. Kasaya[1] and S. Yoshii[1]

Advanced Science Research Center, Japan Atomic Energy Research Institute, Tokai, Ibaraki 319-11
[1]Department of Physics, Tohoku University, Sendai 980-77

PrPtBi crystallize in the cubic MgAgAs-type structure. The temperature dependence of the specific heat in PrPtBi shows an anomaly at about 1.35 K, indicating a phase transition. The magnetic entropy is nearly Rln2 at about 4 K and reaches to the value of Rln5 at about 80 K. Under the cubic symmetry, the crystalline electric field (CEF) level scheme of Pr^{3+} ion consists of a non-magnetic doublet Γ_3, triplet states Γ_4, Γ_5 and a singlet state Γ_1. From the analysis of the magnetic susceptibility and magnetic entropy data based on the CEF model, H. Suzuki et al. proposed the CEF level scheme as shown in Fig.2(a) [1].

In order to determine the crystal field level precisely, we carried out neutron inelastic experiments using the triple axis spectrometer TAS-1(2G) at JRR-3M, JAERI. The spectrometer was set up to generate the incident neutron energy of 33.5 meV with 40'-40'-40'-40' collimation. The sample set in the Al container with ^{4}He gas was mounted on the closed cycle refrigerator (CTI).

Fig. 1 shows the neutron inelastic spectra of PrPtBi. Well-defined peaks are observed at 6.5 meV and 10 meV at lower temperature. The intensities of both peaks decrease considerably at higher temperature or higher Q. This indicates that these peaks correspond to the CEF excitations from the ground to the first and to the second excited states of Pr^{3+} ion. The analysis of integrated intensity of these peaks show that the CEF level scheme consists of a non-magnetic doublet ground state Γ_3, a first excited triplet state Γ_5 with energy of 75K, a second excited triplet state Γ_4 with 116K and a third excited singlet state Γ_1. Thus, the increase of intensity at 3.5 meV at 151K corresponds to a transition from the first excited state Γ_5 to the second excited state Γ_4 because of the increase of the occupational probability of the Γ_5 state with increasing temperature. On the other hand, the peak at around 17 meV corresponds to the phonon contribution. Fig.2(b) shows the CEF level scheme deduced from our measurement. In this scheme, however, the energy of the third excited singlet state Γ_1 is not shown. This is because we could not obtain the information about the energy of Γ_1 state in our experimental energy range.

The cubic MgAgAs-type structure and the non-magnetic ground state Γ_3 are common character between PrPtBi and ternary uranium compound UNiSn, which shows an anomalous phase transition at 43 K caused by a sort of cooperative effect between the ground state Γ_3 with quadropolar moment and the first excited state Γ_4 with magnetic moment[2]. Thus, there is the possibility that the phase transition at 1.35K in PrPtBi originate from a quadropolar ordering and that there exist a magnetic ordering below transition temperature. To check this point, we measured the neutron diffraction pattern at 200 mK using a dilution refrigerator. However, we could not detect a structural distortion with a ferroquadropolar ordering and magnetic reflections, which were observed in UNiSn.

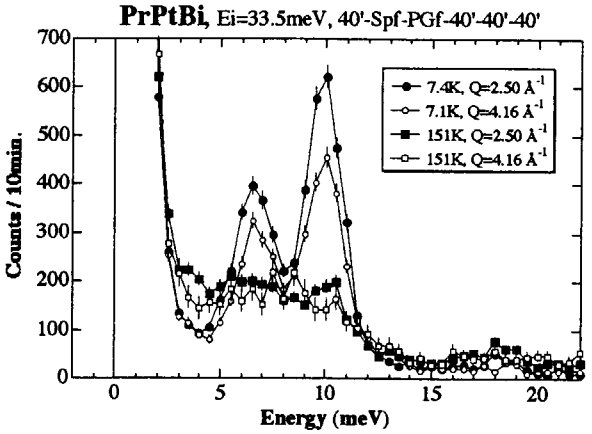

Fig. 1 The neuron inelastic scattering spectra of PrPtBi.

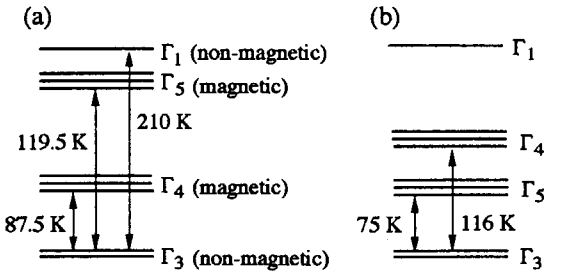

Fig. 2 The possible schematic crystal field level scheme for PrPtBi
(a) The level scheme deduced from bulk measurements [1]
(b) The level scheme from our measurements

References

1) H. Suzuki et al., J. Phys. Soc. Jpn., 66 (1997) 2566
2) T. Suzuki et al., Physica B 199&200 (1994) 483

2.3.8 Neutron Powder Diffraction Study of Rhombohedral $Y_2Fe_{17}N_{3.1}$

K. Koyama, T. Kajitani[2], Y. Morii[3], H. Fujii and M. Akayama

Faculty of Integrated Arts and Sciences, Hiroshima University, Higashi-hiroshima, 724
[2]Department of Applied Physics, Tohoku University, Sendai 980-77
[3]Advanced Science Research Center, Japan Atomic Energy Research Institute, Tokai, Ibaraki, 319-11

In 1990, Coey and Sun reported that the introduction of nitrogen atoms into R_2Fe_{17} (R=rare earth) compounds led to remarkable increases in the Curie temperature and magnetic moments of the Fe sublattice accompanied by a large increase in unit cell volume (~7%) without the their crystal structures[1]. Since then, many experimental studies have been performed to clarify the basic magnetic properties of interstitially modified compounds $R_2Fe_{17}N_3$. However, in detail, the influence of interstitial N atoms on the Fe magnetic moments in the rhombohedral $Y_2Fe_{17}N_3$ has not been reported yet because of the difficulty to obtain a single-phased sample.

In this work, we carried out neutron powder diffraction study on the rhombohedral $Y_2Fe_{17}N_{3.1}$ with a nonmagnetic Y in the temperature range from 10 to 300 K in order to microscopically clarify the crystallographic and magnetic structures in $Y_2Fe_{17}N_3$.

The host compound Y_2Fe_{17} was prepared by arc-melting under argon atmosphere. After annealing it at 1393 K for two weeks, the ingot was quenched in water. The annealed ingot was pulverized into fine powder less than 20 μm in diameter. The nitride $Y_2Fe_{17}N_{3.1}$ was synthesized by heat treating the powder at 713 K for 24 h under a high N_2-gas pressure of 6MPa. Upon nitrogenation, the lattice parameters *a* and *c*, respectively, increase by 2.0% and 2.4% at 310 K without changing the crystallographic symmetry. Neutron diffraction experiment was carried out at the JRR-3M High Resolution Neutron Powder

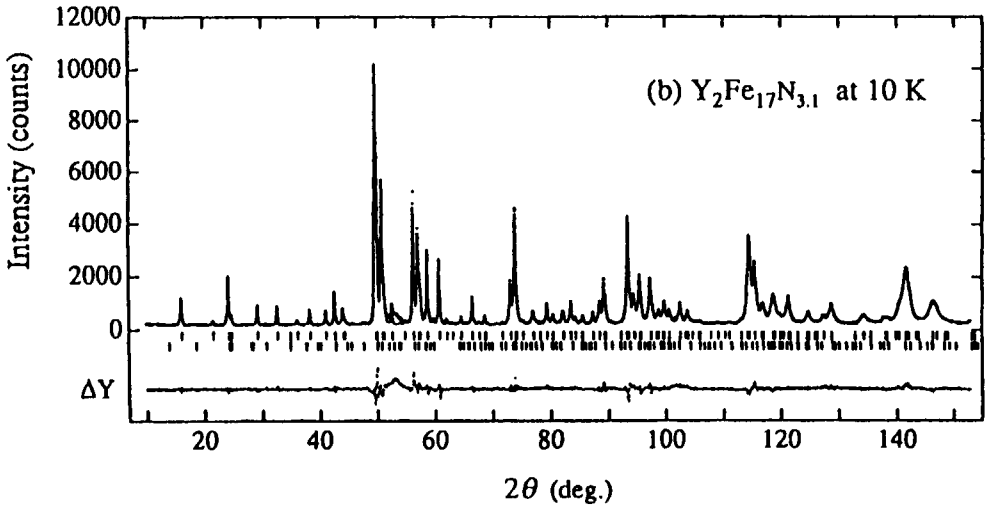

Fig.1. Neutron powder diffraction pattern of $Y_2Fe_{17}N_{3.1}$ at 10 K. The dots and line correspond to the observed and calculated patterns, respectively. The lower part is the difference pattern (observed-calculated).

Table 1. Refined parameters of rhombohedral $Y_2Fe_{17}N_{3.1}$ at 10 K. n is the occupation factor; x, y, and z are the fractional coordinates; B is the isotropic thermal parameter (Å); and m is the magnetic moment (μ_B/atom). Numbers in parentheses are the statistical error given by the refinement program.

$Y_2Fe_{17}N_{3.1}$	10 K		R_p=6.21 %			
Rhombohedral		R_I=2.97 %	R_F=1.97 %			
a=8.6710(3) Å		c=12.7241(4) Å				
Atom	Site	n	x	y	z	B	m
Y	6c	1.0	0	0	0.338(1)	0.85(4)	
Fe(1)	6c	1.0	0	0	0.0949(6)	0.202(7)	2.86(5)
Fe(2)	9d	1.0	0.5	0	0.5	0.202	2.12(8)
Fe(3)	18f	1.0	0.2829(5)	0	0	0.202	2.01(4)
Fe(4)	18h	1.0	0.1703(3)	-0.1703	0.4860(4)	0.202	2.41(5)
N(1)	9e	0.995(5)	0.5	0	0	0.65(5)	
N(2)	18g	0.039(2)	0.08(1)0	0.5	0.65		

Diffractometer (HRPD). The diffraction data was analyzed using RIETAN-94, which was developed for application of the Rietveld method[2].

Figure 1 shows the neutron powder diffraction pattern of $Y_2Fe_{17}N_{3.1}$ at 10 K. As is evident from the figure, in the diffraction pattern of $Y_2Fe_{17}N_{3.1}$, a small and broad peak corresponding to α-Fe segregation upon nitrogenation appears around 2θ=53.4°. Therefore, the refinement for the nitride were performed for the data except 2θ range from 52.5 to 54.5°.

The calculated pattern (line) is in very good agreement with the observed pattern (dots), as shown in the figure. The final R factors were R_I=2.97 % and R_F=1.97 %. The result of the refinement at 10 K is summarized in Table 1. Upon nitrogenation, total magnetic moment M increase by 17%, reaching M=38.6(3) μ_B/f.u.[3]. As is evident from Table 1, the site-dependent Fe moments are observed, such that the magnetic moment of the 18f-Fe atoms is the smallest (~2.0 μ_B), while the moment of the 6c-Fe atoms has the largest (~2.9 μ_B). This result could be understood as the differences of environment around the Fe atoms. That is, when the N atoms are introduced into the 9e interstitial site, all the Fe moments probably increase by a reduction in the Fe-Fe overlap caused by the increase in the Fe-Fe distances. In detail, the smallest Fe moment on the 18f sites which are the nearest to the 9e-N atoms is originated in the strong hybridization between the Fe 3d-states and the N 2p-states. On the contrary, the Fe moment on the 6c sites which are the farthest from the 9e-N atoms has the largest in $Y_2Fe_{17}N_{3.1}$.

References

1) J.M.D. Coey and H. Sun, J. Magn. Magn. Mater. **87** (1990) L251.
2) Y.I. Kim and F. Izumi, J. Ceram. Soc. Jpn. **102** (1994) 401.
3) K. Koyama, T. Kajitani, Y. Morii, H. Fujii and M. Akayama, Phy. Rev. B **55** (1997) 11414.

2.3.9 Charge Ordering in $Pr_{0.75}Ca_{0.25}MnO_3$

H. Hino, N. Ikeda, Y. Yamada,T. Inami, S. Katano

Advanced Research Institute for Science and Engineering, Waseda Univ., Okubo, Shinjuku, Tokyo 169-0072 Japan

Japan Atomic Energy Research Instutute, Tokai, Ibaraki, 319-1106, Japan

Recently, provskite type doped manganese oxides have attracted attentiions du to extraordinary magneto-transport properties such as CMR phenomena.

One of the important aspects is the transition to charge-magnetic ordered states. $Pr_{1-x}Ca_xMnO_3$ (x=0.3) is reported to transform to the charge ordered state with the chage /hole configuration on ab-plane as shown in Fig. 1. However, the nominal hole concentration for the postulated charge structure is n=1/2, which is far from the x-value (x=0.3) of the observed system. One of the possibilities to reconcile the discrepancy would be that the correct structure is an alternative stacking of layers with n=1/2 and n=0 along the c-axis, which is consistent with the x-value of x=0.25.

In order to investigate this possibility, we studied the charge ordering in $Pr_{0.75}Ca_{0.25}MnO_3$. Preliminary electron diffraction study has shown that satellite reflections appear at (h/2 k/2 l/2), which indicates that the lattice is doubled along the orthorhombic c-axis. Neutron scattering studies have been carried out to investigate temperature dependence of the satellite intensity. As shown in Fig. 2, it shows extraordinary behavior : After reaching the maximum value at T (magnetic transition temperature), it starts to decrease upon decreasing temperature. This seems to suggest the competition between charge ordering vs. magnetic ordering. Detailed analysis of the charge structure is now underway. .

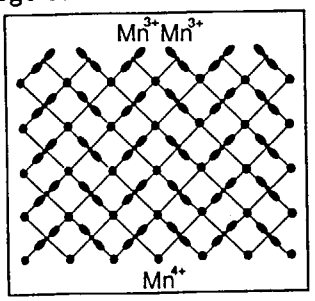

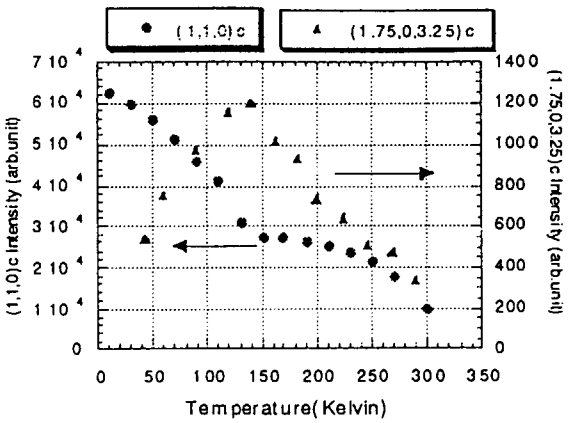

JP9950054

2.3.10

Hole-induced antiferromagnetic ordering in the spin singlet state of the ladder material : $Sr_{2.5}Ca_{11.5}Cu_{24}O_{41}$

J. Akimitsu, T. Nagata, H. Fujino, S. Katano[1], M. Nishi[2], and K. Kakurai[2]

Department of Physics, Aoyama-Gakuin University, Setagaya-ku, Tokyo 157-8572
[1]Neutron Scattering Group, Advanced Science Research Center, Japan Atomic Energy Research Institute, Tokai, Ibaraki 319-1195
[2]Neutron Scattering Laboratory, ISSP, The University of Tokyo, Tokai, Ibaraki 319-1106

It has long been believed that the ground state of the two-leg ladder system is a singlet state called "the spin liquid state" and this has been confirmed experimentally by the NMR and neutron scattering measurements. From NMR (Knight shift) measurements, spin gap values (ladder) of $Sr_{14}Cu_{24}O_{41}$, $Sr_9Ca_5Cu_{24}O_{41}$ and $Sr_{2.5}Ca_{11.5}Cu_{24}O_{41}$ were reported to be 44 meV, 24 meV and 23 meV, respectively [1]. In inelastic neutron scattering measurements, on the other hand, the spin gap of 32.5 meV, 33.5 meV were observed for $Sr_{14}Cu_{24}O_{41}$ and $Sr_{2.5}Ca_{11.5}Cu_{24}O_{41}$ [2,3].

Recently, however, we observed the magnetic long range order by the heat capacity and neutron scattering measurements. In this paper, we report the neutron scattering measurements on $Sr_{14-x}Ca_xCu_{24}O_{41}$ single crystal at low temperatures around 2 K. Our experiments revealed the new results for the magnetic ground state at high Ca concentration x (x = 11.5) under ambient pressure. From the specific heat results, we observed a magnetic long range order at $x \sim 11.5$ under fairly low temperatures ($T_N \sim 2.1$ K) compared with the spin gap value. Magnetic Bragg peaks below T_N were also observed in the neutron scattering measurements on a $Sr_{2.5}Ca_{11.5}Cu_{24}O_{41}$ single crystal.

We performed an elastic neutron scattering for a single crystal $Sr_{2.5}Ca_{11.5}Cu_{24}O_{41}$. From this experiment, we observed a number of Bragg peaks which appeared below 2 K. Figure 1 shows the typical elastic neutron scattering results at (1 0 l), (0 1 l) and (h 0 12), these results were plotted after subtracting the intensity at 5 K from that at 1.4 K. We confirmed that the FWHM of the observed Bragg peaks is nearly the resolution limit. Figure 2 shows the positions of the observed Bragg peaks in the reciprocal lattice space, where the arrow lines and circles correspond to the lines scanned and the Bragg peaks observed, respectively. To clarify whether these Bragg peaks are magnetic or not, we performed the polarized neutron scattering experiments for one of the Bragg peaks, (1 0 12), as shown in figure 3. In both horizontal and vertical field, we observed the spin-flip scattering at 1.4 K. These results clearly show that the

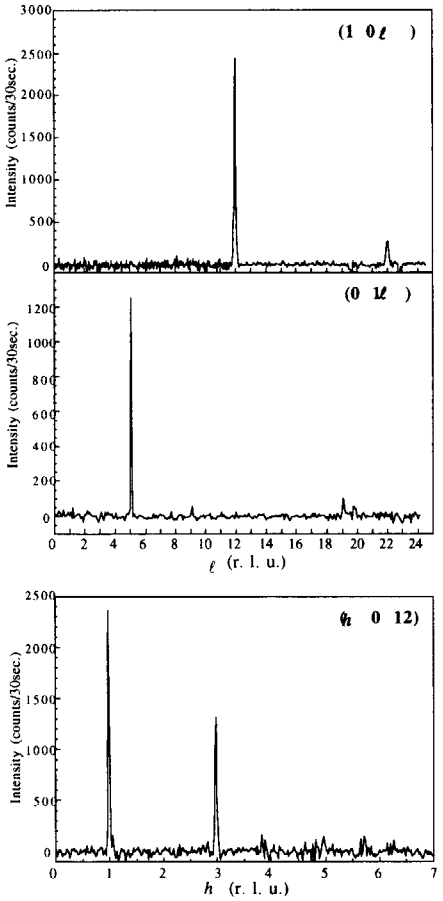

Fig. 1 Typical results by elastic neutron scattering experiments at (1 0 l), (0 1 l) and (h 0 12) of the $Sr_{2.5}Ca_{11.5}Cu_{24}O_{41}$ single crystal, these results were plotted after subtracting the intensity at 5 K from that at 1.4 K.

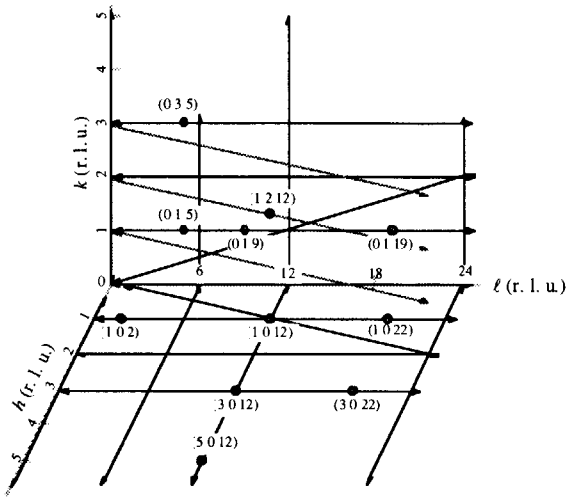

Fig. 2 Positions of the observed Bragg peaks observed by neutron scattering measurements in the reciprocal lattice space of $Sr_{2.5}Ca_{11.5}Cu_{24}O_{41}$ single crystal, arrow lines and circles correspond to the scanned lines and the observed Bragg peaks, respectively.

observed Bragg peak, (1 0 12), is purely magnetic. The static magnetic moments directs almost along the *a*-axis in the ladder planes by taking into account of the scattering vector's direction and the peak intensity at (1 0 12).

Assuming that magnetic spins in the ladders are responsible for the magnetic order, the appearance of (3 0 12) Bragg peak leads to the ferromagnetic order in the *a-c* plane, and this ferromagnetic order aligns antiferromagnetically in the adjacent layers. However, due to the absence of (0 *k* 0) reflection, the possibility of the ferromagnetic or ferrimagnetic order in the plane is excluded. Therefore, we conclude that the spins are antiferromagnetically ordered in the *a-c* plane. However, at present stage, we cannot construct the reasonable magnetic structure in the ladder planes. The final magnetic structure is now under consideration.

We emphasize here the ground state of this system. As described before, inelastic neutron scattering has directly indicated that the spin gap energy for the ladders in the $Sr_{2.5}Ca_{11.5}Cu_{24}O_{41}$, the same material in our present experiment, was found to be 33.5±0.5 meV [3]. Therefore, it is likely that magnetic order is due to some of the unpaired spins, breaking up spin singlet states by introducing the holes into ladders, and these unpaired spins ordered antiferromagnetically at low temperature. Accordingly the ground state of this system at ambient pressure might be one in

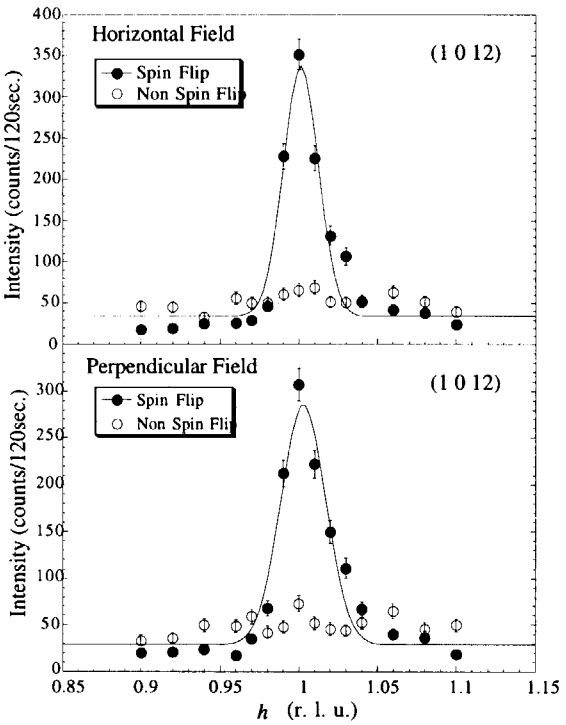

Fig. 3 The experimental results for one of the Bragg peak, (1 0 12) of $Sr_{2.5}Ca_{11.5}Cu_{24}O_{41}$ single crystal at 1.4 K using polarized neutrons. Horizontal field corresponds to the parallel to the scattering vector Q and the vertical field correspond to the perpendicular to the scattering plane at the sample position.

which both paired and unpaired spins coexist and the holes and spins float in a " spin liquid sea " at high temperature. These holes are localized at certain temperature and the spins finally order at $T_N \sim 2.1$ K.

References

[1] K. Magishi, S. Matsumoto, Y. Kitaoka, K. Ishida, K. Asayama, M. Uehara, T. Nagata and J. Akimitsu, Phys. Rev. B **57**, 11533 (1998).
[2] R. S. Eccleston, M. Uehara, J. Akimitsu, H. Eisaki, N. Motoyama and S. Uchida, Phys. Rev. Lett. (to be published).
[3] S. Katano, T. Nagata, J. Akimitsu, M. Nishi and K. Kakurai, preprint.

JP9950055

2.3.11

Neutron Scattering Study of the Spin Gap in the Hole-Doped Spin Ladder System $(Sr_{2.5}Ca_{11.5})Cu_{24}O_{41}$

J. Akimitsu, T. Nagata, S. Katano[1], M. Nishi[2], and K. Kakurai[2],

Department of Physics, Aoyama-Gakuin University, Setagaya-ku, Tokyo 157-8572
[1]Neutron Scattering Group, Advanced Science Research Center, Japan Atomic Energy Research Institute, Tokai, Ibaraki 319-1195
[2]Neutron Scattering Laboratory, ISSP, The University of Tokyo, Tokai, Ibaraki 319-1106

Recently, theoretical prediction has been made that a two-leg ladder, coupling of two spin-1/2 Heisenberg chains, leads to a singlet ground state with a spin gap and a finite correlation length at $T = 0$. The existence of a spin gap is obvious in the limit that exchange interaction along the rung is much larger than that along the leg, since the ground state is then simply a collection of singlets along the rungs. For a general ratio, the ground state is a resonating valence bond state.

Experimentally, it is intriguing that the spin gap value vs. number of holes and the existence of the spin gap in the superconducting state. In this report, we summarize the present situation of the spin gap in the two-leg ladder $(Sr,Ca)_{14}Cu_{24}O_{41}$.

Figure 1 shows the inelastic neutron scattering intensity – the difference between the intensity measured at around the antiferromagntic zone center (0.5 0 1.5) and the background intensity measured at the reciprocal lattice point (1.5 0 1.36) – at 7 K obtained with the constant-Q method. As shown in the figure, the intensity is distributed over a wide energy range beyond the energy resolution. A broad but clear peak in the intensity was, however, observed at 33.5 ± 0.5meV for the zone center (0.5 0 1.5). This energy can be assigned to be the spin gap energy of this heavily doped compound. The inset presents the scattering intensities with this energy along the c^* direction. These intensities were peaked at (0.5 0 1.5) and also at (0.5 0 2.5), which clearly shows that the spin gap observed here has the periodicity of the ladders and, thus, is certainly originated from the ladders of this material. Very recently, neutron scattering experiments for a single crystal showed that the spin gap of the parent material $Sr_{14}Cu_{24}O_{41}$ is about 32.5 meV [1]. Therefore, within the experimental accuracy, the spin gap of the doped compound does not change even if Ca is substituted up to 11.5 (Fig. 2). The present result

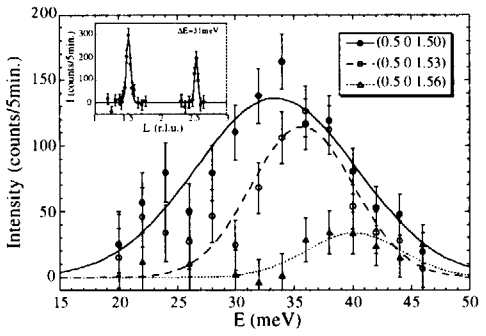

Fig. 1. Inelastic neutron scattering intensities after the subtraction of the background intensity for the constant-Q scans. The solid line shows the spin excitation at the antiferromagnetic zone center, showing the spin gap energy of 33.5±0.5 meV. The inset shows the intensities with this energy along the c^* direction. The dotted lines show the spin excitations at the reciprocal lattice point apart from this zone center. The lines are the results of the Gaussian fitting.

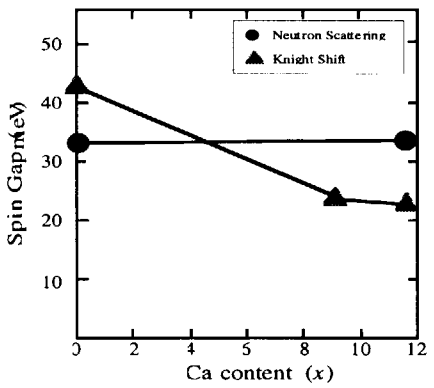

Fig. 2. Spin gap as a function of the Ca content. The circles show the results from neutron inelastic scattering experiments. The triangles are the results of the Knight shift in the NMR experiments in Ref. 4.

is initially unexpected since the transport property of the system is drastically changed from an insulator to a metallic state with the Ca doping. Holes doped by the Ca substitution would affect the spin liquid state of the system. Some theories actually suggested that the spin gap decreases with increasing the Ca content [2,3]. The results obtained here, thus, indicate the necessity of theories that explain the magnetic excitation properties in this spin ladder system.

Fig. 3 (a) shows the constant energy scans with Δ = 34,40,50.5 meV. With departing from the zone center, the excitation energy increases greatly, indicating a dispersive character. The dispersion relation derived from the constant-E scans in Fig. 3 (a) is displayed in Fig. 3 (b). Here, the scans were fitted to Gaussian profiles.

Since the energy is limited up to 55 meV in the present work, the data is not enough to discuss the exchange couplings in the system. However, the dispersion obtained can be explained with large exchange energies of the order of 100 meV. The dotted line is the dispersion curve represented using the exchange constants which was recently obtained by Eccleston *et al.* for the parent compound - the exchange constants along the legs $J_{\parallel}$=130 meV and along the rungs $J_{\perp}$=72 meV [1]. It is clear that to get the whole dispersion curve and then to discuss the exchange interactions precisely, experiments at higher energies up to 200 meV are required. Such experiments are now being planned using a spectrometer on a spallation neutron source.

The inset of Fig. 3 (b) shows an intensity contour map obtained in the present experiments. Strong intensities are concentrated around the antiferromagnetic zone center, and are spread over the wide range of the energies around the spin gap excitation energy of 33.5 meV. This intensity distribution might be a distinctive feature of this system, and should be understood in the future work.

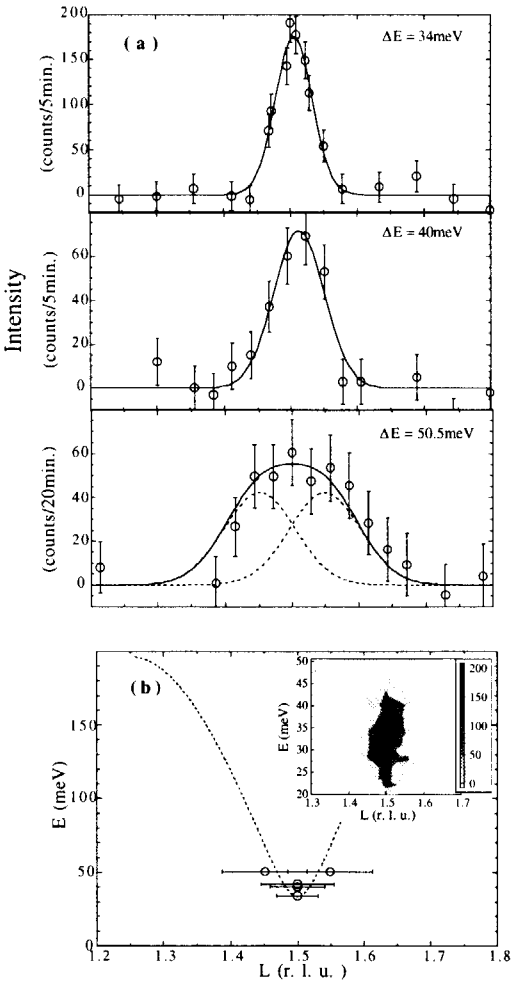

Fig. 3 (a) Inelastic neutron scattering intensities for the constant-E scans. The lines are the results of the fits to a Gaussian, or the sum of two Gaussians displaced equally from the zone center. (b) Dispersion relation at 7 K. The horizontal bars represent the full width at half maximum (FWHM) derived from Gaussians fits to the data shown in (a). The dotted line shows the dispersion relation with the exchange constants along the legs $J_{\parallel}$=130 meV and that along the rungs $J_{\perp}$=72 meV which were proposed for the parent compound. The inset shows the intensity contour map obtained from the present experiments.

References

[1] R. S. Eccleston, M. Uehara, J. Akimitsu, H. Eisaki, N. Motoyama, S. Uchida, (to be published in Phys. Rev. Lett.)
[2] E. Dagotto, J. Riera, and D. Scalapino, Phys. Rev. B**45**, 5744 (1992).
[3] D. Poiblanc, H. Tsunetsugu, and T.M. Rice, Phys. Rev. B**50**, 6511 (1994).
[4] K. Magishi, S. Matsumoto, Y. Kitaoka, K. Ishida, K. Asayama, M. Uehara, T. Nagata, and J Akimitsu, Phys. Rev. B**57**, 11533 (1998).

JP9950056

2.3.12 Magnetic phase diagram of $CuGe_{1-x}Si_xO_3$

J. Akimitsu, O. Fujita, S. Katano[1], M. Nishi[2], K. Kakurai[2], and Y. Fujii[2]

Department of Physics, Aoyama-Gakuin University, Chitosedai, Setagaya-ku, Tokyo 157-8572
[1]Neutron Scattering Group, Advanced Science Research Center, Japan Atomic Energy Research Institute, Tokai, Ibaraki 319-1195
[2]Neutron Scattering Laboratory, ISSP, The University of Tokyo, Tokai, Ibaraki 319-1106

The discovery of the compound $CuGeO_3$, which is the first inorganic spin-Peierls (SP) material, stimulated many extensive studies in order to understand its unique physical properties. The coexistence of the SP state and long range antiferromagnetic (AF) order in Zn and Si doped crystals has attracted much attention since it has been naively believed that this cannot occur at the same time in a unique phase. Evidence for the coexistence of the lattice dimerization and the AF order has, however, been revealed by neutron diffraction experiments; both superlattice reflections originated from lattice dimerization and magnetic Bragg peaks are observed below the Néel temperature (T_N) in $Cu_{1-x}Zn_xGeO_3$ and in $CuGe_{1-x}Si_xO_3$. It has also been shown theoretically with phase Hamiltonian technique that disorder induced AF order is possible in the SP state $CuGeO_3$ doped with Si and Zn.

Although several experiments on the doping effect have been performed, there are still some discrepancies. In the present work, hence, the magnetic phase diagram of the Si doped system has been investigated in more detail over a wide range of the doping concentration. The results show that the effects of the Si doping on the magnetic states are rather weak in comparison with those reported in the previous work on the other hand, the effects of Si are a little stronger than those of the Zn doping.

The magnetic moments of Cu^{2+} ions weredetermined by the magnetic intensities observed. The *effective* magnetic moment is 0.21 μ_B for 1.0%, and 0.29 μ_B for 1.8% sample. All the data are presented in Fig. 1 (a). The magnitude of the magnetic moment roughly has a linear relation with T_N. In this figure the concentration dependence of magnetic moments for the Zn doping previously reported[1)] is also shown by the dotted line. The results show a similar tendency for both impurities. The lattice dimerization along the Cu-chain direction is also obtained. Figure 1 (b) shows the dimerization δ

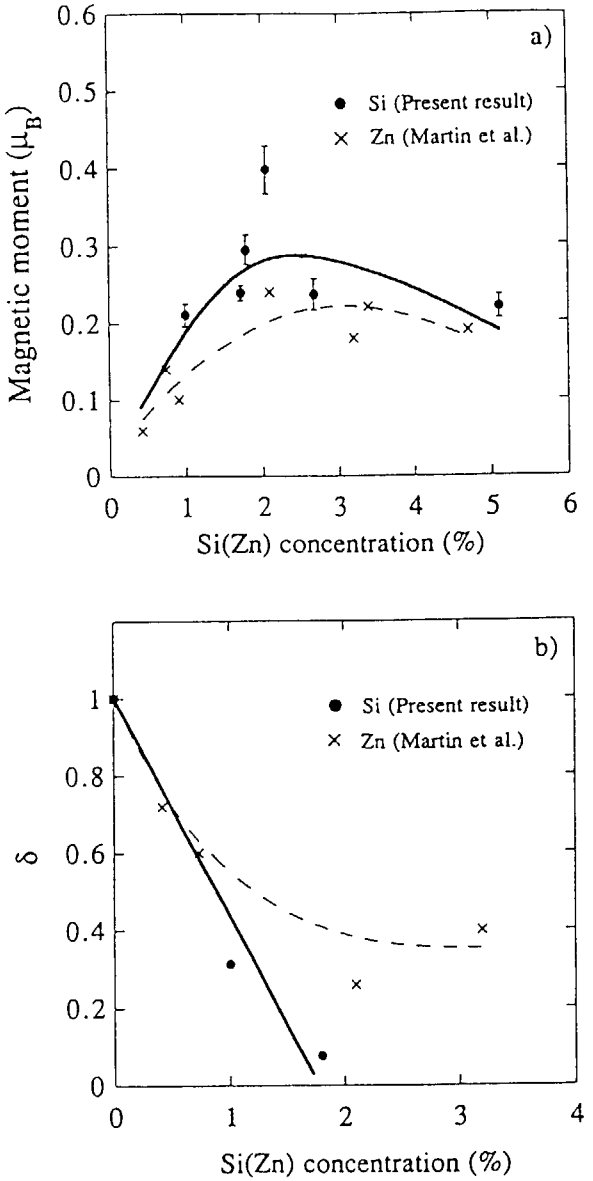

FIG. 1. Magnitude of the magnetic moment (a) and the lattice distortion (b) as a function of the Si concentration. The solid lines are guides to the eye. The dotted lines indicate the data for the Zn doped system observed by Martin *et al.*

at 1.5 K which was normalized by the value of the pure compound. The lattice distortion is greatly suppressed with the Si doping at low temperatures as was mentioned before, and would not be observed over 2.5 % Si. This result is quite different from the work on the Zn doping [1] which is shown by the dotted line in the figure.

Figure 2 shows the magnetic phase diagram as a function of the Si concentration. Comparing with Fig. 1, T_N and T_{SP} are found to have linear relations roughly with the magnetic moments and the lattice dimerization, respectively. The dotted line in this figure shows the results for the Zn doping, and similar discussion mentioned above can be made. For the Si doping, the present result agrees well with the recent work.[2] However, the results show some distinctive discrepancies with those in the previous works[3,4] which is shown by the dash-dotted line. The concentration dependence of T_{SP} reported there is almost twice as large as that of the present result. On this point, a recent report showed that the concentration dependence of these transition temperatures are strongly affected by the preparation temperature for crystals and powdered samples.[5] The discrepancies with the previous results, hence, may be caused by a slight difference of the sample preparation temperatures. As another possibility, the difference in the O_2 deficiency of the samples[5] could be pointed out.

To conclude, the coexistence of the SP and AF states in $CuGe_{1-x}Si_xO_3$ single crystals was carefully examined by neutron diffraction experiments. The Si concentration dependence of the magnitudes of the magnetic moment and the lattice dimerization were presented for a wide range of the concentration.

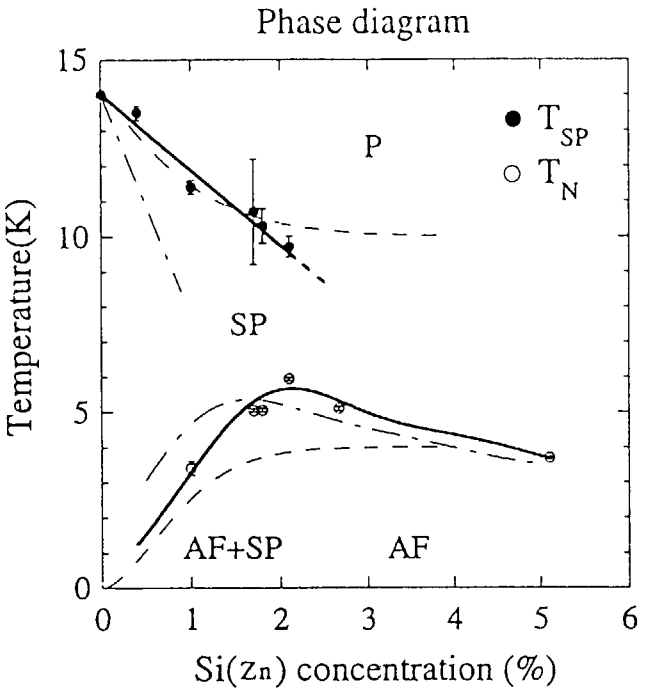

FIG. 2. Magnetic phase diagram as a function of Si concentration. The solid lines are guides to the eye. The dash-dotted lines show the previous results for the Si doped system reported by Renard *et al.*, and the dotted lines represent the data for the Zn doped system observed by Martin *et al.*

References

[1] M. C. Martin, M. Hase, K. Hirota, G. Shirane, Y. Sasago, N. Koide and K. Uchinokura , Phys. Rev. B**56**, 3173 (1997).

[2] K. Hirota, M. Hase, J. Akimitsu, T. Masuda, K. Uchinokura and G. Shirane , J. Phys. Soc. Jpn. (submitted)

[3] J. P. Renard, K. LeDang, P. Veillet, G. Dhalenne, A. Revcolevschi and L. P. Regnault , Europhys. Lett. **30**, 475 (1995).

[4] L. P. Regnault, J. P. Renard, G. Dhalenne and A. Revcolevschi , Europhys. Lett. **32**, 579 (1995).

[5] M. Weiden, R. Hamptmann, W. Richter, C. Geibel, P. Hellmann, M. Köppen, F. Steglich, M. Fishier, P. Lemmens, G. Güntherodt, A. Krimmel and G. Nieva , Phys. Rev. B**55**, 15067 (1997).

JP9950057

2.3.13 Neutron Diffraction Study on $LaBa_2(Fe_{1-x}Cu_x)_3O_y$

T. Ishigaki, K. Kitaguchi, T. Futase and Y. Tsuchiya[1]

Department of Materials Science and Engineering, Muroran Institute of Technology, Muroran, Hokkaido, 050-8585, Japan
[1]Japan Atomic Energy Research Institute, Tokai, Ibaragi, Japan

Since the discovery of the superconductor $YBa_2Cu_3O_{7-y}$, intensive works in substitution effect of transition metals for Cu site in order to make clear the mechanism have been made. In Fe substitute system $YBa_2(Cu_{1-x}Fe_x)_3O_{7+y}$, the substitution limit of iron for copper is less than 0.33. It is well known that Fe atoms occupy the Cu(1) site (chain site) by Neutron diffraction[1]. On the other hand, ^{57}Fe Mössbauer spectroscopy suggested that Fe occupy both the Cu(1) and Cu(2) site[2]. There are different results for the occupation site of Fe.

Hung *et al.* succeeded in synthesis $YBa_2Fe_3O_8$[3]. Its crystal structure was similar to tetragonal $YBa_2Cu_3O_{7-y}$ with full occupation in basal oxygen. Our group also has been succeeded synthesis La substituted $LaBa_2Fe_3O_y$. In this experiment, we have investigated the crystal structure of $LaBa_2(Fe_{1-x}Cu_x)_3O_y$ especially the substituted site of Cu atom in place of determine the Fe substituted site in $YBa_2(Cu_{1-x}Fe_x)_3O_{7+y}$, .

Samples x=0.0 , 0.05 and 0.10 were prepared by the conventional solid state reactions. The oxygen contents determined by Iodometry. Neutron diffraction measurements were performed at Room Temperature and about 10 K using High resolution Powder Diffractometer HRPD at JRR-3M of JAERI. The profile analyses were done using the Rietveld Program RIETAN[4]. Initial structural model were based on $YBa_2Fe_3O_8$ reported by Hung *et al.* The results of idometry suggested the existence of excess oxygen, we add O(4) site on La plane (0, 0, 1/2). Diffraction patterns shows that the samples were consisted with two phase which have different oxygen contents, data were analysed using the feature of multi-phase refinement in RIETAN.

We allocated Cu atoms to both Fe sites at first. In course of refinements, occupation factors showed that Cu atoms preferentially occupied Fe(2) (FeO_5 pyramid) site.

Fe^{3+} ion in pyramid site was easily replaced by Cu, which shows the octahedral oxygen arrangement for Fe^{3+} is more stable than pyramid stie. It seem to be consistent with Fe atom preferentially occupy Cu(1) site in Fe doped YBCO system which is able to be eight coordination according to incorporate excess oxygen.

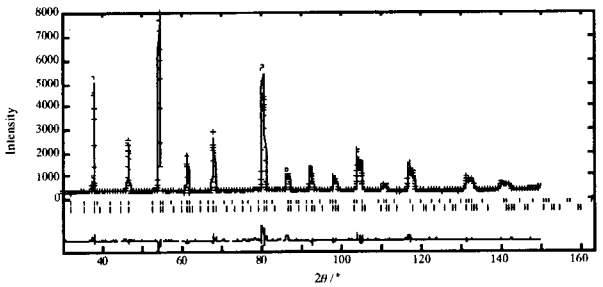

Fig. 1 Neutron diffraction Pattern of $LaBa_2(Fe_{1-x}Cu_x)_3O_y$ (x=0.1) at RT

References

1) T. Kajitani et al., Jpn. J. Appl. Phys. (1988) L354
2) T. Tamaki et al., Solid State Comm., 65 (1988 43.
3) Q. Hung et al., Phys. Rev. B 45 (1992) 9611-9619.
4) F. Izumi, in; The Rietveld Method, ed. R. A. Young (Oxford University press), Oxford, 1933 chap 13.

2.3.14

Small-angle Neutron Scattering Observation of Vortices in $Bi_2Sr_2CaCu_2O_{8+\delta}$

J. Suzuki[1], N. Metoki[1], S. Miyata[1], M. Watahiki[1,2], M. Tachiki[1,3], K. Kimura[4], N. Kataoka[4], and K. Kadowaki[4]

[1]Japan Atomic Energy Research Institute (JAERI), Tokai 319-1195, Japan
[2]Japan Science and Technology Corporation, Kawaguchi 332-0012, Japan
[3]National Research Institute for Metals, Tsukuba 305-0047, Japan
[4]Institute of Materials Science, The University of Tsukuba, Tsukuba 305-8573, Japan

The discovery of high-T_c cuprate superconductors opens a new field with regard to the structure and the stability of the vortex lattice in type II superconductors. Magnetic fields penetrate inside type II superconductors and are quantized as vortices in units of $\Phi_0 = hc/2e$. In conventional superconductors, vortices form a triangular lattice, so called an Abrikosov lattice, because of the repulsive interaction between vortices. In high-T_c superconductors, however, large thermal fluctuations due to high-temperature superconductivity result in the melting of the Abrikosov lattice. Furthermore, high-T_c superconductors have layered structures[1]. The two-dimensional superconductivity produces a highly interesting vortex structure, namely, a pancake structure in which a vortex line is decoupled between different CuO_2 planes. When the magnetic field is parallel to the CuO_2 layers, a new type of vortex called a Josephson vortex appears. A tunneling current between weakly coupled CuO_2 layers takes place to quantize the Josephson vortex. Because of such strong anisotropy and thermal fluctuation effects, complicated phase diagrams of the vortex state have been proposed theoretically and experimentally. Despite the intensive studies, we still do not have comprehensive understanding of the structure and the stability in vortices. It is particularly interesting, when the magnetic field is tilted from the c axis. In this configuration we have coexistence of the out-of-plane and in-plane field component, where the in-plane field component creates the Josephson vortices which are localized between the CuO_2 layers by an intrinsic pinning.

In this report, we discuss SANS experiments on highly anisotropic $Bi_2Sr_2CaCu_2O_{8+\delta}$ with $\gamma \sim 9$[2] in tilted magnetic fields. $Bi_2Sr_2CaCu_2O_{8+\delta}$ is one of the purest high-T_c superconductors without twin boundaries. There already exists a preceding and qualitative observation on this material performed by Forgan *et al.*[3], showing an abrupt decrease in scattering intensity as the field is tilted from the c axis to the *ab* plane.

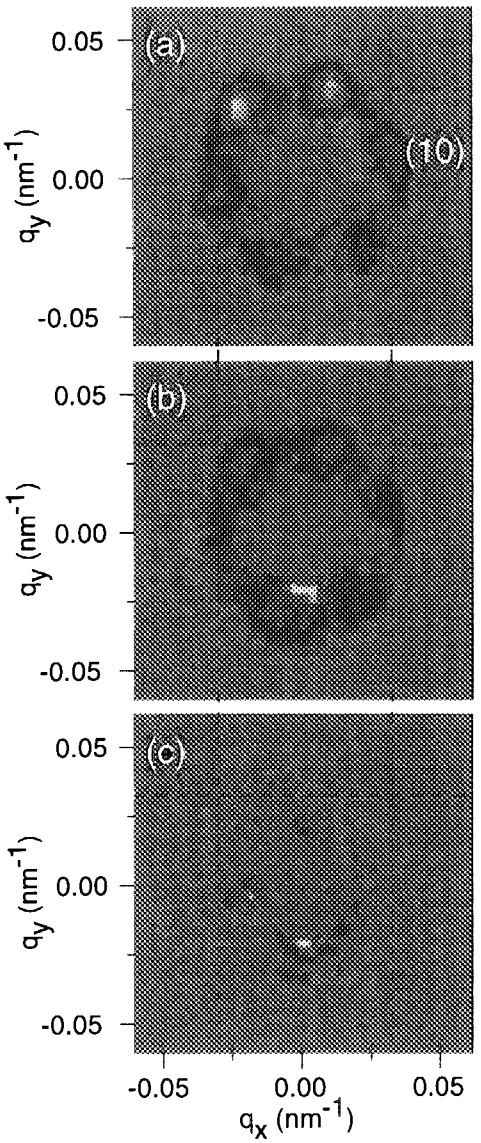

Fig.1 Small-angle neutron scattering patterns from the vortices in an applied magnetic field of 500 Oe tilted by 0° (a), 12.5° (b), and 15° (c) from the crystalline c axis toward the *ab* plane.

We have thus investigated quantitatively the angular dependence of the vortex lattice correlation.

A high quality single crystal of $Bi_2Sr_2CaCu_2O_{8+\delta}$ was grown by the traveling solvent floating zone (TSFZ) method. The dimensions of the sample is $10 \times 5 \times 0.4$ mm^3 with the wide surface perpendicular to the c axis. The superconducting transition temperature T_c was observed at 89.0 K in 2 Oe by a dc-magnetization measurement. SANS experiments have been performed using a small-angle cold neutron scattering instrument (SANS-J). Incident neutrons had a wavelength λ_n = 1.0 nm, a wavelength spread $\delta\lambda_n/\lambda_n$ = 0.24 (FWHM), and an angular divergence of 0.17 °, respectively. Scattered neutrons were detected by an area detector of 58 cm diameter at the 10 m position from the sample in an evacuated chamber. A horizontal magnetic field of 500 Oe was applied using a superconducting magnet. The two dimensional scattering patterns were measured with applying magnetic fields parallel to the incident beam, while the rocking curve measurements were carried out by rotating both the sample and the magnetic field at the same time. During the experiments the sample was cooled in the field through T_c at a cooling rate of about -1 K/min to stabilize the vortex state. The background from the sample holder, cryostat, and the sample itself was measured at 150 K and subtracted from the obtained data.

In Fig. 1 two-dimensional SANS patterns are presented for three different tilting angles. Each pattern is measured at 4 K. When the magnetic field was parallel to the c axis (θ = 0 °), we observed an undistorted hexagonal vortex pattern with the lowest order Bragg spots (Fig. 1(a)). A pair of the spots is preferentially aligned with the crystalline b axis lying 13 ° counterclock-wise to the horizontal direction as shown in Fig. 1(a). An additional diffuse ring, connecting the six Bragg spots, was also observed. Since the radial width of the ring is almost resolution limited, we conclude that the diffuse ring is the scattering from the regularly ordered vortex lattices which are randomly oriented in the ab plane. Figure 1(b) shows the SANS pattern at θ = 12.5 °. Dashed lines are guides to see a change of the Bragg peak position. Obviously we found no significant shift in peak positions, indicating the existence of the undistorted hexagonal lattice even in the tilted magnetic field. This result is consistent with the vortex lattice structure obtained by the Bitter technique[4]. The intensity of the diffuse ring is almost the same as that for θ = 0 °, while the scattering intensity of the spots gradually decreases with tilting the magnetic field. Figure 1(c) is the SANS pattern measured at θ = 15 °. Both the Bragg peaks and the diffuse ring disappear for $\theta \geq 15$ °.

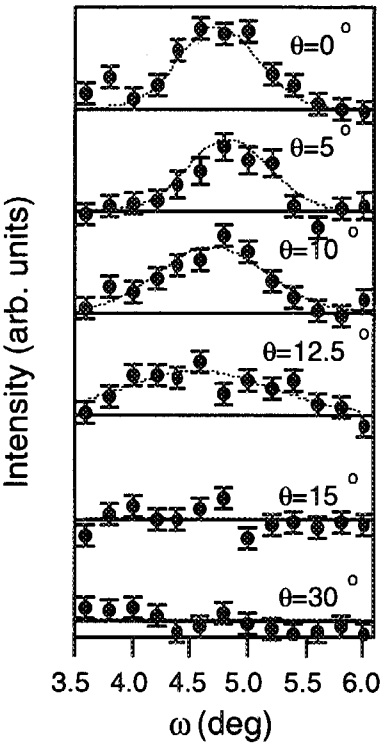

Fig.2 The tilting angle (θ) dependence of the (1 0) rocking curve. The dashed curves denote the fitting results by a Gauss function.

Figure 2 shows the (1 0) scattering profile along the q_z direction. The peak width increases with increasing the tilting angle θ. The correlation length of about 10 μm was estimated from this measurement. The peak position exhibits no significant change with tilting the magnetic field. The peak is observed, when the scattering vector is perpendicular to the magnetic field. It means that the flux line is parallel to the field in the scale of about 10 μm for $\theta \leq 12.5$ °.

Figure 3 shows the result of the parameters obtained by fitting the scattering profile, assuming a Gauss function. The Bragg peak

intensity decreases linearly with increasing θ and becomes zero at $\theta = 15°$ (Fig. 3(a)). The intensity of the diffuse ring is almost constant for θ, but abruptly goes to zero at $\theta = 15°$. These results suggest that an ordered vortex lattice disappears for $\theta \geq 15°$. One of the possibilities to interpret this feature is an intrinsic pinning mechanism of a two-dimensional superconductor composed of weakly coupled superconducting layers. The increase of the tilting angle contributes to the increase of the in-plane component of the magnetic field. The in-plane component of the magnetic flux, namely the Josephson vortex, is expected to penetrate between the superconducting layers weakly coupled each other. The intrinsic pinning center prevents the vortex from going across the layers. The ordering of the vortex lattice would be destroyed with increasing this intrinsic pinning center. As shown in Fig. 3(b) the peak width along the q_z direction increases with increasing θ, indicating the decrease of the correlation along the magnetic field. The decrease of the correlation can be understood from the decoupling of the flux. Therefore, the θ dependence of the correlation length and the intensity are consistently explained by the intrinsic pinning mechanism.

According to the μSR experiments by Forgan *et al.*[3], the inhomogeneity of a magnetic field still remains even in the tilted field giving no Bragg peak in the SANS experiments. Therefore, it is sure that there are magnetic flux lines in the sample. From our SANS experiments, however, it is clear that the flux line shows no clear regular lattice, when the contrast of the magnetic field is integrated over along the field direction. The Bitter patterns[4] would simply demonstrate the existence of a vortex lattice only at the sample surface for a very large tilting angle, e.g., $\theta = 60°$. A clear regular lattice is expected on the sample surface because of the strong vortex decoupling by the Josephson coupled layers, hence the present neutron results would be consistent with the Bitter pattern.

In conclusion, the small-angle neutron scattering experiments on $Bi_2Sr_2CaCu_2O_{8+\delta}$ were carried out in the magnetic field tilted from the crystalline c axis. At $\theta \leq 12.5°$ a vortex lattice aligns along the field direction. However, at $\theta \geq 15°$ the scattering intensity from the vortex lattice disappears. It would be understood by the intrinsic pinning effect of Josephson vortices. This behavior is observed only in the pure $Bi_2Sr_2CaCu_2O_{8+\delta}$ crystal. This result suggests that the superconducting anisotropy owing to the Josephson coupled layers plays an important role for the vortex lattice structures in $Bi_2Sr_2CaCu_2O_{8+\delta}$. The present results suggest that the superconducting anisotropy owing to the Josephson coupled layers plays an important role for the vortex lattice structures in $Bi_2Sr_2CaCu_2O_{8+\delta}$.

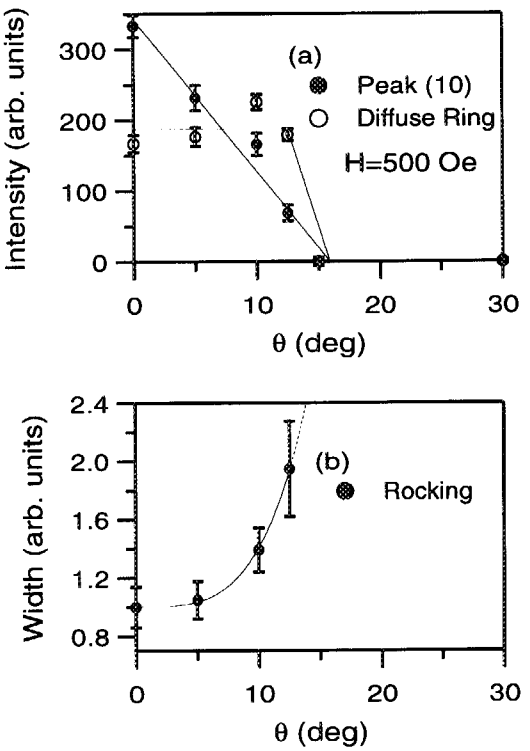

Fig.3 Fitted parameters of the (1 0) Bragg peak by a Gauss function; the peak and diffuse scattering intensities (a), and the normalized peak width along the rocking direction (b).

References

[1] D.Nelson *et al.*: Phys. Rev. B **39** (1989) 9153-9174.
[2] K.Kadowaki *et al.*: Phys. Rev. B **57** (1998) 11674-11683.
[3] E.M.Forgan *et al.*: In: Yamafuji K and Morishita T (eds) Proceedings of the 7th International Symposium on Superconductivity (ISS'94), Kitakyushu, Japan, (1995) pp 413-418.
[4] C.A.Bolle *et al.*: Phys. Rev. Lett. **66** (1991) 112-115.

JP9950059

2.3.15 Observation of Mesoscopic Structure in $NdBa_2Cu_3O_{7-d}$ by Small Angle Neutron Scattering Measurement

K.Osamura, S.Miyata, J.Suzuki[1], K.Kuroda[2] and N.Koshizuka[2]

Department of Materials Science and Engineering, Kyoto University, Kyoto 606-8501, Japan
[1]Advanced Science Research Center, Japan Atomic Energy Research Institute, Ibaraki 319-1195, Japan
[2]Superconductivity Research Laboratory, International Superconductivity Technology Center, Tokyo 135-0062, Japan

$NdBa_2Cu_3O_{7-d}$ (Nd123) is a member of $REBa_2Cu_3O_{7-d}$ family of high-T_c superconductors and have also the quite high transition temperature beyond 90K. It was noticed that Nd123 has high critical current density of 70000A/cm^2 at 77K as reported by Ting *et al*[1]. The critical current of bulk type-II superconductors are produced by vortex pinning in the peak effect, seen in, for example, magnetization measurements. In order to clarify the origin of the peak effect of this material, we performed small angle neutron scattering measurements which give the information of the structure of nano meter scale, which coincides with the scale of important factors like as coherence length, penetration depth, typical vortex spacing and so on. It is necessary that the scale of the pinning potential is the same order of the coherence length to effect a vortex, and also necessary that the pinning potential is distributed as the same order of the vortex spacing and penetration depth to pin vortices collectively.

Small angle neutron scattering measurement was performed with SANS-J apparatus at JRR-3M reactor in JAERI-Tokai. Incident beam was parallel to the c-axis of the crystal and neutron wavelength was selected ranging from 0.6 to 1.5nm. All measurements were performed in room temperature.

Scattering patterns for the sample (Lot.No. 0729-4) with neutron wavelength of 1.5nm obtained on the 2-dimensional position sensitive detector is shown in Fig.1. It can be seen the cross-shaped patterns with its arms stretching along a- and b-axes and it is seen in all other experimental conditions. And it can be seen also weak but apparent four spots in 110 directions.

The cross shaped pattern suggest that the structure with sharp boundaries normal to a- and b-axes, i.e., rectangles and/or squares of nano scale order is distributed in the samples. On the other hand, four spots lead to the existence of periodic structure along 110 crystal direction in the sample. In Y123, twin structure arranging along 110 direction (twin boundaries spread also in 110 planes) is observed by TEM[2]. In Nd123 sample used in this experiments, twin structure is also observed by TEM. Such a spot like pattern is seen in only the sample of 0729-4. The 0729-4 sample heat treated as " 900°C×100hrs+quench / 500°C×100hrs+quench / 320°C×330hrs " shows the largest critical current density calculated from magnetization measurement in all samples with different heat treatments.

In I(q)-q radial average functions which is given by averaging intensities as to absolute value of q, lower q component than around 0.04nm^{-1} seems to grow up in 0729-4 sample. It indicates that, in real space, structures of larger scale than 150nm grows up in 0729-4 sample.

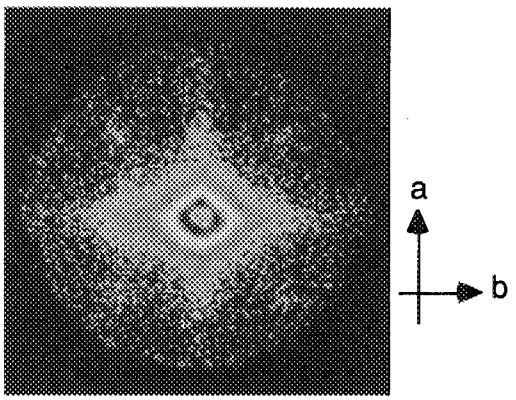

Fig.1 Scattering pattern for 0729-4 sample in room temperature and no applied field obtained on 2-D PSD.

References

1) Wu Ting, T.Egi , K.Kuroda and S.Tanaka, Appl. Phys. Lett., 70(1997), 770-772.
2) C.S.Pande, A.K.Singh, L.Toth, D.U.Gubser and S.Wolf, Phys. Rev B, 36(1987), 5669-5671.

2.3.16 Attempt to Observation of Vortex Lattice in Twin-Free $YBa_2Cu_3O_{7-d}$ by Small Angle Neutron Scattering

K.Osamura, S.Miyata, J.Suzuki[1], S.Okayasu[2]

Department of Materials Science and Engineering, Kyoto University, Kyoto 606-8501, Japan
[1]Advanced Science Research Center, Japan Atomic Energy Research Institute, Ibaraki 319-1195, Japan
[2]Department of Materials Science, Japan Atomic Energy Research Institute, Ibaraki 319-1195, Japan

$YBa_2Cu_3O_{7-d}$ (YBCO), which has high critical point (Tc) beyond the liquid nitrogen temperature, is the one of the most famous superconductors in the application research. As much as the critical point, pinning characteristics is also important for the applications. As YBCO (or 123-family) is the tetragonal structure at high temperature and transforms the orthorhombic structure at low temperature including superconductivity region, so twin structure is formed in the samples . Though the twin structure is thought to play a important role of vortex pining, pinning characteristics of the sample is ,in general, complicatedly composed by different many mechanisms, and it is difficult to estimate the contributions of the elements either qualitatively or quantitatively. For the observation of the vortex pattern by small angle neutron scattering (SANS) measurement, four spots indicating the periodic potential along 110 directions are observed and it is explained that vortices is trapped by twin plane by Forgan *et al.*[1] but, on the other hand, the similar scattering pattern is explained as the result of the effect by vortex core structure by Keimer *et al.*[2]

Recently, "twin-free" YBCO prepared by cooling under the uniaxial pressure has been used in some experiments. As to M-H hysteresis loop in magnetization measurements, it is reported that the magnetic hysteresis disappears at low field and "reentrant" peak effect appears at relatively high field by Nishizaki *et al.* and Okayasu *et al.*

In this experiment, we try to obtain more intrinsic information of the vortex structure free from twin in this "twin-free" YBCO and discuss the contribution of the twin structure to the pinning characteristic by comparison with conventional twinned YBCO. The sample used in this experiment is about 0.5*0.5*0.1 mm^3 (70μg). SANS measurement is performed with SANS-J apparatus at JRR-3M reactor in JAERI-Tokai. Neutron wavelength is selected in 1.0nm and $\Delta\lambda/\lambda$=24.4%. Sample-to-detector is 10m.

In general, due to weak contrast of magnetic induction in mixed state scattering intensity is very weak in high-Tc superconductors. To extract the signal from scattering data, background scattering is measured at zero field and subtracted from raw data. But we failed to find the effective data in it.

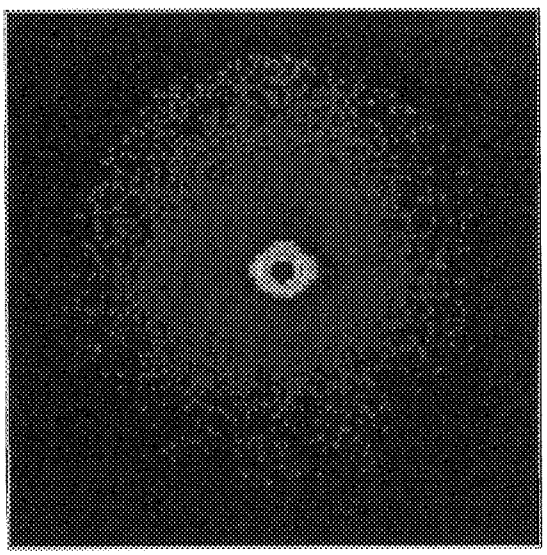

Fig.1 Scattering pattern from twin-free YBCO at 5K and 656G.

References

1) Forgan et al., Physica C, 185-189(1991), 247-252.
2) Keimer et al., Phys. Rev. Lett., 73(1994), 3459-3462.

JP9950061

2.3.17 Small-Angle Neutron Scattering Study of Twinned $YBa_2Cu_3O_y$

M.Watahiki[1,2], J.Suzuki[1], S.Miyata[3], and M.Murakami[4]

[1]Advanced Science Research Center, Japan Atomic Energy Research Institute, Tokai, Ibaraki 319-1195
[2]Japan Science and Technology Corporation, Kawaguchi, Saitama 332-0012
[3]Department of Materials Science and Engineering, Kyoto University, Kyoto 606-01
[4]Superconductivity Research Laboratory, International Superconductivity Technology Center, Koto-ku, Tokyo 105-0023

In conventional type-II superconductors, when an applied field is above the lower critical field (H_{c1}) but below the upper critical field (H_{c2}), flux lines penetrate into the superconductor as quantum flux lines. It is well known that the flux lines in the type-II superconductors form a hexagonal or tetragonal lattice. The small-angle neutron scattering (SANS) technique has been used directly to observe the structure of flux line lattices (FLL) in traditional superconductors[1]. It is not easy to detect the scattering signal from the FLL of high-T_c superconductors due to the large value of a penetration depth. However, extensive researches have been performed in order to investigate the novel properties and phases of the vortex systems of various high-T_c superconductors[2-5]. Forgan et al. have observed the tetragonal lattice in twinned $YBa_2Cu_3O_y$ (Y-123) crystals in an applied field parallel to the crystalline c-axis. When the sample was rotated away from the c-axis, the FLL changed into a hexagonal lattice[3]. The superconducting properties of Y-123 strongly depend on the oxygen content, which affects the anisotropy and doping level. The doping level can be controlled by changing the annealing temperature. The anisotropy parameter estimated from magnetic measurements increases with decreasing the oxygen content. Therefore, it is interesting to study how the anisotropy of Y-123 affects the structure of the FLL. We performed SANS measurements at 4.2K in order to investigate the FLL structures in Y-123 single crystals.

Single crystals of Y-123 used in the present study were grown by the flux method and were post annealed at 430°C for ten days. SANS measurements were performed at SANS-J of the JRR-3M reactor in JAERI using cold neutrons with a wavelength of 1 nm. A magnetic field was applied along the c-axis direction, nearly parallel to the neutron beam. Scattering patterns were observed after cooling through T_c in the applied field (H_{FC}).

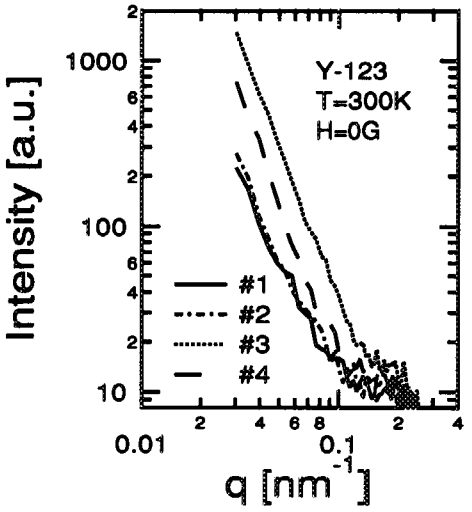

Fig.1 The averaged intensities in a radial direction in Y-123 at T=300 K and zero field. The signal indicates only the scattering from the sample itself without vortices.

Firstly, we have to select the best sample with the lowest background scattering at above T_c. The measurements were performed for four samples grown by different heating cycles. Figure 1 shows the averaged intensities in a radial direction at room temperature and zero field. These signals reveal the scattering from the crystal imperfection of the samples such as twin boundaries, compositional fluctuation, defects, and so on. We then adopt one sample giving the lowest background scattering for low temperature experiments. Figure 2 shows a typical scattering pattern at T=4.2 K and H_{FC}=656 Gauss. If the FLL is well ordered, the diffraction from the FLL should give either the 4-fold or 6-fold symmetric Bragg spots (they are usually distorted)[3]. However, we could not

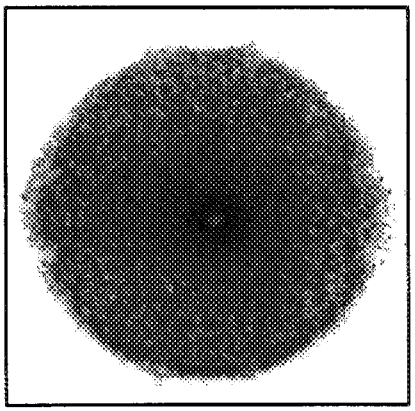

Fig.2 The scattering pattern from Y-123 at T=4.2 K and H_{FC}=656 Gauss. The Bragg spots from a FLL are not observed.

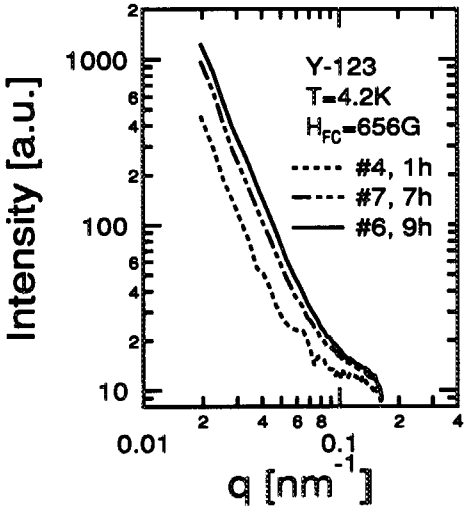

Fig.3 The averaged intensities in a radial direction in Y-123 at T=4.2 K and H_{FC}=656 Gauss. The intensity increases with increasing the time after cooling process.

observe any Bragg spots from the FLL, although the time dependence of the intensity was detected. The imperfection of the sample is thought to make the FLL a less ordered structure and relax the vortex system to a state with a lower free energy. Figure 3 shows the averaged intensities in a radial direction under various measuring times. Increasing the time after cooling the sample, the scattering intensity gradually increases. This time dependence is similar to the results obtained by Miyata et al.[6] for $NdBa_2Cu_3O_y$ and $(La,Sr)_2CuO_{4+\delta}$, and by Suzuki et al. for $(Nd,Ce)_2CuO_{4+\delta}$[7], which also give no Bragg scattering from the FLL. The origin of the time dependence is not clear, but it seems quite important for the observation of the FLL to reduce the sample imperfection resulting in the relaxation effect on the scattering intensity.

References

[1] J.Schelten, G.Lippmann and H.Ullmaier, J. Low Temp. Phys. **14** (1974) 213-226.
[2] E.M.Forgan, D.Paul, H.A.Mook, P.A. Timmins, H.Keller, S.Sutton and J.S.Abell, Nature **343** (1990) 735-737.
[3] E.M.Forgan, D.Paul, H.A.Mook, S.L.Lee, R.Cubitt, J.S.Abell, F.Gencer and P.A.Timmins, Pysica C **185-189** (1991) 247-251.
[4] R.Cubitt, E.M.Forgan, G.Yang et al, Nature **365** (1993) 407-411.
[5] M.Yethiraj, H.A.Mook, G.D.Wignall, R. Cubitt, E.M.Forgan, D.M.Paul and T.Armstrong, Phys. Rev. Lett. **70** (1993) 857-860.
[6] S.Miyata, K.Osamura, J.Suzuki, K.Kuroda and N.Koshizuka, JAERI Review **97-012** (1997) 45-45.
[7] J.Suzuki, S.Miyata and K.Hirata, in this report.

2.3.18

Temperature Dependence and Relaxation Phenomenon of Small Angle Neutron Scattering Intensity on $La_{2-x}Sr_xCuO_4$

K.Osamura, S.Miyata, J.Suzuki[1], T.Sasagawa[2] and K.Kishio[2]

Department of Materials Science and Engineering, Kyoto University, Kyoto 606-8501, Japan
[1]Advanced Science Research Center, Japan Atomic Energy Research Institute, Ibaraki 319-1195, Japan
[2]Department of Superconductivity Engineering, University of Tokyo, Tokyo 113-8656, Japan

On observations of vortex lattices in high-T_c superconductors by the neutron scattering, only a little signal can be detected due to the weak contrast of magnetic induction in the sample. It is, therefore, very important to subtract the background scattering produced by inhomogeneities in the sample from row data. Though it has been considered that the scattering from inhomogeneities is almost temperature independent by now, it turned out to be strongly dependent on the history of temperature in $La_{2-x}Sr_xCuO_4$ (LSCO). In order to investigate the behavior of scattering intensities to the temperature history, we performed small angle neutron scattering (SANS) measurements with $La_{2-x}Sr_xCuO_4$ sample.

The sample is synthesized by traveling solvent floating zone (TSFZ) method and the content of Sr is x=0.20 ($La_{1.8}Sr_{0.2}CuO_4$, T_c=30K). SANS measurements were performed with SANS-J apparatus at JRR-3M reactor in JAERI-Tokai. The total scattering intensity in no field is shown in Fig.1 in a function of temperature. It apparently increases at around 30K and shows irreversible behavior in cooling and warming process. Keeping the temperature at a constant lower than around 30K, the relaxation phenomenon that total intensity increases as time was observed. This phenomenon was enhanced by the applied field and didn't saturate in about ten hours. It should be noticed that this relaxation phenomenon was observed in no applied field. Even though in the field, it wasn't changed. So this case of relaxation is different from typical flux creep relaxations seen as the response to the change of the applied field.

About the origin of additional scattering, it is considered as follows. [1] magnetic induction, [2] atomic spin interaction, [3] nuclear interaction to be the potential for the neutron. For [1], though applied field is indeed zero, some gauss of residual field is detected around the sample. As the observation of Bitter pattern is reported in Bi2212[1)] and Y123[2)] at 8 [G] and 5.5 [G] respectively. So it is though to be possible in also LSCO. But the radial distribution function (I(q)-q profile) is not consistent with existence of vortices, because there is no signal of spatial correlation (even short range correlation) in it. For [2], antiferromagnetic ordering of Cu spins are, in general, thought to be broken in the over-doped region. For [3], tetra-ortho phase transition point is comparable to this anomalous point (30K). In fact, such a phenomena of increasing of intensity and relaxation were not observed in the under-doped sample (x=0.136), which tetra-ortho transition point is quite high temperature far above 30K.

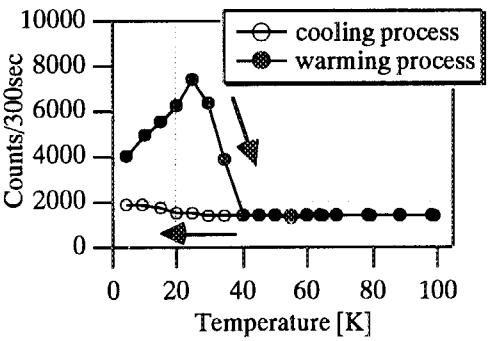

Fig.1 Temperature dependence of total counts of neutrons scattered from LSCO(x=0.20) sample in no field. It icreases apparently at low temperature (under around 30K).

References

1) D.J.Bishop *et al.*, Science, 255(1992), 165-172.
2) K.Sasaki *et al.*, Jpn J. Appl. Phys., 32(1993), L990-L993.

2.3.19

Small-Angle Neutron Scattering Study of Vortices in a Strongly Anisotropic $(Nd,Ce)_2CuO_{4+\delta}$ Superconductor

J.Suzuki[1], S.Miyata[2], and K.Hirata[3]

[1]Advanced Science Research Center, Japan Atomic Energy Research Institute, Tokai, Ibaraki 319-1195
[2]Department of Materials Science and Engineering, Kyoto University, Kyoto 606-01
[3]National Research Institute for Metals, Tsukuba, Ibaraki 305-0047

The $(Nd,Ce)_2CuO_{4+\delta}$ known as a electron-doped superconductor[1] shows strong superconducting anisotropy. We carried out the small-angle neutron scattering (SANS) experiments on this material in order to observe the Josephson vortices[2-3], which is expected to be seen in strongly anisotropic layered superconductors. The evidence of the Josephson vortices was not obtained in this study, but flux creep phenomenon and irreversible behavior were observed at low temperatures.

The single crystal of $Nd_{1.85}Ce_{0.15}CuO_4$ has a volume of 1.126×1.006×2.282 mm^3 and a mass of 18.1 mg. The mosaic spread obtained from the (200) and (006) reflections is less than 0.17°. The SANS experiments were performed using a SANS-J instrument at the JRR-3M reactor in JAERI. The neutron wavelength was 1 nm. A magnetic field was applied along the crystalline a-axis, nearly parallel to the beam direction.

The q dependence of the SANS from the sample follows a power law of $I(q) \propto q^{-3}$ at low temperatures. Figure 1 shows the temperature dependence of the intensity integrated over the whole q range. Its temperature variation shows thermal hysteresis. When the sample was cooled under the field of 5 Gauss (remanent field at the sample position), the integrated intensity gradually increases. On the contrary, during the heating process, the intensity reveals maximum around 25K. This irreversible feature indicates that a flux motion like a flux creep becomes quite slow at low temperatures. Figure 2 shows the time development of the integrated intensities at 3.5 and 20 K. The increase of the intensity obeys a power law $At^{\alpha}+B$ (α=0.82 at 3.5K, and 0.77 at 20K). This formula does not include a time constant, but the SANS result shows that the relaxation time to reach a equilibrium vortex state becomes longer at the lower temperature. These results are similar to the SANS results for $(La,Sr)_2CuO_{4+\delta}$, and $NdBa_2Cu_3O_y$[4]. A study to clarify this relaxation mechanism observed in some oxide high-T_c superconductors is in progress.

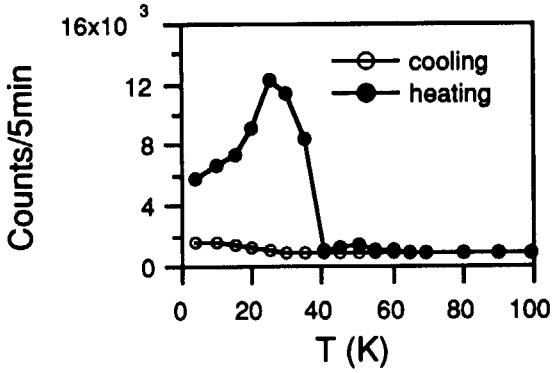

Fig. 1 Temperature dependence of the total scattering counts. Below 40K, the irreversible behavior is observed.

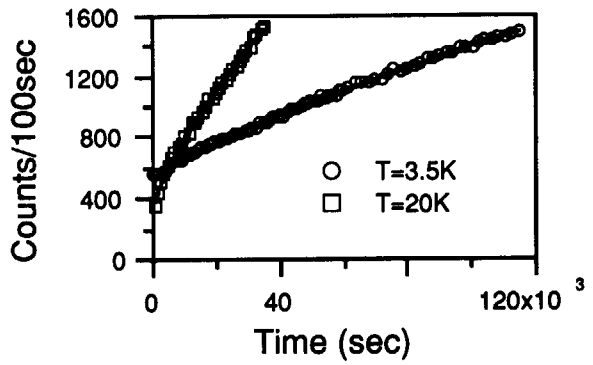

Fig. 2 Time development of the total counts at low temperature. The relaxation follows power laws.

References

[1] Y.Tokura et al., Phys. Rev. Lett. **62** (1989) 1197.
[2] L.N.Bulaevski, Sov. Phys. JETP **37** (1973) 1133.
[3] L.N.Bulaevski, and J.R.Clem, Phys. Rev. B **44** (1991) 10234.
[4] S.Miyata, K.Osamura, J.Suzuki, K.Kuroda, and N.Koshizuka, JAERI Review **97-012** (1997) 45.

2.4 Magnetism and Low Temperature Physics

2.4.1 Magnetic structure of Ca_3BMnO_6 (B=Zn,Ni)

T. Inami, S. Kawasaki[1] and M. Takano[1]

Japan Atomic Energy Research Institute, Tokai, Ibaraki 319-11
[1]Institute for Chemical Research, Kyoto Univ., Uji, Kyoto 611

In recent few years, $A_3BB'O_6$ type oxides (A=Ca, Sr $\cdots$; B=Ni, Cu, Zn $\cdots$; B'=Ir, Pt $\cdots$) with K_4CdCl_6 structure[1)] have been studied from a view point of one-dimensional magnet.[2)] These oxides are composed of alternating chains with face-shared trigonal prisms (BO_6) and octahedra ($B'O_6$), and these chains are isolated by A ions. Here we report on ordered magnetic structures deduced from neutron powder diffraction measurements for two newly synthesized B'=Mn oxides, Ca_3BMnO_6 (B=Zn,Ni).

Polycrystalline samples were prepared using a citrate sol-gel precursor technique and a solid state reaction in air. Neutron diffraction patterns were collected at the temperatures 300K and 10K from 5 to 165° in 2θ with a step interval of 0.05° on the high resolution powder diffractometer HRPD installed at the research reactor JRR-3M with a wave length 2.3005Å. The samples were contained in vanadium cans with a diameter of 10mm with He exchange gas and cooled by a conventional closed cycle ^{4}He refrigerator. All diffraction patterns were analyzed using a Rietveld refinement programs RIETAN and FullProf. Temperature dependence of magnetic Brag reflections was also measured on the triple axis spectrometer TAS-1 installed at JRR-3M.

The neutron diffraction patterns at room temperature could be indexed with space group $R\bar{3}c$. Although a small amount of impurities were observed, refinements under the same crystallographic model of Sr_3NiIrO_6[3)] converged to R_{wp} = 15.78% and R_{wp} = 11.57% for Ca_3ZnMnO_6 and Ca_3NiMnO_6, respectively.

Both compounds show a magnetic long range order at 10K. Magnetic Bragg peaks of Ca_3ZnMnO_6 were indexed with space group $R\bar{3}$. In this space group, we can readily assume two-site collinear antiferromagnetic structure, as shown in fig. 1a. Since (003) reflection is observed, the ordered moments must be contained in the ab-plane, because only the spin component vertical to the scattering vector contributes neutron magnetic scattering. Refinement using this model showed good convergence to R_{wp} = 13.84% and Mn magnetic moment $2.43 \pm 0.15\mu_B$ was obtained. The transition temperature T_N was evaluated to be 25.5K.

The magnetic structure of Ca_3NiMnO_6 is incommensurate and is represented by a single propagation vector (0,0,2+δ). A relative angle between Mn- and Ni-sublattice is required to describe a magnetic structure completely. Since no $(h,k,0)$ reflections were observed, it was found that Ni and Mn moments coupleed almost antiferromagnetically. Here we assumed that Ni and Mn moments were antiparallel. Attempt to refine the incommensurate magnetic structure using FullProf was successful and we yielded R_{wp} = 13.4% and δ = 0.0185(7). The ordered moments lie in the ab-plane and the refined values of Mn and Ni moments are $2.2(2)\mu_B$ and $1.4(2)\mu_B$, respectively. The magnetic structure is illustrated in fig 1b. T_N deduced from (1,1,2+δ) reflection was 19K.

References

[1] G. Bergerhoff and O. Schmitz-Dumont: A. Anorg. Allg. Chem. **284** (1956) 10.

[2] T. N. Nguyen et al.: Science **271** (1996) 489.

[3] T. N. Nguyen and H.-C. zur Loye, J. Solid State Chem. **117** (1995) 300.

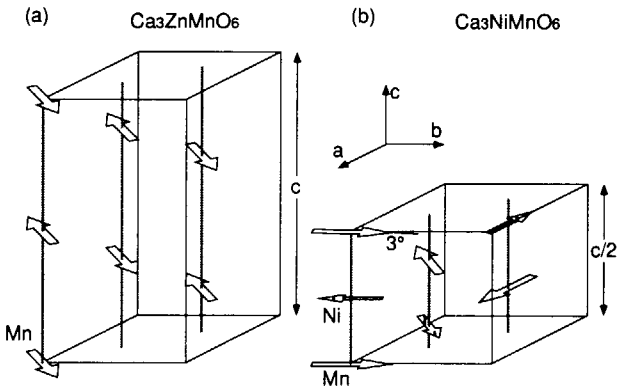

Figure 1: The best models of magnetic structure for (a) Ca_3ZnMnO_6 and (b) Ca_3NiMnO_6.

2.4.2 Magnetic structure of $RbFe(MoO_4)_2$ and $CsFe(SO_4)_2$

T. Inami

Japan Atomic Energy Research Institute, Tokai, Ibaraki 319-11

A series of compounds with the chemical formula $A^{I}M^{III}(X^{VI}O_4)_2$ (A : K, Rb, Cs, NH_4, M: Sc, Fe, Cr, Al, rare earth, X: S, Se, Cr, Mo, W) have layered crystal structures.[1] In particular, for molybdates and sulfates (i.e. X=Mo and S), the M ions form a simple hexagonal lattice. Hence, if M is a magnetic ion, it is expected that these compounds are good models of 2-dimensional (2D) triangular lattice antiferromagnets (TAFs). In fact, in high field magnetization measurements on $RbFe(MoO_4)_2$ and $CsFe(SO_4)_2$ a clear evidence of one-third plateau, which is a specific feature of the magnetization process of 2D-TAF, has been observed.[2] In this research, we carried out neutron powder diffraction measurements on $RbFe(MoO_4)_2$ and $CsFe(SO_4)_2$ in order to determine the crystal and ordered magnetic structures of these compounds.

The powdered samples of the molybdate and sulfate were synthesized using a solid state reaction method and dehydration of corresponding alum, respectively. The data were collected on the triple axis spectrometer TAS-2 installed at JRR-3M guide hall. The cryostat was an ILL-type orange cryostat. The observed date were analyzed using Rietveld refinement programs RIETAN and FullProf.

The space group of $RbFe(MoO_4)_2$ is reported as $P\bar{3}m1$.[3,4] Rietveld refinement of neutron powder diffraction patterns at room temperature actually well converges to R_{wp}=7.84% under this space group. We found that a structural phase transition occured at around 200K. The powder patterns measured at 15K is well reproduced by a calculation in which space group $P\bar{3}$ is assumed; R_{wp}= 7.84% was obtained.

A long range magnetic order sets in at T_N=3.7K. The ordered magnetic structure is commensurate in the hexagonal ab-plane and incommensurate along the c-axis. The ordered vector obtained from Rietveld refinement using FullProf is (1/3, 1/3, 1/2-δ) δ=0.052. The observed, calculated and difference patterns measured at 1.5K is shown in Fig.1. The indices of magnetic reflections are shown. The vertical bars indicate nuclear (upper) and magnetic (lower) reflections.

$CsFe(SO_4)_2$ was poor in quality compared with $RbFe(MoO_4)_2$. It should be mentioned that refinement using reported space group $P321$[5] failed. Instead, we used $P\bar{3}$ and obtained rather good convergence R_{wp}=10.49%. Observed magnetic structure is, probably reflecting a imperfection of the lattice, coexistence of commensurate phase whose ordered vector is (1/3,1/3,1/2) and incommensurate one whose ordered vector is (1/3, 1/3, 1/2-δ) δ=0.11. Both magnetic reflections have finite width. The magnetic phase transition is of first order and the transition temperature is 3.6K.

References

[1] S.Oyetola, et al.: Eur. J. Solid State Inorg. Chem. **25** (1988) 259.

[2] T.Inami, Y.Ajiro and T.Goto: J. Phys. Soc. Jpn. **65** (1996) 2374.

[3] P.V.Klevtsov and R.F.Klevtsova: Zhurnal Strukturnoi Khimii **18** (1977) 419.

[4] R.F.Klevtsova and P.V.Klevtsov: Kristallografiya **15** (1970) 953.

[5] J.Bernard et P.Couchot: Comptes rendus **262** serie C (1966) 209.

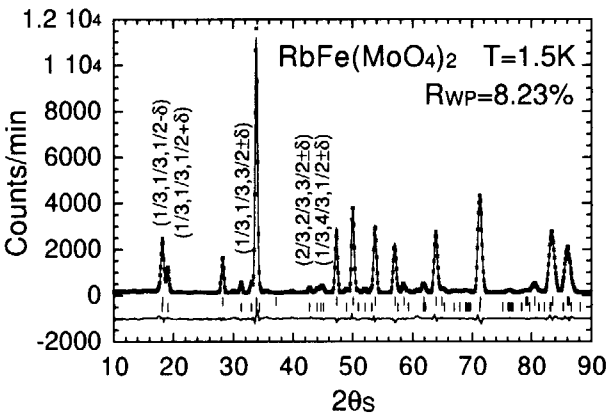

Figure 1: Neutron powder diffraction patterns of $RbFe(MoO_4)_2$ at 1.5K

2.4.3 Magnetic structure of $KCr_3(OD)_6(SO_4)_2$ (Cr-jarosite)

T. Inami and Y. Oka[1]

Japan Atomic Energy Research Institute, Tokai, Ibaraki 319-11
[1] *Faculty of Integrated Human Studies, Kyoto Univ., Kyoto 606-8501*

It is theoretically predicted that Heisenberg spins on the kagomé lattice with an antiferromagnetic coupling show large fluctuations at finite temperatures and therefore the ground state of a kagomé lattice antiferromagnet is a main subject of experimental study of low-dimensional magnets. $KCr_3(OD)_6(SO_4)_2$ (abbreviated to Cr-jarosite, it is not a correct name, though) is a model compounds of kagomé lattice antiferromagnet. μSR measurements indicated that spin fluctuation persists even at T=25mK[1], while heat capacity and neutron diffraction experiments suggest that coexistence of weak magnetic order and strong spin fluctuations[2]. In order to elucidate the ground state of Cr-jarosite, we prepared deuterized sample for the sake of reducing incoherent background from proton and carried out detailed powder neutron diffraction experiments.

A powder sample of deuterized Cr-jarosite was synthesized according to procedures described in Ref. 3. Neutron diffraction patterns were collected on the triple-axis spectrometer TAS-2 installed at JRR-3M with 2-axis mode using an ILL-type orange cryostat.

Neutron diffraction patterns measured at 10K are well reproduced by an alunite structure ($R\bar{3}m$) and a small amount of impurity (water). At 1.5K we observed magnetic Bragg reflections and confirmed these peaks disappeared above 4.0K. The peak width is limited by instrumental resolution and thus our sample certainly has a long-range magnetic order. They were indexed on the same rhombohedral unit cell with the chemical one. In this case, there are three independent magnetic moments and, since no (large) net moment was reported for Cr-jarosite from the susceptibility measurements[4], we can employ a so-called 120° structure for a model of the magnetic structure. As shown in fig. 1, there are two types of triads with opposite chirality each other. For the case of (a), magnetic structure factor is a function of the angle ϕ, while for the case of (b) structure factor is independent of ϕ. The observed intensities of the magnetic reflections are well explained by model (a) with ϕ=45° and model (b) (both have the same structure factor). The refined value of the ordered moment was $2.0\mu_B$. It is, however, not easy to construct a spin Hamiltonian whose ground state is model (a) with ϕ=45°. Similarly, for the case of the model (b), there is no adequate reason the magnetic structure lose the trigonal symmetry.

References

[1] A. Keren et al.: Phys. Rev. B **53** (1996) 6451.

[2] A. P. Ramirez et al.: J. Appl. Phys. **73** (1993) 5658.

[3] C. L. Lengauer et al.: Powder Diffraction **9** (1994) 265.

[4] T. Morimoto et al.: private communication.

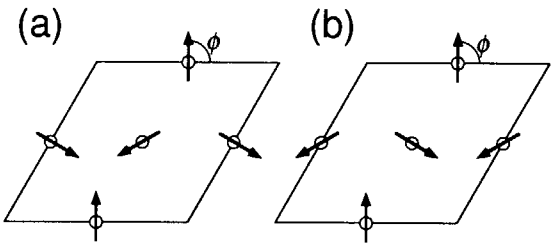

Figure 1: Two possible models of the magnetic structure for $KCr_3(OD)_6(SO_4)_2$

JP9950067

2.4.4 Magnetic structure of jarosite ($KFe_3(OH)_6(SO_4)_2$)

T. Inami, M. Takano[1] and Y. Oka[2]

Japan Atomic Energy Research Institute, Tokai, Ibaraki 319-11
[1]*Institute for Chemical Research, Kyoto Univ., Uji, Kyoto 611*
[2]*Faculty of Integrated Human Studies, Kyoto Univ., Kyoto 606-8501*

It is well known that the ordering phenomena of a frustrated magnetic system is strongly affected by impurities, dislocations and so on. Jarosite $KFe_3(OH)_6(SO_4)_2$ and related materials are models of a Kagomé lattice antiferromagnet and Wills et al. reported that structural disorder plays an important role for magnetic long range order of these compounds.[1)] They proposed an idea that vacancy at A site (potassium in the case of jarosite) lift the degeneracy of ground states and induce a long range magnetic ordering in this system. We measured three jarosites by means of powder neutron diffraction and report on the crystal, magnetic structure and magnetic phase transition.

Powder specimens of jarosite were obtained by hydrothermal treatment. One sample was prepared by one of the authors (MT) before[2)]. The other two samples (one is normal jarosite and the other is deuterized jarosite) were newly prepared by another author (YO). The deuterized sample was settled in 99.75% D_2O solutions. Neutron diffraction measurements were performed on the powder diffractometer HRPD and triple axis spectrometers TAS-1 and TAS-2 installed at the research reactor JRR-3M.

The susceptibility measurements showed that Takano and Oka samples behave differently near the transition point T_N.[3)] Refinement of nuclear structure shows that indeed the Fe and K sites are not fully occupied and different between samples. The occupation factors, however, are nearly unity and the measurements on magnetic reflection $(11\frac{3}{2})$ showed no significant difference between Takano and Oka samples on T_N (66±1K and 68±1K, respectively) and on temperature dependence of the peak intensities.

The magnetic reflections could be indexed under a rhombohedral unit cell. There are three independent spins and we employed a so-called 120° structure as a feasible model. Refinement using this model successfully converged and the obtained magnetic structure is shown in fig. 1.[4)] The ordered moments are confined in the ab-plane. It is noteworthy to mention that the magnetic structure consists of *only* triads of the spins which have clock-wise chirality. In addition, the magnetic structure factor depends on the direction of the triad and weak $(01\frac{1}{2})$ reflection confirms direction of the ordered moments shown in fig. 1. This results can be understood if one consider that there is no trigonal symmetry at the Fe site and straightforwardly we can conclude that the Fe ions have weak Ising-type anisotropy.

References

[1] A.S.Wills and A. Harrison: J. Chem. Soc., Faraday Trans. 92 (1996) 2161.

[2] M. Takano, T. Shinjyo and T. Takada: J. Phys. Soc. Jpn. **30** (1971) 1049.

[3] S. Maegawa et al.: J. Phys. Soc. Jpn. **65** (1996) 2776, Nishiyama et al.: private communications.

[4] T. Inami, S. Maegawa and M. Takano: J. Mag. Mag. Matt. 177-181 (1998) 752.

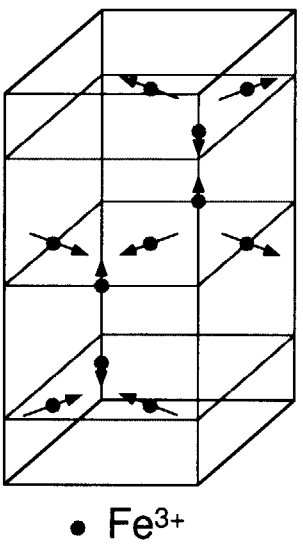

Figure 1: The best model of magnetic structure for jarosite $KFe_3(OH)_6(SO_4)_2$. Only a (lower/upper) half of the unit cell is shown.

JP9950068

2.4.5

Magnetic Neutron Scattaring Study of Layered Mixed Valence System LuFe2O4 under High Magnetic Field

K. Kitsuta, N. Ikeda, Y. Yamada, T. Inami, and S. Katano

Advanced Resercjh Institute for Science and Engineering, Waseda Univ. , Okubo, Shinjuku, Tokyo 169-0072, Japan

Japan Atomic Energy Research Instutute, Tokai, Ibaraki 319-1106,Japan

Hexagonal layered material LuFe2O4 undergoes magnetic phase transition at T=230K to a ferrimagnetic ordered state. Preveous neutron scattering study revealed streak-like diffuse scattering running along [001]-direction on (h/3, h/3, l) (h, l:integers) lines, which persist down to 4K. This suggests that the ordering is formed within each Fe hexagonal layer (2-D ordering), but no correlation between the neibouring layers is developed even at 4K.

One of the possible interpretation of such an extraordinary behavior is that the system can not attain the thermal equillibrium in the cooling process realized in the labolatory time scale. This interpretation is consistent with the hysteresis phenomena observed in magnetization curve M(T): Under zero-field cool (ZFC) condition <M>=0 at 4K, while in FC condition <M>=2 μ_B /Fe ion.

In order to elucidate the properties of the magnetic ordering, especially non-equillibrium nature in ZFC/FC conditions, we carried out neutron scattering exprements under high magnetic field (4T).

(1) ZFC condition : Below T_C , coexistance of Bragg reflections and diffuse streaks are observed on (2/3, 2/3, l)-line where Bragg reflections are indexed as (3/3, 2/3, l/2) (l:integer). Both intensities increases as T is increased.

(2) FC condition : On the same line, the diffuse scattering completely disappeared. Instead, new Bragg reflections appear at (2/3, 2/3, l) (l:integer) while Bragg reflections at (2/3, 2/3, l/2) become relatively weak. The analysis of the magnetic structures under ZFC/FC conditions is now underway.

JP9950069

2.4.6 Crystal Structure and Magnetic Property of Fe_xTiSe_2 Compounds

M. Shintomi[1], Y. Tazuke[1], H. Takahashi[1], Y. Morii[2] and K. Hojou[2]

[1]Faculty of Engineering, Ibaraki University, Hitachi, Ibaraki 316-8511
[2]Japan Atomic Energy Research Institute, Tokai, Ibaraki 319-1195

$TiSe_2$ consists of repetitions of Se-, Ti- and Se-layers, forming hexagonal CdI_2 structure. 3d transition elements, M, are intercalated in the van der Waals gaps (hereafter called as M-layers) between neighboring Se-layers, forming intercalated compounds M_xTiSe_2.[1,2] $Fe_{0.1}TiSe_2$ is paramagnetic in ref.-1, whereas it showed spin glass behavior in ref.-2. In order to elucidate the discrepancy, we have studied Fe_xTiSe_2 crystallographically and magnetically.

In conventional studies it has been assumed that M-atoms are located in the M-layers and the Ti-atoms are located in the Ti-layers as in pure $TiSe_2$. Since the discrepancy may be due to the difference in crystal structure, it is necessary to verify this assumption, and two experiments have been done. In the first experiment $Fe_{0.1}TiSe_2$ samples were prepared from two kinds of starting materials: a mixture of Fe- and $TiSe_2$-powders as in ref.-1, and a mixture of Fe-, Ti- and Se-powders as in ref.-2. Other conditions of sample preparation were kept identical. No difference was found in the susceptibility in 4.2 K$\leqq T \leqq$300 K. This result have suggested that Ti-atoms are located in the Ti-layers in both kinds of samples.

In the second experiment powder neutron diffraction spectrum of $Fe_{0.2}TiSe_2$ was obtained by HRPD-spectrometer located in JAERI-Tokai at room temperature. Fig. 1 shows obtained spectrum. The sample was prepared from a mixture of Fe-, Ti- and Se-powders and after heat-treatment at 750℃ it was rapidly quenched to room temperature. By this method we can reasonably assume that the metal atoms are randomly distributed in the two possible metal layers. The purpose of the experiment is to discriminate among three possible structures. A-structure : Ti- and Fe-atoms are located in the Ti- and M-layers, respectively. B-structure : Ti- and Fe-atoms are randomly distributed both in the Ti- and M-layers, with the M-layers containing 0.2 moles of metal atoms. C-structure : the M-layers contain 0.2 moles of Ti-atoms and the remaining metal atoms are randomly distributed in the Ti-layers.

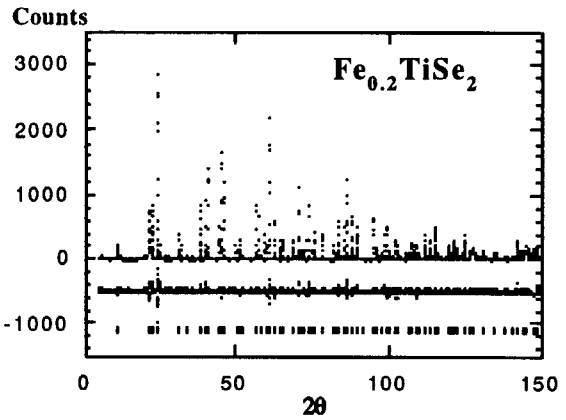

Fig. 1. Neutron diffraction spectrum of $Fe_{0.2}TiSe_2$ at 300K

The reason for selecting the composition of x=0.2 is that we can easily distinguish the A-

structure from B- and C-structures: for the A-structure (001), (111) and several other diffraction lines are expected to be strong, whereas they are expected to be feeble for B- and C-structures. The spectrum shows strong (001) and (111) diffraction lines. Rietveld analyses are done for the three structures by a program presented from Dr. F. Izumi. The A-structure reproduces the spectrum with the R-factor of 0.11 and reasonable values of thermal parameters are obtained. B- and C-structures do not reproduce (001) and (111) lines, and values of thermal parameters are not reasonable.

The results of magnetic experiments and neutron diffraction measurements consistently show that Fe-atoms are intercated into the M-layers. In the subsequent studies, all the powder samples of Fe_xTiSe_2 were prepared from Fe-, Ti- and Se-powders.

Effect of heat-treatment condition on the magnetic property of $Fe_{0.1}TiSe_2$ was Studied. For this purpose the samples were slowly cooled to room temperature after reaction at 750℃, other than rapidly quenching. The rapidly quenched sample showed paramagnetic behavior in 4.2 K≦ T≦300 K. Slowly cooled samples showed susceptibility maximum around 10 K. This temperature is much lower than that, 24 K, reported in ref.-2. The present result has reasonably suggested that in the slowly cooled sample the Fe-atoms are not randomly distributed in the M-layers. Rather, they form clusters, and these clusters give the susceptibility maximum.

Magnetizations were measured for rapidly quenched samples of various compositions x in 4.2 K≦T≦300 K. For 0.15≦x≦0.5 susceptibility maximum was observed. For x=0.15 and 0.2 the forms of the maximum are rounded and below the temperature T_m of the maximum the magnetization was a function of time, suggesting that the susceptibility maximum is due to spin glass transition.[2] For $0.22 \leqq x \leqq 0.5$ the susceptibility maximum is sharp and no time-dependent magnetization was observed. The susceptibility maximum for this composition range may be due to antiferromagnetic transition. Fig. 2 shows tentative T-x magnetic phase diagram.

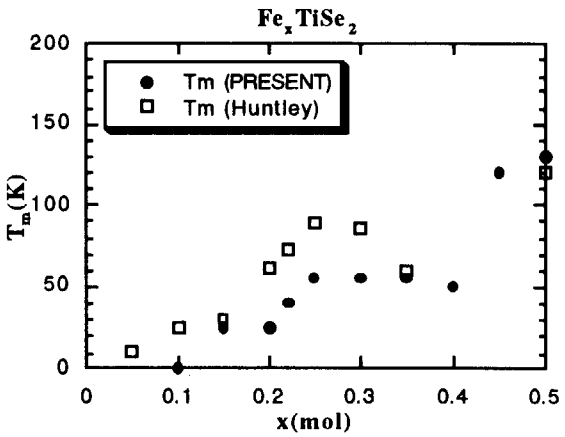

Fig. 2. T-x magnetic phase diagram of Fe_xTiSe_2

Detailed magnetic experiments are in progress. The authors thank Dr. S. Funahashi for neutron diffraction experiment and Miss M. Fukase for magnetic measurements.

References

1) Y. Tazuke and T. Takeyama: J. Phys. Soc. Japan **66** (1997) 827.

2) D. R. Huntley, M. J. Sienko and K. Hiebl: J. Solid State. Chem. **52** (1984) 233.

JP9950070

2.4.7 Successive Magnetic Sublattice Ordering in $Nd_3Pd_{20}Ge_6$

N. Tateiwa[1], N. Metoki[1,2], Y. Koike[2], M. Nakayama[1], N. Kimura[3] and T. Komatsubara[1]

[1]Physics Department, Graduate School of Science, Tohoku University, Sendai 980-8545
[2]Advanced Science Research Center, Japan Atomic Energy Research Institute, Tokai-mura 319-1195
[3]Center for Very Low Temperature Science, Tohoku University, Sendai 980-8545

Recently the new ternary system $R_3Pd_{20}X_6$ (R: rare earth, X: Si, Ge) has been attracted much interest because of the variety of the physical propeties depending on the rare earth metal. The characteristic feature of this system is the successive magnetic phase transitions. For example, the specific heat and susceptibility measurements[1)] of $Nd_3Pd_{20}Ge_6$ show three anomalies at T = 1.75 K, 1.40 K, and 0.54 K. The complicated magnetic phase diagram would be related to the fact that $R_3Pd_{20}X_6$ (space group $Fm\bar{3}m$) has two different crystallographic sites for rare earth atoms ; fcc (4a) site and simple cubic (8c) site. A Donni et al[2)] have reported that the magnetic structure at 1.40 K < T < 1.75 K is characterized by the propagation vector [1,1,1]. The purpose of this study is to reveal the antiferromagnetic phases at lower temperatures.

Neutron scattering experiments were carried out using a cold neutron triple-axis spectrometer LTAS installed at JRR-3M. The sample is cooled by a ^{3}He-^{4}He dilution refrigerator. The incident beam (Ei=4.66meV) is monochromatized by a verticaly bent PG with a Be filter. The collimation was 25'-40'-40'-80'. The single crystal was grown by the Chochralski pulling method in a tetra-arc furnace.

Fig. 1 shows the temperature dependence of the (111), (100) and (011) peak intensities. We found that the (111) Bragg intensity increases below 1.75 K, while (100) and (110) peak appear and increase in intensity below 0.54 K. From the crystal structure, we found that the antiferromagnetic ordering at 0.54 K < T < 1.75 K is a type II structure of the Nd sublattice on simple cubic (8c) site, where the propagation vector [111] corresponds to the [1/2 1/2 1/2] on the basis of the simple cubic lattice; The periodicity of the simple cubic is half of the unit cell. No magnetic ordering of fcc (4a) site is expected in this temperature range because ferromagnetic component is necessary to explain the increase of the (111) peak intensity.

The (100) and (011) antifferomagnetic peak below 0.54 K indicates that the antiferromagnetic type I structure of the fcc (4a) site coexists with the type II structure of the 8c site. The magnetic ordering of the fcc (4a) site gives rise to no anomalous behavior of the (111) peak intensity. It means that the type II structure of 8c site is stabe for the magnetic ordering of the 4a site.

The magnetic peak intensity increases gradually below 0.1K. It might be due to the nuclear magnetic ordering of Nd.

No obvious change of the scattering intensity has been observed at the transition around 1.4 K. The origin of this transition remains an open question which should be studied further.

Very recently we found a similar double transition in $U_3Pd_{20}Si_6$. In this compound, surprisingly however, the antiferromagnetic type II structure coexists with ferromagnetic ordering of fcc (4a) site. Anyhow the successive magnetic sublattices ordering would be a charastric feature in $R_3Pd_{20}X_6$ system.

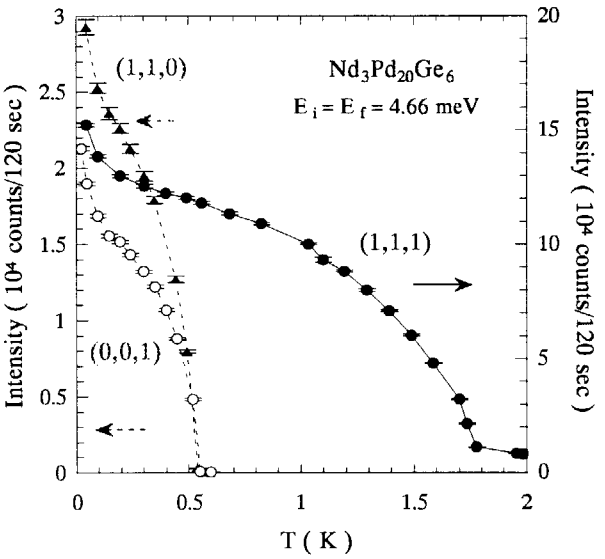

Fig1. The temperature dependences of Bragg intensities of $Nd_3Pd_{20}Ge_6$

References

1) M.Nakayama, et al., unpublished results
2) A.Donni, et al., private communication

JP9950071

2.4.8 The Crystal and Magnetic Structure of a Ternary Uranium Compound $U_3Pd_{20}Si_6$

N. Tateiwa[1], N. Metoki[1,2], Y. Koike[2], N. Kimura[3], and T. Komatsubara[1]

[1]Physics Department, Graduate School of Science, Tohoku University, Sendai 980-8545
[2]Advanced Science Research Center, Japan Atomic Energy Research Institute, Tokai-mura 319-1195
[3]Center for Very Low Temperature Science, Tohoku Univeversity, Sendai 980-8545

Uranium compounds attract much attention because of the variety of the magnetic properties. Uranium intermetallics favor itinerant character, since 5f electrons spread out and hybridized with conduction electrons. The itinerant character is revealed by the quantum oscillation experiments in many systems like UGe_3, URu_3, UIr_3 and URh_3. However there is a localized system like UPd_3 which exhibits clear crystal electric field excitation and quadrupole ordering. UPd_3 is so far understood as a rather exceptional case, which has a localized character.

Very recently we have found a new material $U_3Pd_{20}Si_6$ which is an isostructual compound of $R_3Pd_{20}X_6$ (R = rare earth, X = Si, Ge) series[1]. This compound attracts strong interest because of the localized character of 5f electron; The susceptibility obeys the Currie-Weiss law in the wide temperature range (50K < T < 300K) and the effective moment 3.30 μ_B/U is close to the values expected for free uranium ion. The clear anomalies in specific heat at 19K and around 2K indicate the magnetic transitions. The purpose of this study is to reveal the crystal and magnetic structure of $U_3Pd_{20}Si_6$.

Neutron powder diffraction profiles were measured using HRPD (λ = 1.1624 Å). The temperature dependence of the magnetic scattering is measured by a triple-axis spectrometer TAS1. The samples were cooled down to 100 mK by liquid-helium free dilution refrigerator developped by JAERI. Single crystal samples were prepared by the Chochralski pulling method in a tetra-arc furnace.

Fig. 1 shows a neutron powder diffraction spectrum at room temperature. We found that the profile can be well explained by the crystal structure of $R_3Pd_{20}X_6$ as shown in the Fig. 2. There are two different crystallographic sites for uranium atoms; fcc (4a) site and simple cubic (8c) site. Details about the result of the refinement will be published elsewhere.

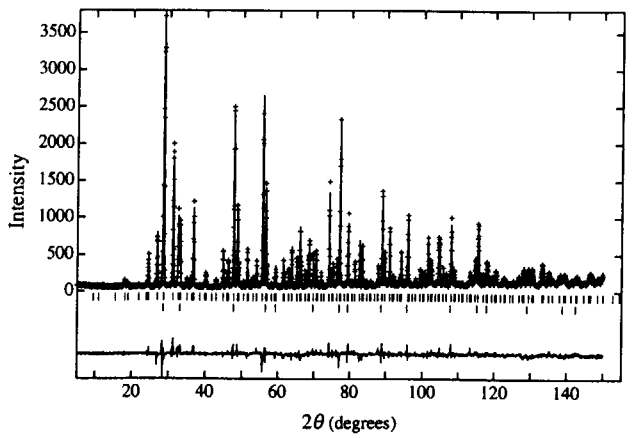

Fig. 1 A neutron powder diffraction spectrum of $U_3Pd_{20}Si_6$ at room temperature.

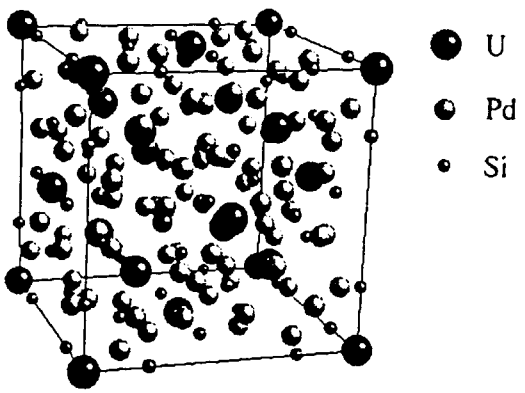

Fig. 2 The crystal structure of $U_3Pd_{20}Si_6$.

Figure 3 shows the result of the spin polarized neutron scattering experiments at the (111) Bragg point. At T = 7K we observed a clear peak in the spin flip (SF) cross section. It indicates the magnetic ordering below the upper transition temperature Tu=19 K. The weak peak in SF at T=21 K is a contamination of the NSF process due to imperfect neutron polarization ratio of our instrument (93%). Figure 4 is the temperature dependence of the SF and non-spin flip (NSF) cross section of the (111) peak. Both SF and NSF cross section exhibits clear increase below Tu=19 K, which is due to magnetic ordering. SF intensities are observed only at (h,k,l)$\pm$(1,1,1), where (h,k,l) is the nuclear Bragg point. At the other Bragg points, a small increase of the SF intensity is observed with decreasing temperature below Tu. However it is obviously due to multiple scattering, because this change dissapears, when we measure polycrystalline samples. It is concluded that the magnetic ordering of the type II antifferomagnetic structure of the simple cubic (8c) site, where the propagation vector [111] corresponds to [1/2 1/2 1/2] on the basis of the simple cubic lattice; The periodicity of the simple cubic is half of the unit cell. No magnetic ordering of fcc (4a) site is expected in this temperature range because ferromagnetic component is necessary to explain the increase of the (111) intensity.

Fig. 5 shows the temperature dependence of the (022) intensity below 2K. We observed a continous increase of the peak intensity below the lower transition temperature Tl = 2K. Similar increase was also found in the observed nuclear Bragg peaks. No half order or incommensurate peak was observed. These results indicate the ferromagnetic ordering of the uranium spins on fcc (4a) site. It is consistent with the magnetization and susceptibility measurements. From the intensity calculations, we found that the type II antiferromagnetic ordering of the simple cubic (8c) site is stable for the ferromagnetic transition of the fcc (4a) site. Therefore there is a coexistence of the ferromagnetic and antiferromagnetic ordering below Tl. The detailed analysis of the magnetic structure will be published very soon.

We thank M. Kohgi for the stimulating discussions.

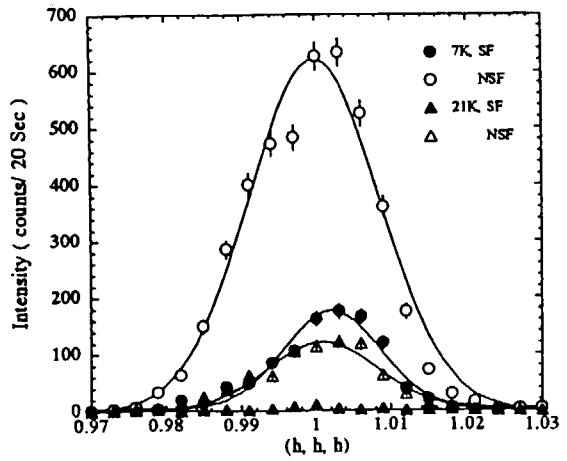

Fig. 3 The result of the spin polarized neutron scattering experiments at the (111) Bragg point.

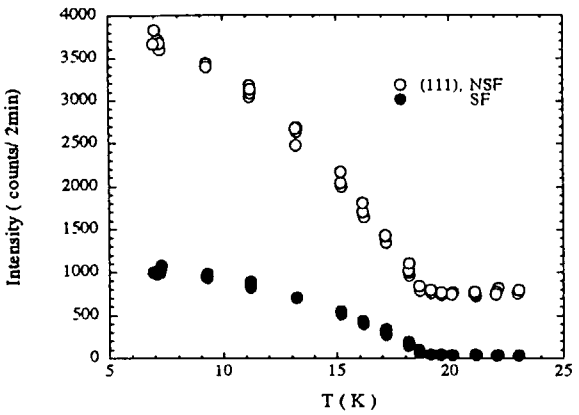

Fig. 4 The temperature dependence of the SF and NSF cross section of the (111) peak.

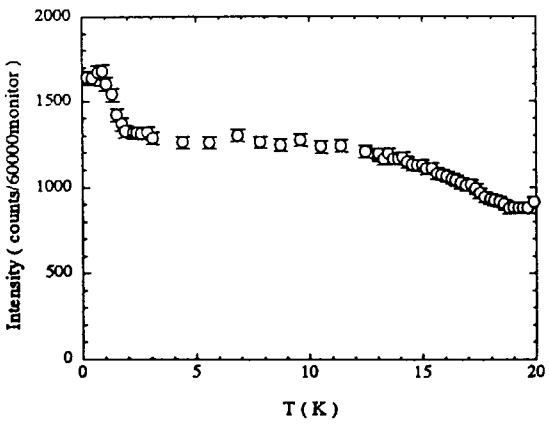

Fig. 5 The temperature dependence of the (022) intensity.

Reference

1) N.Tateiwa, et al., unpubished results.

JP9950072

2.4.9

The Magnetic Structure and Lattice Distortion of YMn_2 and Related Compounds

M. Shiga, H.Nakamura and N.Metoki[1]

Department of Materials Science and Engineering , Kyoto University, Kyoto 606-8501
[1]Japan Atomic Energy Research Institute, Tokai, Ibaraki 319-11

YMn_2 is an antiferromagnet with a helical modulation of an extremely long period (430Å). The magnetic wave vector can be described as (τ 01) [1]. Recently, we found a substitution of small amount of Tb leads to a change of the direction of the helical modulation from [100] to [110][2]. The origin of such a long period helical modulation has not yet been understood. In order to know the factors to determine the spin structure, we carefully measured the period of helical modulation and degree of the tetrahedral distortion for YMn_2 at several temperatures, and those for $Y_{0.97}Tb_{0.03}Mn_2$, $Y(Mn_{1-x}Al_x)_2$ at 10K by using a high resolution powder diffracto-meter and a low-energy triple-axis spectrometer. We discuss the correlation between these two properties and the origin of helical modulation.

In this year, we measured neutron diffraction of $Y(Mn_{0.03}Al_{0.03})_2$ at 10K and room temperature using HRPD with the wave length of 1.1624Å. However, we were not able to obtain clear results to discuss the helical modulation and tetragonal distortion because each Bragg peak becomes fairly broad by only 3% substitution of Al, suggesting strong disturbance of lattice by substitution Al for Mn. We did not observe splitting of magnetic peaks and (400) nuclear peak, which were clearly observed in YMn_2 and $Y_{0.97}Tb_{0.03}Mn_2$

In this report, we summarize the results so far obtained in the series of the present study and discuss the relation between period of helical modulation and degree of lattice distortion. Figure 1 shows the value of τ vs. 1−a/c of YMn_2 at several temperature and rare earth doped compounds including data obtained by other authors. It is interesting to note that data for Tb and Ce doped YMn_2 lie on the same line with those for YMn_2 at different temperatures. We believe that these observation implies that lattice distortion could be an important factor to determine the helical modulation as proposed by Giebultowicz at al for fcc antiferromagnet[3].

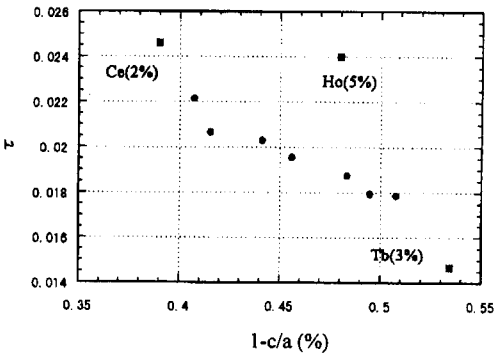

Fig.1 Propagation vector τ against 1-a/c. Closed circles are values for YMn_2 at different temperatures. Closed squares are for rare-earth doped YMn_2 at low temperature

References

[1] R.Ballou et al, J. Magn. Magn. Mater. 70 (1987) 129.

[2] H.Nakamura et al, J. Magn. Magn. Mater. 163 (1996) L1.

[3] C.Ritter et al., Physica B 234-236 (1997) 596.

[4] T.M.Giebultowicz et al., Phys.Rev.B 46 (1992) 1207.

JP9950073

2.4.10 Neutron Diffraction Study on Perovskite $La_{0.85}Sr_{0.15}CrO_3$

K. Tezuka, Y. Hinatsu, A. Nakamura[1], T. Inami[1], Y. Shimojo[1] and Y. Morii[1]

Division of Chemistry, Graduate School of Science, Hokkaido University, Sapporo 060-0810, Japan
[1] Japan Atomic Energy Research Institute, Tokai-mura, Ibaraki 319-1195, Japan

Magnetic properties of perovskite-type compound $La_{0.85}Sr_{0.15}CrO_3$ have been reported. Their DC magnetic susceptibilities were measured from 4.5K to 320K. The compound showed an antiferromagnetic transition and the Néel temperature was determined to be 270K. Below the Néel temperature, other two magnetic transitions were furthermore observed. One of the transitions occurred at *ca.* 150K. The other magnetic transition was found at *ca.* 20K. The compound showed magnetic hysteresis at 50K.

In order to determine the magnetic structures, powder neutron measurements were performed at room temperature, 250K and 50K with a High Resolution Powder Diffractometer (HRPD) in the JRR-3M reactor with a neutron incident wave length ($\lambda = 1.823$Å).

From the Rietveld analysis of these powder neutron diffraction patterns shown in Fig. 1, it was found that the crystal phase and magnetic transition occurred between 50K and 250K. The crystal structure at room temperature and 250K is rhombohedral with space group $R\bar{3}c$, and it transforms to an orthorhombic structure with space group *Pnma* at 50K. The magnetic structures at 50K and at 250K are both the G-type in which chromium atoms are antiferromagnetically coupled with the six neighboring chromium atoms. The direction of magnetic moments is directed to [111] of the rhombohedral unit cell at 250K and changes to be parallel to the *z*-axis of the orthorhombic unit cell (*Pnma*) at 50K as shown in Fig. 2. In fact, antiferromagnetic moments are not collinear at 50K, because there exists the ferromagnetic component in the magnetic moment of chromium at 50K from the magnetization measurements.

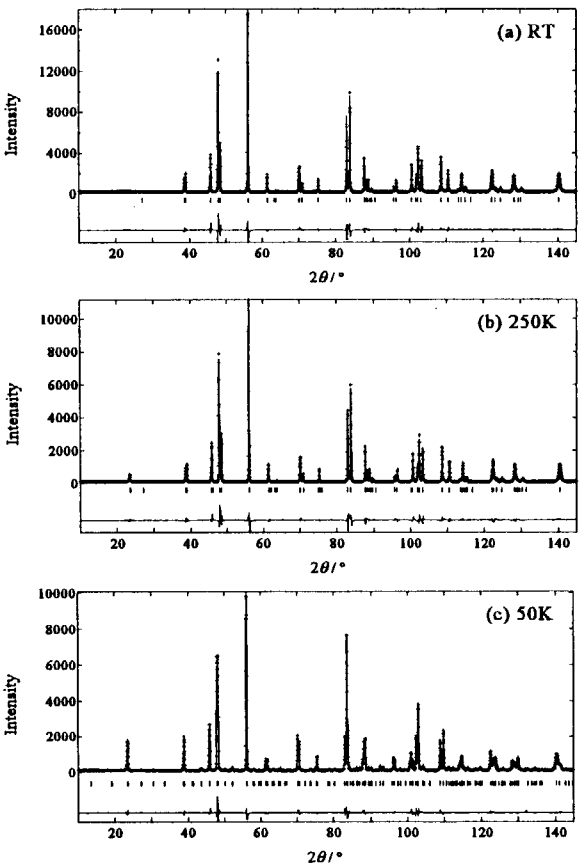

Fig. 1 Powder neutron diffraction pattern fitting for $La_{0.85}Sr_{0.15}CrO_3$.

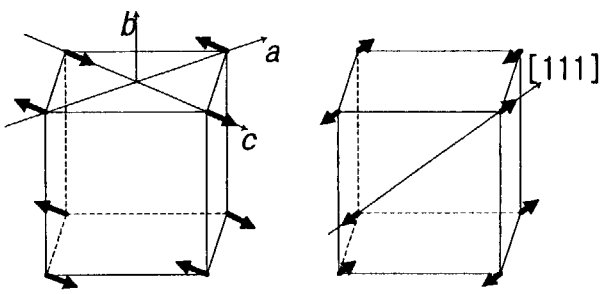

(a) 50K Orthorhombic (*Pnma*) (b) 250K Rhombohedral ($R\bar{3}c$)

Fig. 2 Configuration of magnetic moments of Cr ions in pseudo cubic cell for $La_{0.85}Sr_{0.15}CrO_3$.

JP9950074

2.4.11 Study on the Crystal and Magnetic Structures of $SrTbO_3$ and $BaTbO_3$ by Powder Neutron Diffraction

K. Tezuka, M. Itoh, M. Haga, Y. Hinatsu, Y. Shimojo[1] and Y. Morii[1]

Division of Chemistry, Graduate School of Science, Hokkaido University, Sapporo 060-0810, Japan
[1] Japan Atomic Energy Research Institute, Tokai-mura, Ibaraki 319-1195, Japan

We prepared oxygen stoichiometric $SrTbO_3$ and $BaTbO_3$ in which tetravalent terbium ions are stabilized at the *B* sites of the perovskite ABO_3. Magnetic susceptibility measurements have been performed for both the compounds in the temperature range between 4.5K and room temperature. Both the compounds show the antiferromagnetic transition at *ca.* 33K.

In order to determine the crystal and magnetic structures, powder neutron measurements were performed at room temperature and 10K for $SrTbO_3$ and $BaTbO_3$ with a High Resolution Powder Diffractometer (HRPD) in the JRR-3M reactor with a neutron incident wave length ($\lambda = 1.823$Å).

Their crystal structures at room temperature were determined from the Rietveld analysis of these powder neutron diffraction patterns shown in Fig. 1. $SrTbO_3$ has an orthorhombic perovskite-type structure with space group *Pnma* (No. 62) as shown in Fig. 2. On the other hand, $BaTbO_3$ has a rhombohedral structure with space group $R\bar{3}c$ (No. 167).

Both $SrTbO_3$ and $BaTbO_3$ have the orthorhombic perovskite-type structure with space group *Pnma* at 10K and the G-type magnetic structure in which terbium atoms are antiferromagnetically coupled with the six neighboring terbium atoms as shown in Fig. 3. It was found that in $BaTbO_3$ the rhombohedral-to-orthorhombic phase transition occurred when the temperature was decreased from room temperature to 10K, whereas $SrTbO_3$ showed no crystal phase transition in this temperature range.

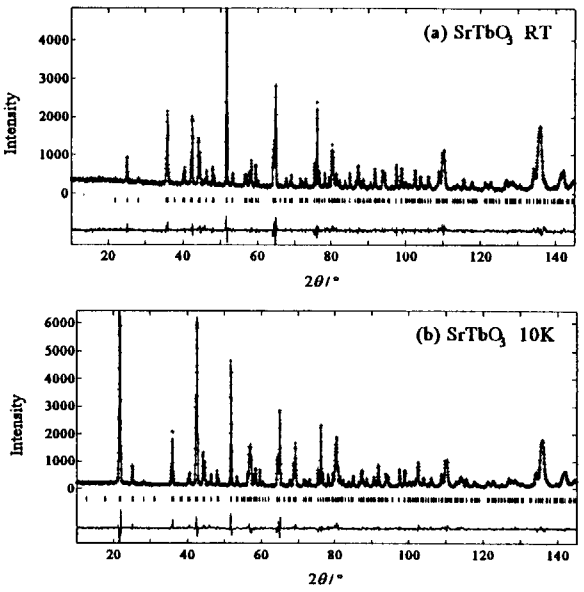

Fig. 1 Powder neutron diffraction pattern fitting for $SrTbO_3$.

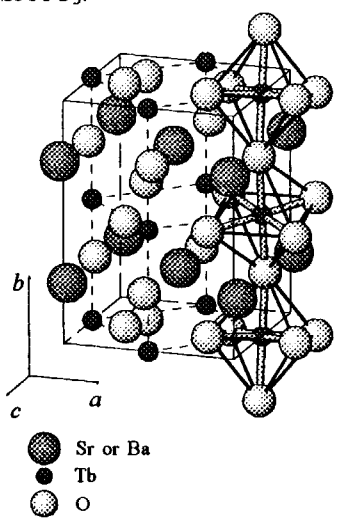

Fig. 2 Crystal structure (orthorhombic *Pnma*) of $SrTbO_3$ at RT and 10K and $BaTbO_3$ at 10K.

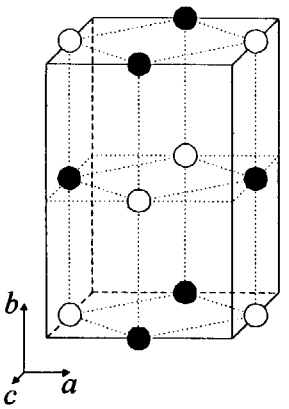

Fig. 3 Magnetic structure for $SrTbO_3$ and $BaTbO_3$ at 10K. O and ● represent directions of magnetic moments of terbium atoms and O is antipararell to●.

2.4.12 Neutron Diffraction Study on Ce_2Fe_{17}

H. Fukuda, Y.Janssen[1], H. Fujii, T. Ekino and Y. Morii[2]

Faculty of Integrated Arts & Sciences, Hiroshima University, Higashi-Hiroshima 739-8521, Japan
[1]Van der Waals-Zeeman Institute, University of Amsterdam, Amsterdam, The Netherlands
[2]Advanced Science Research Center, Japan Atomic Energy Research Institute, Tokai, Ibaraki 319-1195, Japan

In 1997, Janssen et al. reported on the physical properties of Ce_2Fe_{17} with a rhombohedral Th_2Zn_{17}-type structure[1)]. Ce_2Fe_{17} showed three different phases in zero field. With decreasing temperature, Ce_2Fe_{17} ordered antiferromagnetically at T_N = 220 K (AF II) and then another antiferromagnetic order (AF I) appeared at T_C = 125 K. Furthermore, Ce_2Fe_{17} showed a giant magnetoresistance GMR at 4.2 K, accompanied by a metamagentic transition from antiferromagnetic to ferromagnetic state with a hysterisis of about 0.2 T. The magnetoresistance effect $\Delta\rho/\rho = (\rho_{AF} - \rho_F)/\rho_{AF}$ reached about 0.85 at 4.2 K. On the other hand, the value of the electronic specific heat coefficinet γ of 351 $mJmol^{-1}K^{-2}$ in zero field decreased about 20% by the metamagnetic transition. This simply suggests that the Ce sublattice does not act an important role for GMR. In order to clarify the mechanism of GMR, we performed the neutron diffraction for Ce_2Fe_{17} with rhombohedral Th_2Zn_{17}-type structure. Detalis of the preparation method of polycrystalline Ce_2Fe_{17} are given in Ref. 1. The neutron diffraction studies were carried out with High Resolution Powder Diffractometer HRPD using thermal neutrons (wavelength λ = 2.30 Å and λ = 2.97 Å) and with Low Energy Triple-Axis Spectometer LTAS using cold neutrons (λ = 4.19 Å) at the JRR-3M.

In Fig. 1, we show the powder diffraction pattern at typical temperatures10 K, 130 K and 300 K obtained by LTAS. We could characterize by rhombohedral Th_2Zn_{17}-type structure on the diffraction pattern at 300 K. We did not observe any extra peak corresponding to α-Fe and hexagonal Ce_2Fe_{17}, indicating that the sample used in this study

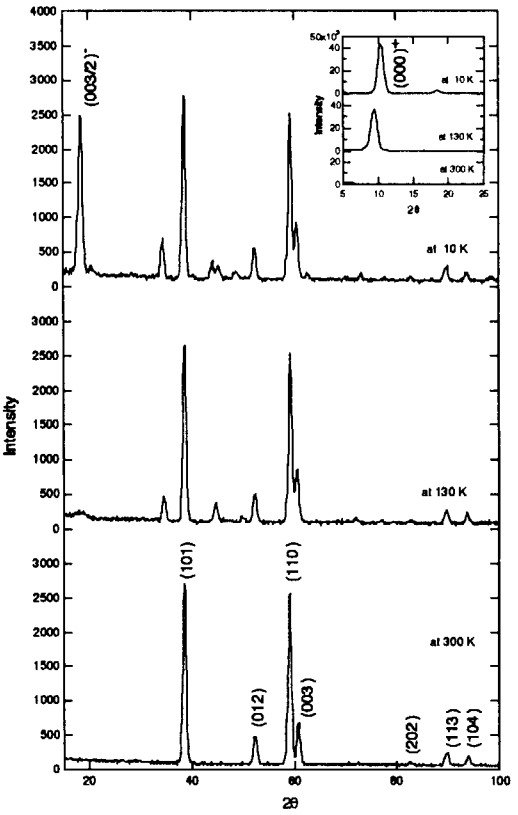

Fig. 1. Powder neutron diffraction pattern at typical various temperatures 10 K, 130 K and 300 K. The inset shows expand one

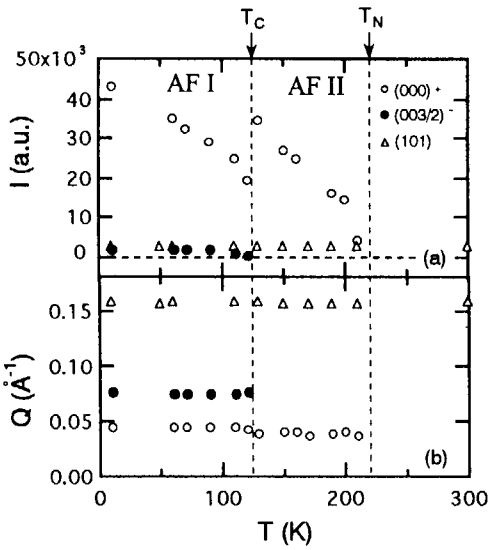

Fig. 2. Temperature variations of integrated intensities (a) and peak positions (b) of the $(000)^+$ and $(003/2)^-$ magnetic reflections for Ce_2Fe_{17}, together with those of nuclear Bragg peak (101).

was single phase. As is obvious in Fig. 1, we can observe some aditional peaks in the diffraction pattern at both 10 K and 130 K without change in the intensity of the nuclear Bragg peaks. Figure 2 shows the temperature variations of the integrated intensities and the peak positions of the two characteristic magnetic peaks $(000)^+$ and $(003/2)^-$, together with those of nuclear Bragg peak (101). As is seen in Fig. 2, the intensity and the peak position of (101) is almost independent of temperature. At T_C the $(000)^+$ peak position shifts to lower the Q position and the intensity suddenly increases during warming. Above T_C, the $(000)^+$ intensity decreases with increasing temperature and then disappears at about T_N, while the $(003/2)^-$ peak disappears at T_C. We consider that AF II has a helix structure with a propergation vecter $\tau = 0.00372$ Å^{-1} along the c-axis, where Fe moments lie in a basal c-plane and are parallel to each other in the c-plane. We estimated the average Fe moment to be about 1.5 μ_B at T_C. On the other hand, the AF I phase has a modified helix structures with $\tau = 0.00435$ Å^{-1} along the c-axis. This indicates the formation of super-structured magnetic cell, in which the magnetic c-parameter is twice as large as the chemical unit cell. The magnetic structure of the AF I phase is completely different from that of the AF II phase. Our results are consistent with the results by Plumier et al.[2] rather than by Givord et al.[3], in which Givord et al. claimed a fan structure below 90 K. So we can simply expect that the magnetic sturecture is the same one as Plumier et al. reported. However, we cannot decide the exact magnetic structure only from these data.

Considering that GMR occured in only the AF I phase, it seems likely that GMR connects to appearence of super-structured magnetic cell in the AF I phase. Hence, we consider that GMR in Ce_2Fe_{17} is mainly caused by the formation of a super-zone gap due to the development of the AF I phase (SDW) of the Fe sublattice. In order to clarify the mechanism of GMR in ditails, it is necessary to determine the exact magnetic structure from the neutron diffraction experiments for Ce_2Fe_{17} single crystal.

References

(1) Y. Janssen et al.: Phys. Rev. B **56**(1997), 13716
(2) R. Plumier & M. Sougi: Proceeding of ICM, Moscow, (1973), 487
(3) D. Givord & R. Lemaire: Proceeding of ICM, Moscow, (1973), 492

JP9950076

2.4.13

Magnetic Structure of Orthorohmbic Phase in γ-MnM, (M=Pt, Pd and Rh) Alloys

T. Hori, Y. Tsuchiya[1], S. Funahashi[1*], Y. Shimojo[1], H. Shiraishi and K. Hojou[1]
Shibaura Institute of Technology, Oomiya, Saitama 330-8570
[1]Japan Atomic Energy Research Institute, Tokai, Ibaraki 319-1106

As is well known, most Mn-rich γ - Mn alloys undergo a distortion from the face centered cubic structure to the face centered tetragonal (f.c.t.) structure with $c/a < 1$ below the Néel temperature. In some cases the distortion to the f.c.t. with c/a > 1 is also observed. In the γ - MnNi alloys, there is a face centered orthorhombic (f.c.o.) region in addition to the f.c.t. regions with $c/a < 1$ and $c/a > 1$ [1]. Recently, the present authors [2] have found that these three regions exist in the γ - MnGa alloys, and determined a non-collinear magnetic structure with 4 sublattices for the f.c.o. phase. The *a*, *b* and *c*-axis components of the magnetic moments, μ_a, μ_b and μ_c are as follows: $\mu_c^2 > \mu_b^2 > \mu_a^2 = 0$ in the f.c.o. structure with $a > b > c$.

We also found that there is the f.c.o. phase in the γ - MnPt with 8 at% Pt, γ - MnPd with 10 at % Pd and γ - MnRh with 10 at % Rh alloys. Neutron diffraction experiments for the powder samples were made by using the HRPD and TAS II diffractometers in the JRR-3M reactor at JAERI. For example, the neutron diffraction pattern using the HRPD at 10 K is shown in Fig. 1. The pattern is explained by assuming the f.c.o. structure with a = 3.807, b = 3.748 and c = A and a non-collinear antiferromagnetic structure with $\mu_a = 0$, $\mu_b = 1.27$ and $\mu_c = 2.38\ \mu_B$ / Mn atom. The angle between the c-axis and magnetic moment, θ, is 32°. We measured the temperature dependence of these lines using the TAS II Although the 110 and 101 reflections for the γ - MnPt with 8 at% Pt were not distinguishably split. We obtained the intensities, I_{110} and I_{101}, by a curve fitting analysis using the double Gaussian functions, and determined the magnetic moment form the I_{110} and I_{101} intensities. The magnetic moment decreases with increasing temperature and vanishes at 510 K which is the Néel temperature. We have also determined magnetic structure for γ - MnPd with 10 at % Pd and γ - MnRh with 10 at % Rh alloys. The results are summarized in table 1.

Jo et al. [3] have proposed a theoretical phase diagram and magnetic structures for various γ - Mn alloys on the basis of Landau expansion of the free energy. For example, three-axis components of the magnetic moments, μ_a, μ_b and μ_c in the f.c.o. structure with $a > b > c$ are as follows; $\mu_c^2 > \mu_b^2 > \mu_a^2$. The results in the present experiments are very consistent with this theory.

Table 1. Magnetic structures

Alloys	Magnetic moments per Mn atom (μ_B) μ_a	μ_b	μ_c	θ
MnPt	0	1.27	2.01	32°
MnPd	0	1.01	1.71	31°
MnRh	0	1.24	2.04	31°

References

[1] N. Honda, Y. Tanji and Y. Nakagawa, J. Phys. Soc. Jpn **41** (1976) 1931
[2] T. Hori, Y. Morii, S. Funahashi, H. Niida, M. Akimitsu and Y. Nakagawa; Physica **B 213&214** (1995) 354.
[3] T. Jo and K. Hirai, J. Phys. Soc. Jpn **55** (1986) 1614.

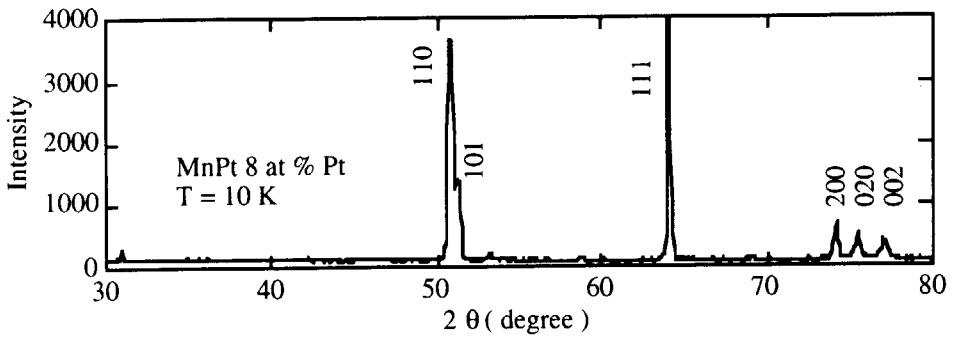

Fig. 1. Neutron diffraction pattern for the γ - MnPt with 8 at % Pt at 10 K.

JP9950077

2.4.14 Recombination Reactions of T + T → T_2 and T + H → HT in Quantum Liquid of ^{3}He-^{4}He Mixtures at 1.3 K

Y. Aratono,[1] T. Matsumoto,[2] T. Kumada[1] and T. Miyazaki[1,2]

[1]Japan Atomic Energy Research Institute, Tokai-mura, Ibaraki-ken 319-1195, Japan

[2]School of Engineering, Nagoya University, Furo-cho, Chikusa-ku, Nagoya 464-8603, Japan

Liquid helium shows very significant quantum effect such as superfluidity due to its small mass and very weak van der Waals interaction. The authors proposed that the liquid helium can be used as a new medium for the investigation of low temperature chemistry in the quantum medium, expecting the unique chemical reactions arising from the quantum characters of the medium.[1,2] During the course of the studies using the liquid ^{3}He-^{4}He mixture as the reaction medium, the authors found the preferential formation of HT over T_2 in the recombination reactions of T + T → T_2 and T + H → HT, where T and H are produced through ^{3}He(n, p)T.

Recent progress of laser techniques has been stimulating the spectroscopic studies of the structures of bubbles formed by electron and neutral atom and of snowball formed by positive ions, which are characteristically observed in the liquid helium.[3-5] Though the optical spectroscopic method has been successfully applied to the study of physicochemical properties of electron, helium ion, neutral and charged metal atoms and some their dimers, no experimental investigation has been performed on the characteristics of the hydrogen isotopes in the liquid helium as well as on their chemical reactions. This is due to the difficulties of the introduction of the isotopes into the liquid helium and of no suitable methods for observation.

The authors proposed the nuclear activation method for study of T reactions in the ^{3}He-^{4}He mixture.[2] According to the phase diagram of the ^{3}He-^{4}He mixture,[6] we can choose the superfluid state at the ^{3}He(0.280)-^{4}He(0.718) mixture or the normalfluid state at the ^{3}He(0.670)-^{4}He(0.330) mixture at 1.3 K. T atom produced by the nuclear reaction of ^{3}He(n, p)T has an initial kinetic energy of 192 keV and is thermalized very efficiently prior to the reaction through the successive collision with surrounding helium atoms. Thermal neutron irradiation was performed at TAS-1 of JRR-3M(Japan Research Reactor No. 3M) for about 10-20 hrs at 1.30± 0.02 K. Since the irradiation port was designed for neutron scattering experiment, γ-ray dose rate was very low and thus the secondary effect caused by γ-ray could be neglected. The thermal neutron flux measured by Au-foil activation method was typically 3.1×10^{11} m^{-2} sec^{-1} but changed from sample to sample because of the difficulty of the setting the sample exactly at the same geometrical position. The reaction products, HT and T_2, were analyzed by radio-gaschromatography.

Table 1 shows the mol % yields of HT(Y_{HT}) and T_2(Y_{T_2}). The values are the average of the twice experiments. A very large difference is seen between Y_{HT} and Y_{T_2}.

The following reactions will occur in the system.

$$H + H \rightarrow H_2 \quad (1)$$

$$T + H \rightarrow HT \quad (2)$$

$$T + T \rightarrow T_2 \qquad (3)$$

Table 1 mol % yields of $HT(Y_{HT})$ and $T_2(Y_{T_2})$

$^3He : ^4He$	state	$Y_{HT}(\%)$	$Y_{T_2}(\%)$
0.282:0.718	s	99.05 ± 0.09	0.95 ± 0.09
0.670:0.330	n	99.53 ± 0.05	0.47 ± 0.05

[a] s: superfluid, n: normal fluid.

Since the reactions (1)-(3) are generally considered as the barrier-free radical reactions, the reaction rate is controlled by the diffusion behaviors of H and T. In such a case, the rate constant(k_D) for the above reaction can be written as follows,[7]

$$k_D=[2k_BT(r_A+ r_B)^2]/[3\eta(T) r_Ar_B], \qquad (4)$$

where k_B, T, η (T), r_A, and r_B represent Boltzmann constant, temperature, coefficient of viscosity, and atomic radii of A and B atoms. The eq. (4) shows that the reaction rates for (1) - (3) are identical each other because the atomic radii of H and T are same and that, therefore, Y_{HT} should be equal to Y_{T_2}. However, the experimental results shown in Table 1 are different from the theoretical prediction by eq. (4).

The definite conclusion cannot be obtained on the controlling mechanism leading to the preferential formation of HT over T_2. However the following is considered to be responsible for this at the present stage of the experiment. It is well known that the electron and the neutral atoms form the bubble due to the strong Pauli repulsive short-range force between He and them. This suggests that the effective atomic radii and masses of H and T change. No report has been published on the bubble structure of H and T but can be predicted to be 1 - 1.7 nm from the radii of Cs bubble[8] and electron bubble.[9] As for the effective masses, both the experimental results and the theoretical calculation predict to be about 10 for H, D and T.[10,11] Moreover, the recombination reaction in the gas phase at around 1 K is reported to be strongly affected by the difference of the energy level structure at low temperature between hydrogen isotopes.[12] Based on these experimental results and theoretical prediction, it seems reasonable that the rate constants for the reactions (1) - (3) cannot be predicted by the simple diffusion model such as eq. (4). They will be controlled by the unique processes arising from quantum properties of the liquid helium.

References

[1] Y. Aratono, "Chemistry in Liquid Helium" (in Japanese), Houshasenkagaku(Radiation Chemistry), **64**(1997), 7-16 .

[2]Y. Aratono, T. Matumoto, T. Kumada, K. Komaguchi, and T. Miyazaki, J. Phys. Chem., A, **102**(1998), 1501-1506.

[3]"Proceedings of the 128th WE-Heraeus-Seminor on Ions and Atoms in Superfluid Helium" Zeitschrift fur Physik B **98**(1995).

[4]A. Fujisaki, K. Sano, T. Kinoshita, Y. Takahashi, and T. Yabusaki, Phys. Rev. Lett., **71**(1993), 1039-1042.

[5]M. Takami, Comments At. Mol. Phys., **32**(1996), 219-231.

[6] "Chemical Kinetics and Dynamics" ed J. I. Steinfeld, J. Francisco, and W. L. Hase, Prentice Hall, Inc., Englewood Cliffs, New Jersey (1989) Chap. 4, P. 162.

[7] D. O. Edwards and M. S. Pettersen, J. Low. Temp. Phys., **87**(1992), 473-523.

[8]H. Bauer, M. Beau, B. Friedl, C. Marchand, and K. Miltner, Phys. Lett., A., **146**(1990), 134-140.

[9]C. C. Grimes and G. Adams, Phys. Rev. B, **41**(1990), 6366-6371.

[10]M. Saarela and E. Krotscheck, J. Low Temp. Phys., **90** (1993), 415-449.

[11]M. E. Hyden and W. N. Hardy, J. Low. Temp. Phys., **99** (1995), 787-849.

[12]M. Arai and T. Mizusaki, Private communication.

JP9950078

2.5 Structural Physics

2.5.1 Neutron Diffraction Study of Proton-conducting Oxides

T. Nagasaki, N. Noda, Y. Ishii[1], T. Matsui and Y. Morii[1]

Graduate School of Engineering, Nagoya University, Nagoya 464-8603
[1] Japan Atomic energy Research Institute, Tokai, Ibaraki 319-1195

Such perovskite-type oxides as $SrCeO_3$ and $BaCeO_3$ doped with, e.g., Yb_2O_3 show protonic conductivity in hydrogen or water vapor atmosphere. Hydrogen (proton) sites in these materials, however, still seem to be an open question. The purpose of the present study is to identify the hydrogen sites in them by using neutron powder diffraction and to thereby cast light on the conduction mechanism.

In the present study, we used $SrTi_{0.97}Sc_{0.03}O_3$ as a sample material because it has a simple crystal structure (perovskite type, Pm3m) at ambient temperature as well as relatively high hydrogen solubility.

Powders of $SrCO_3$, TiO_2, and Sc_2O_3 were mixed and pressed into pellets, which were then heated at 1673 K for 40 h in air for reaction and ground into powder again. We heated some of the powder at 873 K for 30 h in the air flow containing D_2O vapor of 50 kPa. (We refer to this process as D_2O treatment.) This D_2O treatment dissolves 1-2 mol% deuterium atoms in $SrTi_{0.97}Sc_{0.03}O_3$.[1)] We measured the diffraction patterns for the samples with HRPD.

The peak intensity for the sample with the D_2O treatment was different from that for the sample without it. The difference was very small, yet was well above the purely statistical fluctuation. We determined relative changes in the observed intensity and compared them with those in structural factors calculated assuming various occupation sites for deuterium atoms. The results are shown in fig. 1. In the models a)-e), we assumed that the deuterium atoms reside a) in the middle of O-O atoms, c) in the middle of O-Sr atoms, d) in the center of O-O-O triangles, and e) in the middle of O-Ti atoms, respectively. Sata et al.[1)] have concluded that

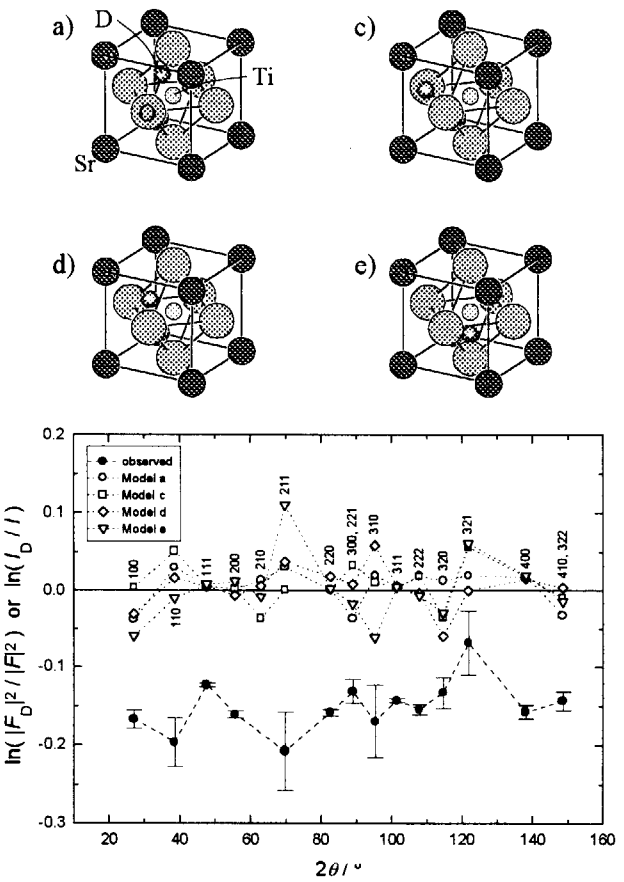

Fig. 1 Comparison of the relative changes due to deuterium dissolution in the observed intensity I with those in the structural factors F; various deuterium sites a)-e) were assumed in calculating F.

deuterium atoms occupy the sites slightly shifted from the sites a), analyzing their neutron diffraction data for single crystals. None of the models, however, can explain the present experimental results satisfactorily. Further analysis is now in progress.

Reference

[1] N. Sata, K. Hiramoto, M. Ishigame, S. Hosoya, N. Niimura, and S. Shin, Phys. Rev. B **54** (1996) 15795.

2.5.2 Neutron Powder Diffraction of CuClTe

M. Hirota, T. Sakuma, H. Takahashi[1], Y. Onoda[2], Y. Ishii[3]

Department of Physics, Faculty of Science, Ibaraki University, Mito 310
[1]Applied Physics Group, Faculty of Engineering, Ibaraki University, Hitachi 316
[2]National Institute for Research in Inorganic Materials, Tsukuba 305
[3]Japan Atomic Energy Research Institute, Tokai 319-11

A group of ternary copper compounds of the composition CuXTe (X = Cl, Br, I) with high copper-ionic conductivity was synthesized by Rabenau et al .[1] These compounds have the tetragonal symmetry in the space group $I4_1/amd$. They clarified a statistical distribution of Cu^+ ions.

It has reported by specific heat measurements that CuBrTe and CuITe show the phase transition at 230 K and 347 K and 281 K, respectively, but CuClTe doesn't show the phase transition below the melting point 400℃.[2] Hitherto, the structural studies of the respective phases of CuBrTe and CuITe have been carried out, but those of CuClTe haven't been done very much.

We performed the neutron powder diffraction study on CuClTe to decide the temperature dependence of the structural parameters of CuClTe. Neutron diffraction measurements were collected from a powder CuClTe at 10 K, room temperatur, 200℃ and 360℃ with a triple-axis spectrometer TAS-2 installed at JRR - 3M in Japan Atomic Energy Research Institute. The incident neutron wavelength of 1.4361 Å was used . The

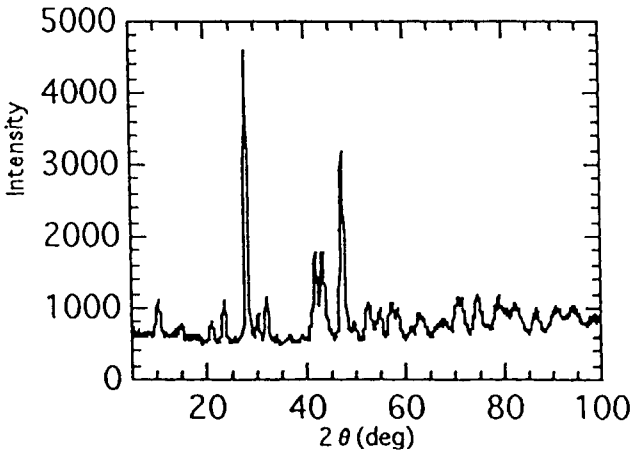

Fig.1. Neutron diffraction pattern of CuClTe at 10 K.

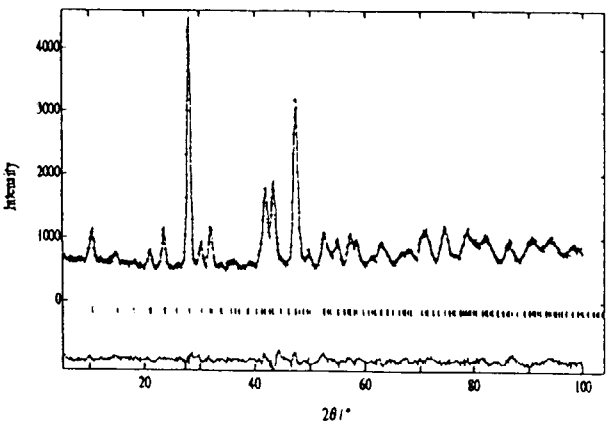

Fig.2. Result of Rietveld refinement of CuClTe at 10 K.

range of diffraction angle covered by the spectrometer was 5° - 100°. Fig.1 shows the result of the double-axis measurement of CuClTe at 10K.

Rietveld analyses were performed with the neutron diffraction data.[3] Fig.2 shows the result of the diffraction pattern at 10 K. R- factors for 10K, room temperature, 200℃ and 360℃ were 2.65%, 3.64%, 6.07%and 6.27%, respectively. It was found from the refined parameters that one of Cu^+-sites exhibited peculiar behavor with the temperature change. We are going to perform conductivity measurement of CuClTe to research the relation with the temperature dependence of the structural parameters.

References

1) A. Rabenau, H. Rau and G. Rosenstein : Z. anorg. Chem. **374** (1970) 43
2) T. Sakuma, T. Kaneko, H. Takahashi and K. Honma : J.Phys. Soc. jpn. **60** (1991) 1136
3) Y.-I. Kim and F. Izumi : J.Ceram. Soc. Jpn. **102** (1994) 401

JP9950080

JAERI-Review 99-003

2.5.3 Short- and Medium-range Order of AgI-Ag_2O-V_2O_5 Glass System

H. Takahashi, K. Shishitsuka, T. Sakuma[1], Y. Shimojo[2] and Y. Ishii[2]

Faculty of Engineering, Ibaraki University, Hitachi 316 Japan
[1]Faculty of Science, Ibaraki University, Mito 310, Japan
[2]Japan Atomic Energy Research Institute, Tokai 311-19, Japan

It is well known that AgI-Ag_2O-V_2O_5 system has wide glass forming region. The purpose of the present investigation is to clarify the short- and medium-range order in silver vanadate glasses. In order to get information about the medium-range order, the first sharp diffraction peak (FSDP) in the low-Q region for $(AgI)_{0.5}((Ag_2O)_{1-X}(V_2O_5)_X)_{0.5}$ glasses is examined by X-ray and neutron diffraction. Raman scattering experiment is also performed to determine the V-O network structure.

Raman scattering peaks for silver vanadate glasses are assigned using the results of those for alkali vanadate crystals. It is concluded that the network structure for metavanadate glass (X=0.5) is mainly composed of one dimensional VO_4 tetrahedral chain, and that for pyrovanadate (X=0.33) glass consists of the $V_2O_7^{4-}$ structure unit similar to other alkali and alkaline earth vanadate glasses. In 0.5>X>0.33 glasses, Raman profiles continuously change from that of metavanadate to pyrovanadate. It is considered that the average VO_4 chain length systematically varies in these composition range. On the other hand, Raman profiles for glasses having X>0.5 resembles each other. Since the ratio of the bridging oxygen to the non-bridging oxygen increases with increasing X, gradual change from VO_4 linear chain to connected two dimentional VO_4 network would form with increasing X.

Figure 1 shows the neutron and X-ray diffraction profiles in the low-Q range. FSDP could not observe for the representative composition by neutron diffraction, while FSDP is detected for all the glasses by X-ray diffraction. It is concluded that FSDP originates from V-O and V-V correlation. The composition dependence of the peak position corresponds to the network structure investigated by Raman scattering. The shift of the peak position to higher Q value means decrease of the interchain correlation length. The change of the correlation length mainly results from the variation of network structure from VO_4 linear chain to $V_2O_7^{4-}$ unit. It seems that FSDP shift reflects the morphological degree of freedom depending on the length of structure unit.

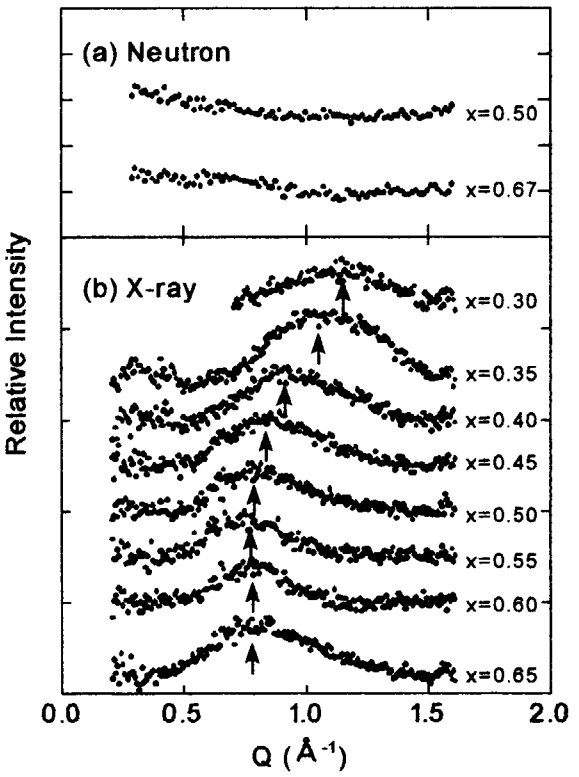

Fig. 1 Neutron and X-ray diffraction profiles for $(AgI)_{0.5}((Ag_2O)_{1-X}(V_2O_5)_X)_{0.5}$ glasses in low Q range.

2.5.4 Neutron Powder Diffraction Study for Imaging of Hydrogen Nucleus in the Hydrogen Bond of KDP

Shigefumi YAMAMURA, Shintaro KUMAZAWA[1], Eiji NISHIBORI[2], Masaki TAKATA[3], Makoto SAKATA[2], Yoko SUGAWARA, Yoshinobu ISHII[1] and Yukio MORII[1]

Department of Physics, School of Science, Kitasato University, Kanagawa 228-8555, Japan
[1]Advanced Science Research Center, JAERI, Tokai, Ibaraki 319-1106, Japan
[2]Department of Applied Physics, School of Engineering, Nagoya University, Nagoya 464-8603, Japan
[3]Department of Material Science, Interdisciplinary Faculty of Science and Engineering, Shimane University, Shimane 690-8504, Japan

In order to explore the nature of hydrogen bond, it is important to examine distribution of hydrogen nucleus together with electron distribution. For first step of this study, we have already performed electron density studies for KDP(KH_2PO_4) and ADP($NH_4H_2PO_4$) by Maximum Entropy Method (MEM) using synchrotron radiation powder diffraction data[1,2]. We have revealed from the electron distribution that the hydrogen bond in O–H–O had a covalent character. For second step of this study, we carried out MEM analysis for KDP using neutron powder diffraction data collected by HRPD diffractometer at JAERI with wave length of neutron, 1.823 Å[3]. It was found that resolution i.e. number of data was not enough to obtain precise distribution of hydrogen nucleus because of relatively long wave length of neutron. In this report, we carried out neutron powder diffraction study at 10 K for KDP using short wave length of neutron, 1.16 Å.

Neutron powder diffraction experiments were performed using HRPD diffractometer at JRR-3M. In order to improve profile shape of powder pattern, data collection range for each detector was overlapped. The powder diffraction data up to 2θ = 140° include 448 reflections, which corresponds to 0.62 Å resolution in real space.

The structure refinement by Rietveld method was performed using the computer program RIETAN-98, which is now in developed by Dr. F. Izumi (NIRIM). By using this program, integrated intensities for the MEM analysis can be precisely calculated from the overlapped measurement data of HRPD. Fitting result of the powder pattern is shown in Fig. 1. The reliable factor for pattern fit, R_{wp}, was 2.50 % and that for integrated intensities, R_I, was 2.45 %. These values were showing fairly good fit comparing with the values, R_{wp} = 2.76 % and R_I = 4.98 % for conventional Rietveld method. The positional parameters for hydrogen atom showed ordering of the hydrogen atom in the hydrogen bond.

MEM analysis for imaging of hydrogen nucleus from the obtained powder data is in progress.

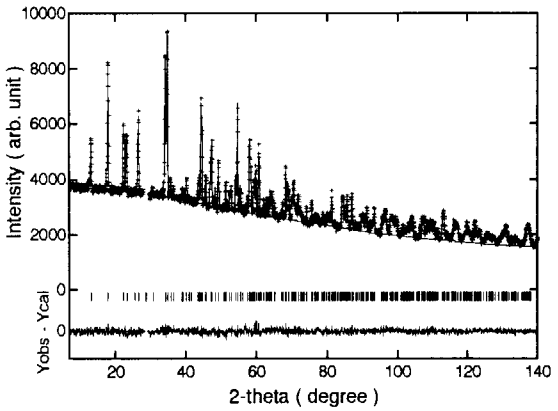

Fig. 1. Fitting result of neutron powder diffraction pattern for KDP at 10 K by Rietveld analysis.

References

1) S. Yamamura et al., Photon Factory Activity Report **14** (1996) 186.
2) S. Yamamura et al., Photon Factory Activity Report **15** (1997) in press.
3) S. Kumazawa et al., JAERI NSL Report April 1995 - March 1996, 99.

JP9950082

2.5.5 Structural Study of Low Temperature Phases of hex-$BaTiO_3$

Y. Noda, K. Akiyama, T. Shobu, Y. Morii[1] and H. Yamaguchi[2]

Faculty of Science, Chiba University, Yayoi, Inage, Chiba 263
[1]JAERI, Advanced Science Research Center, Tokai, 319-11, Japan
[2]Electrotechnical Laboratory, Umezono, Tsukuba 305, Japan

A hexagonal type $BaTiO_3$ undergoes successive phase transitions from the prototype hexagonal phase (phase I) to phase II and phase III on cooling at 222K and 74K respectively. The intermediate phase II was extensively studied, and the space group of phase II is $C222_1$. The phase III is a ferroelectric phase, and detailed structures of the low temperature phases are not known. At the present work, we studied the structure of phase II and phase III to know the mechanism of the phase transition of h-$BaTiO_3$.

Structures of the low temperature phases were studied by neutron powder diffraction at HRPD in JRR3M. In addition, we have preferred a high resolution powder diffraction experiment by using SPring-8 synchrotron radiation to determine the symmetry of phase II and III. The unit cell and the space group of phase II was confirmed to be the orthorhombic and $C222_1$, and the symmetry in phase III was newly determined as monoclinic with the deformation of the γ-angle. The most possible symmetry in phase III is $C112_1$, or equivalently $P112_1$ as a crystallographic conventional unit cell. We have performed neutron powder experiments with the wave length 2.3A and 1.16A. The preliminary results of 2.3A one was already published. Fig. 1 shows the obtained and calculated diffraction profiles, taken in phase I, II and III. Since we used shorter wave length 1.16A, remarkable change of the pattern was found around 80 and 120 degrees, which was not seen in 2.3A experiments. The shift patterns of atoms in phase II and phase III were determined. The atomic shift in phase II is well explained by a soft phonon mode condensation, but the shift pattern in phase III was much more complicated and composed a shift of oxygen atoms.

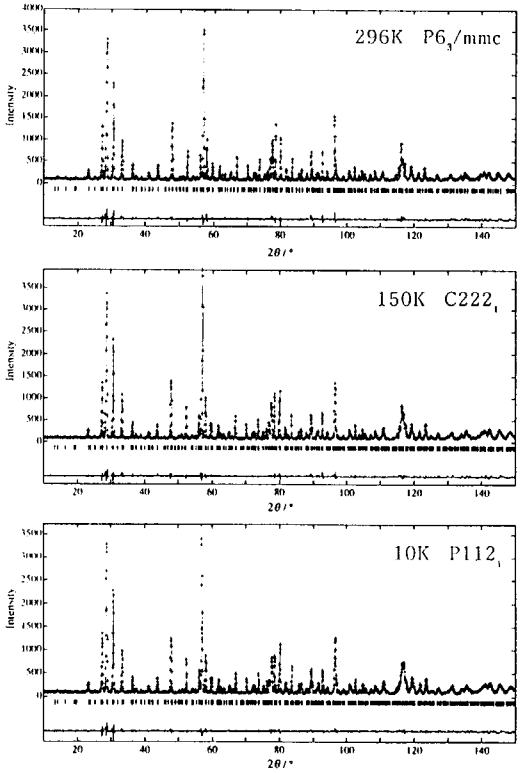

Fig.1 Observed and calculated diffraction profiles.

2.5.6 A Neutron Scattering Study of the Premartensitic State in $Ti_{50}Ni_{30}Cu_{20}$ Alloy

X. Ren, K. Taniwaki, N. Miura, K. Otsuka, Y. Morii[1], Yu.I. Chumlyakov[2]

Institute of Materials Science, University of Tsukuba, Tsukuba, Ibaraki 305-8573, Japan

1. Japan Atomic Energy Research Institute, Tokai, Ibaraki 319-1195, Japan
2. Siberian Physical Technical Institute, Tomsk 634050, Russia

The origin of martensitic transformation (MT) has remained unclear for nearly one century, despite that great technological success has been achieved utilizing MT to harden steels and to develop shape memory alloys. An important step towards understanding the reason why MT needs to occur in a certain alloy was made by Zener[1)] over 50 years ago, who pointed out that MT is closely related to the softening of the resistance to the shear of close-packed plane {110} along <1-1 0> direction, which is reflected by a softening in elastic constant c'. In 60's and 70's, the discovery of soft mode and its success in explaining 2nd order displacive transitions in ferroelectric materials cast new light on the similar MT, and then many researchers tried to find similar mode-softing in martensitic alloys. However, the results were quite puzzling: in most cases {110}<1-1 0> TA2 transverse mode softens prior to MT, but it never go to zero like 2nd order transitions. This feature is now recognized to be common for all 1st order displacive transitions. Then we have to answer why a partially soft mode can induce MT. Recent theoretical studies using Landau-type model suggest that if two (maybe more) order parameters become correlated, a 1st order MT can occur without complete mode-softening. If we go a little further, we can deduce that multiple order parameter is the origin of the 1st order character of MT. It is apparent that there exist many possible order parameters for MT, because MT is a strain transition and there exist many possible strain modes acting as potential order parameters. This may be the reason why MT has frequently been found to exhibit multi-step transition, with each step characterized by different order parameters. Our recent work on elastic constants measurement on TiNiCu alloys gave direct support to this view[2,3)].

The purpose of the present study is to use neutron scattering technique to study phonon mode anomaly prior to MT for a $Ti_{50}Ni_{30}Cu_{20}$ alloy which exhibit B2-B19 martensitic transformation. Compared with elastic constants measurement which can explore only modes near BZ center, neutron inelastic scattering has the advantage of being able to obtain information on the whole BZ, so that we may observe many strain /shuffle modes and their relation to the martensite structure may be understood. In the present study, we pay much attention to the possible multiple mode softening, which has not been reported in the previous studies.

Single crystal sample with a size of $9*9*6mm^3$ was mounted on a triple axis spectrometer TAS-2 with a temperature controlling system. The incident neutron energy was 14.7mV (wavelength 2.35A) , a PG filter was used to reduce higher order reflection, the collimations were 17'-40'-40'-40'. It should be pointed out that Ti-Ni based alloys appear to exhibit strong incoherent scattering, which makes the background very high, thus the accurate determination of peak position is difficult, especially around BZ boundary. We tried to solve this problem by sampling over a wide ΔE range for several times and determine peak position with Guassian fitting.

The main results are as follows:

(1) TA2 phonon branch exhibits two dips, one is around $q_{max}/3$, another one is at $q_{max}/2$ (Fig.1). The phonon energy of both dips become further decreased with approaching transformation temperature, but appear unlikely to reach zero at M_s. Surprisingly, it is found that the former dip is deeper than the latter, although the latter dip is related to B2-B19 transformation.

(2) $q_{max}/3$ dip is appreciably shifted from exact 1/3 position, it is around $0.375q_{max}$.

(3) We also observed elastic scattering along <110> direction and its temperature dependence (Fig.2). We found that no obvious elastic peak exists around $q_{max}/3$and $q_{max}/2$. However, an elastic peak was found around $0.67q_{max}$, but showed little temperature dependence down to M_s. This suggests that $q_{max}/3$ and $q_{max}2/3$ are not equivalent. This is difficult to understand at present.

To summarize, we found that a double mode-softening in $Ti_{50}Ni_{30}Cu_{20}$ alloy prior to B2-B19 martensitic transformation, despite that only one of them is related to the observed martensitic transformation. The other soft mode is related to the R phase (a different martensite) which is not realized in this alloy. This result seems to suggest that the observed MT is merely the winner of several possible candidates, which is characterized by different modes or order parameters. The competition in harmonic and anharmonic energy among them determines which should show up.

Finally, we would like to point out that further experiment should be done in order to verify the above interesting results.

References:

1. C. Zener, Phys. Rev., 71(1947), 846.
2. X. Ren and K. Otsuka, Scripta Mater., 38(1998), in press .
3. X. Ren, K. Taniwaki, K. Otsuka, T. Suzuki, K. Tanaka, Yu.I. Chumlyakow, and T. Ueki, Philo. Mag. A, 75(1998), in press.

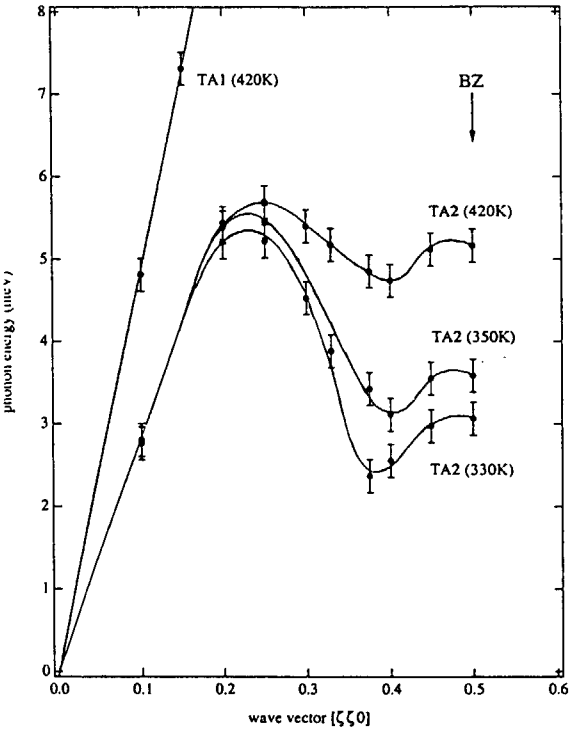

Figure 1. TA2 phonon dispersion relation

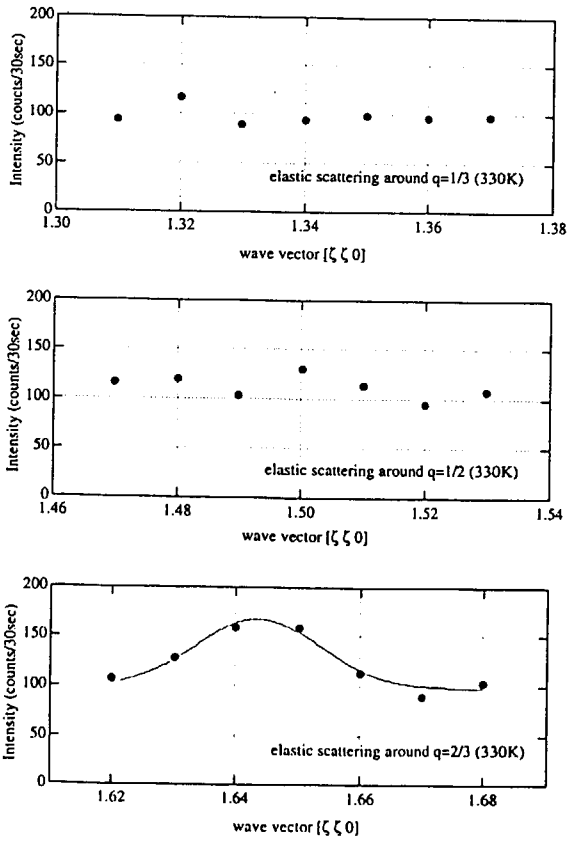

Figure 2. Elastic scattering along <ζζ0>

JP9950084

2.5.7

Photoinversion Mechanism of the Chiral 1-Cyanoethyl Group in a Cobaloxime Complex

Takashi Ohhara, Yuji Ohashi, Ichiro Tanaka,[1] Shintaro Kumazawa,[1] and Nobuo Niimura[1]

Department of Chemistry, Tokyo Institute of Technology, Meguro-ku, Tokyo 152-8551
[1]Advanced Science Research Center, Japan Atomic Energy Research Institute, Tokai, Ibaraki 319-11

It was found that the chiral 1-cyanoethyl group bonded to the cobalt atom in some cobaloxime complexes is racemized on exposure to visible light with retention of the single crystal form. Although the relation between the racemization rate and the crystal structure was clearly explained, the mechanism of the racemization has not been clarified. One of four bonds around the chiral carbon atom should be cleaved by photoirradiation in the process of the racemization. The ESR measurement indicated that the Co-C bond was cleaved by photo-irradiation. In order to ascertain the mechanism, the hydrogen atom bonded to the chiral carbon of the 1-cyanoethyl group was replaced with the deuterium atom for the complex of [(*R*)-1-cyanoethyl-d$^{\alpha}$][(*S*)-phenylethylamine]-cobaloxime and the crystal structure after the irradiation was analyzed by neutron diffraction. The analyzed structure showed that the racemization was not observed since the crystal was too large that light cannot penetrate into the crystal. However, the deuterium atom was exchanged with one of the hydrogen atoms of the neighboring methyl group. This suggested that the C-H bond may be cleaved in the process of the racemization.

Another complex with the deuterium-exchanged cyanoethyl group, [(*R*)-1-cyanoethyl-d$^{\alpha}$](pyridine)cobaloxime, was prepared and its crystal strcutre after the irradiation was analyzed by neutron diffraction. The analyzed structure indicated that the chiral cyanoethyl group was partly inverted to the opposite configuration but the deuterium atom bonded to the chiral carbon is not exchanged with the methyl hydrogen atom. This suggests that the Co-C bond is cleaved on exposure to visible light.

In order to make clear which mechanism is true, the complex of [(*R*)-1-cyanoethyl-d$^{\alpha}$]-(piperidine)cobaloxime was prepared and the crystal structure after 1 month exposure was analyzed by neutron diffraction. There are two crystallographically independent molecules in an asymmetric unit. The A molecule is not significantly different from the initial structure, whereas the molecular structures of B before and after the irradiation are different as shown in Fig. 1. The(*R*)-1-cyanoethyl group is partly (45%) inverted to the opposite configuration and the disordered structure of the (*R*) and (*S*) isomers were observed. All the deuterium atom replaced with the hydrogen bonded to the chiral carbon are bonded to the chiral carbon and are not exchanged with the hydrogen atoms of the neighboring methyl hydrogen atoms. This results is the same as that of the pyridine complex examinexd previously.

The exchange process of the deuterium atom bonded to the chiral carbon with the hydrogen of the neighboring methyl group seems to be rare case when the 1-cyanoethyl group is inverted to the opposite configuration. The Co-C bond should be cleaved in the process of photoracemization.

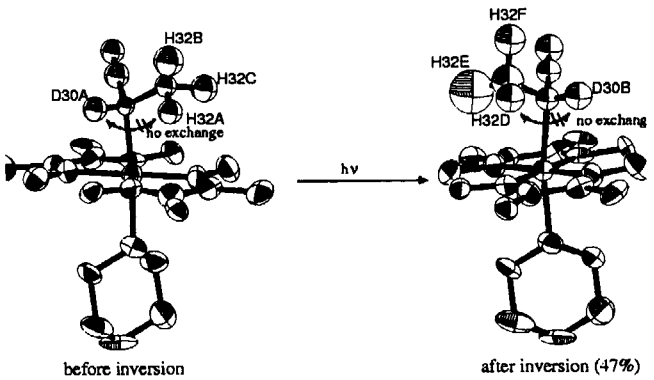

Fig.1

JP9950085

2.5.8

Mechanism of 3 - 1 photoisomerization of the 3-Cyanoethyl Group in a Cobaloxime Complex

Takashi Ohhara, Jun Harada, Yuji Ohashi, Ichiro Tanaka,[1] and Nobuo Niimura[1]

Department of Chemistry, Tokyo Institute of Technology, Meguro-ku, Tokyo 152-8551
[1]Advanced Science Research Center, Japan Atomic Energy Research Institute, Tokai, Ibaraki 319-11

It was found that the 3-cyanopropyl group bonded to the cobalt atom in some cobaloxime complexes is isomerized to the 1-cyanopropyl group in the two step (as shown in the Scheme) on exposure to visible light in the solid state.[1] When the axial base ligand is (*R*)-1-phenylethyl-amine, the 3 - 1 isomerization proceeded with retention of the single crystal form. The structures before and after the change were analyzed by X-rays. The reason why such a large structural change does not destroy the crystal lattice was clearly explained by the reaction cavity for the cyanopropyl group[2].

However, the mechanism of the 3 - 1 isomerization remains equivocal. It must be made clear what is the motive force for the isomerization or why the intermediate structure, 2-cyanopropyl group, was not be observed in the intermediate stages. To examine the mechanism, the complex of (3-cyanopropyl-d^{α},d^{α})[(*R*)-1-phenylethylamine]cobaloxime was prepared. To reduce the background, the hydrogen atoms of (*R*)-1-phenylethylamine and the cobaloxime moities were replaced with the deuterium atoms. A crystal with dimensions 2.0 x 2.0 x 1.0 mm was irradiated with a xenon lamp for 7 days and the crystal strcuture wasanalyzed by neutron diffraction at JAERI.

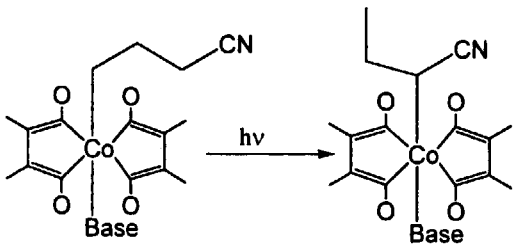

Scheme

Figure 1 shows the molecular strcutures before irradiation. Figure 2 shows the molecular structure after oo hours exposure. Although the conversion rate was about 90 %, the transferred deuterium atoms are clearly assigned. One of the deuterium atom bonded to the carbon atom of the 1 position of the 3-cyanopropyl group is transfered to make a bond with the carbon atom of the 2 position. This indicates that the 2-cyanopropyl group should be made in the process of the 3 - 1 isomerization.

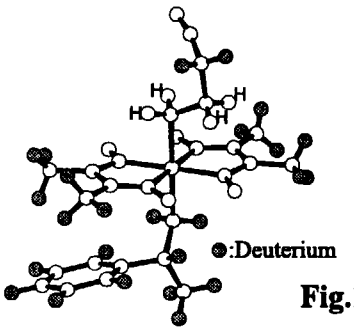

Fig.1

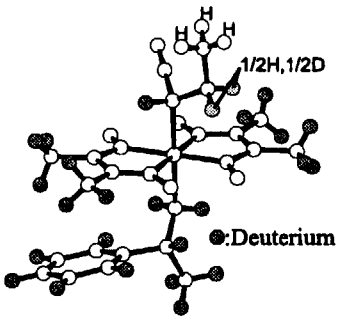

Fig.2

References

[1] F. Kurashima, N. Takatsu, K. Ishida, Y. Arai, S. Takeuchi and Y. Ohgo, Annual Meeting of the Chemical Society of Japan, Kyoto, Abstract I, 290 (1995).
[2] M. Yoshiike, Master Thesis, Tokyo Institute of Technology, 1998.

2.5.9 The Classical Structure of $TaCp_2(H)(SiMe_2H)_2$

R. Bau, I. Tanaka[1], T. Ohhara[2], N. Niimura[1], Y. Ohashi[2], Q. Jiang[3] and D.H. Berry[3]

Dep. of Chem., Univ. of Southern California, Los Angeles, CA 90089, U.S.A.
[1]Advanced Science Research Center, JAERI, Tokai, Ibaraki 319-1195, Japan
[2]Dep. of Chem., Tokyo Insitute of Technology, Meguro, Tokyo 152-8551, Japan
[3]Dep. of Chem., Univ. of Pennsylvania, Phyladelphia, PA 19104, U.S.A.

After the agostic C-H-M interaction was first demonstrated to exist, by neutron diffraction, in the compound $\{Fe(\eta^3\text{-}C_8H_{13})[P(OMe)_3]_3\}^+$, there were numerous attempts to search for analogous Si-H-M systems. Such species are of interest because of their suspected role in hydrosilations and other catalytic reactions involving metallo-silicon compounds. In 1982, Schubert and co-workers published the first (and to date the only) neutron diffraction study of a bona fide Si-H-M agostic (or non classical) interaction in $Mn(H)(SiPh_2F)(C_5H_4Me)(CO)_2$. Since then, other investigators have succeeded in characterizing Si-H-M interactions with X-ray diffraction methods, for example the Si-H-system in $TiCp_2(SiH_2Ph_2)(PMe_3)$.

A large single crystal of $TaCp_2(H)(SiMe_2H)_2$ (0.8x0.8x4.0mm) was grown via recrystallization from toluene/hexane[1] and sealed in quartz cap under a nitrogen atmosphere. Neutron diffraction data were collected at room temperature at JRR-3M reactor of JAERI using the BIX-I single-crystal diffractometer,[2] equipped with two area detectors. A neutron difference-Fourier map, phased by the positions of the non-hydrogen atoms (and the calculated C-H hydrogen atoms) derived from the X-ray analysis,[1] yielded only one large peak corresponding to the unique hydride ligand. Exhaustive least-squares refinement yielded final agreement factors of R=8.9% and Rw=9.5% for all 1295 reflections in the data set.

A plot of $TaCp_2(H)(SiMe_2H)_2$ is given in Figure 1. Within experimental error, the unique hydride ligand is symmetrically located between the two silicon atoms: the Ta-H distance is 1.785(15)Å, the non-bonding H...Si distances are 2.18918) and 2.190(17)Å, and the H-Ta-Si angles are 55.2(5)° and 55.5(5)°. All distances and angles in the molecule are quite normal: the afore-mentioned Ta-H distance agree quite well with that found in TaH_3Cp_2 [average 1.774(3)Å], [3] while both single-bonded Si-H distances (of the $SiMe_2H$ ligands) have the expected value of 1.48(2)Å.

The classical structure of $TaCp_2(H)(SiMe_2H)_2$ reported here is consistent with the NMR spectrum of the compound, which essentially shows the two dimethylsilyl ligands as being equivalent.[1] Our result does not, of course, imply that all complexes of this type $MCp_2(H)R_2$ (M=Nb, Ta) are classical, although we note that one other compound originally thought to have an unsymmetrical geometry, $NbCp_2(H)(SiMe_2Cl)_2$, has recently had its structure revised in favor of a symmetrical one.

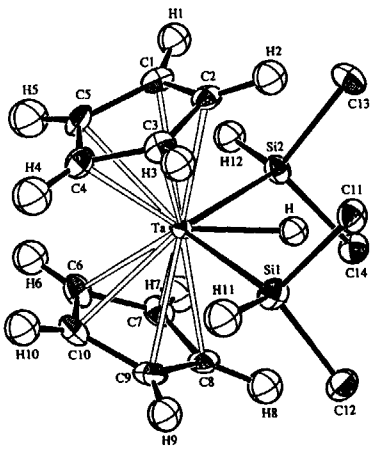

Fig. 1 Molecular plot of $TaCp_2(H)(SiMe_2H)_2$, with hydrogen atoms of the methyl groups removed for clarity.

References

[1] Q. Jiang, P.J. Carroll and D.H. Berry , Organometallics **10** (1991) 3648.
[2] N. Niimura, I. Tanaka and *et al.* , Physica **B 213&214** (1995) 786.
[3] R.D. Wilson, T.F. Koetzle, R. Bau and *et al.*, J. Am. Chem. Soc. **99** (1977) 1775.

JP9950087

2.5.10 Intermediate-Range Order in Lead Metasilicate Glass

K. Suzuya, D.L. Price[1], M.L. Saboungi[1] and H. Ohno

Japan Atomic Energy Research Institute, Sayo, Hyogo 679-5143, Japan
[1]Argonne National Laboratory, Argonne, Illinois 60439-4814 U.S.A

The nature of intermediate-range order in glasses remains one of the outstanding problems in condensed matter physics[1]. The most general and persistent evidence of intermediate-range order is the first sharp diffraction peak (FSDP), the feature observed at low wave vector in the structure factor $S(Q)$ of many systems, including oxide and chalcogenide glasses and complex liquids[2,3]. The wave vector Q_1 of the FSDP corresponds to a length scale $L_1 = 2\pi/Q_1$ on the order of 2.5 r_1 (r_1 is the nearest-neighbor distance in the glass), greater than the dimensions of the nominal building blocks of the glasses[3,4]. One of the features, the generality of which has not been emphasized in earlier work, is that the position of the first peak corresponds closely to that of a strong diffraction peak in a related crystalline phase and, therefore, to associated Bragg planes. We believe this to be an important clue to the origin of the FSDP.

We investigate this relationship by neutron diffraction (ND) studies of lead metasilicate ($PbSiO_3$) glass and crystal. The ND measurements for $PbSiO_3$ glass and crystal were done on the GLAD (IPNS, ANL) and on the TAS-1 (JRR-3, JAERI), respectively. Figure 3 shows ND data for $PbSiO_3$. (a) and (b) are original neutron weighted $S(Q)$'s for $PbSiO_3$ crystal and glass, respectively, which has been Fourier transformed to the 1-D real space correlation function $G(r)$. (c) and (d) are backtransformed $S(Q)$'s which are obtained from the $G(r)$ of $PbSiO_3$ crystal associated with truncation at two values R_{max}. For R_{max} = 7 Å, the FSDP is unrecognized, but for R_{max} = 9 Å, the FSDP is reproduced at Q = 1.2 Å^{-1}, a value similar to that of the original $S(Q)$ for $PbSiO_3$ glass. This shows, with little ambiguity, that a intermediate-range structure in $PbSiO_3$ glass consistent with FSDP can be specified by the $G(r)$ of the crystal extending to values of $r \sim 9$ Å.

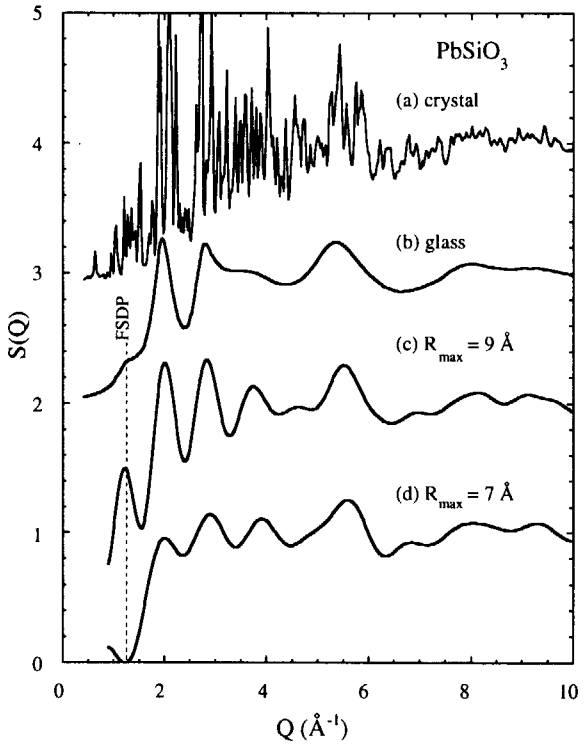

Fig. 1 Experimental neutron structure factor $S(Q)$ for $PbSiO_3$ crystal (a) and $PbSiO_3$ glass (b), and back Fourier transforms $S(Q)$ of the reduced pair correlation function $G(r)$ for $PbSiO_3$ crystal obtained by a transforms of experimental neutron $S(Q)$, associated with truncation at R_{max} = 9 Å (c) and 7 Å (d). Each $S(Q)$ plot is displaced by 1.0 for clarity.

References

[1] S.R. Elliott, Nature 354 (1991) 445-452
[2] S.C. Moss and D.L. Price, in: Physics Disordered Materials, eds. D. Adler, H. Fritzsche and S.R. Ovshinsky (Plenum, New York, N.Y., 1985) p. 77-95.
[3] D.L. Price, S.C. Moss, R. Reijers, M.-L. Saboungi and S. Susman, J. Phys. Condens. Matter 1 (1989) 1005-1008
[4] P.H. Gaskell, M.C. Eckersley, A.C. Barns and P. Chieux, Nature 350 (1991) 675-677

JP9950088

2.5.11

Hydration Structure of Lanthanum Ion in Aqueous Chloride Solution Determined by Neutron Diffraction Method

T. Yaita, S. Suzuki, H. Narita, S. Tachimori and Y. Ishii
Japan Atomic Energy Research Institute, Tokai, Ibaraki 319-1195, Japan

Introduction

Recently the hydration of lanthanide (III) ions in aqueous solution has been studied using X-ray and neutron diffraction[1], XAFS[3] and NMR[2]. Since these studies provide us several interesting results, for example, the hydration number changing in going from the lighter to the heavier lanthanides in the series; it is very important for separation chemists to elucidate separation behavior of these elements in solvent extraction and ionic exchange processes. However, the above methods can not provide us positions of hydrogen. Neutron diffraction is a unique tool for probing the structure of materials containing hydrogen, such as water and aqueous solutions. Accordingly, in this study, we determined the hydration structure of aqueous lanthanum chloride solution by neutron diffraction.

Experimental Methods

Sample solutions were prepared with heavy water (99.9% D) in order to eliminate the strong incoherent scattering of protons. The ^1H content of the final solution was checked by ^1H-NMR. To prepare the salt sample solution, we dissolved $LaCl_3$ salt into the D_2O solution. The neutron experiment was carried out with TAS-1 of JRR-3(2G) at Japan Atomic Energy Research Institute by using about 1-Å neutrons. The samples were contained in a quartz tube. The measured intensities were corrected for D_2O-D_2O background. In this way, the correlations of the solutions, namely, Cl-D_2O and Cl-Cl did not cancel, therefore, this result included these interactions.

Results and Discussion

The radial distribution function (Fig.1) shows that the first hydration sphere of water molecules around a lanthanum ion is almost defined. Since the peaks in the distribution function are quite well separated, it is possible to make an estimate of hydration structure. The first peak at 2.55-Å is attributed to oxygen of water. The previous x-ray diffraction study[1] reported that the bond distance between lanthanum and oxygen of water is 2.58-Å, and is approximately equal to this work's result. The second peak at 3.24-Å arises from deuterium of water, suggesting that water molecules orient themselves about ionic core. The third broad peak around 5.0-Å arises from chloride ion. Chloride ion exist outside the primary coordination sphere and isolate the hydrated lanthanum from the bulk structure of water by braking hydrogen bonds around hydrated waters. This result agreed with the ^{139}La NMR results[2].

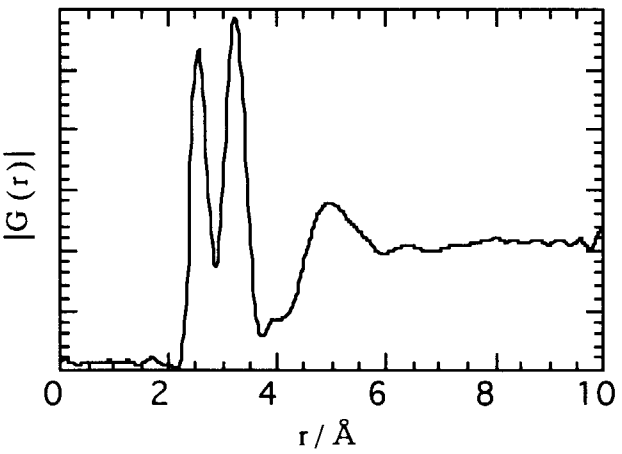

Fig.1
Radial distribution function in $LaCl_3$-D_2O system

References

1)A. Habenschuss and F. H. Spedding, J. Chem. Phys., **70(8)**,3758 (1979).
2)T.Yaita, D.Ito, S.Tachimori, J. Phys. Chem., **102(20)**, 3886(1998).
3)T.Yaita et al., J. Radioanal. Nucl. Chem. in press.

JP9950089

2.6 Materials Science and Industrial Applications

2.6.1 SANS Study of precipitation phenomena of Fe-Cu alloy

K. Aizawa, A. Iwase, T. Tobita and M. Suzuki

Japan Atomic Energy Research Institute, Tokai, Ibaraki 319-1195, Japan

There are many studies for precipitation phenomena in the Fe-Cu alloy system. In order to understand the relation of hardening and precipitate during thermal aging for dilute copper concentration in this system, we studied Fe-0.6at%Cu alloy by small-angle neutron scattering (SANS).

Samples were solution-treated at 1123 K for 2 hours and they were quenched in water. Then they were aged at 773K from 8h to 1000h. Each sample dimension is about $10\times10\times2mm^3$. SANS measurements were performed using SAN-J instrument at JRR-3M in JAERI. The covered q-range ($q=2\pi\theta/\lambda$, θ : scattering angle, λ : neutron wavelength) is from 0.02 to $2nm^{-1}$.

Except very early stage of thermal aging, it is well known that the chemical composition of precipitate is almost identical that of pure copper. Because of low copper concentration, we can treat the SANS profile as form factors of copper precipitates with particle size distribution. All SANS intensities showed independent component about aging with nearly q^{-6} behavior in the very low-q region. This may be attribute the contribution such as grain boundary or large scale inhomogeneity that doesn't relate to copper precipitation. So we subtracted that component from SANS intensities to extract the cross section of copper precipitate.

Figure 1 shows the aging time dependence of SANS cross section of copper precipitate. In the case of 100h aging, the SANS cross section shows q^{-1} dependence clearly. In this case, the scattering body has dimension considerably larger along one axis than along the other two. Therefore we assume that the shape of the precipitate is a ellipsoid of rotation with a : a : av (a : radius of the minor axis of precipitate, v : ratio of the major axis and the minor axis) during thermal aging. We assume the major axis and the minor axis have Gaussian distribution also.

Figure 2 shows the aging time dependence of the major axis and the minor axis obtained by least square fitting of the above model. The minor axis grows with the aging time monotonously. On the other hand, the major axis grows up to 100h aging, then it shrinks with the aging time. In the case of 1000h aging, the shape of copper precipitate tends to spherical.

We measured the Vickers hardness of this sample to compare SANS results. The hardness of the as quenched sample is about 80 DPH. Then the hardness gradually increases and the profile of hardness forms a peak around 100h aging with about 110 DPH. The time to the maximum of the major axis about thermal aging corresponds to that to the maximum of hardening by Vickers hardness measurement.

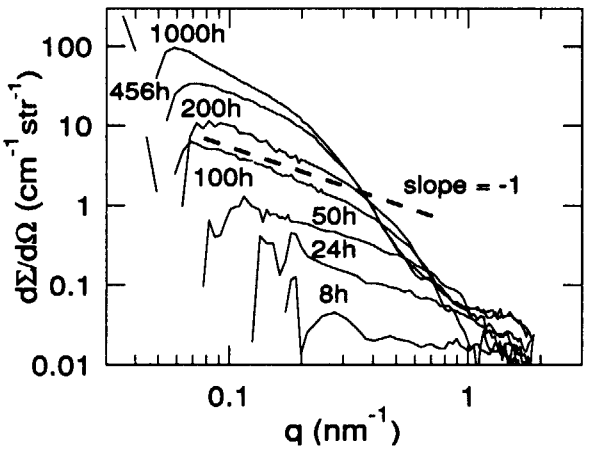

Fig. 1 The aging time dependence of SANS cross section of Fe-0.6at%Cu alloy.

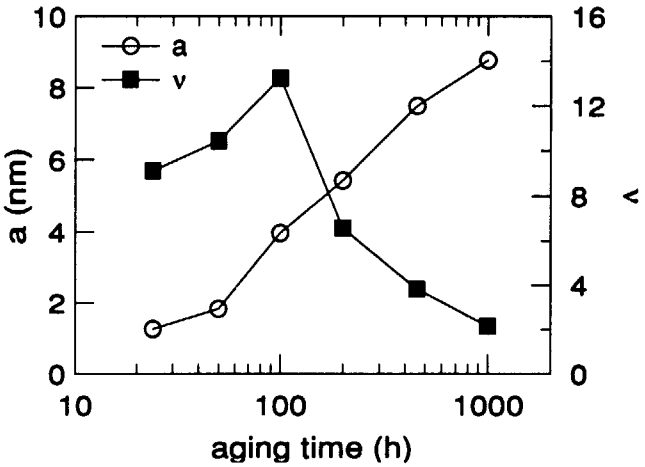

Fig. 2 The aging time dependence of the major axis and the minor axis obtained by least square fitting of Fe-0.6at%Cu alloy.

JP9950090

2.6.2

Characterization of single-crystal Ni-base superalloy CMSX-4 with creep damage (II)

K. Aizawa, H. Tomimitsu, H. Tamaki[1] and A. Yoshinari[1]

Japan Atomic Energy Research Institute, Tokai, Ibaraki, 319-11
[1]Hitachi Research Laboratory, Hitachi, Ltd., Hitachi, Ibaraki, 317

In order to check the possibility of nondestructive testing to the expected life of operated blades made from Ni-base superalloy, we have applied small-angle neutron scattering (SANS) experiments to the CMSX-4 superalloy with creep damage as a model case. We reported the morphological change with creep damage caused by tensile stress of that sample in previous report[1]. The range of observation corresponded to that of less than 30% to creep rupture time. The purpose in this article is to show the morphological change up to near creep rupture.

The sample is a single crystal CMSX-4. In the case of as heat-treatment sample, the morphology observed by SEM is aligned cuboidal precipitate of γ' phase in γ matrix. It was loaded tensile stress to introduce creep damage with 14kgf/mm^2 at 1313K. The stress direction was parallel to <001> direction of a sample. In this case, the morphology observed by SEM is lamella structure of γ and γ' phases with normal direction being parallel to stress. Samples were cut into 30mm×19mm×2mm^t. The SANS measurements were carried out using PNO instrument with the q-range ($q=2\pi\theta/\lambda$, θ : scattering angle, λ : neutron wavelength) of 2×10^{-4}-6×10^{-2}nm^{-1} at JRR-3M in JAERI. This instrument is a double crystal SANS machine using Si perfect crystal with (5,-5) setting. Incident neutron beams were parallel to <100> direction of a sample.

Figure 1 shows the smeared SANS intensity of single crystal CMSX-4 with damage rate from 10% to 85% to creep rupture time. The q-vector is parallel to stress direction. The 1st peak from lamella structure is clearly shown. It shifts to lower q with increasing creep damage. This means the average distance of lamella structure grows with increasing creep damage. So that is a good parameter to describe the morphological change due to creep damage. After desmearing the data for infinite slit height system, we obtained that parameter by least square fitting of 1st peak from lamella structure, assuming Gaussian peak shape.

The average distance of lamella structure as a function of creep rate for rupture time is shown in fig. 2. It gradually increase up to 54% creep damage, then rapidly grows. The SANS results is good agreement with SEM observation.

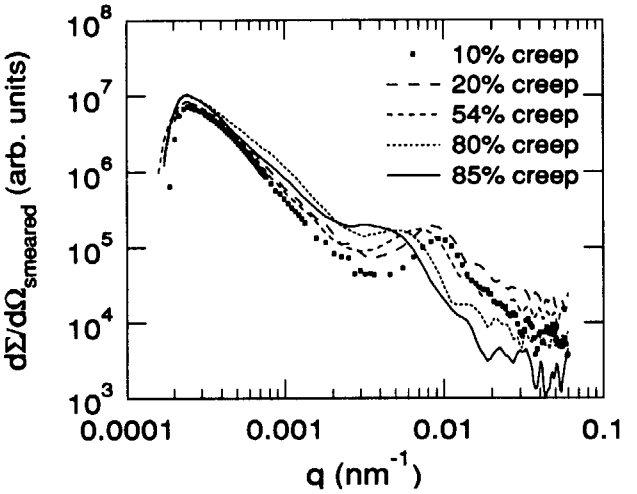

Fig.1 The dependence of SANS cross section for damage rate to creep rupture time

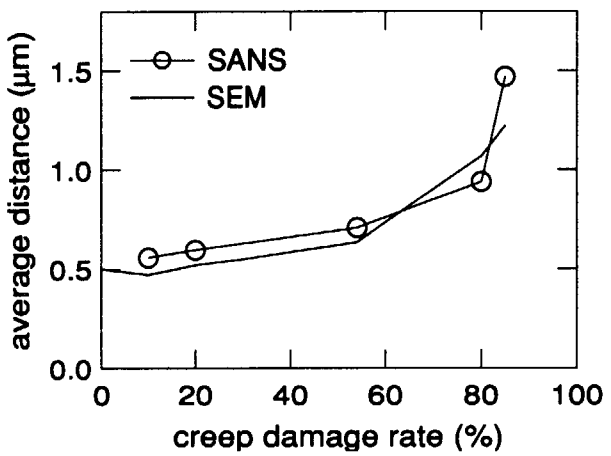

Fig. 2 The dependence of the average distance of γ and γ' phase as a function of damage rate to creep rupture time

References

[1] K. Aizawa, H. Tomimitsu, H. Tamaki and A. Yoshinari: (PROGRESS REPORT ON NEUTRON SCATTERING RESEARCH, April 1, 1996-March 31, 1997, 54

JP9950091

2.6.3

Residual Stress Measurement of Superconducting Coil Jacket by Neutron Diffraction

Y. Tsuchiya, N. Minakawa[1], Y. Morii[1], T. Kato, H. Nakajima, K. Ishio, and H. Tsuji

Naka Fusion Research Establishment, Japan Atomic Energy Research Institute, Ibaraki 319-01 Japan

[1]Advanced Science Research Center, Japan Atomic Energy Research Institute, Ibaraki 319-11 Japan

Some improvements on neutron spectrometer for residual stress analysis (RESA) installed at JRR-3M reactor in JAERI were made recently. Monochrometor system of bent Si single crystals was adopted to RESA instead of a pyrolytic graphite monochrometor. The monochrometed neutron beam was converged at the position of the sample by the monochrometor system. As an other improvement, a conventional ^{3}He detector was installed to RESA besides an one-dimensional position sensitive detector (PSD). A solar collimator can be set into the diffracted beam line when the conventional detector is used. Using the improved RESA, internal residual stress measurement of a superconducting coil jacket was performed.

A sample is a jacket of a superconducting central solenoid coil (CS coil) for international Thermonuclear Experimental Reactor (ITER). The jacket material, INCOLOY 908, is a nickel-iron based precipitate hardening type alloy. INCOLOY908 has a possibility of fracture due to Stress Accelerated Grain Boundary Oxidation (SAGBO) in the region of tensile residual stress above 200MPa. It is advisable that the residual stress of the jacket is to be a value below 200MPa to avoid the SAGBO cracking.

The square cross section of the coil jacket was 45 ≈ 45 mm^2 and the inside diameter of about 35 mm. The sample jacket tube enclosed a bundle of Cu wire of 35mmΙ instead of Nb^3Sn superconducting wire to reproduce a condition of the actual use. The coil was cut to a length of about 150mm for a neutron diffraction measurement. The sample was confirmed to be FCC single phase by neutron diffraction measurement. A solid solution of INCOLOY 908 was used as the standard sample of stress-free condition. The thickness of the jacket material for the measurement is about 4.5 mm.

The incident beam wave length of 2.0995Å was used. In order to define the sampling volume within the sample, incident beam and scattering beam were restricted for 2 ≈ 4mm^2 of cross section by Cadmium masks before and after the sample. Zero-dimensional counter was used and a collimator of 20' was set before the counter. For the three principal orientations x, y and z corresponding to longitudinal, transverse and vertical directions of the sample, (111) plane spacings were measured scanning from outer surface of the jacket to inside every 1mm in depth. The residual stress distributions of the CS coil jacket that were obtained in this study are shown in fig. 1. These spatial distributions of the residual stress show the same tendency as the data by PSD mode. A peak/background ratio was improved successfully by using modified RESA.

Reference

Y. Tsuchiya, et al. Physica B 241-243 (1998) 1264-1266

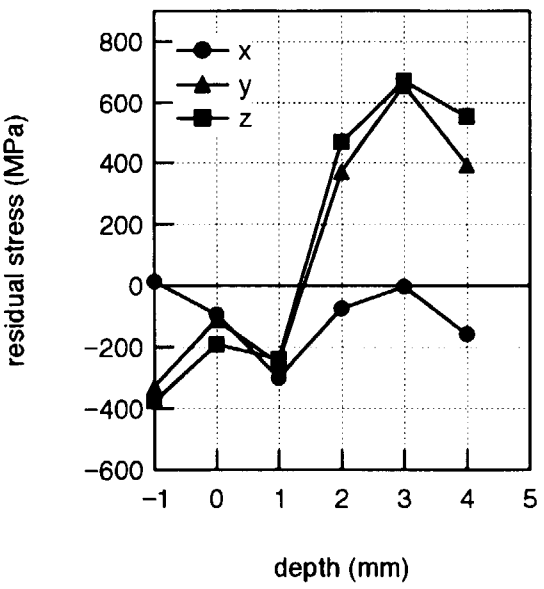

Fig. 1 The residual stress distributions of the CS coil jacket for three orthogonal direction, x, y and z.

JP9950092

2.6.4 The internal residual stress measurement for VAMAS Round Robin Sample by neutron diffraction method

N. Minakawa, Y. Morii, Y. Tsuchiya, M. Hayashi[1], S. Ohokido[1], K. Tanaka[2], Y. Akiniwa[2]
JAERI, 1. Ech. Eng. Res. Lab., Hitach Ltd., 2. Nagoya university

1, The outline

VAMAS is the abbreviated designation of Versailles Project on Advanced Materials and Standards. It aims at the international standardization of the residual stress measurement by the neutron diffraction method. VAMAS made a standard sample and it has around in every country organization and which degree was the similar strain distribution gotten or measured in the comparison. This time, we measured VAMAS standard sample by RESA at JRR-3 in Guide Hall and the excellent result could be gotten.

2, The standard sample

Outer ring diameter is 50mm and ring caliber is 25mm with a column plug diameter is 25mm which was manufactured by aluminum 7050. These are put in to each other at the liquid-nitrogen temperature, after that returning the room temperature, the stress occurs to the boundary surface by the thermal expansion. It measured the internal residual strain distribution of $\Delta d/d$. A sample size is shown in Figure -1.

3, The measurement condition

The measurement position was used the direction of Figure-1 and measured RADIAL, HOOP and AXIAL planes. The condition of the equipment and neutron beam is shown next.

The monochromator crystal : Si(311)
The mosaicnes of the crystal : 0.22°
Scattering angle of monochromator crystal : $2\theta M = 79.75°$
The neutron wavelength : 0.20995 nm
The insident and reflection beam slit size :
measurement of Radial and Hoop 3 mm (width) x 10mm (Height)
measurement of Axial 3mm(Width) x 3mm(Height)
Beam Collimation : 0.2° - 0.33° - 0.33°
Neutron detector : Zero dimensional ^{3}He detector

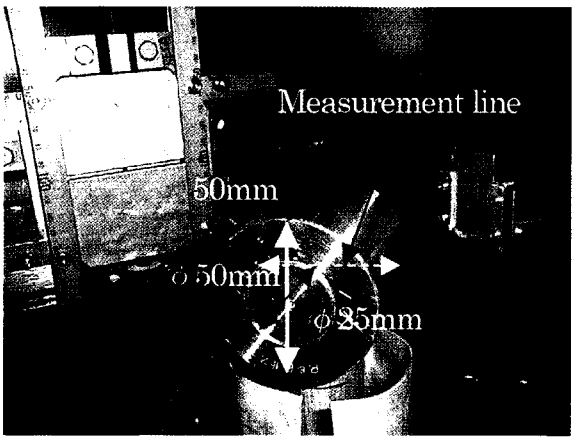

Fig-1 RING & PLUG SAMPLE

4, The measurement procedure

(1) To look for the lattice constant of the material, it measured plug material by neutron diffraction.
(2) It measured texture to know the nature of the material and decision of the measurement Miller index. It was measured based on the neutron diffraction result of (1), it used χ, ϕ

axis - goniometer at the plug (111), (200) and (220).

(3) It fixed a measurement Miller index from the result of the neutron diffraction and the result of the texture measurement. It installed a plug sample in 3 axis (X,Y,Z) goniometer and based on the arrow marking which is written in the sample surface, it fixed the measurement surface of RADIAL, HOOP, AXIZL. Every direction was measured by θ - 2θ scan method, it measured each index in $d_0(h,k,l)$.

(4) It installed a ring and a plug sample on the 3 axis goniometer and it was selected the neutron diffraction measurement which is the index, (111), (200), (220). The ring and plug (111) strain distribution is shown in Figure-2.

5, The consideration

The purpose of VAMAS measurement is to make the standard of the standardization by measuring the same sample with the equipment of every country organization and comparing it. The measurement result by RESA agreed with the strain distribution over each American and European organization approximately. It is possible to say that it is the strain distribution which is quite near the result which was computed by the finite element method. Because we weren't informed of a value with Young's modulus and Poisson's ratio every each index of aluminum 7050, we could not done calculation.

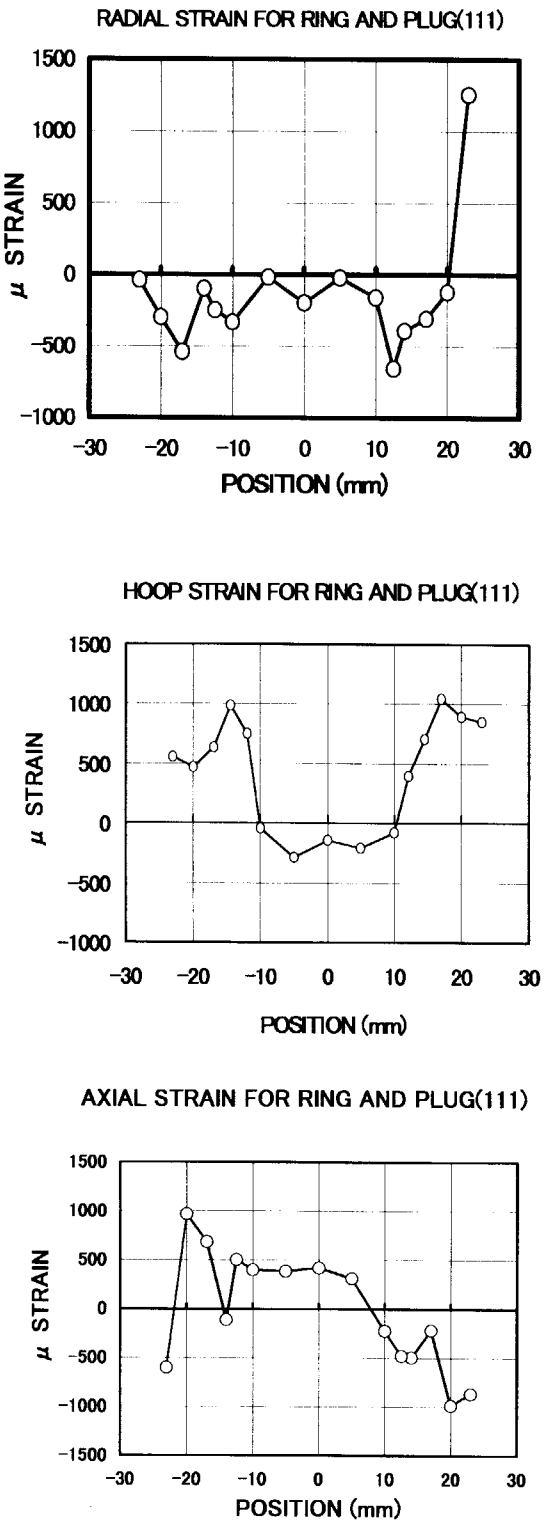

Fig-2 Distribution of Strain for VAMAS Ring & Plug (111)

JP9950093

2.6.5 Measurement for Redistribution of Residual Stress with Crack Progress near the Weldment on Stainless Steel Pipe.

S. Okido, M. Hayashi*, Y. Morii**, N. Minakawa** and Y. Tsuchiya**

Mechanical Engineering Research Laboratory, Hitachi, 3-1-1 Saiwai, Hitachi, Ibaraki 317-8511
* Mechanical Engineering Research Laboratory, Hitachi, 502 Kandatsu, Tsuchiura, Ibaraki 300-0013
**Japan Atomic Energy Research Institute, Tokai, Ibaraki 319-11

The distribution of welding residual stress is known to change when cracks occur. The welding residual stress distributes along not only the surface but also the cross section of the structural components. The change in residual stress distribution in the cross section is important in evaluating the fracture caused by crack growth, because crack growth behavior is affected by changes in residual stress distribution.

Change in residual stress distribution in the cross section were examined using a method for neutron diffraction method of welded stainless steel pipe.

An apparatus for measuring neutron diffraction was used residual stress analyzer (RESA) established in JRR3M. The neutron wavelength λ was 0.199 nm. A Cd slit was used to limit the area for measurement to $2\times2\times4$ mm. The lattice strains were measured based on (200) diffraction. Stresses were calculated using Hooke's law from the lattice strain values measured in three directions. In the calculation, the elastic constant E was 134 GPa and Poisson's ratio ν was 0.34.

The circumferentially butt-welded pipe specimen was made of type 304 stainless steel, which had an outer diameter of 114.3 mm, a thickness of 8.6 mm and a 10 mm wide weld line. Measurements were taken 1 mm away from the fusion line at a 1mm deep pitch in the thickness direction. A circumferential defect simulating inner surface crack, that was 2mm deep and 16mm long, was notched by an electric discharge machine 1 mm away from the fusion line.

The distribution of longitudinal residual stress was measured using the neutron diffraction method before and after notching of the defect. The data obtained are plotted in Fig.1. The residual stress in the region from the inner surface to the tip of the notch was found to be relieved by this notching of the defect. The values for residual stress distribution before and after notching of the defect were almost the same, in spite of near the defect tip. The residual stress distribution was not changed by the present of the defect. This suggests that the defect may have been too small to disturb the residual stress field.

The distribution of the residual stress in the cross section of welded pipe is recognized as measurable by the neutron diffraction method. We plan to measure a welded pipe specimen having a larger notch in order to examining the change in residual stress distribution.

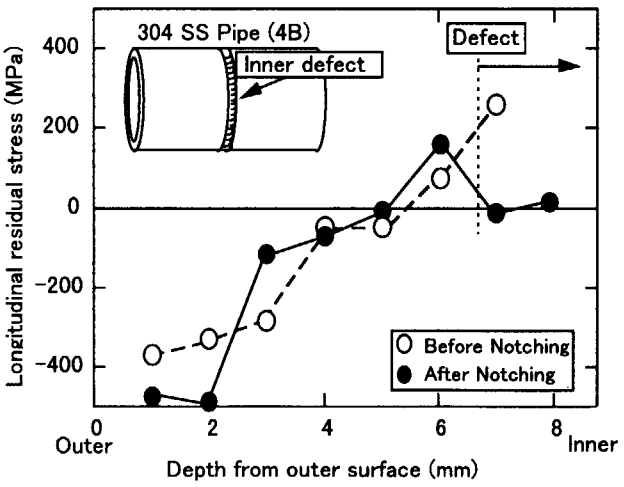

Fig. 1 Distribution of longitudinal residual stresses 1 mm away from fusion line

2.6.6 Residual Strain Measurements of a Round Steel Bar with a diameter of 40 mm

K.INOUE, T.HORIKAWA, H.NAKAMURA, N.MINAKAWA,[1] Y.MORII[1] and RUDIONO[2]

Fac. Sci. & Tech. Ryukoku Univ. Seta, Otsu 520-2194, Japan
[1]Japan Atomic Energy Research Institute, Tokai-Mura, Ibaraki 319-1195, Japan
[2]Dep. Materials Sci. Eng. Ibaraki Univ. Hitachi, Ibaraki 316-0033, Japan

A preliminary experiment was done to prove usefulness of neutron diffraction for residual strain measurements of a round steel bar with rather large diameter. The residual stress analyzer RESA of JRR-3M was used. As the first step, the lattice spacing of an annealed steel bar which should be constant at any radial position was measured to confirm the accuracy of the measurements. In case of RESA, the cross section of the neutron beam is at least 2mm in diameter, to obtain a reasonable intensity. The larger sample size is better for good resolution, whereas the long path length of the beam in a large sample reduces the intensity of the scattered beam and the time necessary for measurements increases. In this experiment, the measured sample was S15C round steel bar with an annular circular notch of 40mm diameter. It was annealed at 700℃ for 2 hours and cooled down to room temperature in a furnace to exclude the strain caused by machining.

The wave length of the neutron beam was 2.0996 Å. We tried to measure the three dimensional lattice spacing at a 1mm step of the local position on a radius of the notch root. For the measurements of lattice spacing of (110) planes of radial and hoop direction, the bar was set up, where $2 \times 15mm^2$ slits were used for incident and reflected beams. For the axial direction, the bar was reclined, where both $2 \times 8mm^2$ slits were used.

The (110) peak from the axial plane at the center of the notch root is shown in Fig.1. It took 360 sec. to obtain one measuring point. The cross points show the measured raw data. The black circle at each angle shows the averaged value of both three neighboring values. The radial dependence of the obtained lattice spacing for three directions is shown in Fig.2. It is almost constant for all three directions at each position on the radius. This fact is reasonable for the specimen without fatigue test. The effect of the fatigue test on the residual strain of the same type bar will be studied in near future.

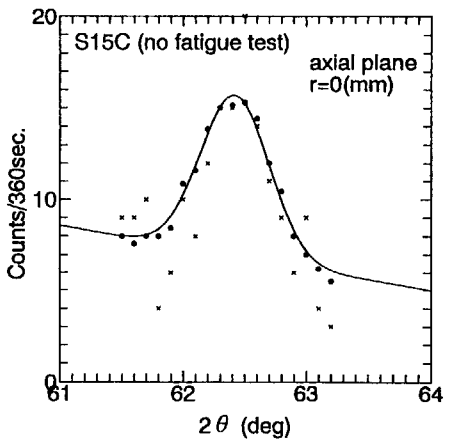

Fig. 1 (110) reflection from the axial plane at the center of the notch root of 40 mm ϕ.

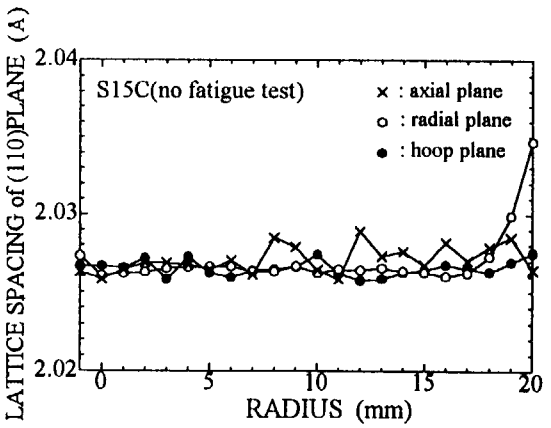

Fig.2 Radial dependence of each lattice spacing.

JP9950095

2.6.7 Residual Strain Measurements of a Heat Treated Steel Pipe

K.INOUE, H.KAWASHIMA, J.SAKAGUCHI, N.MINAKAWA,[1] Y.TSUCHIYA[1] and Y.MORII[1]

Fac. Sci. & Tech. Ryukoku Univ. Seta, Otsu 520-2194, Japan

[1]*Japan Atomic Energy Research Institute, Tokai-Mura, Ibaraki 319-1195, Japan*

The 13% Cr steel pipe for the oil well is heat treated after plastic rolling, to obtain the desired strength. The pipe with diameter of 73mm and the thickness of 5.51mm, used for this experiments, was quenched from 900℃ to the room temperature by spraying the water on the outer surface. The crystal structure of the material becomes bcc, owing to the martensitic transformation. As the rate of cooling is different at each position of the wall thickness, the residual stress appears.

To know nondestructively the residual stress at each position, we have made the neutron diffraction study and observed a small change of the lattice spacing at intervals of 1mm of the wall thickness. RESA, installed at T2-1 port in JRR-3M was used. As a vertically focussed monochromator, (004) reflection of three pieces of pyrolytic graphite was used.. The wave length of the neutron beam was 2.1034 Å. The (110) reflection from each position of the pipe was observed. To see a small area of the x(radial) and y(hoop) planes, the pipe was set up, where the slits of $2\times15mm^2$ for incident beam and $2\times20mm^2$ for reflected beam were used. To observe the z(axial) plane, the pipe was reclined, where the slits of $2\times4mm^2$ for incident beam and 2×6 mm^2 for reflected beam were used. The residual stress was estimated from the observed strain, and was compared with the stress calculated by means of the finite element method.

The experimentally obtained residual stress distribution is shown in Fig.1 and the calculated one in Fig.2. It is found that the coincidence between experimental and calculated stress values for axial direction are good.. However, for radial and hoop direction some difference were observed near the outer and the inner surface. It may be caused by the pre-treatment of the specimen before neutron diffraction.

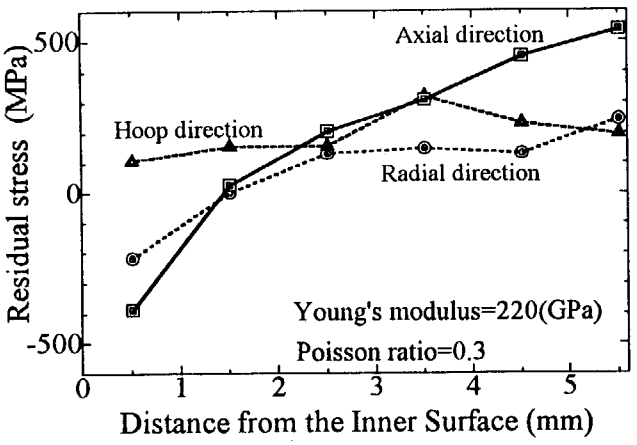

Fig. 1 Residual stress distribution obtained by neutron diffraction.

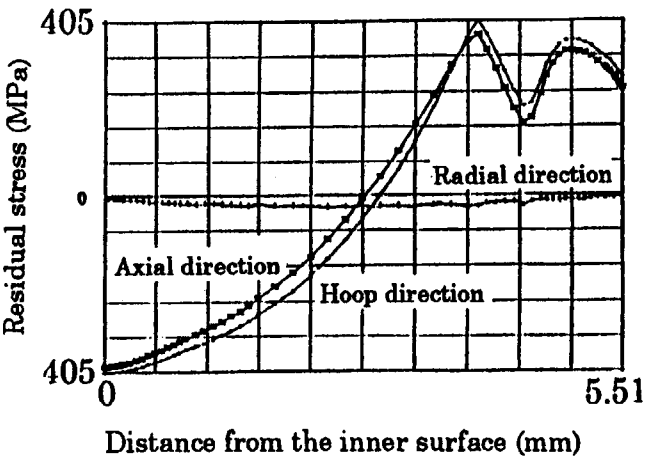

Fig.2 Residual stress distribution calculated by finite element method.

JP9950096

2.6.8 Neutron and X-ray Diffraction Study of Phase Stresses in SiC Particulate Reinforced Aluminum Alloy

Yoshiaki AKINIWA, Keisuke TANAKA, Takuya TAKEZONO,
Nobuaki MINAKAWA[1], and Yukio MORII[1]

Nagoya University, Nagoya 464-8603, Japan
[1]Japan Atomic Energy Research Institute, Tokai, Ibaragi 319, Japan

Aluminum alloys reinforced with silicon carbide particles (SiCp) have several advantages in structural applications such as nearly isotropic mechanical properties, high specific stiffness and strength, and high wear resistance. Since the strength of the composites depends on that of matrix and particles, it is important to evaluate the stress state of each material under loading. The neutron and X-ray diffraction methods can detect separately the stress in each constituent phase of the composite. The neutron and X-ray diffraction methods were used to measure the phase stresses in the aluminum alloy reinforced by SiCp under uniaxial loading. The measured phase stresses were compared with the predicted values calculated by Eshelby's inclusion models[1].

The experimental materials used were monolithic aluminum alloy (Al2024) and aluminum alloy reinforced by silicone carbide particles (SiCp/Al2024). The volume fraction of SiC particles of the composite is 20% and their average size is 3 μm. An extruded rod of the composite was heat-treated under T6 conditions. The grain size of the matrix is about 5 μ m. On the other hand, the grain size of the unreinforced material is 5～10 μm in the rolling direction and about 5 μm in the transverse direction.

The X-ray diffractions from Al 222 and SiC 116 by Cr-K α radiation were used for X-ray stress measurement. The stress was evaluated by the 2θ-$\sin^2\psi$ method obtained from the specimen strained to several known stresses by using a specially designed four point bending device under the iso- or side-inclination condition along parallel and perpendicular direction to the loading axis, respectively. For the diffraction of SiC 116, the stress constant (S=-1880 MPa/deg), Young's modulus (E=433 GPa) and Poisson's ratio (ν =0.129) were calculated by using Krö ner's model from the elastic constants of single crystals. The measured X-ray elastic compliances agree well with the predicted values calculated by using Krö ner's model [2]. The phase stress measured by the X-ray method in matrix and SiC particles of composite increased in proportion to the applied stress. The macrostress calculated from the phase stress by using the rule of mixture was equal to the applied stress.

The neutron stress measurement was performed for the same diffraction planes as the X-ray stress measurement with the RESA (REsidual Stress Analyze equipment) at JAERI. The specimen was uniaxially strained with a hydraulic tensile testing equipment. The wave length used was 1.8065 Å. The direction of the lattice strain measured was parallel and perpendicular to the loading axis. The strain was calculated on the basis of the initial lattice spacing at σ_A=0. The phase stress measured by the neutron method in the matrix is nearly equal to that by the X-ray method, and is less than the theoretical prediction using the self-consistent model and Eshelby-Tanaka-Mori model [3]. For the case of SiC particles, measured phase stress is close to the theoretical prediction.

References

[1] J. D. Eshelby, Proc. Roy. Soci. London, A241 (1957), 376.
[2] E. Krö ner, Einkristalls, Zeitschrifts f. Phys., 151 (1958), 504.
[3] T. Mori and K. Tanaka, Acta Met., 21, (1973), 571.

JP9950097

2.7 Fundamental Physics

2.7.1 Precise Neutron Scattering Lengths of Gallium-Isotopes Obtained by Interferometry at PNO in JRR-3M

Hiroshi Tomimitsu, Yuji Hasegawa[1], Kazuya Aizawa and Seishi Kikuta[1]

Advanced Science Research Center, JAERI, Tokai, Ibaraki, 319-1102 Japan
[1]Faculty of Engineering, Tokyo University, Hongo, Bunkyo, Tokyo, Japan

As the neutron scattering lengths of elements or isotopes are very important as the basic quantity, many values measured by various methods have been tabulated[1]. Some of them, however, seem to be made much more accurate. We determined the accurate of gallium isotopes with the interferometry at the PNO-apparatus.

^{69}Ga of 99.7% purity and ^{71}Ga of 99.6% purity were used as the specimen. They were melt and put in a flat glass cell, respectively. The thickness was 2.000 mm for both specimen. Those isotopes stayed in the liquid state during all the measurements at the room temoerature.

Neutron interferometry was carried out at the PNO. With the beam-collimator of 30min. of arc., the wavelength was selected as 0.15123nm. The cross section of the neutron beam was restricted to 2mm in width and 4mm in height. An LLL-type Si interferometer was used. Because of their small amount, the specimens were set so as to receive the transmitted-beam only behind the 1'st reflecting plate(splitter) of the interferometer.

We measured the oscillation of the intensities with the specimen-rotation within ±30 deg. of arc. or so. Measurements were repeated ten times for both specimens, and very similar curves were obtained, respectively. Fig.1 shows the typical example of the measured oscillation curves of ^{69}Ga, with the least square fits on the experimental data.

Next, we analyzed the experimental data following the equation;

$$I=A\cos(B/\cos(\omega+C)+D)+E, \quad \cdots\cdots(1)$$

where the parameters mean as following;

ω: the amount of specimen rotation from the original angular position,
A: apparent amplitude of the intensity-oscillation,
B: this includes all of the physical meanings as

$$B=-N\lambda tb, \quad \cdots\cdots(2)$$

with N=atomic density of the specimen,
λ=wavelength of the neutron used,
t=thickness of the specimen, and
b= the coherent scattering length to be determined;
C: amount of the angular mis-setting from the ideal origin of the specimen,
D: intrinsic phase term of the interferometer, and
E: apparent back-ground part in the intensity-oscillation including all of the imperfectness of the experimental condition, respectively.

In this study, we determine the coherent neutron scattering length in four significant figures, because the B-value, the atomic weight and the specimen thickness are known to four figures or less. Then, we should take account of the effect of the glass cell containning the specimen and of the air excluded by the specimen and cell from the neutron path. Eq.(2) is , thus, modified as follows;

$$B=(B_s-B_a)+(B_c-B_a)$$
$$=-\{(N_sb_s-N_ab_a)\lambda t_s-(N_cb_c-N_ab_a)\lambda t_c\}$$
$$=-\{b_s-b_a\times(1+t_c/t_s)\times N_a/N_s\}N_s\lambda t_s+B_c, \quad \cdots\cdots(2')$$

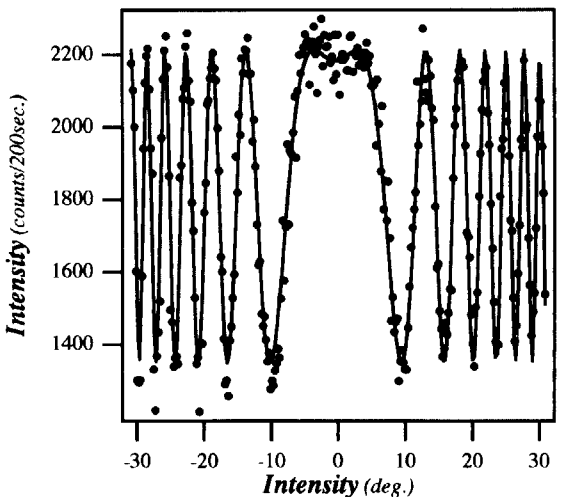

Fig.1 Example of the Intensity Oscillation Curve of ^{69}Ga

where suffixes s, c and a mean the specimen, the glass cell and the air, respectively.

With a conventional least square method, we analyzed all the experimental curves, as already shown in Fig.1, and obtained the B's for the Eq.(2'). Thus, we obtained the coherent neutron scattering length as;

b=8.051 fm for ^{69}Ga, and
b=6.173 fm for ^{71}Ga,

respectively, after reducing the effect of the glass cell and the air. Here, B_c for the glass cell was determined by measuring the empty cell. b_a was estimated as 12.52 fm by assuming the air composion of 20.9 % O_2 with b=5.83×2 fm, 78.1 % N_2 with b=6.44×2 and 1.0 % Ar with b=2.07. The atom number density of the air was estimated as 2.488×10^{19} atoms/cm^3 with the relation of density=V/N_A, with V=RT/p = 2420.7 cm^3 with pressure p=1 atm., T=295 K and the gas constant R=82.0567 cm^3 × atm/K.

As the first stage, we refined the b-values of the gallium isotopes, by taking the effect of the impurities into account. The total effects of the "pure" impurities, except for the isotopic mutual contamination of ^{69}Ga and ^{71}Ga, were estimated as 0.002 fm for ^{69}Ga and 0.003 fm for ^{71}Ga, respectively, making use of the tabulated b-values of the impurity atoms[1]. Accordingly, the b-values were slightly modified to be 8.049 fm and 6.170 fm for ^{69}Ga and ^{71}Ga, respectively.

As the next step, the effect of the isotopic mutual contamination was resolved by solving a simple set of the linear equations with two variables as follows:

$$0.996\times b^{(69)} + 0.003\times b^{(71)} = 8.049$$
$$0.004\times b^{(69)} + 0.995\times b^{(71)} = 6.170,$$

because ^{69}Ga was contamined by 0.3% ^{71}Ga and ^{71}Ga by 0.4% ^{69}Ga, respectively. $b^{(69)}$ and $b^{(71)}$ temporally stand for the final b-values, b_0, to be determined here for ^{69}Ga and ^{71}Ga, respectively, and both right side members are the b-values just obtained. The b-values for the two isotopes were finally determined as:

b_0 = 8.063 fm for ^{69}Ga, and
b_0 = 6.169 fm for ^{71}Ga, respectively.

In the final stage, we estimated the uncertainties of the b-values determined above. Uncertainties of the Avogadro constant, the density and the wavelength are so small compared to the others that they can be neglected. For the sake of a reasonable estimation of other uncertainties, we explicitly treated B-value as $B=B_0(1\pm\beta)$, the atomic number density as $N=N_0(1\pm\nu)$ and the thickness as $t=t_0(1\pm\tau)$. The ambiguity of the b-value, δb, can be written, then, as $\delta b = b_0(\beta+\nu+\tau)$, where, for example, B_0 means the main B-value derived in the curve-fitting and β means the ratio of the ambiguity of the B-value to the main B-value, and so on. In the present analysis, these errors can be estimated for both isotopes, $\tau = \delta t/t_0$ = 0.0005/2.000 =0.00025 and $\nu=(\delta N_A/N_A+\delta\rho/\rho+\delta A/A) \fallingdotseq \delta A/A$ =0.005/69.72 =0.00007. As β is equal to 0.0017 in the case of ^{69}Ga, δb was estimated as 0.016 fm. Since β equals to 0.0021 in the ^{71}Ga case, on the other hand, δb was estimated as 0.015 fm. Accordingly, we conclude the final b-values their uncertainties as follows:

b = 8.063±0.016 fm for ^{69}Ga , and
b = 6.169±0.015 fm for ^{71}Ga,

respectively.

Results, determined above, were significantly different from the known values obtained by other method, i.e., the former is larger by about 2% and the latter is less by about 4% compared with the tabulated values[1], respectively. On the other hand, the values of the high purity aluminum, niobium and natural gallium, which were also measured as the standard specimens in the present experiment, were almost the same as the known values.

The coherent neutron scattering lengths of ^{69}Ga and ^{71}Ga were, thus, successfully obtained by the neutron interferometry at the PNO[2].

References

1) L.Koester, H.Rauch and E.Seymann: Atomic Dta and Nuclear Data Tables 49(1991) 65.
2) This work will be published in NIM-A.

JP9950098

2.8 Instrumentation and Methods

2.8.1 Development of liquid-He-free dilution refrigerator for the neutron scattering

Y. Koike[1], Y. Morii[1], T. Igarashi[2], M. Kubota[2], Y. Hiresaki[3] and K. Tanida[3]
1 Japan Atomic Energy Research Institute, Tokai, Ibaraki 319-1195, Japan
2 Institute for Solid State Physics, University of Tokyo, Roppongi 7-22-1, Tokyo 106-8558, Japan
3 Suzuki Shokan Co., Ltd. Kawagoe, Saitama 350-0833, Japan

We have developed a liquid-He-free dilution refrigerator named mK cryocooler[1)] which is composed of a pulse-tube/GM hybrid cryocooler[2)] and a JT dilution refrigerator unit[3)].

Figure (a) shows the precooling process by the hybrid cryocooler. Typically, we precooled the cryostat to 4 K in about 1 day . As shown in Fig. (b), it took about 8 hours to cool down from 4 K to the lowest temperature, 77 mK in a preliminary experiment. At the lowest temperature, the ^{3}He circulation rate was estimated to be 1 x 10^{-4} mol/s from the flow rate of the rotary pump. The still temperature was about 0.8 K. The cooling power was 22 μW at 100 mK.

We used the mK cryocooler in the neutron scattering experiments at JRR-3M to study rare-earth compounds and uranium compounds. The lowest temperature achieved in the study was 41 mK.

The obtained lowest temperature will be lowered by improving the heat exchanger. For example, we are planing to install the step heat exchangers. The precooling time of one day to reach 4 K was too long. We installed the liquid N_2 pot on the pulse tube flange for quick precooling. At present, the gas handling system is operated manually. This causes another time consumption for researchers. Therefore, we will make a new gas handling system in order to control it by a computer, i.e. mK temperature can be achieved only by pushing a start switch. The two stage pulse tube refrigerator is preferred for our mK cyocooler because it has no mechanical vibration at all. We have a plan to replace the hybrid cryocooler by the two stage pulse tube refrigerator at the final phase of the development if a suitable cooling power become available.

We believe that the mK cryocooler benefit not only neutron scattering researcher but also any researchers in the various scientific fields.

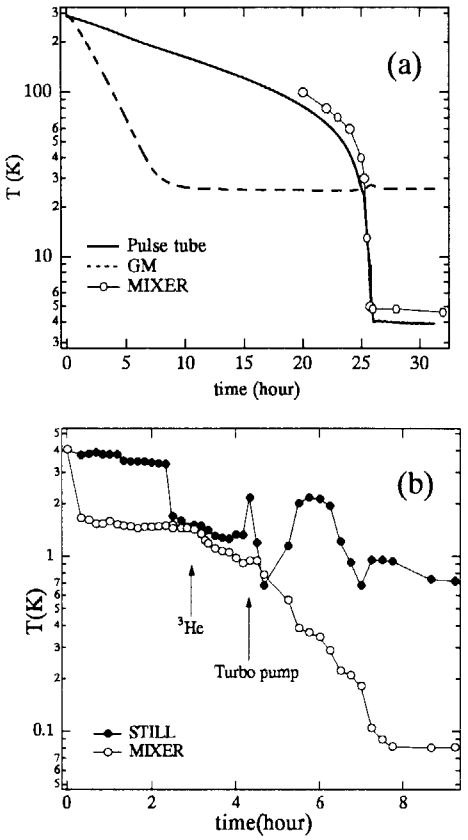

Fig. (a) Cooling test to 4. 2K and (b) condensation time of mixture gas and cooling test to the lowest temperature.

References

[1] Y. Koike et al., to be published in Proceedings of ICEC17 (1998).
[2] K. Tanida et al., Proceedings of ICEC16/ICMC (1996) 303.
[3] M. Sawano et al., Proc. 3. Japan-Sino Joint Seminar on Small Refrigerators and Related Topics, Okayama (1989) 27.;M. Kubota et al.,to be published in Proceedings of ICEC17 (1998).

JP9950099

2.8.2 Performance Test of a System for Simultaneously Generating Triple Extreme Conditions for Neutron Scattering Experiments II

A. Moriai, S. Ichimura, A. Ohtomo, S. Kawano[1], A. Onodera[2]

Department of Research Reactor, JAERI, Tokai, Naka, Ibaraki, 319-1112
[1] Research Reactor Institute, Kyoto University, Kumatori, Sennan, Osaka, 590-0451
[2] Faculty of Engineering Science, Osaka University, Toyonaka, Osaka, 560-0043

In recent years neutron scattering studies of condensed matters have shown predominant trend of studies of under extreme conditions such as low temperature, high magnetic field and high pressure. These parameters of temperature, pressure and magnetic field have been selected as independent thermodynamic variables for sample environment. However, those parameters have been only selected as a single-variable or a double-variables at most in neutron scattering so far because of various technological difficulties existing in the development of a system available for simultaneously controlling those three parameters.

As previously reported, we have developed a cryomagnet system with a high pressure cell[1)], and carried out several tests for the system to verify its performance. The present article represents the results of one of related experiments derived from measuring magnetic phase transition for $TbNi_2Si_2$ rare-earth compound under triple extreme conditions by neutron scattering. The $TbNi_2Si_2$ compound crystallizes in a tetragonal $ThCr_2Si_2$-type structure, which undergoes two successive magnetic transitions: an amplitude modulated antiferromagnetic structure with a propagation vector $\boldsymbol{Q}_1=(1/2\pm\tau, 1/2\mp\tau, 0)$ with $\tau=0.075$ for $9K<T<T_N(=15K)$ and a simple antiferromagnetic structure with $\boldsymbol{Q}_2=(1/2, 1/2, 0)$ for $T<9K$[2)]. For another interesting respects, the compound exhibits typical multi-step metamagnetic phase transitions in a external field: at 4.2K six long period modulated structures are induced in the c-axis magnetization process up to 5T[2)]. It is, therefore, interesting to observe pressure effect of those structure, since several numbers of intermediate phases will be imply comparable free energy between those field-induced structures.

The neutron scattering experiments were carried out in the $\boldsymbol{a}^*$-$\boldsymbol{b}^*$ reciprocal lattice plane with a triple axis spectrometer, TAS-2 installed at the $T_{2\text{-}4}$ beam port of JRR-3M in JAERI, and wavelength of incident neutrons was 2.44Å. Pressure was generated hydrostatically and was measured by the change of lattice constant of NaCl single crystal placed together with $TbNi_2Si_2$ single crystal in the cell. Magnetic field was applied along the c-axis up to 5T.

Figure 1 shows the field dependence of several magnetic Bragg peaks under ambient pressure at 1.7K. At low fields below about 1.5T the magnetic structure of this compound changes with a simple commensurate antiferromagnetic structure with a propagation vector $\boldsymbol{Q}_2=(1/2, 1/2, 0)$. On the other hand, four intermediate phases III, IV, V and VI associated with each propagation vectors appear and then vanish successively with increasing

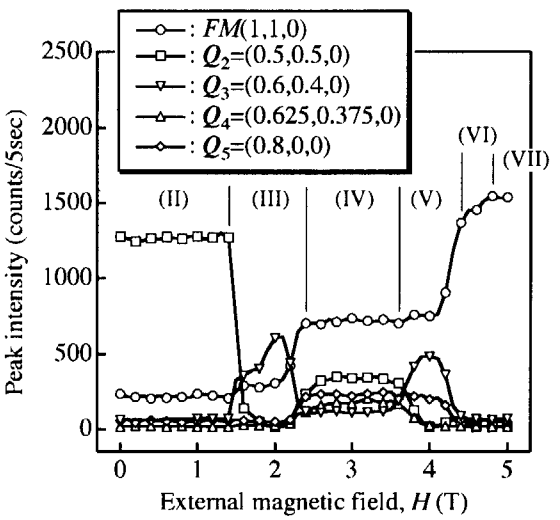

Fig. 1 Field dependence of several magnetic Bragg peaks of $TbNi_2Si_2$ under ambient pressure at 1.7K.

field as well as ferromagnetic component (phase VII) grows step by step.

Figure 2 shows the schematic drawing of the magnetic Bragg peaks in the a^*-b^* reciprocal plane under ambient pressure and under 0.7GPa in various fields at 2K. In an ambient pressure, while according to Blanco *et al.*[3], two intermediate phases (corresponding to phases III and V in Fig.1) under zero-pressure at 1.7K

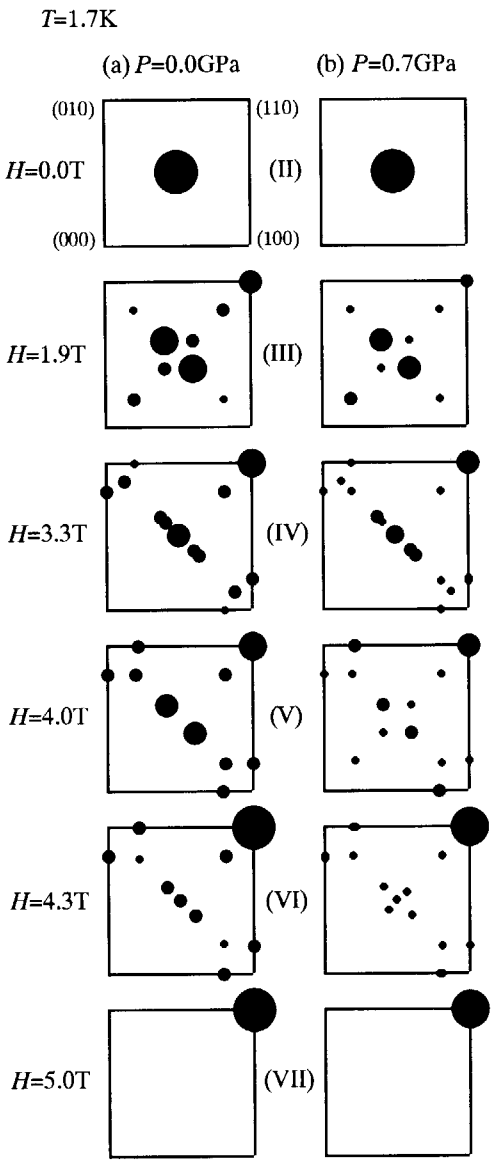

Fig. 2 Schematic drawing of the magnetic Bragg peaks in the a^*-b^* reciprocal plane under ambient pressure (a) and under 0.7GPa (b) in various fields at 1.7K

exists, we found new two phases (phases IV and VI) beside them. The phases III and V are characterized by vanishing of the peaks associated with propagation vector $\boldsymbol{Q}_2$=(1/2, 1/2, 0) and by the appearance of four peaks with the vector $\boldsymbol{Q}_3$=(1/2±τ, 1/2∓τ, 0) with τ=0.1 together with its higher harmonics. Particularly in the phase V the four peaks along the <110> direction vanishes except for an additional four peaks related to $\boldsymbol{Q}_5$=(±0.8, 0, 0) and $\boldsymbol{Q}_5'$=(0, ±0.8, 0). The phases IV and VI are characterized by the peaks associated with the same propagation vector $\boldsymbol{Q}_3$, $\boldsymbol{Q}_5$ and $\boldsymbol{Q}_5'$. No peaks exhibits along <110> direction in both phases. For the phase IV the difference is the existence of another four peaks associated with $\boldsymbol{Q}_4'$=(1/2±τ, 1/2∓τ, 0) with τ=0.125 together with its harmonics.

For pressure up to 0.7GPa in Fig. 2(b), no significant changes were shown up to 3.3T on the spin structure and the propagation vectors for the phases II, III and IV, but in the phases V and VI above 4T additional peaks were observed along <110> direction. The four peaks are indexed with $\boldsymbol{Q}_3'$ for the phase V in 4T, while the peaks for the phase VI in 4.3T are indexed with difference propagation vector $\boldsymbol{Q}_4'$=(1/2±τ, 1/2∓τ, 0) with τ=0.125. The resurgence of the four peaks along <110> direction suggests that two independent domains are present. Expected domains include a single-Q magnetic structure and a double-Q one in this view point. In the case of the former, the domain is characterized by D_1 associated with $\boldsymbol{Q}_3$, or the domain D_2 associated with $\boldsymbol{Q}_3'$, while for the latter both the domains appear[3]. Pressure seems to stabilize the other domain in relatively high fields.

Reference(s)

1) S. Kawano *et al.*, Physica B (1998) in press.
2) H. Fujii, T. Shigeoka, J. Magn. Magn. Mat. **90 & 91** (1990) 115-120
3) J. A. Blanco *et al.*, J. Magn. Magn. Mat. **97** (1991) 4-14

JP9950100

2.8.3 Sapphire-Anvil Cell for Neutron Scattering at High Pressure

A.Onodera, K.Furuno, Y.Ishii[1] and Y.Morii[1]

School of Engineering Science, Osaka University, Toyonaka, Osaka 560-8531, Japan
[1]Japan Atomic Energy Research Institute, Tokai, Ibaraki 319-1106, Japan

Recent development in high-pressure technique, that of diamond-anvil cell (DAC) in particular, has enabled to reach static pressure as high as 500 GPa. X-ray diffraction investigations of pressurized solids are now being carried out up to about 200 GPa. This owes to a combination of the synchrotron source and imaging plate, which permits to study a sample with a volume in the order of 10^{-3} mm^3. Such a small volume will not basically allow neutron scattering measurement where, normally, a volume larger than 10 mm^3 is needed. In fact, this requisite volume can be achieved with a piston-cylinder type apparatus as exemplified by our design [1].

Although the volume requirement can be answered, the highest attainable pressure is limited to a level of a few GPa as far as the piston-cylinder type apparatus is used. To reach higher pressure, opposed anvil designs, DAC for instance, should be employed. With DAC, however, the volume of the sample to be studied is very small. Enlarging the volume within DAC, in turn, costs extraordinarily high.

An alternative way is to use sapphire as the anvil material. The mechanical properties of sapphire are inferior to those of diamond, but the maginitude in the mechanical differences is about an order. In addition, for the same sizes, sapphire is less expensive than diamond by about one order of magnitude.

Under the backgrounds described above, we have designed a sapphire-anvil cell (SAC) for neutron scattering. The cell simply consists of a minipress and a pair of opposed sapphire anvils. A sample with a volume of 2 mm^3 can be studied. The volume is believed to be adequate for neutron scattering to be performed if supermirror is installed at the neutron facility. The pressure attainable with this specific SAC has not been assessed. Instead, we have undertaken prototype studies using small-sized anvils.

The prototype anvil measures 5 mm in diameter and 3 mm in height. The volume of the sample studied is about 10^{-2} mm^3. In principle, the pressure attainable with the opposed anvils is governed by the mechanical strength of the material employed for the anvil, the area of top face, the angle for taper from the top face down to the flank, the mechanical properies of the gasket, and some other issues. Of these, the most important is the taper angle. By fixing the top face at 1 mm in diameter, by aligning the compression axis parallel to the crystallographic *c*-axis, and by using enrolled Cu plate as the gasket, we have studied five different designs with different taper angles. The attainable pressures for each anvil design was known by monitoring the pressure from shift of fluorescence of ruby which was incorporated into the sample space.

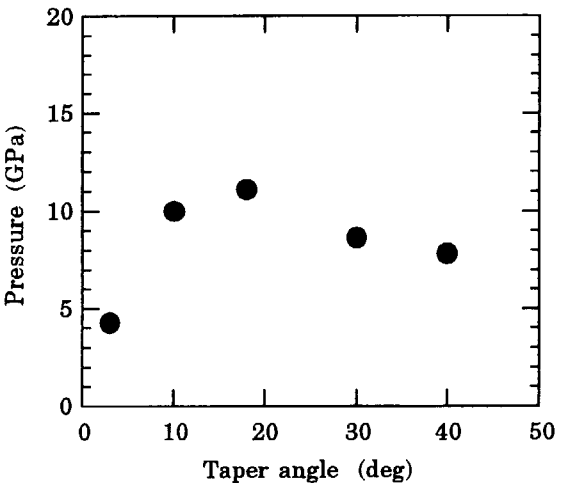

Fig. 1. Pressure generation with different tapers.

Figure 1 shows average of maximum pressure obtained from total of at least five experiments for each anvil design. It appears that the tapering angle is optimized between 10 and 18°. This experimentally derived optimization turned out to be in good agreement with our finite-element analysis. The optimum angle can change relative to the gasket as well as the sample materials.

Reference

[1] A.Onodera *et al.*: Jpn.J.Appl.Phys., 26 (1987) 152.

JP9950101

2.8.4 Polarized Neutron Option using Multilayer Polarizer Controlled under a Very Low External Magnetic Field

K Soyama, M. Hino[1] and S. Tasaki[1]

Japan Atomic Energy Research Institute, Tokai, Ibaraki 319-11
[1]Research Reactor Institute, Kyoto University, Kumatori, Osaka 590-04

A polarized neutron experiment system has been developed to perform the neutron optics experiment and polarized neutron reflectometry at the reflectometer installed on the cold neutron triple-axis spectrometer (LTAS, C2-1) at JRR-3M.

A multilayer of Permalloy/Ge, which was coated in a magnetic field and can work under an external magnetic field less than 50 gauss[1)], was chosen as a spin polarizer and analyzer, because it can be set in a restricted space and control the neutron spin state easily and precisely.

The polarized neutron experiment system consisted of a spin polarizer, a π-flipper coil of Mezei type, and a spin analyzer. Each coil for the polarizer and analyzer consisted of a pair of solenoids : each was made from 200 turns of copper wire of 0.78mm^2 cross section and a inside diameter of solenoid was 90mm. The π-flipper coil consisted of a precession coil and a cancel coil of guide field. The guide coil consisted of a pair of multiwires : each was made from 20 turns of copper wire of 0.78mm^2 and had an area 700mm × 400mm. The current to produce the each magnetic field was controlled by a VAX computer (VAX-2600) which was connected with a remote computer.

Preliminary polarizing efficiency measurement of the multilayer polarizer was performed. Schematic draw of an experimental set-up is shown in Fig. 1. Monochromatic 3.6 Å neutrons were provided by a pyrolytic graphite monochromator (α=0.5°). The collimation of the beam was achieved by a couple of B_4C slits placed at a distance of 0.3 mm to 1.5 m a part. The magnetic field of 20 Gauss was produced at the polarizer and analyzer site between two solenoids, and 5 Gauss was produced at the central site of the guide coil. The polarized neutrons were detected by a position- sensitive proportional counter (ORDELA Moder-1150N) with a spatial resolution, FWHM of 1.0mm. The distance from the center of the polarizer to the detector was 765mm. The polarizing efficiency is defined through the following relation,

$$P = (N_{off} - N_{on}) / (N_{off} + N_{on})$$

where, N_{off} and N_{on} are the number of neutrons which are detected when the spin-flipper are on and off. The first obtained polarizing efficiency was 60%. The coil configuration and magnetic field at each polarizing component are being optimized to enhance the polarizing efficiency.

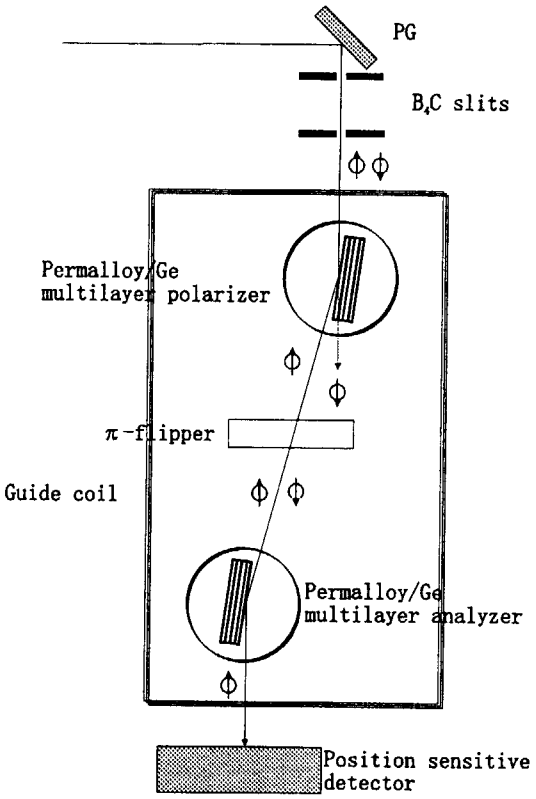

Fig.1 Schematic draw of an experimental set-up for polarization measurement

Reference

[1] T. Kawai, T. Ebisawa, S. Tasaki, T. Akiyoshi, M. Hino, N. Achiwa, Y. Otake and H. Funahashi, J. Phy. Soc. Jpn. **65** (1996) Suupl.A pp.245

JP9950102

2.8.5 Characterization of NiCr Thin Film

K. Soyama

Japan Atomic Energy Research Institute, Tokai, Ibaraki 319-11

In order to enhance the reflectivity of Ni/Ti multilayer mirrors, many improvements have been conducted to decrease the interface roughness of Ni/Ti multilayers, because the large grained Ni layers with a structure of columnar growth lead to rough interfaces with an increase in the number of layers and decrease the reflectivity. In this study, the decrease of crystallization of Ni has been carried out by mixing chromium atoms to Ni layers.

NiCr monolayers with a thickness of 2000Å were deposited with changing Cr mixing ratios in Ni layers. The mixing ratios were 10%, 20%, 30%, 40% and 50%, which were determined by an electron spectroscope for chemical analysis (SHIMADZU ESCA-850). They were coated on Si substrates using an ion beam sputtering technique. The crystal structure and the critical angle of external total reflection of each NiCr monolayer were studied by high angle X-ray diffraction measurements and the neutron reflectometry.

X-ray measurements were performed in a θ-2θ mode using CuK_α radiation (λ=1.54Å). Figure 1 shows the observed patterns from the NiCr monolayers as a function of the Cr mixing ratio. At a mixing ratio of 10%, the Ni(111), Ni(200) and Ni(220) textures are clearly observed. The NiCr layer remains crystalline, and forms the cubic structure. At a mixing ratio of 20%, the intensity of the Ni(111) and Ni(200) peaks are reduced. On the other hand, the intensity of Ni(220) peak increases. At mixing ratios of 30% and 40%, Ni(220) orientation are still observed. The shift of Ni(220) peak to lower angle may be due to the solid solution of chromium atoms into Ni layers and the Ni(220) intensity reduction may be due to Ni alloying or amorphization. At a mixing ratio of 50%, Ni crystalline is not observed, and Cr_3Ni_2 (Tetragonal) peaks are recorded.

The critical angles of external total reflection of the NiCr monolayers were determined by neutron reflectivity measurements. They were performed in a θ-2θ mode using the reflectometer installed on the cold neutron triple-axis spectrometer (LTAS, C2-1) at JRR-3M. The wavelength was 3.8Å and the wavelength resolution was 1%. The dimension of the beam was 0.2mm in width and 10mm in height, and the collimation of the beam was achieved by B_4C and Cd slits placed at a distance of 1.5m apart. The obtained critical angles of total reflection were $0.0182Å^{-1}$, $0.0176Å^{-1}$, $0.0164Å^{-1}$, $0.0156\ Å^{-1}$ and $0.0144Å^{-1}$ as for the Cr mixing ratios of 10%, 20%, 30%, 40% and 50% respectively. The critical angle of total reflection is given by $\phi_c = \lambda(Nb/\pi)^{1/2}$, where N is the average number of atoms per unit volume and b is the bound coherent scattering length. Then Nb were 6.58E+10 cm^{-2}, 6.16E+10 cm^{-2}, 5.38E+10 cm^{-2}, 4.83E+10 cm^{-2} and 4.14E+10 cm^{-2}, which were derived from above mentioned results. They are decreased with an increase in the Cr mixing ratio.

From Fig. 1, it is clearly observed that the Ni(111) and Ni(200) textures are reduced, then it is expected to decrease the interface roughness of Ni/Ti multilayers by adding chromium atoms.

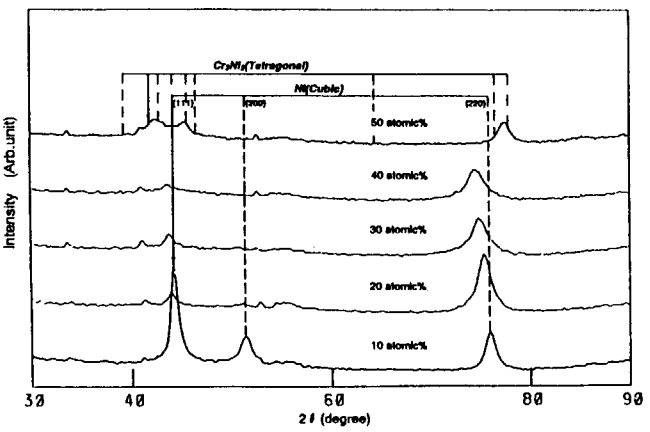

Fig. 1 X-ray diffraction patterns from the NiCr monolayers as a function of Cr mixing ratio.

JP9950103

2.8.6 The actual proof of the optimization of Neutron Imaging Plate

Y.Karasawa and N.Niimura
Japan Atomic Energy Research Institute, Tokai, Ibaraki 319-1195, Japan

We have optimized the neutron imaging plate (NIP) by estimating a color center creation efficiency(ε_{cc}) experimentally and have already reported the preliminary results[1]. In case of the NIP Gd doped, the optimized NIP is realized when the thickness is 200 μm, the molar ratio of PSL material (ϕ_{PSL}) is 0.6 at neutron wavelength 2Å . However, in the estimation of ε_{cc}, gamma-ray effect has not been considered even though it is rather large when ϕ_{PSL} is high.

The optimization of the NIP (Gd doped) was again tried. This time the gamma-ray effect has been carefully considered in the experimental arrangement. The BIX-1 was used for the experiment. In order to reduce the gamma-ray contribution as much as possible, the neutron beam, which was monochromatized by Si(111) firstly and diffracted by PG (004) secondly, was prepared. By irradiating this neutron beam on the NIP, ε_{cc} was estimated as previously reported[1] and the result is shown with the old one in Fig.1.

The old ε_{cc} increases monotonously with ϕ_{PSL}, but the present ε_{cc} tends to saturate around ϕ_{PSL} 0.5. Neutron sensitivity has been calculated by using the new ε_{cc}, and the optimized NIP is given, that is, ϕ_{PSL} is 0.5 when thickness is 200 μm and neutron wavelength is 2.1Å .

The actual proof for the optimization was examined by observing the Bragg reflections on the three different kinds of the NIPs which ϕ_{PSL} = 0.25, 0.5 and 0.75, respectively. Thickness of the three NIPs are the same and are 200μm. The Bragg reflections from a tetragonal hen egg-white lysozyme were measured with the above mentioned NIPs at BIX-II. The exposure time was two hours, neutron wavelength was 2.16Å and the distance between the NIP and the crystal was 30cm.

The results are as follows:

1) The obtained numbers of Bragg spots, whose intensities are higher than 2σ, are 20, 11 and 7 on the NIP of ϕ_{PSL} 0.5, 0.25 and 0.75, respectively.

2) Fig.2 shows the integrated intensity of the four Bragg spots taken on the NIPs of the different ϕ_{PSL} 0.25, 0.5 and 0.75.

It was proved that the optimized NIP provided the best diffraction pattern from the protein single crystal.

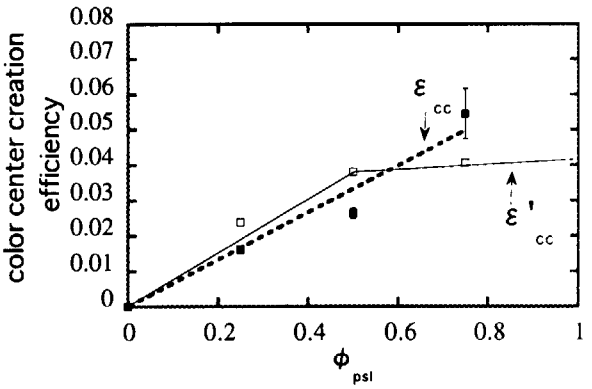

Fig.1 The color center creation efficiency
ε_{cc}: not corrected gamma-ray effect
ε'_{cc}: corrected gamma-ray effect

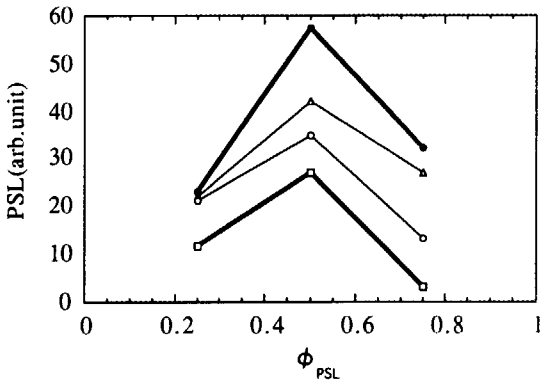

Fig.2 The integrated intensities of HEW-lysozyme Bragg spots

Reference

[1] Y.Karasawa, N.Niimura, A.Moriai, J.Miyahara, K.Takahashi, S.Tazaki, NSL -report 1996

JP9950104

2.8.7 Measurement of background at BIX-1 site using Neutron Imaging Plate

K. Kurihara, I. Tanaka, Y. Karasawa, N. Niimura

Advanced Science Research Center, Japan Atomic Energy Research Institute, Tokai, Ibaraki 319-1195

We are planing to replace the detector of BIX-1 in the reactor site of JRR-3M to a neutron imaging plate (NIP) which has been developed by our group[1]. We have measured background contributing to the NIP around the BIX-1 in order to shield the NIP effectively. The background comes from various origins: incoherent scattering neutron from a sample, air scattering of direct beam, leak from other diffractometers, and so on. We have measured the background in various kinds of conditions and evaluated the components of background.
50% of Gd doped 200μm thick NIP was put at the detector position and at $2\theta = 40°$ and the distance from a sample was 200mm. The wavelength of neutron was 1.06Å. A tetragonal lysozyme crystal grown from D_2O solution was used as the sample whose volume was 4×3×3 mm^3.

The total background at the detector position was classified into four groups for the convenience of the planing of shielding method. The first one (B1) comes from the environment radiation. The second one (B2) consists of leak from other diffractometers and spectrometers. The third one (B3) is composed of leak from a flight tube at BIX-1 site and scattering of direct beam at a beam narrower and the air. The forth one (B4) comes from the sample itself. B1 was measured during suspension of the reactor. To determine the background of each group the NIP was exposed under three conditions such as 1) neutron beam on and with the sample, 2) neutron beam on and without the sample, and 3) neutron beam off.

The results are summarized in Table 1. B1 was 0.1 PSL/h/mm^2. Under the first condition the intensity of the total background (B1+B2+B3+B4) was measured to be 15.9 PSL/h/mm^2. B1+B2+B3 was obtained to be 13.4 PSL/h/mm^2 under the second condition. B1+B2 was determined to be 1.8 PSL/h/mm^2 under the third condition. According to these results B1, B2, and B3 were determined to be 1.7, 11.6, and 2.5 PSL/h/mm^2, respectively.

Shielding from γ-ray must be taken into account because NIP is sensitive to γ-ray. B1 could be restrained by shielding the diffractometer with B_4C and Pb bricks. 20mm thick B_4C reduces neutron background to 0.1%[2] and 30mm thick Pb does γ-ray background to 10%[3]. These bricks could also shield the NIP from the background originated from the beam narrower and the flight tube. The neutron background from the air scattering of direct beam might be repressed by putting a cylinder containing He gas just behind a sample on the way of direct beam. To reduce the forward direction γ-ray background we plan to attach 1mm thick Pb film in front of the NIP, which effect has been well proved[4, 5].

Experimental condition			Source	Intensity (PSL/h/mm^2)
No.	Sample	Beam		
1	with	on	B1-B4	15.9
2	without	on	B1-B3	13.4
3		off	B1,B2	1.8
			B1	0.1

Table 1 The experimental conditions and corresponding sources of the backgrounds and their intensities.

References

1) N. Niimura et al., Nucl. Instr. Methods **A349** (1994) 521-525.
2) Y. Karasawa, Master Thesis, Tohoku University (1995).
3) Y. Karasawa et al., This report **12** (1997) 91-92.
4) Y. Karasawa, Doctor Thesis, Tohoku University (1998).
5) S. Kumazawa et al., This report (1998).

JP9950105

2.8.8 Shielding Neutron Imaging Plate from Forward Direction γ-ray

S.Kumazawa, Y.Karasawa and N.Niimura
Advanced Science Research Center
Japan Atomic Energy Research Institute, Tokai, Ibaraki 319-1195, Japan

We have developed a neutron imaging plate (NIP), which has been widely adapted in the fields of neutron diffractometry and radiography. The NIP is superior to the conventional 2-dimensional ^{3}He type detector with respect to high spatial resolution, wide dynamic range, high capture efficiency for thermal neutrons, a wide sensitive area. There is, however, a problem to be overcome, when the NIP is applied in case that the background of γ-ray is comparable to that of neutrons. The NIP is sensitive to not only neutron but also γ-ray which becomes a background noise. The NIP can not discriminate γ-ray from neutrons, since the NIP is an integration type detector. For example, the background of γ-ray in the reactor site is about 10 times larger than that in the guide hall. It must be considered that the NIP is shielded from γ-ray in order that the neutron signal is effectively captured on the NIP.

For the environment γ-ray, the effective shield can be achieved by enclosing the NIP with Pb bricks of an appropriate thickness. For the γ-ray coming from a sample direction, the background noise of γ-ray will not be avoided by the above method. One of the improvement way is to put a thin Pb foil on the NIP surface. The Pb foil has high transparency for the neutron signal and dumps low energy γ-ray by the absorption effect. In this study, the effect of γ-ray shielding by using the various thick Pb foils is examined.

Diffraction spots, which consist of neutrons, and background around the spots, which consist of both neutron and γ-ray, were measured with the BIX-I diffractometer. The sample was hen egg-white lysozyme crystal and the exposure time of one frame was 20 min. The integrated intensities of several diffraction spots and the background intensities of corresponding spots were sampled. The integrated intensities of neutron diffraction spots do not depend on the thickness of Pb foil so much. The reduction of neutron intensities is about 3 % even if the thickness of Pb foil is 3 mm. On the other hand, the background intensities are exponentially dumped with increasing the thickness of Pb foil. Fig. 1 shows the neutron signal ratio to the background intensities. As shown in the figure, the ratios tend to saturate, when the Pb foil is thicker than 1.5 mm.

It is concluded that the signal to noise ratio is improved about twice, when a 1.5 mm thick Pb foil is put on the NIP surface.

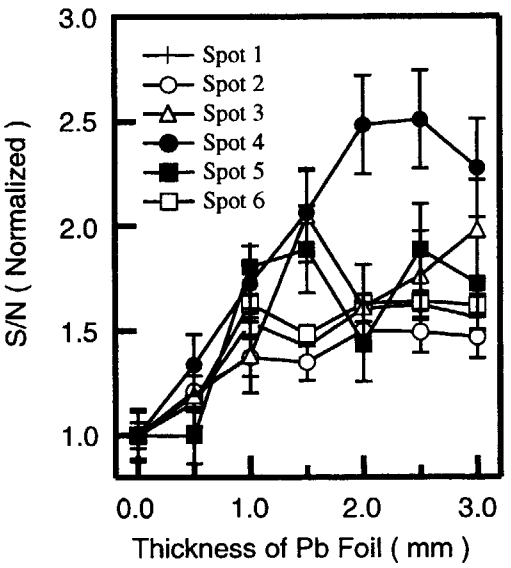

Fig.1 S/N ratios plotted against thickness of Pb foil.

JP9950106

2.8.9 Upgrade of the Wide Angle Neutron Diffractometer

Y.Ishii, H.R.Child*, J.Suzuki, S.Katano, K.Aizawa, Y.Morii and J.A.Fernandez-Baca*

ASRC, Japan Atomic Energy Research Institute, 319-11 Japan

* Solid State Division, Oak Ridge National Lab., Oak Ridge, TN 37831, USA

In 1984, a wide angle neutron diffractometer (WAND) was installed at the HB-4A port in the High Flux Isotope Reactor at Oak Ridge National Lab. under the US-Japan cooperative research in the field of neutron scattering. The WAND is a unique machine which can measure the neutron scattering intensity over the wide diffraction angles at a time from a single crystal in the flat corn configuration. Recently, it became difficult for us to keep the WAND's detector in good condition against it's age and upgrade of the WAND had been strongly requested from many scientists to carry new experiments. Therefore, an upgrade project was planned and had been started in 1993. In 1998, a new detector is constructed and installed in the WAND.

The new detector has individual 624 active anodes with 0.2 deg. pitches and cover the range about 126 deg. in scattering angle. Individual electronics system such as discriminators, pre-amplifiers, data buffers and micro processors is connected to each anode wire, behind the detector. This detector has been controlled by a computer with a serial communication line. This computer is also controlled as a slave by a master computer of the data acquisition system.

Specification of the new WAND was evaluated with some standard powder materials and single crystals. Evaluated value of some important characteristics of the detector are 1) Maximum neutron counting rate per anode(pixel): $2x10^5$ neutrons/s and 2) angular resolution: 0.25 degrees. This new detector has the highest counting capability and resolution among the similar type detectors in the world. In uniform counting test with vanadium rod, there is no major difference in the counting efficiency in 624 pixels.

Figure 1 shows an experimental result of the crystal scans of $LuFe_2O_4$ as a demonstration.

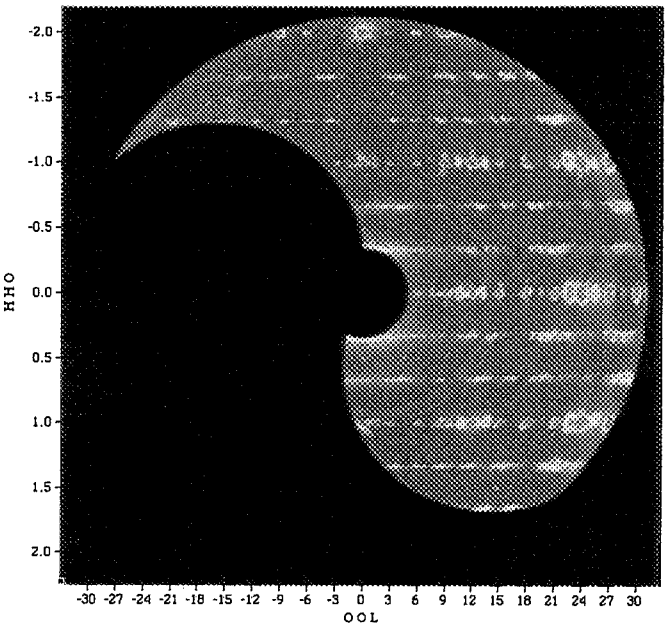

Fig.1. Diffraction pattern of $LuFe_2O_4$ at room temperature.

This figure was obtained from 800 crystal scans with 0.25 deg. step. Measuring time per a crystal scan was 90 sec in this experiment. In this figure, one can see the diffuse scattering pattern at Q= (H$\pm$1/3, H$\pm$1/3, L-1/2) due to the incommensurate charge ordering in this material. Because the specimen used this experiments, unfortunately, has three large grains at least, some extra peaks appeared in this picture.

This new WAND is a high performance diffractometer having the high counting rate and the high resolution.

JP9950107

2.8.10 3-dimensional Small-angle Neutron Scattering (3D-SANS)

J.Suzuki
Japan Atomic Energy Research Institute, Tokai, Ibaraki 319-1105

Small-angle neutron scattering (SANS) is a useful technique to investigate the submicron structures inside materials. Usually, 1- or 2-dimensional SANS data sets, namely, $I(q)$ or $I(q_x,q_y)$, are obtained by measurements using a 2-dimensional detector. However, it is not enough to study anisotropic scattering, because in genaral the anisotropic scattering is not limited in the 1- or 2-dimensional reciprocal space. I then show the importance of measuring the SANS in 3-dimensional reciprocal space. The 3-dimensional data set $I(q_x,q_y,q_z)$ can be easily obtained just by rotating a sample about the vertical axis. If an orthogonal (q_x,q_y,q_z) coordinate is defined as the q_y axis is parallel to the vertical direction, and the q_z axis is antiparallel to the beam direction, each component can be expressed as

$$q_x(i,j)=k_i\cdot x(i)/L(i,j)\cdot\cos(\omega_s) - k_i\cdot(1+z(i)/L(i,j))\cdot\sin(\omega_s),$$

$$q_y(i,j)=k_i\cdot y(j)/L(i,j),$$

$$q_z(i,j)=k_i\cdot x(i)/L(i,j)\cdot\sin(\omega_s) + k_i\cdot(1+z(i)/L(i,j))\cdot\cos(\omega_s), \quad (i,j=1,nch)$$

where (x,y,z) denotes the position of a detector element, L is a distance between the element and the center of a sample. k_i is a wavenumber of the incident neutrons. and ω_s defines a rotation angle. (See Fig.1)

Figure 2 is an example of a 3-dimensional SANS pattern. The sample demonstrated here is a single crystal of a superconductor $CeRu_2$ [1]. The SANS measurements were carried out at RT. The sample was rotated 3 degrees a step around the q_y axis. The data for totally 60 steps were combined together by means of a visuallization software. Diffuse streaks were observed along the crystalline [100], [110], and [111] axis of the sample. This result suggests the existence of the compositional inhomogeneitiy inside the sample correlated well with the crystalline symmetry. In this case, plates with ~50 nm in thickness align along the highly symmetric plane.

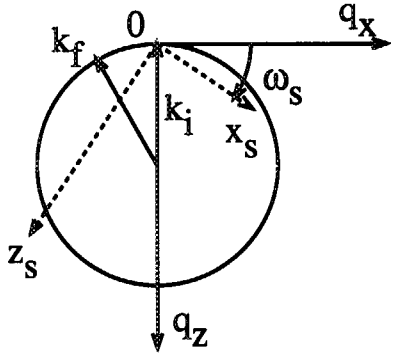

Fig.1 Scattering geometry. The q_z axis is antiparallel to the incident neutron beam. The orientation of the sample can be rotated about the vertical axis. The symbol ω_s denotes the rotation angle.

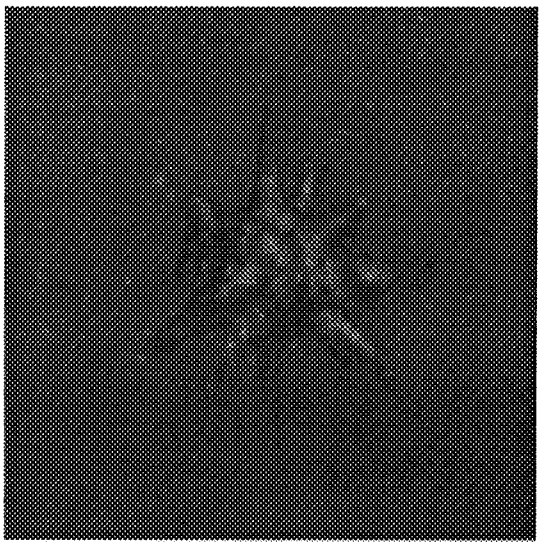

Fig.2 An example of the 3-dimensional SANS pattern. The sample studied is a single crystal of a *f*-electron superconductor $CeRu_2$. Diffuse streaks are observed along the crystalline [100]-, [110]-, and [111]-axis. The q_z axis is nearly perpendicular to this sheet.

References

[1] J.Suzuki et al., Physica B241-243 (1998) 871.

Appendix A

Neutron Scattering Research Committee of 1997

(Chairman)	Nobuyoshi	Wakabayashi	Professor, Faculty of Science and Technology, Keio University
(Vice-Chairman)	Kunihisa	Soda	Deputy Director General, Tokai Research Establishment
	Hironobu	Ikeda	Professor, National Laboratory for High Energy Physics
	Masahiko	Utsuro	Professor, Research Reactor Institute, Kyoto University
	Yasuo	Endoh	Professor, Graduate School of Science, Tohoku University
	Koichi	Katsumata	Principal Researcher, The Institute of Physical and Chemical Research
	Nobuhiro	Go	Professor, Faculty of Science, Kyoto University
	Takeji	Hashimoto	Professor, Graduate School of Engineering, Kyoto University
	Makoto	Hayashi	Department Manager, Mechanical Engineering Research Laboratory, Hitachi Ltd.
	Hironobu	Fujii	Professor, Faculty of Integrated Arts and Sciences, Hiroshima University
	Yasuhiko	Fujii	Professor, the Institute for Solid State Physics, The University of Tokyo
	Yasuo	Yamaguchi	Professor, Institute for Materials Research, Tohoku University
	Takehiko	Mukaiyama	Director, Center for Neutron Science, Tokai Research Establishment
	Osamu	Shimomura	Principal Scientist, Department of Synchrotron Radiation Facilities Project, Kansai Research Establishment
	Hiroshi	Katsuta	Director, Department of Materials Science and Engineering, Tokai Research Establishment
	Masakazu	Tanase	Deputy Director, Advanced Science Research Center
	Fumio	Sakurai	General Manager, Department of Research Reactor, Tokai Research Establishment
	Nobuo	Niimura	Invited Researcher, Advanced Science Research Center
	Toru	Ogawa	Principal Scientist, Department of Chemistry and Fuel Research, Tokai Research Establishment
	Yasusada	Yamada	Invited Researcher, Advanced Science Research Center
	Yukio	Morii	Principal Scientist, Advanced Science Research Center
(Secretary)	Shuji	Takagi	Head, Advanced Science Research Center
	Susumu	Katano	Principal Scientist, Advanced Science Research Center
(Observer)	Naoto	Metoki	Principal Scientist, Advanced Science Research Center
	Shoichi	Ohtomo	Office of Planning, Tokai Research Establishment

Appendix B

Themes of Cooperative Research Projects with Universities in JFY 1997

1.	Hydrogen Transfer in Photoisomerization of Cobaloxime Complexes	Y. Ohashi	Tokyo Inst. of Tech.
2.	Mechanism of Crystal Growth of Protein: Formation of Oligomers and Its Role in Crystallization	H. Ooshima	Osaka City Univ.
3.	Antiferromagnetism of $CuGe_{1-x}Si_xO_3$	J. Akimitsu	Aoyama Gakuin Univ.
4.	Vortex Structures in Large Anisotropic Superconductors	K. Osamura	Kyoto Univ.
5.	Neutron Scattering Study on Mesoscopic Scale System of Flux Line Lattice etc.	S. Shamoto	Tohoku Univ.
6.	Magnetism and Structure of Uranium Compounds	T. Takabatake	Hiroshima Univ.
7.	Study of Correlation between Magnetism and Superconductivity in a Uranium Intermetalic Compound	T. Komatsubara	Tohoku Univ.
8.	Magnetic Structure and Magnetic Excitaiton in the Strongly Correlated Ce-pnictides Systems	M. Kohgi	Tokyo Metropolitan Univ.
9.	Structural Fluctuations and Transport Properties in Oxides Conductors	Y. Yamada	Waseda Univ.
10.	Magnetic Structure and Lattice Distortion on Frustrated Magnets RMn_2	M. Shiga	Kyoto Univ.
11.	Studies on Pattern Formation in Multicomponent Polymer Alloy	T. Hashimoto	Kyoto Univ.
12.	Static Hierarchical Structure of Multicomponent Macromolecular Systems	Y. Izumi	Yamagata Univ.
13.	Magnetic Structures of Insulating States of Low Dimensional Organic Superconductors	Y. Nogami	Okayama Univ.
14.	Development of Dilution Refrigerators for Neutron Experiments	M. Kubota	The Univ. of Tokyo
15.	Imaging of Hydrogen Nucleus in the Hydrogen Bond by Maximum Entropy Method	M. Sakata	Nagoya Univ.

16.	Applied Development of Neutron Reflectometry to Polymer Interfaces	Y. Matsushita	The Univ. of Tokyo
17.	Study of Neutron Optics with Dynamical Diffraction Effect	T. Takahashi	The Univ. of Tokyo
18.	Studies on Damage Inspection of Engineering Metallic Materials	T. Horikawa	Ryukoku Univ.
19.	Study of Crystal Structure and Phase Transformation at High Pressure	A. Onodera	Osaka Univ.
20.	Study of Structural Phase Transition in Dielectric Compounds at Low Temperature	Y. Noda	Chiba Univ.
21.	Study on Crystal Structures and Physical Properties of Electronic Device Materials	T. Kajitani	Tohoku Univ.
22.	Crystallographic Study of Protonic and Ionic Conduction	T. Nagasaki	Nagoya Univ.
23.	Crystal Distortion and Magnetic Structure of γ–Mn Alloys	T. Hori	Shibaura Inst. Tech.
23.	Crystal Structure and Magnetism of Intercalation Compounds	Y. Tazuke	Ibaraki Univ.
24.	Magnetic Structure of Lanthanide Complex Oxides	Y. Hinatsu	Hokkaido Univ.

Appendix C

Themes of Cooperative Research Projects with Private Enterprises and National Laboratories in JFY 1997

1.	Residual Stress Measurement by Neutron Diffraction	M. Hayashi	Hitachi Ltd.
2.	SANS Study on Miscibility and Phase Separation of Multicomponent Polymer Blends	H. Jinnai	Japan Science and Technology Corporation
3.	PNO-observation of the Ni-based Superalloy Single Crystals	A. Yoshinari	Hitachi Ltd.

Appendix D

Publication List in the Period of JFY 1997

1. Neutron Powder Diffraction Studies of Rhombohedral Y_2Fe_{17} and $Y_2Fe_{17}N_{3.1}$
   K. Koyama, T. Kajitani, Y. Morii, H. Fujii, and M. Akayama
   Phys. Rev. B **55-17** (1997) 11414-11421

2. Elastic and Inelastic Neutron Scattering Studies on the Martensitic Phase Transformation in Cu-39 at%Zn Alloy
   Y. Kuroiwa, A. Konishi, T. Shobu, Y. Noda, N. Fuchizaki, Y. Morii, Y. Yamada, H. R. Child, H. Chou, and S. C. Moss
   J. Phys. Soc. Japan **66-4** (1997) 1033-1043

3. Quasielastic Neutron Scattering Study on Rotational Aromatic Groups of a Thermotropic Copolyester (Vectra)
   S. Koizumi
   J. Chem. Phys. **107-2** (1997) 603-612

4. Strong Correlation between Magnetism and Superconductivity in a Single Crystalline UNi_2Al_3 and UPd_2Al_3
   N. Sato, N. Aso, N. Tateiwa, N. Koga, T. Komatsubara, and N. Metoki
   Physica B **230-232** (1997) 367-369

5. Coupling between Magnetic and Superconducting Orderparameters and Evidence for the Spin Excitation Gas in the Superconducting State of a Heavy Fermion Superconductor UPd_2Al_3
   N. Metoki, Y. Haga, Y. Koike, N. Aso, and Y. Onuki
   J. Phys. Soc. Japan **66-9** (1997) 2560-2563

6. Mössbauer and Neutron Diffraction Studies of BCC Cr-Fe-Mn Ternary Alloys
   Y. Tsuchiya, H. Nakamura, S. Murayama, K. Hoshi, Y. Shimojyo, Y. Morii, and Y. Hamaguchi
   Physica B **237-238** (1997) 446-448

7. Diffuse Neutron Scattering of the High Temperature Phase of Fe_3O_4
   K. Siratori, Y. Ishii, Y. Morii, S. Funahashi, and A. Yanase
   J. Phys. IV France **7** (1997) Colloque C1, Supplément au Journal de Physique III de mars 1997 C1-585

8. Magnetic Properties of La-Ni System
   Y. Tazuke, M. Abe, and S. Funahashi
   Physica B **237-238** (1997) 559-560

9. Progress Report on Neutron Scattering Research (1996.04.01-1997.03.31)
   (eds.) Y. Ishii, J. Suzuki, and S. Fujiwara
   JAERI-Review **97-012**

10. Recent Development of Basic Magnetism in Interstitially-Modified Rare-Earth Iron Nitrides $R_2Fe_{17}N_3$
H. Fujii, K. Koyama, K. Tatami, S. Mitsudo, M. Motokawa, T. Kajitani, Y. Morii, and P. C. Canfield
Physica B **237-238** (1997) 534-540

11. Neutron Scattering Study of the Magnetic Structure of $DyCu_2$
Y. Koike, N. Metoki, Y. Morii, Y. Yoshida, R. Settai, and Y. Ōnuki
J. Phys. Soc. Japan **66-12** (1997) 4053-4054

12. X-Ray Rocking Curve Study of the Strain Profile Formed by MoV Ion Implantation into (III) Silicon Wafers
M. Kuribayashi, K. Takumi, A. Inoue, H. Tanaka, H. Tomita, Yi-Chao Jiang, H. Katoh, K. Ishida, K. Aizawa, S. Okayasu, H. Tomimitsu, and Y. Kazumata
Japanese J. Appl. Phys. **36** (1997) 7296-7301

13. Small-angle Neutron Scattering Study of Magnetic Microstructures in Co-Cr Films
J. Suzuki, H. Takei, Y. Maeda, and Y. Morii
J. Mag. Mag. Mater. **184** (1998) 116-125

14. Re-Examination of the Autiferroelectric Structure of $PbZrO_3$
T. Fujishita and S. Katano
J. Phys. Soc. Japan **66-11** (1997) 3484-3488

15. Observation of Pressure-Induced Superconductivity of Sulfur
S. Yoneya, M. I. Erements, K. Shimizu, M. Kobayashi, and K. Amaya
J. Phys. Soc. Japan **66-9** (1997) 2564-2565

16. Magnetic Phase Diagram of the Spin-Peierls and Antiferromagnetic System $CuGe_{1-x}Si_xO_3$
S. Katano, O. Fujita, J. Akimitsu, M. Nishi, K. Kakurai, and Y. Fujii
Physical Rev. B **57-17** (1998) 10280-10283

17. X-ray Absorption Fine Structure and Neutron Diffraction Analyses of De-intercalation Behavior in the $LiCoO_2$ and $LiNiO_2$ Systems
I. Nakai, K. Takahashi, Y. Shiraishi, T. Nakagome, F. Izumi, Y. Ishii, F. Nishikawa, and T. Konishi
J. Power Sources **68** (1997) 536-539

18. Spin Correlation in the Dilutied Triangular-lattice Antiferromagnet $LuFeMgO_4$
Y. Todate, E. Himoto, C. Kikuta, M. Tanaka, and J. Suzuki
Phys. Rev. B **57-1** (1998) 485-491

19. Neutron-diffraction Study on Na- and K-jarosites
T. Inami, S. Maegawa, and M. Takano
J. Mag. Mag. Mater. **177-181** (1998) 752-753

20. Neutron Scattering Study of the Correlation of Magnetism and Superconductivity in heavy-fermion superconductor UPd_2Al_3
N. Metoki, Y. Haga, Y. Koike, N. Aso, and Y. Onuki
J. Mag. Mag. Mater. **177-181** (1998) 449-450

21. Neutron Diffraction and Mössbauer Measurements for Magnetism of BCC Cr-Fe-Mn Alloys
Y. Tsuchiya, H. Nakamura, S. Murayama, K. Hoshi, Y. Shimojo, Y. Morii, and Y. Hamaguchi
J. Mag. Mag. Mater. **177-181** (1998) 1447-1448

22. Neutron Diffracition Study on hp 13 type $M_{7-x}Mn_xGe_6$ (M=Co, Fe)
T. Hori, Y. Tsuchiya, S. Funahashi, M. Akimitsu, Y. Shimojo, H. Shiraishi, and Y. Nakagawa
J. Mag. Mag. Mater. **177-181** (1998) 1425-1426

23. Neutron Laue Diffractometry with an Imaging Plate Provides an Sffective Data Collection Regime for Neutron Protein Crystallography
N. Niimura, Y. Minezaki, T. Nonaka, J.-C. Castagna, F. Cipriani, P. Hoeghoej, M. S. Lehmann, and C. Wilkinson
Nature, Structural Biology, **4** (1997) 909-914

24. Direct Observation of Correlation between Crystalline-State Deuterium Transfer and Racemization of 1-Cyanoethyl Cobaloxime Complex by Neutron Diffraction
T. Ohhara, H. Uekusa, Y. Ohashi, I. Tanaka, S. Kumazawa, and N. Niimura
Chem. Lett. (1998) 365-366

This is a blank page.

国際単位系（SI）と換算表

表1　SI基本単位および補助単位

量	名称	記号
長さ	メートル	m
質量	キログラム	kg
時間	秒	s
電流	アンペア	A
熱力学温度	ケルビン	K
物質量	モル	mol
光度	カンデラ	cd
平面角	ラジアン	rad
立体角	ステラジアン	sr

表2　SIと併用される単位

名称	記号
分，時，日	min, h, d
度，分，秒	°, ′, ″
リットル	l, L
トン	t
電子ボルト	eV
原子質量単位	u

1 eV=1.60218×10^{-19}J

1 u=1.66054×10^{-27}kg

表3　固有の名称をもつSI組立単位

量	名称	記号	他のSI単位による表現
周波数	ヘルツ	Hz	s^{-1}
力	ニュートン	N	$m\cdot kg/s^2$
圧力，応力	パスカル	Pa	N/m^2
エネルギー,仕事,熱量	ジュール	J	N·m
工率，放射束	ワット	W	J/s
電気量，電荷	クーロン	C	A·s
電位，電圧，起電力	ボルト	V	W/A
静電容量	ファラド	F	C/V
電気抵抗	オーム	Ω	V/A
コンダクタンス	ジーメンス	S	A/V
磁束	ウェーバ	Wb	V·s
磁束密度	テスラ	T	Wb/m^2
インダクタンス	ヘンリー	H	Wb/A
セルシウス温度	セルシウス度	℃	
光束	ルーメン	lm	cd·sr
照度	ルクス	lx	lm/m^2
放射能	ベクレル	Bq	s^{-1}
吸収線量	グレイ	Gy	J/kg
線量等量	シーベルト	Sv	J/kg

表4　SIと共に暫定的に維持される単位

名称	記号
オングストローム	Å
バーン	b
バール	bar
ガル	Gal
キュリー	Ci
レントゲン	R
ラド	rad
レム	rem

1 Å=0.1nm=10^{-10}m

1 b=100fm^2=10^{-28}m^2

1 bar=0.1MPa=10^{5}Pa

1 Gal=1cm/s^2=10^{-2}m/s^2

1 Ci=3.7×10^{10}Bq

1 R=2.58×10^{-4}C/kg

1 rad=1cGy=10^{-2}Gy

1 rem=1cSv=10^{-2}Sv

表5　SI接頭語

倍数	接頭語	記号
10^{18}	エクサ	E
10^{15}	ペタ	P
10^{12}	テラ	T
10^{9}	ギガ	G
10^{6}	メガ	M
10^{3}	キロ	k
10^{2}	ヘクト	h
10^{1}	デカ	da
10^{-1}	デシ	d
10^{-2}	センチ	c
10^{-3}	ミリ	m
10^{-6}	マイクロ	μ
10^{-9}	ナノ	n
10^{-12}	ピコ	p
10^{-15}	フェムト	f
10^{-18}	アト	a

(注)

1．表1－5は「国際単位系」第5版，国際度量衡局1985年刊行による。ただし，1 eVおよび1 uの値はCODATAの1986年推奨値によった。

2．表4には海里，ノット，アール，ヘクタールも含まれているが日常の単位なのでここでは省略した。

3．barは，JISでは流体の圧力を表わす場合に限り表2のカテゴリーに分類されている。

4．EC閣僚理事会指令ではbar，barnおよび「血圧の単位」mmHgを表2のカテゴリーに入れている。

換算表

力	N(=10^{5}dyn)	kgf	lbf
	1	0.101972	0.224809
	9.80665	1	2.20462
	4.44822	0.453592	1

粘度　1 Pa·s(N·s/m^2)=10 P(ポアズ)(g/(cm·s))

動粘度　1m^2/s=10^{4}St(ストークス)(cm^2/s)

圧力	MPa(=10bar)	kgf/cm^2	atm	mmHg(Torr)	lbf/in^2(psi)
	1	10.1972	9.86923	7.50062×10^3	145.038
	0.0980665	1	0.967841	735.559	14.2233
	0.101325	1.03323	1	760	14.6959
	1.33322×10^{-4}	1.35951×10^{-3}	1.31579×10^{-3}	1	1.93368×10^{-2}
	6.89476×10^{-3}	7.03070×10^{-2}	6.80460×10^{-2}	51.7149	1

エネルギー・仕事・熱量	J(=10^7 erg)	kgf·m	kW·h	cal(計量法)	Btu	ft·lbf	eV
	1	0.101972	2.77778×10^{-7}	0.238889	9.47813×10^{-4}	0.737562	6.24150×10^{18}
	9.80665	1	2.72407×10^{-6}	2.34270	9.29487×10^{-3}	7.23301	6.12082×10^{19}
	3.6×10^6	3.67098×10^5	1	8.59999×10^5	3412.13	2.65522×10^6	2.24694×10^{25}
	4.18605	0.426858	1.16279×10^{-6}	1	3.96759×10^{-3}	3.08747	2.61272×10^{19}
	1055.06	107.586	2.93072×10^{-4}	252.042	1	778.172	6.58515×10^{21}
	1.35582	0.138255	3.76616×10^{-7}	0.323890	1.28506×10^{-3}	1	8.46233×10^{18}
	1.60218×10^{-19}	1.63377×10^{-20}	4.45050×10^{-26}	3.82743×10^{-20}	1.51857×10^{-22}	1.18171×10^{-19}	1

1 cal= 4.18605J（計量法）

= 4.184J（熱化学）

= 4.1855J（15℃）

= 4.1868J（国際蒸気表）

仕事率　1 PS(仏馬力)

= 75 kgf·m/s

= 735.499W

放射能	Bq	Ci
	1	2.70270×10^{-11}
	3.7×10^{10}	1

吸収線量	Gy	rad
	1	100
	0.01	1

照射線量	C/kg	R
	1	3876
	2.58×10^{-4}	1

線量当量	Sv	rem
	1	100
	0.01	1

(86年12月26日現在)

PROGRESS REPORT ON NEUTRON SCATTERING RESEARCH (APRIL 1, 1997 – MARCH 31, 1998)